Functional Dynamics of Ribonucleic Acids

—

Development and Application of Spectroscopic Tools

Dissertation
zur Erlangung des Doktorgrades
der Naturwissenschaften

vorgelegt beim Fachbereich 14
der Goethe-Universität Frankfurt am Main

von
Andreas Reuß
aus Bamberg

Frankfurt am Main 2016
(D30)

Vom Fachbereich 14 der

Goethe-Universität Frankfurt am Main als Dissertation angenommen.

Dekan	Prof. Dr. Michael Karas
1. Gutachter	Prof. Dr. Josef Wachtveitl
2. Gutachter	Prof. Dr. Thomas Prisner

Datum der Disputation: _____

Contents

Abbreviations

1PyA ..... 2-(1-pyrenylethynyl) adenosine
2PyA ..... 2-(2-pyrenylethynyl) adenosine
4PyA ..... 2-(4-pyrenylethynyl) adenosine
5′-UTR ..... upstream untranslated region

AD ..... aptamer domain
AOM ..... acousto-optical modulator

BO ..... Born-Oppenheimer
btuB riboswitch ..... coenzyme-B_{12}-binding riboswitch

CD ..... circular dichroism
CPA ..... chirped-pulse amplification
cps ..... counts per second
CT ..... charge transfer
cw ..... continuous wave

DAS ..... decay-associated spectrum/spectra
ΔG^o ..... change of the standard (folding) free energy
$\Delta G^o_{\mathbf{a}}$ ..... change of the apparent standard (folding) free energy
ΔH^o ..... change of the standard (folding) free enthalpy
Δ**SASA** ..... change of the solvent-accessible surface area
ΔS^o ..... change of the standard (folding) free entropy
DOX ..... doxycycline
ds ..... double stranded

E(E)S ..... excited (electronic) state
ε_r ..... relative dielectric constant

FC ..... Franck-Condon
FMN ..... flavin mononucleotide
FWHM ..... full width at half maximum

GLA ..... global lifetime analysis
glmS glucosamine-6-phosphate
GVD ..... group-velocity dispersion

HOMO ..... highest occupied molecular orbital

IC ..... internal conversion
IRF ..... instrument response function
ISC ..... intersystem crossing
ITC ..... isothermal titration calorimetry
IVR ..... intramolecular vibrational (energy) redistribution

k_B ..... Boltzmann constant
K_d ..... dissociation constant
$k_{\mathbf{IC}}$ ..... rate constant of internal conversion
$k_{\mathbf{n}}$ ..... non-radiative rate constant
$k_{\mathbf{r}}$ ..... radiative rate constant
$k_{\mathbf{ISC}}$ ..... rate constant of intersystem crossing
$k_{\mathbf{IVR}}$ ..... rate constant of intra-/intermolecular vibrational (energy) relaxation

LDA ..... lifetime-density analysis
LDM ..... lifetime-density map
LE ..... locally excited
LED ..... light-emitting diode
LUMO ..... lowest unoccupied molecular orbital

MICT ..... mesomeric intramolecular charge transfer
miRNA ..... micro ribonucleic acid
MO ..... molecular orbital
mRNA ..... messenger ribonucleic acid

ncRNA ..... non-coding ribonucleic acid
Nd:YAG ..... neodymium doped yttrium-aluminium garnet
NOPA ..... non-collinear optical parametric amplification

OA ..... optical activity
OD ..... optical density
OPA ..... optical parametric amplification

PAA ..... polyacralamide
PBS ..... potassium phosphate
PES ..... potential-energy surface
ϕ_f ..... fluorescence quantum yield
PMT ..... photomultiplier
pre-mRNA ..... preprocessed messenger ribonucleic acid
Py ..... pyrene
PyA ..... 2-(pyrenylethynyl) adenosine

RS ..... riboswitch
rms(d) ..... root-mean-square (deviation)
rRNA ..... ribosomal ribonucleic acid

SAM ..... S-adenosyl methionine
SASA ..... solvent-accessible surface area
scaRNA ..... small Cajal body ribonucleic acid
SCC ..... sodium cacodylate
SE ..... stimulated emission
SHG ..... second-harmonic generation
siRNA ..... small interfering ribonucleic acid
snoRNA ..... small nucleolar ribonucleic acid
SPM ..... self-phase modulation
SR ..... switching region
ss ..... single stranded

tRNA ..... transfer ribonucleic acid
τ_f ..... fluorescence lifetime
TA(S) ..... transient absorption (spectroscopy)
TC ..... tetracycline
TC aptamer ..... tetracycline-binding aptamer
TCSPC ..... time-correlated single-photon counting
TICT ..... twisted intramolecular charge transfer
Ti:Sa ..... titan doped sapphire

T_m ..... melting temperature
T^o ..... standard ambient temperature, 298 K
TPP ..... thiamine pyrophosphate
TTS ..... transit-time spread

v_g ..... group velocity

WC ..... Watson-Crick
WT ..... wildtype

List of Figures

List of Tables

Publications

Peer-reviewed publications with contributions from the author of this thesis.

Journal Contributions

Photo-physical properties of 2-(1-ethynylpyrene)-adenosine: influence of hydrogen bonding on excited state properties

P. Trojanowski, J. Plötner, C. Grünewald, F. F. Graupner, C. Slavov, **A. J. Reuss**, M. Braun, J. W. Engels, and J. Wachtveitl

Physical Chemistry Chemical Physics, 2014, **16**, 13875 – 13888, doi: 10.1039/c4cp01148a

Discrimination between FRET and non-FRET quenching in a photochromic CdSe quantum dot/dithienylethene dye system

L. Dworak, **A. J. Reuss**, M. Zastrow, K. Rück-Braun, and J. Wachtveitl

Nanoscale, 2014, **6**, 14200 – 14203, doi: 10.1039/c4nr05144k

Tetracycline Determines the Conformation of Its Aptamer at Physiological Magnesium Concentrations

A. J. Reuss, M. Vogel, J. E. Weigand, B. Suess, and J. Wachtveitl

Biophysical Journal, 2014, **107**, 2953 – 2962, doi: 10.1016/j.bpj.2014.11.001

Charge reduction and thermodynamic stabilization of substrate RNAs inhibit RNA editing

W.-M. Leeder, **A. J. Reuss**, M. Brecht, K. Kratz, J. Wachtveitl, and H. U. Göringer

PLOS ONE, 2015, **10**, e0118940 (17 pages), doi: 10.1371/journal.pone.0118940

The Three Possible 2-(Pyrenylethynyl) Adenosines: Rotameric Energy Barriers Govern the Photodynamics of These Structural Isomers

A. J. Reuss, C. Grünewald, M. Braun, J. W. Engels, and J. Wachtveitl

ChemPhysChem, published online january 2016, **0000**, 0 – 0, doi: 10.1002/cphc.201500958

Conference Contributions

Influence of Intramolecular Hydrogen Bonding on the Photodynamics of 2-(1-Ethynylpyrene)-Adenosine (PyA)

P. Trojanowski, C. Grünewald, F. F. Graupner, M. Braun, **A. J. Reuss**, J. W. Engels, and J. Wachtveitl

International Conference on Ultrafast Phenomena, Okinawa (Japan), July 7 – 11, 2014, ISBN: 1-55752-279-0, Poster Session 3 (09.Wed.P3)

Photodynamics of Structural Isomers of Pyrenylethynyl-modified 2-Adenosines – Effect of Altered Electronic Interaction

A. J. Reuss, C. Grünewald, P. Trojanowski, C. Slavov, J. W. Engels, and J. Wachtveitl

The Hamburg Conference on Femtochemistry, Hamburg (Germany), July 12 – 17, 2015, Poster Session 1 (P1-01)

The Tetracycline-binding Aptamer: Solvation and Thermodynamics

A. J. Reuss, M. Vogel, P. Trojanowski, J. E. Weigand, B. Suess, J. Wachtveitl

10^{th} European Biophysics Congress, Dresden (Germany), July 18 – 22, 2015, Poster P-767

Abstract printed in European Biophysics Journal with Biophysics Letters, 2015, 44, Suppl. 1, p. S243, ISSN: 0175-7571, doi:10.1007/s00249-015-1045-6

Chapter 1

Introduction

The central dogma of molecular biology was coined by Francis Crick in 1958. It describes the possible directions of the information flux in gene expression: information flows always from ribonucleic acids (RNA) and deoxyribonucleic acids (DNA) to proteins, but never from proteins back to both, RNA and DNA.[1]

Despite the considerable range provided by the dogma for possible functions of RNA and DNA, the understanding of gene expression was for a long time dominated by a quite narrow perception of the roles of DNA and RNA. In the standard view of gene expression, DNA serves as template and long-term information storage and RNA is merely the short-lived messenger (transcription into mRNA) and mediator (translation via transfer RNA, tRNA) of the information. All essential processes for (protein) biosynthesis and their tight regulatory control are hereby performed by other proteins.[2,3]

In eukaryotes, the freshly transcribed mRNA is usually not yet in its final form; therefore, it is called pre-mRNA. The pre-mRNA has to be processed into mature mRNA and one of the processing steps—splicing—alters the primary sequence insofar as non-coding regions of the RNA (introns) are removed and the remaining coding parts (exons) are recombined in a meaningful way. In principle any step of the gene-expression process is affected by the cellular environment, which may result in the synthesis of different proteins starting from the same DNA template.

So far, the role of RNA is completely passive given that any processing and signaling may be performed by proteins.

In the last few decades, several new classes of non-coding RNAs (ncRNA) were recognized to actively affect the pathways of gene regulation. The classes encompass micro and small interfering RNAs (miRNAs and siRNAs) which trigger

the degradation of target (m)RNAs through imperfect and perfect base pairing, respectively. Small nucleolar RNAs (snoRNA) and the closely related small Cajal-body RNAs (scaRNA) perform both, signaling and catalytic function.[4] Longer ncRNAs (> 200 nucleotides) such as macroRNAs or mRNAs may act as antagonists to the protein which they encode.[5] Even larger circular RNAs were recently found to regulate miRNA concentrations by acting as miRNA sponges.[6] Beyond the familiar examples of RNAs as catalytic key elements in ribonucleoproteins such as the ribosome (rRNA), RNAs are furthermore involved in DNA methylation, chromatin modification, imprinting, telomerase processing[7] and editing[8].

The aforementioned ncRNAs and the associated conditional gene expression pathways are primarily present in eukaryotes and their frequency increases with the organizational complexity of the considered organism.[3,9–12] In contrast to this, riboswitches are present in all three kingdoms of life, which is a strong hint for their early appearance in the course of evolution.[13] Riboswitches are non-coding parts of mRNA and they are expressed prior to any coding parts. They can selectively bind target ligands and the binding state affects the secondary and tertiary structure of parts of the mRNA distal from the binding site itself. This causes a ligand-dependent alteration of gene expression.[14]

Besides naturally occurring riboswitches, there are engineered ones, which are based on ligand-sensing (aptamer) domains found by in-vitro selection experiments.[15] Engineered riboswitches proved to be valuable tools for biological research.[16] However, only very view artificial aptamers are capable of serving as sensing unit in an engineered riboswitch.[17]

Probably the most versatile engineered riboswitch to date with applications in different organisms from yeast[18,19] to human cells[20] is the tetracycline-binding aptamer[21]. Due to its relatively small size and its highly selective and affine ligand-binding properties[22], it attracted appreciable attention as model system for the investigation of tight ligand binding and the influence of Mg^{2+} on induced structural preformation[23–25].

One peculiarity of RNA within—and beyond—the biological context is its substantial conformational flexibility and the fact that this flexibility possesses functional relevance.[26,27] Fast structural changes such as base-flipping occur on sub-nanosecond time-scales and fluorescence is the optimal observable to follow such processes[28,29] due to its sensitive and fast response to environmental changes combined with a potentially excellent signal-to-noise ratio[30]. The fluorescent

probes may be randomly intercalating dyes[31] or they may be site-specifically introduced. They can be used in steady-state[32], fast mixing[33], and fluorescence–lifetime-based assays[34], which may be affected by the conformational state of the RNA, equally well.

Within this work, pyrene is used as fluorescent marker due to its numerous convenient properties: it has high fluorescence quantum-yields and lifetimes in oxygen-free solvents[35], its emission is highly sensitive to the solvent polarity[36], and it can form fluorescent excimers[37,38]. Therefore, it is frequently used in various biophysical investigations such as measuring the speed of molecular redistribution across lipid membranes[39] or their depth[40].

Pyrene was found to be particularly useful for investigations of nucleic acids including their application as molecular beacons.[41] In part, this is so because it can discriminate between DNA and RNA targets.[42,43] The aptitude of pyrene as probe for nucleic acids is closely related to its tendency to intercalate into the strands[44–46] and with the observation that it maintains its ability to emit as excimer within nucleic acid scaffolds[47,48].

This thesis is centered around the linkage between structure and function of RNA.

The projects presented in the chapters 4 and 5 describe the implementation of a time-resolved fluorometer and its use for the characterization of two newly available pyrene-based, fluorescent RNA-nucleotide analogs. The characterization of the analogs is to be understood as a first necessary step on the path to establish them as fluorescence labels for the structural investigation of RNA.

In chapter 6, the response of the TC aptamer to its ligand and the Mg^{2+} concentration is investigated. The main aim is to answer the question, what the structural prerequisites for the TC aptamer to function as riboswitch under physiological Mg^{2+} conditions are and how its function is related to Mg^{2+}-induced preformation.

Chapter 2

Theoretical background

This chapter introduces the basic theoretical concepts and the terminology necessary to understand the aims and subjects of this thesis. Section 2.1 is devoted to molecules and their response to optical excitation. Section 2.2 focuses on the intra- and intermolecular structure of ribonucleic acids (RNA), its biological relevance and its photophysical properties.

2.1 Molecular properties

Molecules are atomic assemblies of finite size. They are defined by the configuration of their atomic nuclei and the appertaining electrons. This configuration is essentially governed by the mutual interactions of all constituting particles with each other. Mathematically, a molecule can be described by the theory of quantum mechanics, as it is described in numerous standard textbooks (see for example[49,50]). The description of time-dependent perturbation theory for interstate transitions mainly follows the references [51] and [52].

The Hamiltonian operator $\mathcal{H}$ casts the intramolecular interactions into a mathematical frame by its action on a wavefunction $|\Psi\rangle$. It contains the kinetic and potential energy terms $\mathcal{T}$ and $\mathcal{V}$ of the molecular constituents.

$$\mathcal{H}\,|\Psi\rangle = \Big(\mathcal{T} + \mathcal{V}\Big)\,|\Psi\rangle = \left(-\sum_j \frac{\hbar^2}{2m_j}\boldsymbol{\nabla}_i^2 + V(\mathbf{r}_j, t)\right)|\Psi\rangle \tag{2.1}$$

The wavefunctions $|\Psi\rangle$ are eigenvectors of $\mathcal{H}$. The time-dependence (t) of the wavefunctions is determined by the Schrödinger equation.

$$i\hbar\frac{\partial}{\partial t}\left|\Psi, t\right\rangle = \mathcal{H}\left|\Psi, t\right\rangle \tag{2.2}$$

For a molecule under static environmental conditions, it is valid and plausible to assume a stationary solution for equation 2.2, resulting in the time-independent Schrödinger equation

$$E\left|\Psi, t\right\rangle = \mathcal{H}\left|\Psi, t\right\rangle \tag{2.3}$$

with solutions of the form

$$\left|\Psi, t\right\rangle = \mathrm{e}^{-i\cdot E\cdot t/\hbar}\left|\Psi, 0\right\rangle \tag{2.4}$$

where $|\Psi, 0\rangle$ represents the state of the wavefunction at $t = 0$.

It is important to note that $|\Psi\rangle$ does not necessarily represent a single and unique solution to the eigenvalue problem of equation 2.2. In general, there is an infinite amount of orthogonal states $|\Psi_j\rangle$ with (usually) distinct eigenenergies E_j. Without an external perturbation, transitions between distinct states of the system are not possible.

To understand the processes related to transitions between eigenstates $|\Psi_j\rangle$ of a molecule, it is necessary to introduce a perturbation to the Hamiltonian $\mathcal{H}$ by adding a term $\mathcal{V}'(\mathbf{x}, t)$ to it, where $\mathbf{x}$ denotes spatial coordinates.

$$\mathcal{H} \rightarrow \mathcal{H}' = \mathcal{H} + \mathcal{V}' \tag{2.5}$$

The eigenvectors $|\Psi\rangle$ of $\mathcal{H}$ are not eigenvectors of $\mathcal{H}'$. Especially when the magnitude of the perturbation $\mathcal{V}'$ is small compared to the magnitude of $\mathcal{H}$, the eigenvectors $|\Psi\rangle$ are chosen as starting points for finding the new eigenvectors $|\Psi'\rangle$ to $\mathcal{H}'$. In the simplest case, this is achieved by applying first order perturbation theory to the problem. In terms of the eigenvectors $|\Psi\rangle$, $\mathcal{V}'$ introduces a mixing of the states that can be interpreted as transitions between two distinct eigenstates $|m, t\rangle = \mathrm{e}^{-i\cdot E_m\cdot t/\hbar}\left|m\right\rangle$ and $|n, t\rangle$ of $\mathcal{H}$:

$$P_{m,n}(t) = \left|\left\langle n, t|m', t\right\rangle\right|^2 = \frac{1}{\hbar^2}\left|\int_0^t \mathrm{d}t'\left(\mathrm{e}^{i(E_n - E_m)t'/\hbar}\left\langle n\right|\mathcal{V}'\left|m\right\rangle\right)\right|^2 \tag{2.6}$$

with

$$|m', t\rangle = |m\rangle + \frac{1}{i\hbar}\int_0^t \mathrm{d}t' \left(\mathrm{e}^{i(E_n - E_m)t'/\hbar} \langle n| \mathcal{V}' |m\rangle \right) \tag{2.7}$$

being the first order approximate eigenstate of $\mathcal{H}'$ characterized by the quantum number m. Equation 2.6 is known as Fermi's golden rule.

In general, transitions occur from a (coherently) coupled manifold of states $|M\rangle = \{|m_j\rangle\}$ to the whole set of suitable target states $|n\rangle = \{|n_j\rangle\}$. This is described by summing over the mixing terms of all initial states $|m_j\rangle$ to all existing states $|\Psi\rangle$. For this approach to be valid, all states $|m_j\rangle$ have to be in thermal equilibrium with each other during the transition process.

In section 2.1.1, the absorption and emission of light by a molecule will be described and in section 2.1.2, the photoinduced reactions of the molecule will be presented.

2.1.1 Absorption and emission of light

A physical description of light begins with the notion, that it is quantized and therefore a particle.[53] The quanta are termed photons and behave like bosons. As bosons, two ore more photons can simultaneously occupy the same quantum state.[i54,55] Having stated that light consists of particles, one has to add that it is oftentimes convenient to describe light as classical electromagnetic wave with the well-known Maxwell equations.[56]

Light can interact with matter, which includes molecules in condensed phase. It is for example the interaction with light that can serve as the perturbation required to induce transitions between different eigenstates of a molecule. The Schrödinger representation of quantized electromagnetic radiation in the Coulomb gauge is given by the vector potential $\mathbf{A}$

$$\hat{\mathbf{A}}_{\mathbf{k},\sigma_\mathbf{k}}(\mathbf{x}, t) = \mathbf{A}_0(\omega_k) \sum_{\mathbf{k},\sigma_\mathbf{k}} \left[\sigma_\mathbf{k} \left(\hat{a}_{\mathbf{k},\sigma_\mathbf{k}} \mathrm{e}^{i(\mathbf{k}\cdot\mathbf{x} - \omega_k t)} + \hat{a}^*_{\mathbf{k},\sigma_\mathbf{k}} \mathrm{e}^{-i(\mathbf{k}\cdot\mathbf{x} - \omega_k t)} \right) \right] \text{ with } \omega_k = ck \tag{2.8}$$

$\hat{a}$ and $\hat{a}^*$ are the harmonic lowering and raising operators of standing light waves, respectively. Accordingly, they can for example represent absorption and

[i] They obey the bosonic distribution statistics in thermal equilibrium.

emission of a single photon by a molecule. $\mathbf{k}$ is the propagation vector of the photon and $\sigma_{\mathbf{k}}$ describes the polarization state of the photon with $\mathbf{k} \cdot \sigma_{\mathbf{k}} = 0$. ω_k is the frequency of the photon and c is the speed of light. $\mathbf{A}_0(\omega_k)$ is an arbitrary amplitude. The electric and magnetic fields $\mathbf{E}$ and $\mathbf{B}$ are related to $\mathbf{A}$ via

$$\mathbf{E} = -\frac{1}{c}\frac{\partial}{\partial t}\mathbf{A} \text{ and } \mathbf{B} = \nabla \times \mathbf{A} \tag{2.9}$$

The interaction of matter with light is described by the product of the electric field $\mathbf{E}$ with the dipole moment $\boldsymbol{\mu}$ of a transition between the electronic configurations associated with two molecular states m and n. For a quantum mechanical description, the associated term in the Hamiltonian is:

$$\begin{aligned} \mathcal{V}_{ML} &= -\hat{\boldsymbol{\mu}} \cdot \mathbf{E}(\mathbf{x})\Big|_{\mathbf{x}=0} \\ &= -i \sum_{\mathbf{k},\sigma_{\mathbf{k}}} \mathbf{E}_0(\omega_k)\Big(\hat{\boldsymbol{\mu}}_{nm} \cdot \boldsymbol{\sigma}_{\mathbf{k}} |n\rangle \langle m| + \hat{\boldsymbol{\mu}}_{mn} \cdot \boldsymbol{\sigma}_{\mathbf{k}} |m\rangle \langle n|\Big)(\hat{a}_{\mathbf{k},\sigma_{\mathbf{k}}} - \hat{a}^{\dagger}_{\mathbf{k},\sigma_{\mathbf{k}}}) \end{aligned} \tag{2.10}$$

where $\hat{\boldsymbol{\mu}}_{mn}$ is the transition dipole moment between two states m and n:

$$\hat{\boldsymbol{\mu}}_{mn} = \langle m| \hat{\boldsymbol{\mu}} |n\rangle = \int \mathrm{d}^3 r \left(\Psi^*_n(\mathbf{r}) \hat{\boldsymbol{\mu}} \Psi_m(\mathbf{r})\right) \tag{2.11}$$

$\mathbf{r}$ are the coordinates of all molecular electrons involved in the interaction.

Equation 2.10 implies that transitions are only possible, when suitable photons are available as indicated by the lowering and raising operators. Combined with equation 2.6, suitable in this context means that the available photons must have the appropriate energy $\hbar\omega_k = E_n - E_m$ to bridge the energy gap between the eigenenergies of the states n and m.

Accordingly, in the presence of an external radiation source, such as a lamp or a laser, states with an energy higher than the one of the initial state can be populated to an appreciable amount. This process is called absorption.

The same external source can at the same time drive transitions from the higher state back to the initial state, which is called stimulated emission (SE). In absence of any other kind of interaction of the molecule with its environment, the molecule would rest in the higher energy state forever, after the external light source is switched off.

Spontaneous emission (fluorescence and phosphorescence) is driven by the interaction of the excited molecule with the omnipresent fluctuations of the vacuum state of the electromagnetic radiation field. The population density of the photons in the quantized radiation field is calculated from the density of standing harmonic modes in a fixed volume $\Omega = L_x \times L_y \times L_z$. The calculation results in a universal expression for $\mathbf{A}_0(\omega_k)$ introduced in equation 2.8.

$$\mathbf{A}_0(\omega_k) = c \sqrt{\frac{2\pi\hbar}{\varepsilon_0 \Omega \omega_k}} \tag{2.12}$$

c denotes the vacuum speed of light and ε_0 is the vacuum dielectric constant. Finally, the extreme case $\lim_{\Omega\to\infty}$ is considered. Then, the energetic distance between the different standing modes approaches zero and the quantized eigenenergy spectrum becomes quasi-continuous.

Another important implication of the equations 2.6, 2.10, and 2.12 is that the light-induced transition probability between any two states m and n is proportional to $|\hat{\boldsymbol{\mu}}_{mn}|^2$. Because $|\hat{\boldsymbol{\mu}}_{mn}|^2 = |\hat{\boldsymbol{\mu}}_{nm}|^2$ is obviously true, transitions from n to m and m to n have identical probabilities as far as only the properties of the involved molecular states are considered. This is the quantum mechanical justification of the proportionality of the Einstein coefficients at any given ω. They relate absorption, spontaneous emission, and SE to each other.[50,55]

2.1.2 Molecular photodynamics

The molecular Hamiltonian $\mathcal{H}$ is split into the Hamiltonians of its constituents—electrons and atomic nuclei—and their Coulomb interaction.

$$\mathcal{H} = \mathcal{H}_\mathrm{e} + \mathcal{H}_\mathrm{n} + \mathcal{V}_\mathrm{e\text{-}n} = \mathcal{T}_\mathrm{e} + \mathcal{V}_\mathrm{e} + \mathcal{T}_\mathrm{n} + \mathcal{V}_\mathrm{n} + \mathcal{V}_\mathrm{e\text{-}n} \tag{2.13}$$

The nuclear coordinates are denoted as $\mathbf{R}$ and those of the electrons as $\mathbf{r}$. The wavefunction of the molecular states $|\Psi\rangle$ depends on both sets of coordinates. The form of $\mathcal{H}$ as sum of electronic and nuclear contributions coupled by Coulomb attraction motivates a product as ansatz for $|\Psi\rangle$:

$$|\Psi_{m\upsilon}(\mathbf{R},\mathbf{r})\rangle = |\phi_m(\mathbf{R},\mathbf{r})\rangle\,|\chi_\upsilon^{(m)}(\mathbf{R})\rangle \tag{2.14}$$

$$(\mathcal{T}_\mathrm{e} + \mathcal{V}_\mathrm{e} + \mathcal{V}_\mathrm{e\text{-}n})\,|\phi_m(\mathbf{R},\mathbf{r})\rangle = E_m(\mathbf{R})\,|\phi_m(\mathbf{R},\mathbf{r})\rangle \tag{2.15}$$

$$(\mathcal{T}_\mathrm{N} + \mathcal{V}_\mathrm{N} + E_m(\mathbf{R})\,|\chi_\upsilon^{(m)}(\mathbf{R})\rangle = E_{m\upsilon}(\mathbf{R})\,|\chi_\upsilon^{(m)}(\mathbf{R})\rangle \tag{2.16}$$

$|\phi_m(\mathbf{R},\mathbf{r})\rangle$ is the solution to the electronic part of the molecular Schrödinger equation (2.15) for the electronic state m. However, the energy eigenvalues $E_m(\mathbf{R})$ of the electrons are not independent of the coordinates of the nuclei. In order to achieve a separation of the variables of electrons and nuclei, the Born-Oppenheimer (BO) approximation is necessary. Here, the large mass of the nuclei compared to the electrons and hence the relatively slow motion of the nuclei justifies to take the nuclear coordinates as frozen. Consequently, the dependence of $|\phi_m(\mathbf{R},\mathbf{r})\rangle$ on $\mathbf{R}$ is reduced to a purely parametric one. Equation 2.15 has to be solved for each electronic state with any possible configuration of the nuclei, but the nuclei do not contribute to the dynamics, anymore.

The electronic energy eigenvalues $E_m(\mathbf{R})$ enter the nuclear part of the Schrödinger equation (2.16). $|\chi_\upsilon^{(m)}(\mathbf{R})\rangle$ is the vibrational eigenstate υ of the electronic eigenstate m with the energy eigenvalue $E_{m\upsilon}(\mathbf{R})$. $E_{m\upsilon}(\mathbf{R})$ is also the eigenvalue of $|\Psi_{m\upsilon}(\mathbf{R},\mathbf{r})\rangle$ within the BO approximation.

The transition dipole moment of electrons between two different molecular states $|\Psi_{m\upsilon}\rangle := |m\upsilon\rangle = |m\rangle\,|\upsilon\rangle$ and $|\Psi_{n\upsilon'}\rangle$ described by equation 2.11 becomes

$$\hat{\boldsymbol{\mu}}_{(m\upsilon)(n\upsilon')} = \langle m\upsilon|\,\hat{\boldsymbol{\mu}}\,|n\upsilon'\rangle = \langle m|\,\hat{\boldsymbol{\mu}}\,|n\rangle_\mathbf{r}\,\langle\upsilon|\upsilon'\rangle_\mathbf{R} \tag{2.17}$$

Lower case $\mathbf{r}$ and $\mathbf{R}$ denote integration over the electronic and nuclear coordinates, respectively. Equation 2.17 strongly resembles equation 2.11, but additionally it has the Franck-Condon (FC) factor at the right-hand-side, which depends solely on the nuclear wavefunctions.[ii] It determines the line shape of an electronic transition of a molecule resulting in vibrational fine structure.

Dynamics of large molecules (number of atoms ≥ 10) after photoexcitation can be illustrated with a Jablonski-diagram[58] (figure 2.1). The electronic states j

[ii] Actually, a third factor, the Hönl-London (HL) factor, appears additionally at the right-hand-side of equation 2.17. The HL factor depends on the rotational states. Here, it is neglected, because the time-scales of the rotational diffusion are either too fast to be observed in a given experiment, or it is suppressed by adjusting the relative polarizations of the excitation and the response light beams to the magic angle.[57]

contain several vibronic states υ, rotational states are neglected because they are not visible in the condensed phase.

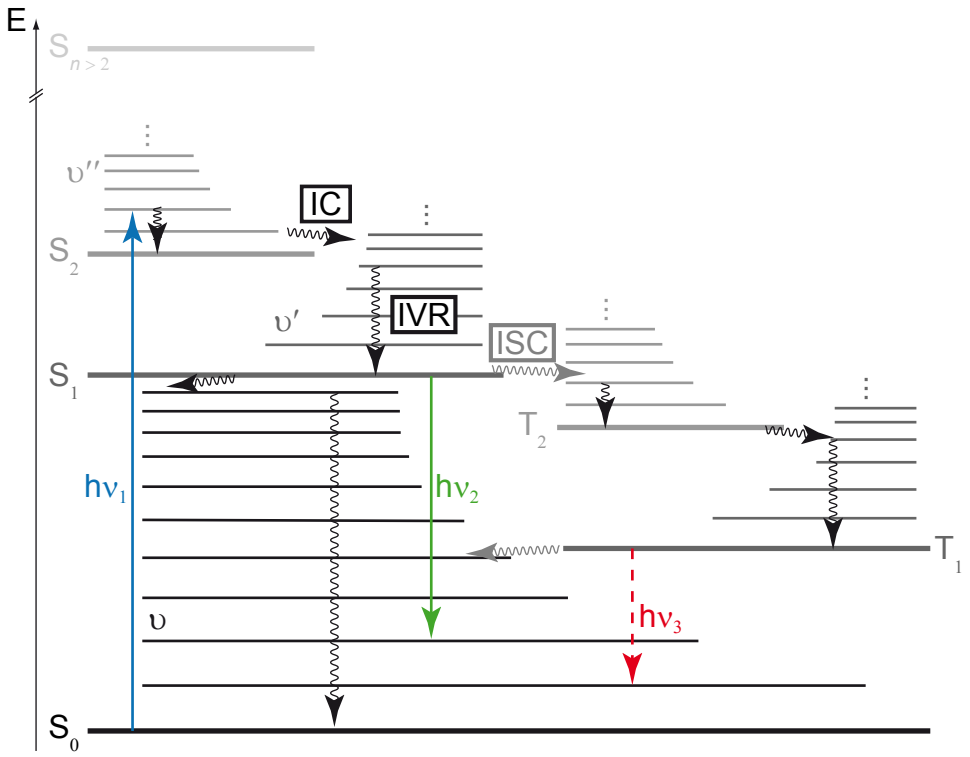

Figure 2.1: Jablonski diagram. Electronic singlet and triplet states are depicted as bold horizontal lines and labeled S_j and T_j, respectively. Thin horizontal lines are related to the vibrational substates within the electronic states and termed υ to υ''. Vertical straight arrows are optical transitions, the arrowheads indicate the final state. Vertical, black and wiggled arrows represent intramolecular vibrational relaxation (IVR). Horizontal, black and wiggled arrows represent internal conversion (IC) and the gray wiggled arrows represent intersystem crossing (ISC).

Events involving photons are represented by straight, vertical arrows. This directly reflects the BO approximation, where electronic transitions are too fast for the nuclei to react. Therefore, they occur at a fixed nuclear configuration. The overlap of the nuclear wavefunctions and the thermal population distribution in the starting state of the transition define which transitions between vibrational substates dominate the spectrum. Absorption (blue arrow, $h\nu_1$) occurs at room temperature for thermal reasons mostly from the vibronic GS ($\upsilon = 0$) of S_0 to those vibronic states of the electronic target state S_n that match the available photon energies best and have large FC factors. Therefore absorption occurs usually from $|S_0, \upsilon = 0\rangle$ to $|S_{n>0}, \upsilon^{(n)} \geq 0\rangle$.

Radiative decay processes (luminescence) from excited electronic states (EESs) usually occurs from the vibronic GS of the lowest EES of one of the two possible

manifolds: $\upsilon' = 0$ in S_1 and T_1 with $h\nu_2$ and $h\nu_3$, respectively. This is also known as Kasha's rule.[59] Fluorescence is the transition from $|S_1, \upsilon' = 0\rangle$ to $|S_0, \upsilon \geq 0\rangle$ leading directly to the conclusion that fluorescence is always bathochromically shifted relative to the absorption. Triplet states are always lower in energy than the corresponding singlet states. Therefore, phosphorescence, which is a radiative transition from $|T_1, \upsilon' = 0\rangle$ to $|S_0, \upsilon \geq 0\rangle$ is expected to be bathochromically shifted with respect to the fluorescence.[60] One consequence of Kasha's rule is the independence of the luminescence quantum yield from the excitation wavelength known as Kasha-Vavilov rule.[61]

Figure 2.1 shows additional wiggled arrows representing intramolecular vibrational (energy) redistribution or relaxation (IVR), internal conversion (IC), and intersystem crossing (ISC), respectively. These transitions are not vertical because they are related to nuclear movements. Although the $|\Psi_{m\upsilon}\rangle$ are eigenstates of the molecular Hamiltonian in the BO approximation, they are not long-lived because real molecules do not strictly obey the BO approximation.

The neglected movement of the nuclei in a diabatic description leaves a perturbing contribution for transitions from $|n\upsilon'\rangle$ to $|m\upsilon\rangle$ ($n > m$) of the form

$$\begin{aligned}\langle m\upsilon|\mathcal{T}_\mathrm{n}|n\upsilon'\rangle &= \langle\upsilon(\mathrm{R})|\,\langle m(\mathrm{R},\mathbf{r})|\mathcal{T}_\mathrm{n}|n(\mathrm{R},\mathbf{r})\rangle\,\upsilon'(\mathrm{R})\rangle_\mathrm{R} \\ &= -\kappa\int \mathrm{dR}\left(\chi_\upsilon^{(m)*}(\mathrm{R})\chi_{\upsilon'}^{(n)}(\mathrm{R})\left\langle m(\mathrm{R},\mathbf{r})\middle|\frac{\partial^2}{\partial\mathrm{R}^2}\middle|n(\mathrm{R},\mathbf{r})_\mathbf{r}\right\rangle\right) \\ &\quad -2\kappa\int \mathrm{dR}\left(\chi_\upsilon^{(m)*}(\mathrm{R})\frac{\partial}{\partial\mathrm{R}}\chi_{\upsilon'}^{(n)}(\mathrm{R})\left\langle m(\mathrm{R},\mathbf{r})\middle|\frac{\partial}{\partial\mathrm{R}}\middle|n(\mathrm{R},\mathbf{r})_\mathbf{r}\right\rangle\right)\end{aligned} \tag{2.18}$$

which describes IC. For simplicity, the equation is restricted to a single nuclear coordinate R.

IC is essentially isoenergetic. That says $E_{m\upsilon}(\mathbf{R}_\mathrm{IC}) = E_{n\upsilon'}(\mathbf{R}_\mathrm{IC})$ has to hold, where $\mathbf{R}_\mathrm{IC}$ denotes the nuclear configuration in which the IC occurs. In principle, all isoenergetic configurations with their corresponding excitation patterns have to be taken into account, which leads to fast IC processes (< 10 ps) in solution. This assumes that the vibrational modes of the starting state are in thermal equilibrium, which is true for most molecules even in the gas phase. If it is true, a golden-rule-like expression for the transition rate from the vibronic GS $\upsilon' = 0$ of EES n to the vibronic manifold υ of the lower electronic state m will hold.

In the case of ISC, isoenergetic states are necessary, but not sufficient. Additionally, an electronic spin has to flip its orientation. This kind of process is mediated by interaction of the electronic spin and orbital angular momenta (spin-orbit coupling). In molecules without heavy atoms, the spin-orbit coupling is small, which is why ISC is very rare in molecules that contain only hydrogen, carbon, nitrogen, and oxygen as is the case for the molecules studied in this thesis. In the special case of pyrene (Py), however, triplet excitation rates in thoroughly degassed solvents can be of considerable magnitude due to the extraordinary long S_1 lifetime of the fluorophore.[62]

IVR is a dissipative process and it is only possible in the presence of a heat bath that accepts the excess energy. The heat bath is the manifold of unexcited vibrational modes of the molecule. The redistribution of the vibrational energy leads to the internal thermalization of the molecule. Then, the occupation numbers of the vibrational modes end up being Boltzmann distributed, though they started from a non-equilibrium regime. A very similar coupling occurs also between the vibronic states of the considered molecule and the vibronic states of its host material, for example the solvent. The latter is referred to as intermolecular vibrational redistribution. The description of both kinds of vibrational redistribution is formally very much alike each other but the intramolecular one is faster and in the context of this work more important. It will occasionally be termed cooling, as well.

All of the transition processes described can be expressed in terms of golden-rule expressions (compare equation 2.6) provided the molecule is in thermal equilibrium while the processes occur. Accordingly, rate constants can be assigned to them. The transition rate connected to spontaneous emission is called radiative rate k_r. IVR, IC, and ISC are non-radiative processes and they are related to rates termed k_IVR, k_IC, and k_ISC, respectively. The non-radiative depopulation of a given electronic state is described by non-radiative rate constant k_n.

$$k_\mathrm{n} = k_\mathrm{IVR} + k_\mathrm{IC} + k_\mathrm{ISC} \tag{2.19}$$

Taking into account Kasha's rule[59], the balance between k_r and k_n of S_1 governs the fluorescence of a chromophore[63]: the total fluorescence lifetime τ_f, which is actually the S_1 lifetime, and the fluorescence quantum yield ϕ_f are given by

$$\frac{1}{\tau_f} = k_\mathrm{r} + k_\mathrm{n} \tag{2.20}$$

and

$$\phi_f = \frac{k_\mathrm{r}}{k_\mathrm{r} + k_\mathrm{n}} \tag{2.21}$$

respectively.

2.2 Ribonucleic acids

The following two sections are largely based on reference [2].

Unmodified ribonucleic acids (RNA) consist of four distinct building blocks: adenosine (A), uridine (U), guanosine (G), and cytidine (C). They share the ribose ring, from which their name is derived and are distinct from each other due to the nucleobase (adenine, uracile, guanine, and cytosine, respectively)[iii], which is attached to the sugar (figure 2.2). The total of nucleobase and sugar is called nucleoside. Additionally, one to three phosphate groups may be attached to the 5′-carbon (C5′) of each nucleoside. The complete molecule is then called nucleoside mono-, bi-, or triphosphate or, as collective term, nucleotide.

An RNA oligomer is a chain of arbitrary composition containing the four natural nucleoside monophosphates. The chain is formed by a covalent bond of the 5′-linked phosphate group of one nucleotide to the C3′ of the neighboring nucleotide. This linkage pattern is referred to as phosphate backbone.

One important feature of the phosphate backbone is its negative electrostatic charge. It is responsible for the water-solubility of nucleotides and RNA oligomers. Additionally, the mutual electrostatic repulsion of the neighboring phosphate groups prevents the structural collapse of oligomers in solution because the hydrophobic nucleobases prefer to stack upon each other in order to minimize the contact area with water.

The sequence of nucleobases within an oligomer defines the primary structure of the oligomer. The nucleobases are separated in two distinct classes with respect to their molecular scaffold: A and G are purines, U and C are pyrimidines. In principle both, the length and the sequence of an oligomer are unrestricted, which gives rise to an infinite amount of possible primary structures.

[iii] The abbreviations A, U, C, and G may represent the nucleobases alone or the ribonucleic-acid building blocks in a context-dependent manner.

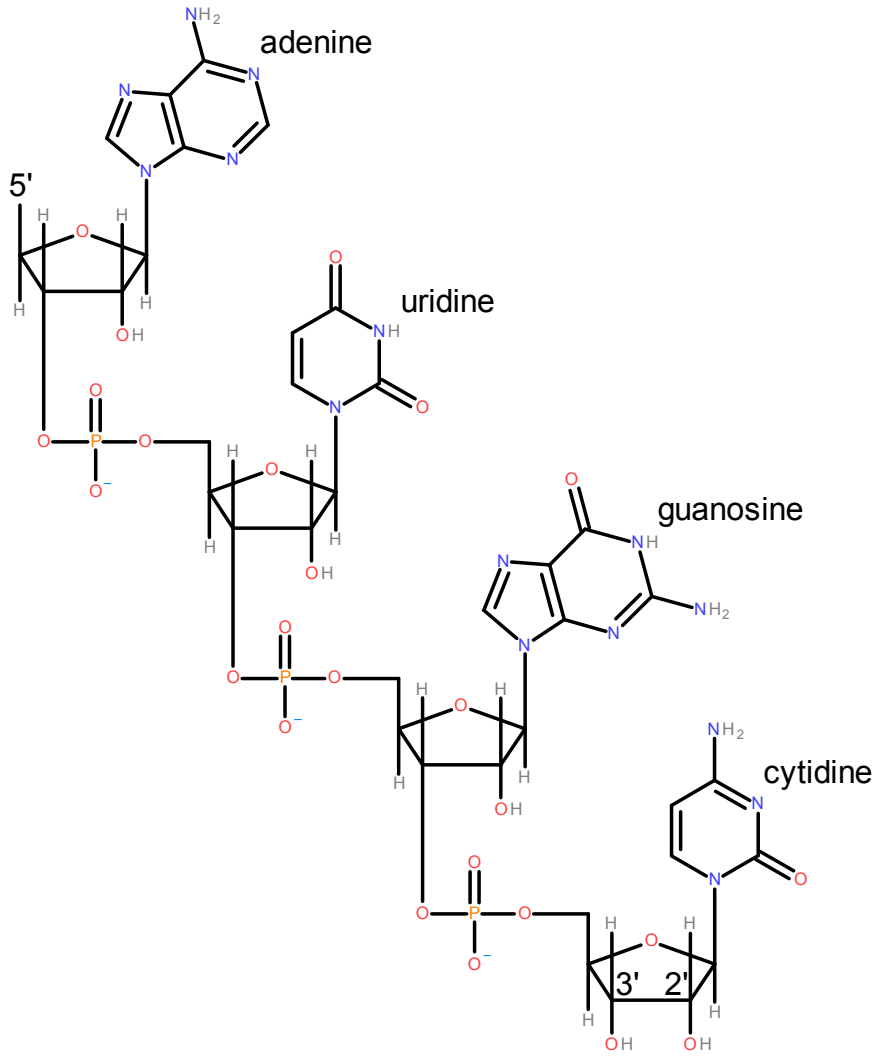

Figure 2.2: Lewis structures of the four naturally occurring ribonucleotides in a short oligomer.

Besides the primary structure, RNA can form stable and well-defined inter- and intramolecular hydrogen-bonding (H-bonding) networks with other nucleic acids. This is in the center of section 2.2.1. The H-bonding patterns are in general very sensitive to environmental conditions. Section 2.2.2 covers the particular importance of (divalent) cations. In section 2.2.3, the biological functions of RSs will be introduced. Many experiments within this thesis exploit the sensitivity of the extinction coefficient and—closely related to that—of the optical activity (OA) of RNA to its conformational state. Therefore, the molecular mechanisms underlying these effects will be sketched in section 2.2.4.

2.2.1 Secondary and tertiary interactions

RNA can form complexes of A with U and G with C stabilized by two and three H-bonds, respectively. This type of base pairing is named Watson-Crick (WC) and is illustrated in figure 2.3. G≡C base pairs are more stable than A=U base pairs because of the different number of H-bonds. However, the stability also depends on the neighboring bases and the general context (terminal base pairs melt easier than central ones).

Two single-stranded (ss) RNA oligomers can form a stable hybrid structure when they are complementary to each other in the sense, that each base of one strand finds the appropriate partner base in the second strand. The two strands pair head to tail. That says that the 5'-end of one strand binds to the 3'-end of the other one. The hybrid structure has the form of a double helix and the RNA is said to be double stranded (ds).

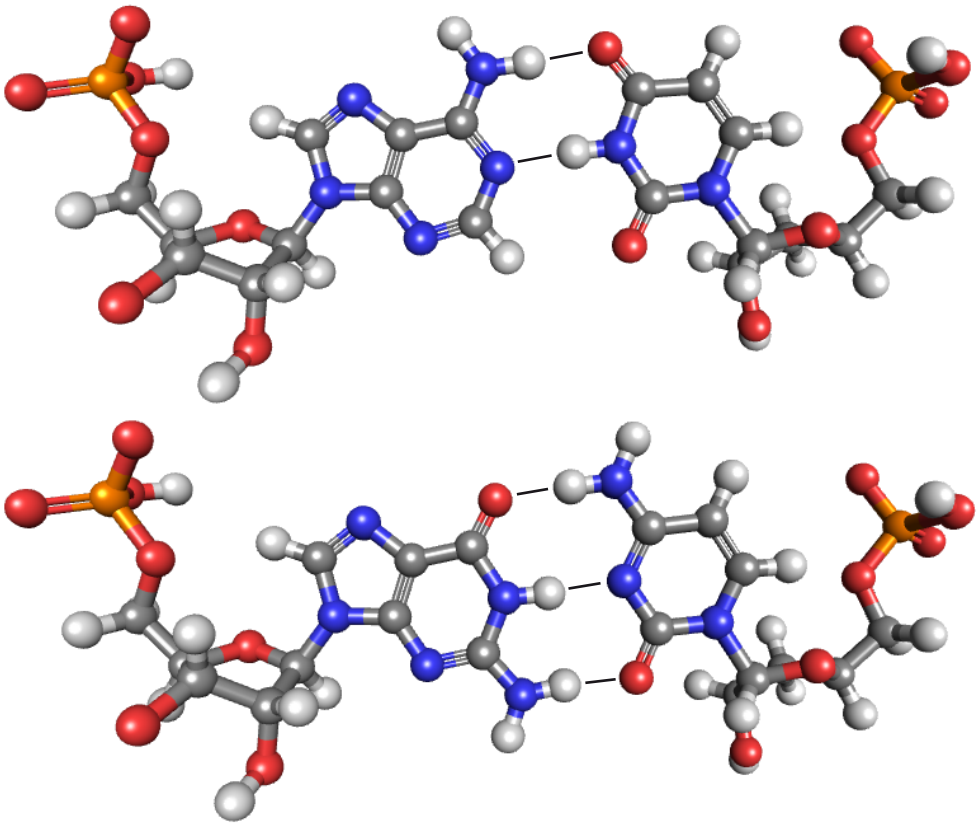

Figure 2.3: WC base-pairs of RNA. Top: A=U. Bottom: G≡C. Elements are color coded as in figure 2.2.

So far, everything written holds true for deoxyribonucleoic acid (DNA), as well, with only two differences. In DNA, uracile is replaced by thymine and the

hydroxyl group at the 2'-site of the ribose is replaced by hydrogen. The sugar is then a deoxyribose.

The impact of the first point on the primary structure is obvious, as every T has to be replaced by a U or vice versa. Less obvious is, that G frequently forms fairly stable wobble base pairs with U, but not with T. The G•U-wobble base pairs have two H-bonds and add significantly to the variability of what can be considered as a complementary sequence in RNA.

The second point does not affect the primary structure, at all. Yet, it does affect the three-dimensional structure of ss and ds oligomers. Deoxyribose can be in the C3'-endo conformation, which corresponds to an A-form helix, or C2'-endo. The latter is related to B-form and C-form helices, respectively. In aqueous solution, B form dominates for DNA and the DNA has to be dehydrated—for example with significant amounts of EtOH—to be converted into A form.[64] B-form helices have less internal strain (10.5 base pairs per turn (bppt), a length per turn (lpt) of 3.5 nm and a width of 2.4 nm) than A-form helices (11 bppt, lpt of 2.5 nm, and 2.6 nm wide). Ribose can, for sterical reasons, not be in C2'-endo. Therefore, RNA is always in A form in aqueous solution.

B-form helices have two grooves, a wide and deep major groove, that allows for specific recognition of the primary sequence for example by proteins and a less accessible, narrow minor groove, where mainly non-specific parts of the sugar and the phosphate backbone can be recognized. In A-form helices, minor and major groove are more similar to each other, with the major groove being narrower and the minor groove being wider as compared to B-form helices.

A further aspect to be considered are the biological functions of RNA and DNA. The main task of DNA is to preserve the genetic code in an unaltered form.[iv] Within the cellular context, DNA is usually dsDNA except for cell division and transcription. Besides that, ssDNA oftentimes signals a disease or some other kind of severe problem. Accordingly, the structural repertoire of DNA in a biological context is strongly limited to being a ds B-form helix.

RNA works oftentimes as temporary information storage and is usually ssRNA in a cellular context, with some exceptions such as RNA interference.[4] ssRNA of sufficient length folds back onto itself and can for example form ds intramolecular structures, provided there exist self-complementary subsequences.

[iv] A small rate of mutational change of the genetic code is essential for evolution. Accordingly, the preservation of the genetic code is not absolute and a small amount of change is tolerated.

Besides such secondary-structure motifs, tertiary interactions between distinct parts of an RNA strand frequently occur. That means that ss and/or ds regions of the oligomer form non-WC H-bonds leading to complex three-dimensional structures.

Already in 2002, a total of 38 different base-pairing schemes in crystal structures of biologically relevant RNAs was identified, including purine-purine, purine-pyrimidine, and pyrimidine-pyrimidine interactions.[65] In addition, tertiary interactions can involve nonspecific contacts with the ribose (namely the 2'-OH group) or backbone, base stacking, base triples and quadruples[66], and the four natural nucleotides can be modified, for example methylated.[67] The tremendous wealth of resulting structures include bulges[68], stem-loops with varying sizes and content-dependent shapes of the stems[69–73], pseudoknots[74], and kissing-loop complexes[75], where the latter are rather quaternary structure.

2.2.2 Salt dependence of RNA structures

The negative electrostatic charge of RNA is a severe obstacle to the assembly of secondary and higher order structures. Without any electrostatic shielding, RNA is a linearly out-stretched molecule. In aqueous solution, shielding is provided by cations. In cells, the most important monovalent ions are K^+ and Na^+.

The need for electrostatic shielding leads to an increased concentration of cations close to an RNA molecule in comparison to the bulk. The consequence is a cation-concentration gradient, which is supported by the favorable interaction energetics between the cations and the RNA.[76] The interaction of these shielding ions is non-specific and the ions can be imagined as a diffuse cloud surrounding the RNA. The ion cloud induces a structural collapse of the RNA without necessarily stabilizing a specific structure.[77] This kind of shielding can be provided by any cation.

Some cations can also induce specific higher order structures. K^+ as monovalent cation is a mandatory prerequisite for the formation of G-quadruplexes in DNA and RNA, where it can be biologically relevant.[78] More often, divalent cations are necessary to induce specific tertiary contacts. Some particular structures can be induced by various divalent cations, but not by monovalent ones.[79]

In a cellular context, the most important divalent cation is Mg^{2+}, both, due to its availability and its high charge density. In comparison to the interactions of

other divalent cations with RNA, Mg^{2+} is usually found to have better binding affinities[80] and to stabilize tertiary structures more efficiently[81]. The reason for this is that Mg^{2+} has the highest charge density due to its small volume and consequently the highest packing efficiency of the condensed cations.

The simultaneous presence of monovalent cations and Mg^{2+} leads to competition between the ionic species. Due to electrostatic repulsion, the cations displace each other from the RNA and the outcome of the competition is to a high degree governed by the ability of the monovalent ions to support tertiary structures at varying Mg^{2+} concentrations.[82] In view of these findings, the number of involved monovalent cation species was kept low (for details, see section 3.4.2).

The presence of the hydroxyl group at the C2'-carbon of the ribose has another important implication: the deprotonated 2'-OH group can perform a nucleophilic attack on the phosphorus in the neighboring phosphate group, yielding a 2',3'-cyclic phosphate intermediate finally leading to either a 2' or a 3' nucleotide. The attack can be base-[83] or metal-ion catalyzed[84,85] and the efficiency depends sensitively on the orientation of the 2'-OH group with respect to the phosphorus. The most favorable geometry for this reaction is the so-called in-line geometry and one aspect of the Mg^{2+}-RNA interaction is that Mg^{2+} can stabilize this geometry via tetrahedral coordination.[86]

2.2.3 Riboswitches and aptamers

Riboswitches (RSs) are most common in prokaryotes, although they exist in all three kingdoms of life.[87] They are long ncRNA elements and in prokaryotes, they are contained in the upstream part of the untranslated region (5'-UTR) of an open reading frame.[88] That says, they are expressed as part of an mRNA prior to the coding sequence.

RSs bind small metabolites without the assistance of additional molecules (namely proteins) and binding triggers an allosteric change of parts of the RS, which are distant to the binding site.[87] The binding competent region of the RS is called aptamer domain (AD). It binds its ligand with high affinity and specificity.

The regulatory activity is conveyed via a switching region (SR) to the expression platform (EP). In prokaryotes, the EP oftentimes contains the Shine-Dalgarno sequence, which may be exposed to the machinery for translation initiation in absence of the metabolite and sequestered in its presence, or vice versa.[88] Ligand

binding leads to a change in the tertiary structure of the AD, which affects the secondary structure of the (bistable) SR that is nested with both, the AD and the EP. Thus, the binding state of the aptamer alters the structural context of the EP and affects the pathway of gene expression.

In 2014, twelve classes of RSs with numerous subclasses were known.[89] They bind for example nucleosides or nucleotides (purine-binding RSs), negatively charged ligands such as thiamine pyrophosphate (TPP), flavin mononucleotide (FMN), and glucosamine-6-phosphate (glmS), coenzyme B_{12} (adenosylcobalamin, btuB),[90] the amino acid lysine, and even cations like Mg^{2+} that control genes for ion transporters[91].

As consequence of the wide spread of some classes of RSs, there is not one single primary sequence for a given RS. For the purine-sensing RS, more than 500 variants were identified in 2011[88] and already in 2004, two years after its discovery, more than 200 variants of the btuB-RS were predicted[13].

In accord with the diversity of the ligands, the sequences, and the host species, the regulatory mechanisms utilized by RSs are numerous. They may target transcription, translation, splicing, and mRNA stability. Furthermore, they may effect termination and antitermination of transcription, inhibition and activation of translation, mRNA degradation after ribozyme cleavage, and alternative self-splicing. One RS can act differently in different species. The TPP-RS generates two different proteins via alternative splicing in fungi, whereas it causes translation termination in algae, and leads to mRNA degradation in higher plants.[87] Most RSs act in *cis*[88], but two S-adenosyl methionine (SAM) RSs function additionally in *trans* as small ncRNAs[92].

Despite the large number of ADs present in natural RSs, they only represent a tiny fraction of the total of available oligonucleotide-based aptamers. The vast majority is derived from systematic evolution of ligands by exponential enrichment (SELEX) for targets that range from small organic molecules to proteins[93] or even complete cells[94]. Among many other applications, SELEX succeeded in generating the first catalytically active DNA (a DNAzyme)[95] and aptamers against the vascular endothelial growth factor, which led to the first clinically approved therapeutic aptamer[93], and against parasite target molecules[96].

The SELEX procedure starts with a randomized pool of 10^{13} – 10^{15} oligonucleotide sequences (DNA or RNA). The ligand, for which an aptamer is to be found is typically covalently bound to a linker that is fixed to a surface (matrix).

The oligonucleotide pool is then directly incubated with the fixed ligand and after incubation, the binding complexes are separated from the unbound strands by a washing procedure.

After separation, the binding constructs are eluted, amplified, and used as enriched starting pool for a new selection round. Iterative repetition of this cycle under increasingly rigid washing conditions finally leads to a enriched pool of strongly binding aptamers. The final pool is then amplified, sequenced, and analyzed. Additionally, it may be subjected to binding studies and mutational modifications to test and/or improve the aptamers.

The washing process is the most crucial step in the SELEX, because (i) it is the step, where the necessary quasi-Darwinian selection stress is exerted on the pool and (ii) it is the most error-prone step. The latter is due to the fact, that only here sequences that bind unspecifically to the linker or the matrix can be identified before the SELEX is finished. This can be difficult and of pivotal importance to the success of the SELEX at the same time. Therefore, several diverse strategies exist to exert selection stress: by lowering the ligand concentration, by changing the washing parameters and the SELEX buffer, and to avoid unspecific binding, matrix and linker materials may be varied.[97]

Remarkably, the number of artificial aptamers that can serve as functional ADs in an RS in vivo is surprisingly small.[15] This topic will be detailed in chapter 6 and is therefore not further discussed, here.

2.2.4 Excitonic coupling in helical oligomers

The conformation dependence of the extinction coefficient and the optical activity OA of helical macromolecules, such as RNA, originates in the interaction of the single chromophores ($\pi \rightarrow \pi^*$ in the nucleobases and $n \rightarrow \pi^*$ in the backbone[98]), with all other chromophores arranged in the helical scaffold. If the chromophores and thus their transition moments are oriented randomly between each other, there will be no net effect on the spectrum.[99]

Within the frame of this thesis, two effects are of particular interest: the hypochromicity[v], which is the decrease of the extinction of a helical oligomer upon a transition from an unordered state towards the fully ordered helix, and the change of the OA of an oligomer related to the same order transition. Both

[v] An increase of the extinction is called hyperchromicity.

effects can be traced back to the excitonic coupling of chromophores with each other. In the following, a brief explanation (mainly based on reference [100]) of excitonic coupling for the simple case of two interacting chromphores will be given.

Starting from two independent chromophores 1 and 2 with the Hamiltonians $\mathcal{H}_1$ and $\mathcal{H}_2$, a solution to the global unperturbed wavefunction of both chromophores is

$$|\Psi\rangle = |\psi_1, \psi_2\rangle = |\psi_1\rangle\,|\psi_2\rangle \tag{2.22}$$

and coherent superpositions of the products at the right-hand side. The two chromophores are then coupled to each other by a potential $\mathcal{V}_{12}$ resulting in a total Hamiltonian $\mathcal{H} = \mathcal{H}_1 + \mathcal{H}_2 + \mathcal{V}_{12}$. Assuming the distances between the chromophores large enough, direct electron exchange can be neglected and the leading contribution are dipole-couplings derived from the dipole in one chromophore induced by the interaction with light and the reaction to it in the other chromophore.

The total energy of the system becomes then

$$\langle\mathcal{H}\rangle = \langle\psi_2|\psi_2\rangle\,\langle\psi_1|\mathcal{H}_1|\psi_1\rangle + \langle\psi_1|\psi_1\rangle\,\langle\psi_2|\mathcal{H}_2|\psi_2\rangle + \langle\Psi|\mathcal{V}_{12}|\Psi\rangle$$

E_E is here introduced as the excitonic interaction energy and it gives the total energy splitting between the states of the interacting chromophores. As already mentioned, the total wavefunction $|\Psi\rangle$ is in general a superposition of product states, which is why E_E may contain contributions from E_{12} and E_{21}. E_{12} corresponds to exciting molecule 1 and ending up in an ES of 2 and E_{21} to exciting molecule 2 and ending up in an ES of molecule 1. For identical molecules, the statements $E_1 = E_2$ and $E_{12} = E_{21}$ hold. In order to find non-trivial solutions for the mixing Hamiltonian, its determinant has to be set to zero.

$$\begin{vmatrix} E_1 - E_E & E_{12} \\ E_{12} & E_1 - E_E \end{vmatrix} = 0 \tag{2.23}$$

Perfectly symmetric and antisymmetric superpositions of the initial wavefunctions are found as eigenstates of the coupled system:

$$\Psi_{\pm} = \frac{1}{\sqrt{2}}(|\psi_1\rangle\,|\psi_2\rangle \pm |\psi_1\rangle\,|\psi_2\rangle) \tag{2.24}$$

The eigenvalues are $E_{\pm} = E_1 \pm E_{12}$ and the total splitting is $E_E = 2 \times E_{12}$. That says, the two (degenerate) states of the unperturbed chromophores lead to two new (non-degenerate) coupled states.

In the approximation of two interacting point dipoles, E_{12} is geometry dependent:

$$E_{12} = \frac{\boldsymbol{\mu}_1 \cdot \boldsymbol{\mu}_2}{\mathrm{r}^3} - \frac{3\,(\boldsymbol{\mu}_1 \cdot \mathbf{r})(\boldsymbol{\mu}_2 \cdot \mathbf{r})}{\mathrm{r}^5} \tag{2.25}$$

$\boldsymbol{\mu}_j$ is the transition dipole moment of a single chromophore j, $\mathbf{r}$ is the spatial displacement vector of the two dipoles, and r is the magnitude of the displacement and thus their mutual distance.

The result of this treatment are first-order wavefunctions and zeroth-order energies for the coupled system. In order to cast the relative amplitudes of the two resulting transitions correctly, a further round of perturbation theory is necessary. From the second-order wavefunctions, which are coupled to each other via London-type induced-dipole dispersion terms[101], relatively simple expression for the strengths of the dipole moments $\mu_- = |\boldsymbol{\mu}_-|$ and μ_+ in dependence of the relative dipole orientations can be given. Here, μ_- and μ_+ correspond to the eigenstates Ψ_- and Ψ_+, respectively. Keeping in mind that $|\boldsymbol{\mu}_1| = \mu_1 = \mu_2$ holds for identical chromophores 1 and 2, the following expressions result:

$$\mu_- = 2\,|\boldsymbol{\mu}_1|\,|\sin(\theta)| = 2\,\mu_1\,|\sin(\theta)| \text{ and } \mu_+ = 2\,\mu_1\,|\cos(\theta)| \tag{2.26}$$

2θ is the angle between the dipole moments. The integral magnitude μ_{total} of the transition-dipole moments of both chromophores $j = 1, 2$ does not change due to the dipole coupling and is twice as large as the transition moment of one isolated chromophore μ_1 (or μ_2).

$$\mu_{\text{total}}^2 = \mu_1^2 + \mu_2^2 = \mu_-^2 + \mu_+^2 = 2\,\mu_1\left(\sin^2(\theta) + \cos^2(\theta)\right) \tag{2.27}$$

The second-order coupling thus redistributes the relative transition intensities between the coupled states in such a way, that μ_- vanishes for parallel molecules

oriented perpendicular to the axis that connects them with each other and is maximal for two molecules oriented in parallel with respect to the same axis.

In nucleic acids, the couplings of all transitions of all (in general not identical) nucleotides have to be summed up in this way to calculate the hysochromicity of a given structure. Because the shift angles between neighboring bases are fairly small in RNA and because the transition moments of the four natural nucleotides are oriented relatively similar, μ_- typically decreases upon helix formations.

A theoretical description of the optical activity OA of polynucleotides is by far more challenging, although the basic idea is relatively simple. One has to calculate the transition probabilities for the absorption of right and left-circularly polarized light and subtract them from each other. The resulting quantity is called rotational strength R_{sf} for transitions between the start state s and the final state f.

Rosenfeld[102] showed that this problem can with some approximations be reduced to calculating

$$R_{sf} = \mathcal{I}\left\{\boldsymbol{\mu}_{sf} \cdot \mathbf{m}_{fs}\right\} \tag{2.28}$$

$\mathcal{I}$ denotes the imaginary part and $\mathbf{m}_{sf} = \langle \Psi_s | \mathbf{m} | \Psi_f \rangle$ is the magnetic transition-dipole moment. $\boldsymbol{\mu}_{sf}$ is the electrical transition dipole moment. Alternatively, cross products of only the electronic transitions can be used to calculate R_{sf} in a relatively simple approximation.[98]

In practical terms, the aim is usually to calculate the spectral circular dichroism (CD) because it is the physical effect, which is used most often to measure the OA. As stated above, the chromophores in a polynucleotide chain are electronically coupled to each other, which makes it difficult to define the transitions properly. It is for example necessary to include high-energy transitions ($\lambda < 200\,\mathrm{nm}$) with a generalized polarization model to explain the fact that the CD spectrum of DNA and RNA is non-conservative at wavelengths longer than 200 nm.[103,104]

In general, a gain in accuracy is only achievable by the inclusion of additional terms, which oftentimes masks the physics behind the OA of helical structures. Therefore, a qualitative model may be considered, here. Besides the excitonic coupling between the nucleobases, the decisive aspect for OA in helices is their helicity. This is demonstrated by a model of minimal complexity, that still delivers OA: it is sufficient to confine the movement of a free electron to a helix.[105] The

electron behaves largely like a particle in a one-dimensional box, but the coupling of lateral movement in the one-dimensional box to a screw motion in three dimensions induces non-vanishing rotatory strength R. The sign of R is indicative of the handedness of the helix.

Chapter 3

Experimental background

In section 3.1, coherent light pulses and selected non-linear processes are explained, whereas section 3.2 presents the spectrometer used for transient absorption spectroscopy (TAS). The sections 3.3 and 3.4 contain the preparation of the samples investigated in this thesis and the experimental procedures used in combination with commercially available equipment.

3.1 Ultrashort laser pulses

This section is largely based on the references [106] and [107].

The availability of pulsed excitation sources is pivotal for time-resolved experiments. In the frame work of this thesis, a series of experiments were conducted using pulsed lasers. Therefore, this section delivers a mathematical description of coherent light pulses and their linear interaction with matter.

As stated in section 2.1.1, the collective behavior of high photon-density fluxes can be well described with the Maxwell equations.[56] Such a situation is encountered in the peak of a ultrashort laser pulse, because the peak power is inversely proportional to the temporal pulse width δt for a given pulse power or total intensity. The transient intensity $I(t)$ is related to the transient electric field $\mathbf{E}(t)$ via

$$I(t) = \frac{c\varepsilon_0 n\omega_0}{2\pi} \int_{t-\pi/\omega_0}^{t+\pi/\omega_0} \mathrm{d}t' \, |\mathbf{E}(t')|^2, \tag{3.1}$$

where n is the refractive index of the medium, and ω_0 is the carrier or central frequency of the light pulse (2.43 PHz for a pulse centered at 775 nm).[108] Because it is sufficient to consider **E**, the following description will be limited to it. In the picture of light as electromagnetic wave, the interaction with matter can be cast into the formula

$$\boldsymbol{\nabla} \times \Big(\boldsymbol{\nabla} \times \mathbf{E}(t, \mathbf{x}) \Big) + \frac{1}{c^2} \frac{\partial^2}{\partial t^2} \mathbf{E}(t, \mathbf{x}) = -\mu_0 \frac{\partial^2}{\partial t^2} \mathbf{P}(t, \mathbf{x}) \tag{3.2}$$

Equation 3.2 is the inhomogeneous wave equation of **E** in a non-magnetic medium.[106] μ_0 is the vacuum permeability, which satisfies the relation $\mu_0 = 1/(\varepsilon_0 c^2)$ and **P** is the dielectric polarization of the medium. For the sake of simplicity, the polarization state of **E** will be neglected, where it is possible: $\mathbf{E} \rightarrow \mathrm{E}$. In the plane-wave approximation, the temporal dependence of $\mathrm{E}(t, x)$ can be separated from the spatial one.[109] Therefore, it is sufficient to consider the time dependence at a fixed point in space.

For any temporal shape, $\mathrm{E}(t)$ can be represented through its Fourier transform:

$$\mathrm{E}(\omega) = \frac{1}{\sqrt{2\pi}} \int_{-\infty}^{+\infty} \mathrm{d}t \left(\mathrm{E}(t)\, \mathrm{e}^{-i\omega t} \right) = \mathcal{F}\Big\{ \mathrm{E}(t) \Big\} \tag{3.3}$$

with

$$\mathrm{E}(t) = \frac{1}{\sqrt{2\pi}} \int_{-\infty}^{+\infty} \mathrm{d}t \left(\mathrm{E}(t)\, \mathrm{e}^{i\omega t} \right) = \mathcal{F}^{-1}\Big\{ \mathrm{E}(t) \Big\} \tag{3.4}$$

The Fourier transform $\mathcal{F}$ is isomorph, which guarantees the existence of its inverse transform $\mathrm{E}(t) = \mathcal{F}^{-1}\Big\{\mathrm{E}(\omega)\Big\}$.[110] From $\mathrm{E}(t) \in \mathbb{R}$ follows $\mathrm{E}(\omega) = \mathrm{E}^*(-\omega)$.Thus, contributions to the electric field $\mathrm{E}(\omega)$ with $\omega < 0$ contain no physically relevant information and it is possible to use $\mathrm{E}^+(\omega) = \Theta(\omega) \times \mathrm{E}(\omega)$ instead of $\mathrm{E}(\omega)$ without loss of generality. $\Theta(\omega)$ is the Heavyside-function[109] and sets all values of $\mathrm{E}^+(\omega)$ to 0 for $\omega < 0$ and to $\mathrm{E}(\omega)$ otherwise. The resulting $\mathrm{E}^+(t) = \mathcal{F}^{-1}\Big\{\mathrm{E}^+(\omega)\Big\}$ is then complex.[vi]

The complex quantities $\mathrm{E}^+(t)$ and $\mathrm{E}^+(\omega)$ can be represented in their Euler forms $\mathrm{E}_0^+(t)\mathrm{e}^{i\,\varphi(t)} = \mathrm{E}_0^+(t)\mathrm{e}^{i\,(\omega_0 t + \Phi(t))}$ and $\mathrm{E}_0^+(\omega)\mathrm{e}^{-i\,\Phi(\omega)}$, respectively. The instantaneous frequency ω_{inst} of the electric field $\mathrm{E}^+(t)$ is the first derivative of $\varphi(t)$ with respect to t:

[vi] The measurable quantity $I(t)$ is not affected by this definition.

$$\omega_{\text{inst}} = \frac{\mathrm{d}\varphi(t)}{\mathrm{d}t} = \omega_0 + \frac{\mathrm{d}\Phi(t)}{\mathrm{d}t} \tag{3.5}$$

The first derivative of ω_{inst} with respect to t is called chirp c_{ch}

$$c_{\text{ch}} = \frac{\mathrm{d}\omega_{\text{inst}}(t)}{\mathrm{d}t} = \frac{\mathrm{d}^2\varphi(t)}{\mathrm{d}t^2} = \frac{\mathrm{d}^2\Phi(t)}{\mathrm{d}t^2} \tag{3.6}$$

where $c_{\text{ch}} > 0$ is called positive (or normal) chirp and $c_{\text{ch}} < 0$ negative (or anomalous) chirp because it is usually not introduced by dispersive media, alone. Within the context of this thesis, chirp is introduced intentionally as part of the chirped–pulse-amplification technique (see section 3.2) and unintentionally upon the passage of the laser pulses through any medium such as lenses or the solvent containing the sample. The latter case can deteriorate the temporal resolution of an experiment. The chirp is related to the dispersive properties of a medium via the so-called group velocity dispersion (GVD):

$$\text{GVD} = \left.\frac{\mathrm{d}(1/v_{\text{g}}(\omega))}{\mathrm{d}\omega}\right|_{\omega=\omega_0} \tag{3.7}$$

$v_{\text{g}}(\omega)$ is the group velocity of the different components of a pulse upon the passage through a dispersive medium of length l and it is closely related to the first derivative of the spectral phase $\Phi(\omega)$ of the electric field $\mathrm{E}^+(\omega)$ with respect to ω. Due to the dispersion of a medium, different spectral components of the pulse travel with different velocities. Therefore an additional, material-dependent term has to be added:

$$\left.\frac{\mathrm{d}\Phi(\omega)}{\mathrm{d}\omega}\right|_{\omega=\omega_0} \propto \left.\left[\frac{l}{c}\left(n(\omega) + \omega\frac{\partial n(\omega)}{\partial\omega}\right)\right]\right|_{\omega=\omega_0} = \left.\frac{l}{v_{\text{g}}(\omega)}\right|_{\omega=\omega_0} \tag{3.8}$$

The chirp that an ultrashort laser pulse takes up upon the passage through a dispersive medium is therefore a direct consequence of the differences in the propagation speed of the different spectral components. Normal dispersion causes low-energy components to propagate faster than high-energy components.

Beyond that, higher order derivatives of ω_{inst} with respect to t may be significant. They introduce structures such as satellite pulses or pulse trains but they are not a subject of this thesis.

Because $\mathrm{E}^+(t)$ and $\mathrm{E}^+(\omega)$ are connected to each other via a Fourier transform, the temporal width δt and the bandwidth $\delta\omega$ of a pulse fulfill the relation

$$\delta t \, \delta\omega \geq 2\pi \, c_{\text{env}}, \tag{3.9}$$

where c_{env} is a constant that depends on the shape of the pulse envelope. In the simplest case, the pulse shape is Gaussian and $c_{\text{env}} \approx 0.44$.[111] δt and $\delta\omega$ correspond to the full-width-at-half-maximum (FWHM) values of the transient pulse intensities in the time and the spectral domain, respectively. Equation 3.9 shows that a short pulse (optimal time resolution) requires a large bandwidth. At the same time, a larger bandwidth leads to stronger pulse-broadening due to material dispersion. The equality holds only, when the spectral phase $\Phi(\omega)$ is flat.

3.1.1 Non-linear optics

For time-resolved experiments—including transient absorption (TA) and time-correlated single-photon counting (TCSPC)—pulses of appropriate wavelengths are required as detailed in section 2.1.1. Solid-state laser systems usually work optimally at material-dependent spectral position with only a relatively small spectral range being accessible.

In order to achieve spectral tunability for the pump and a high spectral width for the probe light, several non-linear optical processes are employed in the frame of this thesis. Many processes rely on interpulse phase matching (section 3.1.2) like for example optical parametric amplification (OPA), second harmonic generation (SHG), and sum-frequency generation (SFG) in section 3.1.3. Supercontinuum generation (SCG) on the opposite rather relies on the matter-mediated self-interaction of a single light pulse and is a process of third order (see section 3.1.4).

3.1.2 Phase matching

Parts of this section are based on reference [112].

Non-linear wave-mixing processes have to conserve both, energy

$$\sum_{j_{\text{in}}} g_{j_{\text{in}}} \, \omega_{j_{\text{in}}} = \sum_{j_{\text{out}}} g_{j_{\text{out}}} \, \omega_{j_{\text{out}}} \tag{3.10}$$

and momentum

$$\sum_{j_{\text{in}}} g_{j_{\text{in}}} \mathbf{k}_{j_{\text{in}}} = \sum_{j_{\text{out}}} g_{j_{\text{out}}} \mathbf{k}_{j_{\text{out}}} \tag{3.11}$$

of all participating photons (or waves).[113] The factors g_j denote the number of photons of a given kind to participate in the mixing process. Effectively, the g_j give the stoichiometry of educt and product photons. Equation 3.11 is also referred to as phase-matching condition.

Non-linear interactions generally need matter to occur because it is the matter (refractive index n) that mediates the interaction between the photons. Assuming a collinear geometry, equations 3.10 and 3.11 translate into

$$\sum_{j_{\text{in}}} \tilde{g}_{j_{\text{in}}} n(\omega_{j_{\text{in}}}) = \sum_{j_{\text{out}}} \tilde{g}_{j_{\text{out}}} n(\omega_{j_{\text{out}}}) \tag{3.12}$$

and

$$\sum_{j_{\text{in}}} \tilde{g}_{j_{\text{in}}} \omega_{j_{\text{in}}} n(\omega_{j_{\text{in}}}) = \sum_{j_{\text{out}}} \tilde{g}_{j_{\text{out}}} \omega_{j_{\text{out}}} n(\omega_{j_{\text{out}}}), \tag{3.13}$$

respectively. The $\tilde{g}_j$ correspond to the g_j but they include the proper sign that is lost by omitting the directional component of the $\mathbf{k}$ vectors because collinear pulses may travel antiparallel, as well.

Equations 3.12 and 3.13 cannot be fulfilled simultaneously in isotropic media with normal dispersion. Choosing geometries other than the collinear one can help to circumvent that, but more important is the use of birefringent media.[114] Birefringent crystals have different dispersion relations $n(\omega)$ for different polarization directions of $\mathbf{E}$ with respect to a single, optically anisotropic crystal axis (uniaxial crystals). This axis is called optical axis.

The component of $\mathbf{E}$ polarized perpendicular to the optical axis of the crystal experiences the same dispersion $n_{\text{o}}(\omega)$ irrespective of the angle of incidence with respect to the crystal lattice.[115] It is therefore termed ordinary component (o). The component of the $\mathbf{E}$ oscillating within the plane containing the optical axis experiences a dispersion $n_{\text{e}}(\omega)$ that depends on the angle between the optical axis and the propagation direction of the light. This component is termed extraordinary (e). The effective refractive index of the extraordinary beam assuming perpendicular incidence on the crystal surface is given by

$$\frac{1}{n_e^2(\omega,\theta)} = \frac{\sin^2(\theta)}{n_o^2(\omega)} + \frac{\cos^2(\theta)}{n_e^2(\omega,\pi/2)}. \tag{3.14}$$

θ is the cut angle of the crystal, which specifies the angle between the optical axis and the crystal front face.

3.1.3 Three-wave mixing

The basis of non-linear interactions is the dielectric susceptibility χ of matter.

$$\mathbf{P} = \varepsilon_0 \chi \mathbf{E} \tag{3.15}$$

In linear optics, χ describes the linear response of a dielectric medium to $\mathbf{E}$. For interactions with intense light fields—as is typically the case for the peaks of ultrashort laser pulses—terms of higher order in $\mathbf{E}$ become important, which is covered by an expansion of χ:

$$\mathbf{P} = \sum_{n=1}^{\infty} \mathbf{P}^{(n)} = \sum_{n=1}^{\infty} \prod_{j=1}^{n} \varepsilon_0 \chi^{(n)} \mathbf{E}_j \tag{3.16}$$

The order n gives the number of electric fields $\mathbf{E}_j$ being coupled within one process to yield an additional field. $\mathbf{P}^{(n)}$ is the (non-linear) polarization, which generates the product electric field. Because the $\mathbf{E}_j$ are vectors with three components in the most general case, the $\chi^{(n)}$ are tensors. A mixing process is characterized by the $\mathbf{E}_j$ and the generated field. A process, which mixes two electric fields on the right-hand side of equation 3.16 to yield one new field on the left-hand side, is termed three-wave mixing process.

Three-wave mixing is the simplest case of non-linear optics and is sufficient to describe the majority of the processes employed within this thesis[107]:

$$\mathrm{P}_k^{(2)}(\omega_3) = \varepsilon_0 \sum_{l,m} \sum_{\omega_1,\omega_2} \chi_{klm}^{(2)}(-\omega_3,\omega_1,\omega_2)\mathrm{E}_{1,l}(\omega_1)\mathrm{E}_{2,m}(\omega_2) \tag{3.17}$$

k, l, and m represent the possible polarization directions x, y, and z. The k^{th} component of the second order polarization $P_k^{(2)}$ yields the corresponding component of the resulting field $\mathrm{E}_{3,k}^{(2)}$:

$$\mathrm{E}^{(2)}_{3,k}(t) = \varepsilon_0 \chi^{(2)}_{klm} \mathrm{E}_{1,l}(t) \mathrm{E}_{2,m}(t) \tag{3.18}$$

The most general representation of a light wave at a given point in space is of the form

$$\mathrm{E}(t) = \mathrm{E}_0 \left(\mathrm{e}^{-i\,\omega t} + \mathrm{e}^{+i\,\omega t}\right) = \mathrm{E}^{-}(t) + \mathrm{E}^{+}(t). \tag{3.19}$$

With equation 3.19, the product at the right-hand side of equation 3.18 yields mixing terms such as $\mathrm{E}^{+}_{1,l}(t) \times \mathrm{E}^{+}_{2,m}(t)$ and $\mathrm{E}^{+}_{1,l}(t) \times \mathrm{E}^{-}_{2,m}(t)$. Terms with equally signed waves interacting with each other lead to the generation of an electric field with the carrier frequency ω_3, which is the sum of the two incident waves: $\omega_3 = \omega_1 + \omega_2$. This process is called sum-frequency generation (SFG). Mixing of terms with different signs is possible, as well. This would lead to $\omega_3 = |\omega_1 - \omega_2|$. Whether one of these processes occurs and which one is dominating is solely determined by the relative orientation of the cut angle and the propagation direction of the electric fields. This determines, which phase-matching condition is fulfilled.[vii]

For $\omega_1 = \omega_2$, the resulting frequency for efficient SFG is $2\omega_1$. This kind of degenerate SFG is an important special case and it is called second harmonic generation (SHG).

Three-wave mixing can also be run in such a way that one intense incoming pump pulse (ω_p) generates two outgoing pulses, signal (ω_s) and idler (ω_i). Such a situation is encountered in optical parametric amplification (OPA) processes. There, the pump is the pulse with the largest photon energy.

$$\omega_\mathrm{p} = \omega_\mathrm{s} + \omega_\mathrm{i} \tag{3.20}$$

In order to achieve phase matching, two fields are polarized parallel to each other and the third one is polarized perpendicular to them. Besides the crystal orientation and its cut angle, a low-intensity, broadband pulse is used as seed to define and stabilize the ω_s. The generation of such a broadband pulse is explained in the next section.

[vii] The efficiency and the bandwidth of the phase-matching process are additionally affected by the thickness of the crystal. Longer propagation path lengths lead to stronger product electric fields, but this comes at the price of a smaller supported bandwidth and hence inferior time resolution.

If the parametric process is driven in a collinear beam geometry, the resulting power of the signal will be large, but the bandwidth will be rather small. Therefore, the OPA used in this thesis was a non-collinear one (NOPA), which supports superior bandwidths.[116,117] A NOPA uses the non-collinear beam geometry as additional parameter to effectively match the propagation velocities of the three interacting pulses in the medium. As consequence, the acceptance bandwidth of the mixing process is increased.

3.1.4 Supercontinuum generation

A supercontinuum (SC) is a low-intensity laser pulse with a potentially extremely broad[118], ideally flat spectrum. The processes involved in supercontinuum generation (SCG) cover spatial[119] and temporal[120] self focusing, multi-photon ionization[121], self-phase modulation[122] stimulated Raman scattering[123], and their material dependent interactions. Although SCG is not completely understood, the relevant processes are known to be dominated by four-wave mixing and are thus related to $\chi^{(3)}$.

Self-phase modulation is particularly interesting because it is responsible for the SC parts with photon energies larger than the energy of the SC-generating pulse. Only the high-energy parts of the SC spectrum were used within this thesis. SCs are typically generated by a single input pulse with $\mathrm{E_{in}}$. This leads to an emitted field $\mathrm{E}_4^{(3)}$:

$$\mathrm{E}_4^{(3)}(t) = \varepsilon\chi^{(3)}\mathrm{E}_{\mathrm{in}}^3 \propto I_{\mathrm{in}}\mathrm{E}_{\mathrm{in}} \tag{3.21}$$

For cubic crystals ($\chi^{(2)} = 0$) an intensity-dependent refractive index $n(I)$ results:

$$n(I) = n_0 \sqrt{1 + \frac{3\chi^{(3)}I(t)}{2c\varepsilon_0 n_0^2}} \approx n_0 + n_2\, I(t) \tag{3.22}$$

The final expression is the result of a Taylor expansion in $2n_2I(t)$ with $n_2 = (3\chi^{(3)})/(4c\varepsilon_0 n_0^2)$. The dependence $n \propto I$ is termed quadratic electro-optical Kerr effect.[108]

The spectral broadening is a result of the influence of n on the time-dependent phase $\varphi(t)$ at a given point in space x. There, the proportionality to $\omega_0 t$ translates into $\omega_0(t - nx/c)$. This leads to the following additional contribution to the instantaneous frequency $\omega_{\mathrm{inst}} = \mathrm{d}\Phi(t)/\mathrm{d}t$:

$$\omega_{\text{inst}} \propto -\frac{\omega_0 n_2 x}{c} \frac{\mathrm{d}I(t)}{\mathrm{d}t} \tag{3.23}$$

At the leading edge of the pulse, $\mathrm{d}I(t)/\mathrm{d}t$ is positive and the spectrum is shifted to smaller energies. At the falling edge of the pulse, however, contributions with higher photon energies are added.

3.2 Transient absorption spectroscopy in the UV/Vis spectral range

TA measurements were performed with a home-built pump-probe setup based on a Clark-MXR-CPA-2001 oscillator/amplifier system (Clark-MXR Inc., Dexter, Michigan, USA). It delivered pulses with 150 fs length and 800 μJ energy at 990 Hz laser repetition rate at 775 nm. The setup is shown in a schematic fashion in figure 3.1. For a theoretical description of the relevant non-linear optical processes, please see section 3.1.

The Clark-MXR-CPA-2001 is based on the principle of chirped-pulse amplification (CPA). CPA relies on an ultrafast oscillator (here an erbium-doped SErF fiber oscillator[124,125]) that delivers pulses of 100 fs duration with an excitation rate of 35 MHz. It is continuously pumped at 980 nm and runs passively mode-locked at 1550 nm. The oscillator output is the SHG of its fundamental (775 nm) and it is overlapped in a titan-doped sapphire (Ti:Sa) crystal as active medium with the ns-amplifier-pump pulse of a frequency-doubled ORC-1000 neodymium-doped yttrium-aluminium-garnet (Nd:YAG) pump laser (532 nm, 7 W). The latter is itself pumped by a flash lamp. The pump laser has a repetition rate of 990 Hz and renews the population inversion by cyclic repumping with this rate. The oscillator output is used as seed radiation, which is amplified via the population inversion induced by the Nd:YAG laser in the Ti:Sa crystal. The seed pulse makes typically 10 to 20 round trips in the amplifier cavity, gaining power upon each passage of the crystal. When the amplification of the seed pulse is saturated, the amplified pulse is coupled out of the amplifier. Coupling in and out of the amplified pulses is controlled by Pockels cells that modulate the polarization state of the pulses.

The amplification scheme is termed 'chirped pulse' because the seed pulses have to be elongated temporally (stretched) to 200 ps before they are introduced into the amplifier cavity to avoid damage of the active medium due to high

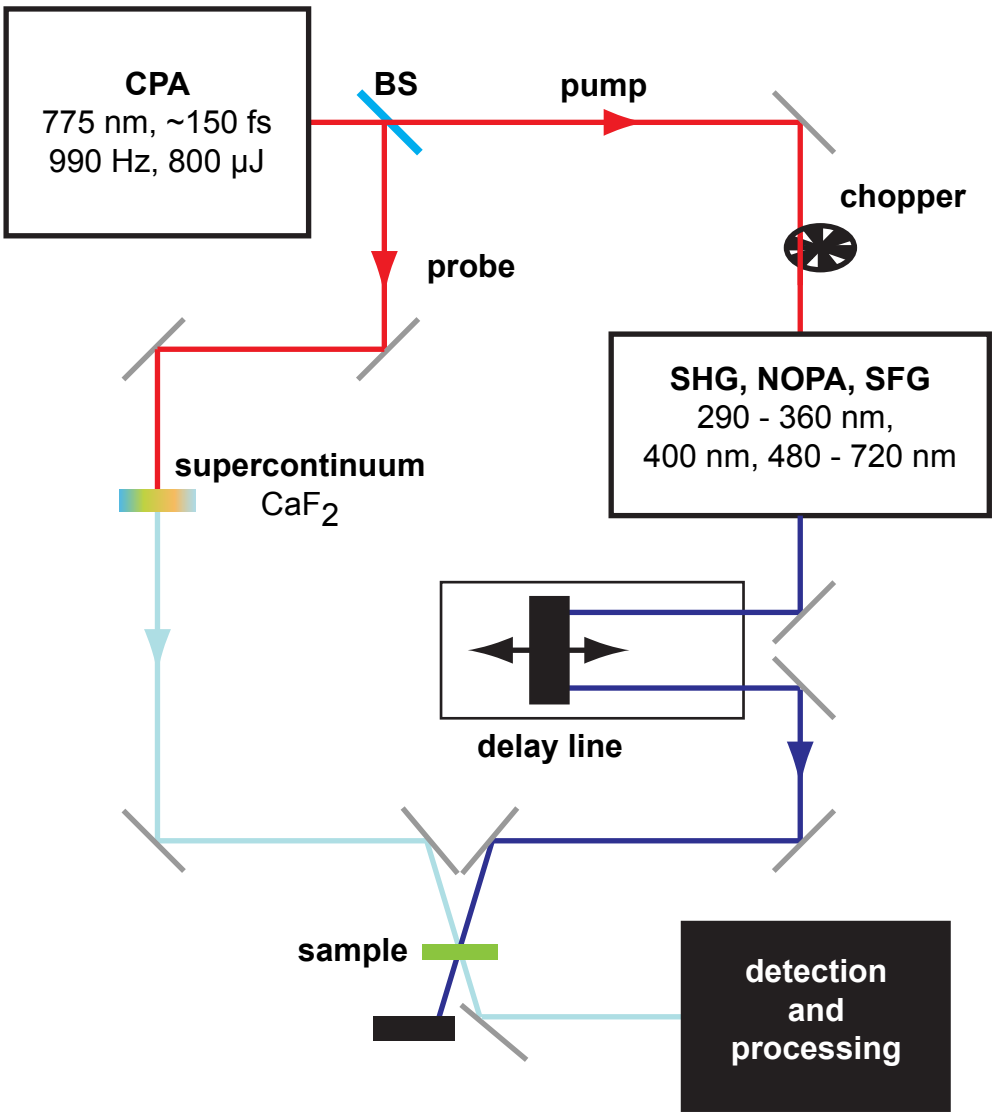

Figure 3.1: The TA setup used for ultrafast time-resolved experiments in the UV/Vis.

peak electric field strengths.[126] After the amplification, the pulses have to be recompressed with a compressor. Stretcher and compressor are combinations of diffraction gratings and refocusing optics.[127,128] The laser pulse is dispersed into its spectral components by the grating and the components are parallelized. Because the components are displaced relative to each other in the plane of the grating, the geometrical and thus optical path lengths of low and high-energy components are distinct. By adjusting the total path length within the stretcher and compressor, a large range of effective dispersions can be applied to the pulse, including anomalous ones. Anomalous dispersion means that the high-energy components travel faster through the geometrical path than the low-energetic ones. Thereby, pulses can be (re)compressed even in the presence of dispersive

media, such as lenses or the gain medium itself.

The CPA output was split by a beam splitter (BS) into two parts, the pump and the probe branch. In the pump branch, an 0.5-mm-thick BBO crystal ($\Theta = 30\,°$, type I[129]), which is part of a NOPA[116,130,131], was used for SHG to provide the excitation pulses at 388 nm or to pump the parametric process. The parametric process itself occured in an 2-mm-BBO ($\Theta = 29\,°$, type II) with an SC generated in a sapphire crystal. Another portion of the laser fundamental was split off in front of the NOPA to serve as pump pulse for SFG[132] performed in BBO ($\Theta = 39\,°$, 0.5 mm, type I). After all nonlinear processes, the pump ran over a programmable delay line used to alter the optical path lengths of pump and probe relative to each other.

In the probe branch, an SC was generated in a 5-mm-thick CaF_2 window with a usable probe spectrum from 340 to 680 nm. The window was continuously moved in the plane perpendicular to the beam path to avoid its early degradation.

SC and excitation were focused to spots with diameters of 100 and 200 µm, respectively, and overlapped in the sample. A 600-grooves/mm-grating resulted in a spectral dispersion of 3.6 nm per pixel. Excitation pulse energies were attenuated to ensure that < 5 % of the sample was excited. The cross-correlation width of pump and probe in pure solvent was found to be 0.2 ps. A chopper was used to block every other pump pulse. Accordingly, the measurement software used a two-pulse scheme to calculate one single absorption value, yielding an effective data-acquisition rate of about 500 Hz. One saved data point was the average of 1500 of such two-pulse measurement cycles. For a series of defined positions of the delay stage, the the averaging procedure was repeated and from all delays, the decay behavior was recovered. The stage driving cycle was repeated several times (50 – 100) and the results were averaged in order to improve the signal-to-noise ratio.

Data analysis is based on global lifetime analysis (GLA) as implemented with Optimus[viii].[133] The approach uses a (multi-)exponential model of the form

$$S(\lambda_{\text{pump}}, \lambda_{\text{probe}}, t) = \sum_{i=1}^{N} A_i(\lambda_{\text{pump}}, \lambda_{\text{probe}}) \times \exp\Big[-t/\tau_i(\lambda_{\text{pump}}) \Big] , \tag{3.24}$$

[viii] available from http://optimusfit.org/index.php

where N represents a finite number of decay components (typically ≤ 5). The dependence of the amplitudes A_i from the probe wavelength generates spectra that are associated with the discrete time constants τ_i. The τ_i are expected to be universal throughout the whole spectral probe range. Accordingly, the A_i are named decay-associated spectra (DAS).

The model is folded with an idealized instrument response function (IRF) represented by a Gaussian error function in its integral form. This fit delivers the width of the IRF that can be used to estimate the time resolution of the experiment.

A plot of the transient spectra ordered by the delay times is called transient card. The transient cards can be corrected for the chirp of the probing SC by fitting the time zero (which is a parameter included in the IRF) to a polynomial of the order $n \leq 4$ (an order of 2 was found to be sufficient for all data sets shown in this work). Additionally, the coherent artifact is fitted to a model of Gaussian functions plus its first and second derivative.[134,135] Presented raw data and fits are routinely corrected for both, the artifact and the chirp.

3.3 Sample preparation

The chapters 5 and 6 present the work that was performed on the three possible isomers of 2-(pyrenylethynyl) adenosine (PyAs) and the tetracycline-binding aptamer (TC aptamer), respectively. The isomers of PyA are 2-(1-pyrenylethynyl) adenosine (1PyA), 2-(2-pyrenylethynyl) adenosine (2PyA), and 2-(4-pyrenylethynyl) adenosine (4PyA), respectively. The samples were prepared and provided by collaboration partners and are thus not contained in the chapters describing results obtained within this thesis. Section 3.3.1 describes the synthesis of the PyAs and section 3.3.2 the transcription of the aptamer.

3.3.1 Pyrenylethynyl adenosines

The synthesis of the PyAs largely follows the procedures published for 1PyA.[48,136] Synthesis was performed by Dr. Christian Grünewald. Dimethylformamide and triethyl amine were mixed in a 12:1 volume ratio and degassed to exclude O_2. X-ethynylpyrene (X equals 1, 2, or 4)[137] was reacted with 0.77 equivalents of 2-iodoadenosine[138,139] for 24 to 48 hours at room temperature under argon atmosphere. Various steps of the synthesis employ a Sonogashira coupling.[140]

2-Iodoadenosine was synthesized from guanosine in a four-step synthesis. An acetylation of the hydroxy groups was followed by a chlorination at the 6-position of the nucleobase and an iodination at the 2-position. Finally, the resulting 6-chlorine-2-iodopurine was converted with ammoniacal MeOH, which leads to a simultaneous elimination of the acetyl groups and a substitution of the chlorine at position 6 by amine.[138,141,142]

1-Ethynylpyrene was synthesized via bromination of Py at the 1-position in a mixture of HBr and H_2O_2 in MeOH and diethyl ether[143] followed by an alkylation in morpholine with mole fractions of 2 % of Pd catalysator and 6 % of CuI. 2- and 4-ethynylpyrene cannot be synthesized directly from pyrene, but need aromatic intermediates because these positions are non-reactive for an electrophilic substitution.[144] Py was converted into 4,5,9,10-tetrahydropyrene and 1,2,3,6,7,8-hexahydropyrene via partial reduction.[145,146] 4,5,9,10-Tetrahydropyrene and 1,2,3,6,7,8-hexahydropyrene served as intermediates for the synthesis of 2-ethynylpyrene and 4-ethynylpyrene, repectively.

The coupling reaction was performed in the presence of 10 and 17 % of 2-iodoadenosines amount of substance of PD catalysator and CuI, respectively. The resulting mixture was filtrated and absorbed on silica gel. Purification was performed via column chromatography with a 9:1 volume ratio of dichloromethane and MeOH as an eluent. Recrystallization from MeOH gives the different PyAs as a yellow powder. The yields are 80, 65, and 85 % for 1-, 2-, and 4PyA, respectively. The solubility of the PyAs is best in DMSO. Therefore, they were dissolved in DMSO to a final concentration of 10 mM as a stock solution. From this stock, sample solutions were derived via serial dilution. Consequently, in each final solution, one volume per cent DMSO is contained per 100 µM sample. The PyAs showed excellent long-term stability in DMSO and MeOH.

The 2PyA samples were relatively lately discovered to contain triethyl amine or its salt in a stoichiometric ratio of 1:2 relative to 2PyA. In order to estimate the impact of this contamination on the photophysical behavior of 2PyA, a further purification step was performed: the 2PyA batch which was purified according to the described standard procedure was washed with Milli-Q water. Because triethyl amine is water soluble and 2PyA is hardly, the ratio of triethyl amine to 2PyA could be reduced to at most 1:20. Afterwards, the washed sample was dried and redissolved in DMSO.

Section A in the appendix shows a comparison between the two batches. The differences of the fluorescence between the two batches were found to be smaller

than 5 %, with respect to the number of the decay constants, their values, and their relative contributions to the total decay. Therefore, the conclusions drawn for the photophysical behavior of 2PyA are also valid in the absence of any triethyl amine. All experiments shown in this thesis were performed with 2PyA purified according to the standard procedure.

3.3.2 Tetracycline-binding aptamer

All RNA used within this thesis was prepared via in-vitro transcription. The transcription was performed by Dr. Julia E. Weigand and Marc Vogel, using a HindIII linearized plasmid as template. The plasmid contains the T7 promoter, the desired aptamer sequence and a self-cleaving HDV ribozyme. The ribozyme ensures heterogeneous 3'-ends of the aptamer sequence. Transcription was performed over twelve hours at 37 °C. The reaction volume was 10 ml and contained 20 mM magnesium acetate buffer with 200 mM Tris-HCl (pH 8.0), 2 mM spermidine, 20 mM dithiotreitol. In the reaction volume, 7.5 µg/ml of in-house T7 polymerase was added to 200 µg/ml of the linearized plasmid together with 4 mM of each nucleoside triphosphate.

Precipitated pyrophosphate as side product of the transcription reaction was removed as pellet after centrifugation. The supernatant was mixed with 10 volume per cent of 0.5 mM ethylenediaminetetraacetic acid (pH 8.0). Then, the RNA was precipitated with ethanol and the product was put on denaturing polyacrylamide (PAA) gel for electrophoresis. The gel contained 8 % of PAA and 8 M urea. On the gel, the RNA was detected via UV-shadowing. The corresponding region was cut out of the gel and the RNA was eluted at 4 °C from the gel in 300 mM sodium acetate (pH 6.5) for twelve hours. The supernatant of the elution solution was filtered through an 0.45 µm filter (Sarstedt, Nümbrecht, Germany) to remove rests of the gel. The RNA was once more precipitated with ethanol. As final step, the RNA was dissolved in double-distilled water. In this state, it was stored at −20 °C, where it was found to remain stable for several years.

3.4 Experimental conditions

Here, the experimental procedures used with commercially available experimental equipment are described. Section 3.4.1 details the experimental conditions for

the experiments with the PyAs and section 3.4.2 is devoted to the TC aptamer.

3.4.1 Pyrenylethynyl adenosines

Absorption spectra of 15 μM MeOH solutions were recorded in 4x10 mm fused-silica absorption cuvettes (Hellma GmbH & Co. KG, Müllheim, Germany) with a Jasco V-650 absorption spectrometer (Jasco Labor- u. Datentechnik GmbH, Groß-Umstadt, Germany), spectra in THF and MeCN were recorded with 30 μM solutions in 10x10-mm cuvettes (Hellma GmbH & Co. KG, Müllheim, Germany). Extinction coefficients were measured with serial dilution in 4x10 and 10x10 fused-silica cuvettes with a Specord S 100 absorption spectrometer (Analytik Jena AG, Jena, Germany) with sample concentrations ≤ 30 μM. All spectra were routinely background corrected.

TA experiments were performed on the setup described in section 3.2. The sample was contained in UV-absorption cuvettes with 1 mm optical path length (Starna Scientific Ltd., Hainault, UK). The cuvette was moved perpendicularly to the probe-beam propagation direction to avoid reexcitation of already excited molecules in successive pump-probe cycles. All experiments were performed under magic-angle conditions[57,147] to exclude anisotropy-induced artifacts. Before and after each experiment, steady-state absorption spectra were recorded with a Specord S 100 absorption spectrometer (Analytik Jena AG, Jena, Germany) to check for excessive photodamage. No significant damage could be observed. Sample concentrations are indicated, where the data are presented.

Fluorescence was recorded with a Jasco FP-8500 spectrofluorometer (Jasco Labor- u. Datentechnik GmbH, Groß-Umstadt, Germany). For concentrations up to 300 μM in MeOH no signs for complex and excimer formation could be observed. Sample concentrations are ≤ 10 μM, unless stated otherwise. Measurements were performed in 4x10 mm fused-silica fluorescence cuvettes (Hellma GmbH & Co. KG, Müllheim, Germany). Emission spectra in THF and MeCN were recorded at concentrations of 2.4 and 3.8 μM, respectively. All spectra are routinely corrected for their background and for the color-dependent detector response.

ϕ_f was measured in MeOH relative to quinine sulfate in 0.5 M H_2SO_4 as standard (ϕ_f = 0.60).[148] ODs were ≤ 0.1 and all spectra were corrected for excitation attenuation and the mismatch of the indexes of refraction. ϕ_f of 1PyA was determined for excitation at 350 nm, 2PyA and 4PyA were excited at 335 nm.

The sample conditions for the time-resolved fluorescence emission experiments are essentially as described above for the steady-state fluorescence experiments. The time-resolved fluorometer is described in detail in chapter 4.

3.4.2 Tetracycline-binding aptamer

All experiments were performed either in 20 mM potassium phosphate (PBS) buffer (pH 7.5) or in 20 mM sodium-cacodylate (SCC) buffer. NaCl concentrations varied between 80 and 120 mM, RNA and ligand concentrations were less than 15 and 40 μM, respectively. The exact buffer conditions are indicated for every experiment presented in chapter 6. An ND-1000 spectrophotometer (Thermo Fischer Scientific, Wilmington, USA) was used to measure the RNA concentration in distilled water via the extinction at 260 nm. The concentrations of TC and doxycycline (DOX) were measured in aqueous solution using their respective extinction coefficients of 13320 l/mol/cm at 355 nm and of 13180 l/mol/cm at 351 nm, respectively. Ligand stock solutions were prepared freshly when needed to prevent hydrolysis. Samples were prepared by mixing all components directly before the experiment.

UV-proof fused-silica absorption cuvettes (Hellma Analytics, Müllheim, Germany, 4x10 mm) were used for UV-absorption experiments. The experiments were performed with a Jasco V-650 spectrophotometer (Jasco Germany, Groß-Umstadt, Germany). The total extinction of the RNA at 260 nm was between 0.5 and 0.8 OD (optical density). [RNA]= 1.5 μM, [ligand]= 7.5 μM.

CD measurements were performed on a Jasco J-710 spectropolarimeter (Jasco Germany). UV-absorption cuvettes (Hellma Analytics) with optical path lengths of 2, 4, and 10 mm were used for 7.5, 4.5, and 1.5 μM RNA, respectively. The ligand concentration was 7.5 μM. This resulted in ODs of 0.5 – 0.8 at 260 nm.

10x2 mm UV-fluorescence cuvettes (Hellma Analytics) were used to measure fluorescence spectra with a FLUOROLOG FL3-22 spectrofluorometer (HORIBA Jobin Yvon, Unterhaching, Germany). Excitation was performed at 375 nm and the emission was detected between 390 and 690 nm with a data pitch of 1.5 nm and spectral bandwidths of 2.5 nm. [RNA]= 1.5 μM, [ligand]= 7.5 μM.

Measurements of the dissociation constant K_d of aptamer and ligand were based on the ligand fluorescence, which strongly increases upon binding[25] and followed essentially previously published procedures[22]. Briefly, aptamer was

titrated to a buffer solution containing a defined amount of TC. The fluorescence response of TC was measured upon each titration step. In contrast to the described procedures, the bandwidths of the fluorescence spectrometer were set to 4 nm with an integration time of 0.1 s. The waiting time between successive titration steps was 4 minutes to guarantee sample equilibration. Because the K_d-values were found to depend on the Mg^{2+} concentration, different TC concentrations had to be used with different $MgCl_2$ concentrations: 25 and 0.5 nM TC with 0.3 and 0.8 mM $MgCl_2$, respectively.

UV–absorption- and CD-monitored $MgCl_2$ titrations were performed manually with a Hamilton MICROLITER syringe (Hamilton Bonaduz, Bonaduz, Switzerland) that had a maximal volume of 5 µl at 25 °C. Suitable $MgCl_2$ solutions were added stepwise in 2 µl portions to 1 ml starting volumes in the cuvette. The solutions were thoroughly mixed and allowed to equilibrate for another three minutes before acquisition of each data point. The total volume change was ≤ 5 % and corrected mathematically. UV absorption was monitored from 220 to 330 nm and eleven data points in the range of 260 ± 5 nm were averaged and plotted over [$MgCl^{2+}$] for the evaluation. CD was measured between 220 and 320 nm and eleven data points at 270 ± 2 nm were treated as described for the UV absorption. Uncertainties in the Mg^{2+} concentrations were calculated from the cumulative uncertainty of the titration syringe via Gaussian error propagation, uncertainties on the abscissa are estimated from the standard deviation of all replicate titrations performed (at least two in each case). Under the applied experimental conditions, the OD of TC alone was well below 0.1 with Mg^{2+}-induced changes being even considerably smaller. Accordingly, there was no necessity to correct the titrations for changes of the background absorption. For fluorescence-monitored titrations, the complete fluorescence spectra were summed up, yielding estimates of the relative fluorescence quantum yields.

Thermal de- and renaturation profiles of 1.5 µM aptamer in absence of any or presence of 7.5 µM ligand were monitored with UV absorption at 260 nm and fluorescence emission, respectively. The temperature gradient was 1.5 °C/min between 20 and 80 °C. Heating and cooling profiles were averaged to compensate for hysteresis. The evaluation of the melting curves is described in detail in the section 6.4.2.

Isothermal Titration Calorimetry (ITC) was used to measure the binding enthalpy. Therefore, the sample is contained in a cell with defined volume in a temperature-stabilized pocket together with a reference cell containing the same

amount of buffer. The titrant is added stepwise to the sample solution under constant stirring. The binding reaction of the ligand with the aptamer is exothermic. Therefore, the sample has to be actively cooled in order to keep the temperature constant and the ITC measures the amount of heat needed to achieve this. This amount of compensating heat equals the amount of heat released by the binding reaction per titration step. The sum over all titration steps then yields the total enthalpy of the binding reaction.

An iTC200 microcalorimeter (MicroCal, GE Healthcare, Chalfont St. Giles, UK) was used with a sample cell containing 200 µl of RNA-ligand-buffer solution without $MgCl_2$. The titration was performed with an automated syringe containing the titrant ($MgCl_2$ solution in buffer). Because the calorimeter measures any kind of heat change in the sample cell, particular care has to be taken to match the buffer conditions between sample cell and syringe. Therefore, each sample measurement is complemented by a buffer measurement, where the heat of dilution of the titrant in the absence of RNA is measured. The dilution is subtracted from the binding heat prior to analysis. At the beginning of the experiment, the ITC was pre-equilibrated and after an additional delay of 180 s, an initial injection of 0.2 µl titrant was performed. This first step is usually of poor quality and not considered for evaluation. Thereafter, a series of 15 2.5 µl injections with waiting times of 180 s was performed and the compensating heat was recorded in µcal/s over time. The titration syringe performed stirring at a speed of 1000 rounds per minute, the reference power was 6 µcal/s. The heat associated with each titration step is found by integration of the transient heats. The integrated (differential) heats are plotted against $[Mg^{2+}]$. The thermodynamic evaluation of the titrations is described in section 6.3.

Chapter 4

Results I — Time-resolved fluorometer

The technical approach chosen to realize the time-resolved fluorometer is based on time-correlated single-photon counting (TCSPC). TCSPC combines detectors capable of single-photon detection with high precision timing units to correlate the time delay between the pulsed optical excitation event (start signal) of a fluorophore to the moment of the detection of the emitted photon (stop). It is a mature technique with its origins coming from nuclear physics[149] and most of the relevant principles are extensively discussed in text books[63,150,151]. More specific information given in this chapter is in general derived from technical data sheets available from the supplier of the used devices. Particularly helpful are also dedicated technical notes from suppliers such as PicoQuant GmbH[ix] or Becker & Hickl GmbH[x].[152] Despite the high degree of maturation, TCSPC is still under permanent development.[xi]

As mentioned above, in TCSPC, the time delay between excitation and emission of a fluorescence photon is measured. As stated in section 2.1.1, spontaneous emission of fluorescence is a process with a certain probability for photon emission in a given time interval. Therefore, a lifetime cannot be derived from a single photon-counting event. Instead, a large number of counting events is needed. This is realized by an even larger number of excitation-emission cycles being performed one after each other yielding a series of start-stop delay times. Ordering

[ix] url: www.picoquant.com/scientific/technical-and-application-notes, checked 03/2016

[x] url: www.becker-hickl.de, checked 03/2016

[xi] The current world record for the minimum width of an IRF is 17.8 ps. url: http://www.becker-hickl.de/pdf/scontel-appnote-04.pdf, checked 03/2016

all events by the abundance of the occurring delay times results in a histogram from which the lifetime can be extracted.

Single-photon detectors typically suffer of a dead time after a detection event that is considerably longer than the lifetime of an average fluorophore. Accordingly, excitation conditions have to be adjusted in such a way that—per excitation cycle—at most one fluorescence photon reaches the detector. Otherwise, a hypothetically emitted second photon could not be detected, anymore. For excessive emission rates, photons emitted early after excitation would be overrepresented, leading to a distortion of the decay traces known as pile-up. In practice, the detection count rate must not exceed one per cent of the excitation rate.

After having given a brief description of the basic working principle of TCSPC, above, the rest of this chapter presents the setup of a partially home-built time-resolved fluorometer. In section 4.1, the components of the setup and their interaction are described. In section 4.2, the time resolution of the fluorometer is determined and section 4.3 demonstrates the timing accuracy of the setup.

4.1 The setup of the time-resolved fluorometer

The setup is composed of four key units: an excitation source, a sample compartment, a single-photon detector, and the data-processing unit. The sample compartment and the optics used for directing the excitation pulses from the source to the sample are home-built or self-assembled. Excitation sources, the detector and the data-processing unit are purchased (PicoQuant GmbH, Berlin, Germany) and were connected and tested in-house. The final assembly is sketched in figure 4.1.

Pulsed excitation can be derived from two independent sources: a PDL 800-B diode driver with a set of pulsed UV-LEDs (PLS 310, PLS 320, PLS 340-10, and PLS360, FWHM (500 – 800) ps, pulse energy $\leq$ 0.12 pJ) from PicoQuant or a Tsunami 3941-X3BB Ti:Sa oscillator ((700 – 1180) nm, Newport Spectra Physics, Darmstadt, Germany). The diode driver along with the diodes is ready-to-use as it is and provides five repetition frequencies between 2.5 and 40 MHz. In combination with the the pulsed LEDs, its maximum repetition rate is limited to 10 MHz.

The Tsunami is pumped by a Millenia eV 10S laser (532 nm, 10 W, Newport Spectra Physics) and requires an additional pulse picker based on an acousto-

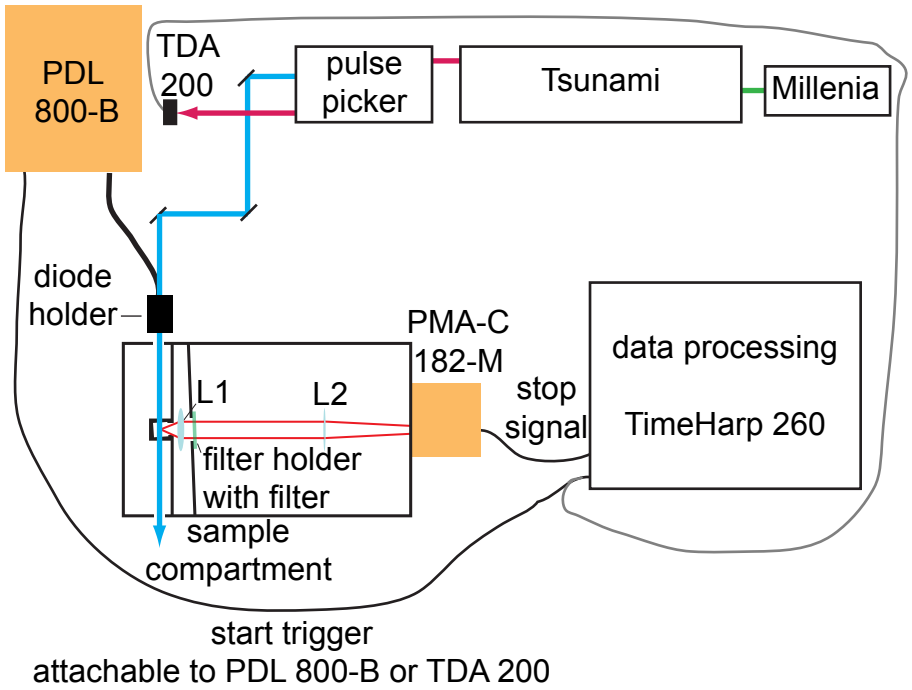

Figure 4.1: Scheme of the time-resolved fluorometer. The upper part contains the two alternative excitation possibilities. On the left is the diode driver PDL 800-B with a diode in the dedicated holder connected via a cable. The second black cable is the trigger signal for the counting card TimeHarp 260. On the right is the Tsunami including the Millenia and the pulse picker. Green is the emission of the pump laser, red is the oscillator fundamental, and blue is the SHG. The photo diode TDA 200 provides the trigger signal via the gray cable, when the Tsunami is used. The detector (PMA-C 182-M) delivers the stop signal in either case. The two trigger sources are mutually exclusive. The sample compartment contains—from left to right—a water-cooled sample holder, a first wall, the collimating lens L1 (f = 40 mm), a second wall with a filter holder (light green), the softly focusing lens L2 (f = 175 mm). The thin red lines starting at the sample indicate extreme paths of the detected fluorescence light.

optical modulator (AOM; 3980-6S, Newport Spectra Physics) to adjust the repetition rate to the sample requirements. The pulse picker is also used to generate the second harmonic of the Tsunami output from 350 to 550 nm. The pulse picker reduces the 80 MHz rate of the Tsunami to 8 MHz or less (down to single shot operation) and can be run in a continuous-wave (cw) mode, too. Operation of the setup with the Tsunami requires a BG40 filter to be placed into the excitation beam to suppress stray light from the oscillator fundamental. For operation beyond 900 nm, the Tsunami needs to be purged with nitrogen gas; the pivotal gas flow control is provided by the controller model 3910 (Newport Spectra Physics).

Both, the diode driver and the AOM can be externally triggered, too.

The two excitation sources complement each other in the sense that the Tsunami provides a widely tunable excitation source with good time resolution

(FWHM typically < 200 fs), whereas the pulsed LEDs extend the available spectral excitation range to the near UV, which is required for example for 2-aminopurines (λ_{max}^{abs} = 310 nm in RNA/DNA) and other biologically relevant samples. Additionally, the spectral range can be easily extended by further LEDs, if necessary.

The sample compartment in figure 4.1 is self-designed in the course of this work and the workshop of the IPTC (Feinmechanikwerkstatt) built it. It contains a sample holder, which is temperature stabilized by a water bath, a separating wall to minimize stray light and to keep heat away from the detector, if the sample holder is used for thermal denaturation experiments, a collimation segment with lens L1, a second wall with a fixed holder for color filters, and a detection segment with room for additional filters (such as polarizers, for example). Lens L2 is used to project the complete fluorescence light onto the detector. Excitation and detection occur under an angle of 90°. Both, the sample holder and the second separating wall are tilted by a few degrees away from perfect 90°-geometry to avoid reflections between the cuvette or the filter surface and the surface of the detector, which would cause artifacts. Spectral separation of excitation and emission is currently achieved via color filters. The incorporation of a spectrograph between the sample compartment and the detector is however possible.

The entrance and the detection side of the compartment are equipped with apertures. The exit of the excitation side is equipped with a closeable pinhole to facilitate adjustment. The LEDs can be placed directly in front of the sample compartment with a dedicated holder that does not have to be removed for operation with the Tsunami. The bottom of the compartment is equipped with regular threaded holes (M6) to facilitate the addition of new optical components.

The detector is a PMA-C 182-M cooled photomultiplier tube (PMT; PicoQuant, (185 – 820) nm, transit-time spread (TTS) typically < 200 ps). The Peltier based cooling option is important for samples with low quantum efficiency and extinction, because it allows to reduce the thermal dark counts from 200 to 300 counts per second (cps) to some ten cps. It should however be used with caution because it degrades the PMT faster. The PMT is built in a special housing by the supplier that is equipped with a fast protection shutter. Additionally, it is contained in a copper box built in the workshop to minimize high-frequency cross talk between the detector and the diode driver. The diode driver is also contained in a copper box.

Data processing is performed by the dedicated TimeHarp 260 PICO Single PCIe card (PicoQuant) and the corresponding TimeHarp software. The card

is special in the sense that it can handle peak count rates around 10 MHz in a forward start-stop mode. The counting card requires no additional constant fraction discriminator, as it is already part of the card. The minimal electronic bin width is 25 ps, but it can be longer.

Signal transduction, both from the excitation trigger and the PMT is performed by shielded SMA cables. When operated with the diode driver, the trigger is derived directly from the driver. In this case the trigger signal needs to be attenuated by a 10dB attentuator inserted directly between the counting card and the cable. The trigger level is set to −150 V. Operation with the Tsunami requires the use of a fast photodiode TDA 200 (PicoQuant, FWHM 500 ps, fall time 250 ps, (350 – 1100) nm), which is triggered by the rest of the Tsunami fundamental left after SHG and which is directed out of the pulse picker through the dedicated output port. In this case, the attenuator has to be removed and the trigger level of the card has to be set to −50 V. The trigger level for the PMT is always −150 V and no attenuator is needed.

The FluoFit package version 4.6.0 Professional from PicoQuant was used for data analysis by iterative reconvolution of exponential decay models with the experimental IRF.

4.2 Time resolution

The time resolution of a TCSPC device is essentially determined by the width of its IRF and the sampling rate. The total time spread depends on the individual contributions to the time spread s_i from the various components constituting the device. From Gaussian error propagation, the resulting time spread can be estimated to be

$$S = \sqrt{\sum_i (s_i)^2} \,. \tag{4.1}$$

As all individual time-spread components are squared prior to summation, the resulting time spread will be dominated by the largest individual contribution.

The most critical components for the time resolution of a TCSPC device are the detector, the excitation source, and the electronic components necessary for data acquisition. In difference to analogue measurement techniques, the width of the

rise and fall times of the electronic parts is not decisive for the width of the IRF. The relevant parameter is rather the timing stability. That says the time resolution is in general limited by the jitter of the response to a periodically incoming signal. The jitter is quantified as the root-mean-square deviation (rmsd) of the response from perfect periodicity.

The IRF of the PMT is specified with being typically smaller than 200 ps and IRFs down to 180 ps were obtained under testing conditions at the supplier. The width is essentially limited by the electrostatic TTS of the photoelectron burst caused by a photon-detection event within the detector.

The excitation sources are very different in their widths. The LEDs are specified with IRFs between 500 and 800 ps, whereas the Tsunami could in principle deliver pulse widths below 1 ps. However, the pure width of the light pulse alone is not the only relevant contribution to the broadening. Equally important is the jitter of the electronic trigger with respect to the laser emission. The jitter of the PDL 800-B diode driver is < 3 ps and thus negligible. In case of the Tsunami, the time spread might rather be dominated by the trigger diode, although the jitter related to it is below the measurement limit of the supplier ($\ll 3$ ps).[xii]

As opposed to many older TCSPC systems, all relevant electronic components are contained on the TimeHarp 260 PCIe counting card. The intrinsic jitter of the card is 16 ps. The minimum electronic bin width, which is 25 ps, has to be considered separately because according to the Nyquist-theorem, only signals can be retrieved adequately, that are slower than two times the smallest sampling time step. Here, that says that the counting card sets a lower limit of the time resolution of ~ 50 ps independent of the total width of the IRF.

Figure 4.2 A displays IRFs for six different excitation wavelengths. Figure 4.2 B contains the values of the FWHM for the six IRFs. It is obvious that the IRFs of the pulsed LEDs are considerably broader than the ones obtained with the Tsunami as excitation source. The latter are around (200 – 230) ps with uncertainties of 40 ps. The uncertainties are essentially determined by the electronic bin width and therefore identical for all IRFs. This implies that for the Tsunami, the IRF is dominated by the TTS of the PMT. Hence, this component would have to be replaced, if an improvement of the IRF should be achieved. For the pulsed LEDs, the widths of the IRFs are the widths of the light pulses, themselves. In this case, a better detector would not result in an improved time resolution.

[xii] PicoQuant uses TCSPC to measure this quantity (personal communications with Dr. Andreas Bülter, PicoQuant GmbH).

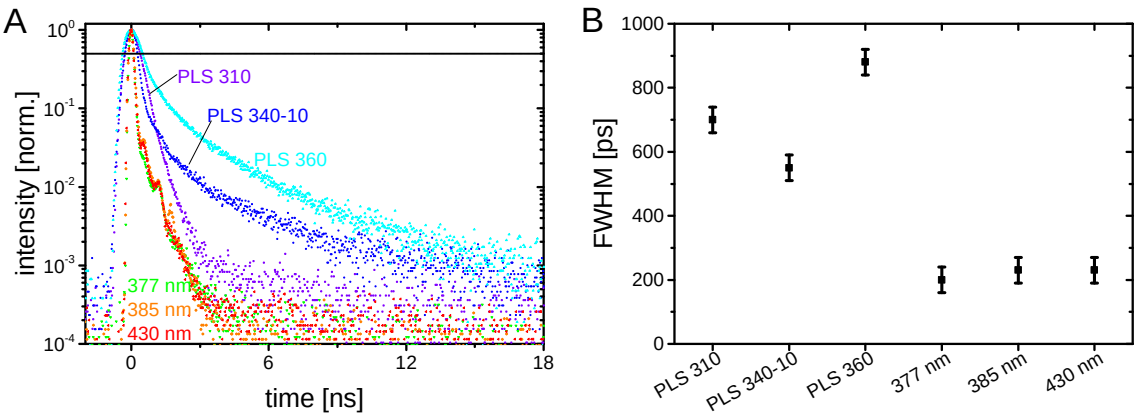

Figure 4.2: IRFs of the time-resolved fluorometer. A: IRFs for different excitation sources. The three different wavelengths indicated at the bottom of the figure are derived from the Tsunami. The straight black line indicates 50 % of the maximum intensity. B: FWHM values of the IRFs shown in part A.

As a rule of thumb, lifetimes as short as the width of the IRF divided by ten (here between 20 and 80 ps) can be recovered under favorable conditions. Because the lower limit of the time resolution imposed by the electronic sampling rate is approximately 50 ps, both the detector and the counting card would have to be replaced to achieve a better time resolution. In general, the fastest time components retrievable with the setup are about 50 ps or slightly longer ($\leq$ 80 ps) for some of the pulsed LEDs.

4.3 Timing accuracy

The electronic clock of the counting card might be systematically detuned, which means that the 25 ps given as nominal bin width do not correspond to 25 ps in reality. In order to check for the timing accuracy of the counting device, the Tsunami was employed. The pulse picker can be run in both, a quasi-cw mode and in a frequency-reducing mode as described above. The experiment was bipartite: firstly, the Tsunami-fundamental output was measured directly in the pulse-picker cw mode (80 MHz) with the TDA 200 photodiode and a LeCroy waveRunner 62Xi oscilloscope (600 MHz, 10 GS/s, Teledyne LeCroy, Heidelberg, Germany). Secondly, the pulse picker was switched to 8 MHz repetiton frequency and the stray light of the fundamental was measured with the TCSPC electronics. Here, the fact was exploited that in absence of the fundamental filter BG40, some stray light of the fundamental is always detectable even when the AOM is not

active. Please note, that these side pulses are not visible when the SHG of the Tsunami is detected.

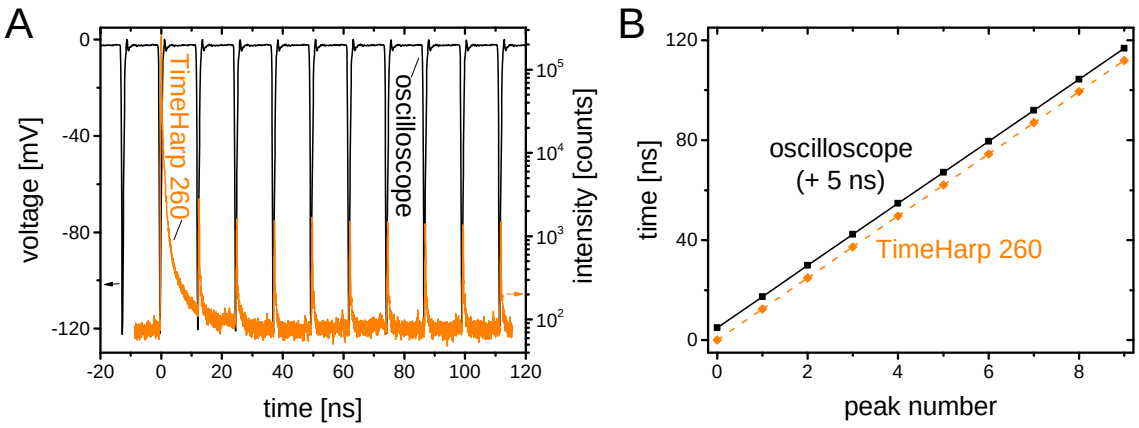

Figure 4.3: Timing accuracy of the time-resolved fluorometer. A: Time traces of the regular Tsunami operation with a repetition rate of about 80 MHz monitored with a fast digital oscilloscope (black, left axis) and the Tsunami/pulse-picker fundamental output at 790 nm with a repetition rate of 8 MHz as recorded by the TimeHarp 260. B: Time points of the peaks detected with the oscilloscope (black symbols) and the TimeHarp 260 (orange symbols) along with linear fits (solid and dashed, respectively). The oscilloscope data are shifted by +5 ns on the ordinate for the sake of clarity.

Figure 4.3 A gives the results of the two experiments. In black is the pulse train measured on the oscilloscope, in orange is the pulse train measured with the TCSPC setup. There, the main peak, on which the setup was triggered at time zero is followed by nine minor peaks with approximately 0.2 % amplitude of the main pulse.

For the evaluation of the time traces, the time points of the different intensity extrema were extracted and are plotted against the number of the maximum as is shown in figure 4.3 B. The resulting data sets are fitted linearly and the slopes represent the time spacing between two laser pulses. With the oscilloscope, a slope of (12.419 ± 0.004) ns and with the TimeHarp 260 of (12.4199 ± 0.0015) ns was found. The uncertainties represent the statistical deviation of the fit from the data with Pearson-R values that are 1.0000.

The results are identical within the experimental error and correspond to a laser repetition rate of 80.52 MHz. The uncertainty of the TimeHarp 260 is smaller than the one of the oscilloscope and this is reasonable, given that the sampling of the TimeHarp 260 is considerably better than the one of the oscilloscope (25 ps versus 100 ps).

To conclude this chapter, a precise and reliable time-resolved fluorometer based on the TCSPC technique was designed and implemented. Testing resulted

in a time resolution between 50 and 80 ps and a timing accuracy that is reliable within < 0.02 %. A set of application examples is given in chapter 5.

Chapter 5

Results II — Characterization of pyrene-based fluorescent RNA labels

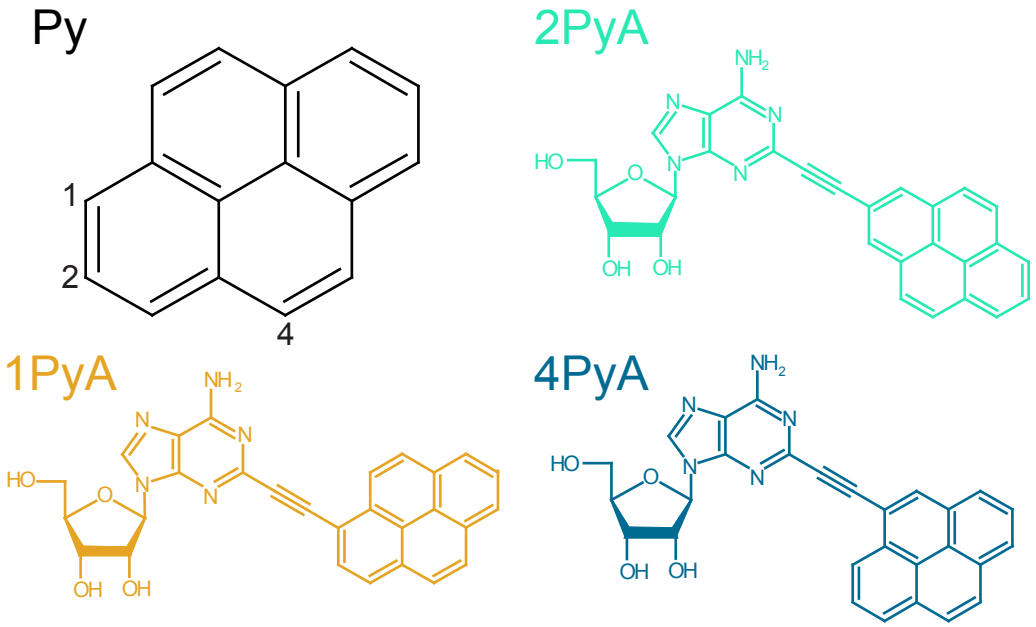

Figure 5.1: Chemical structures of Py (black), 1PyA (orange), 2PyA (light green), and 4PyA (blue). The positions 1, 2, and 4 of Py are labeled.

In this chapter, the findings on the photophysical properties of the chemical compounds 2-(1-pyrenyletynyl) adenosine (1PyA), 2-(2-pyrenyletynyl) adenosine (2PyA), and 2-(4-pyrenyletynyl) adenosine (4PyA) will be presented. They are fluorescent A-analogs with Py being attached to the 2-position of A and bridged with an ethynyl group. The three compounds are structural isomers to each other

with the only difference being the linkage position of the ethynyl bridge to the Py. The structures are shown in figure 5.1.

The apparently small differences have a severe impact on the electronic properties of the labels. It is known that π-electron accepting groups, such as dimesitylboron have little impact on the absorption properties of Py linked to the 2-position, whereas the absorption is bathochromically shifted by 90 nm, when it is attached to the 1-position.[153]

The parent fluorophore Py and its spectral features will be briefly described in section 5.1. Then, the findings of steady-state (section 5.2) and TA spectroscopy (section 5.3) will be presented along with TCSPC experiments (section 5.4). The experimental findings will be complemented by quantum-chemical calculations (section 5.5) and in section 5.6, the results will be used to develop a model describing the distinct photophysics of the labels.

Parts of this chapter have been published in the references [136] and [154].

5.1 Pyrene

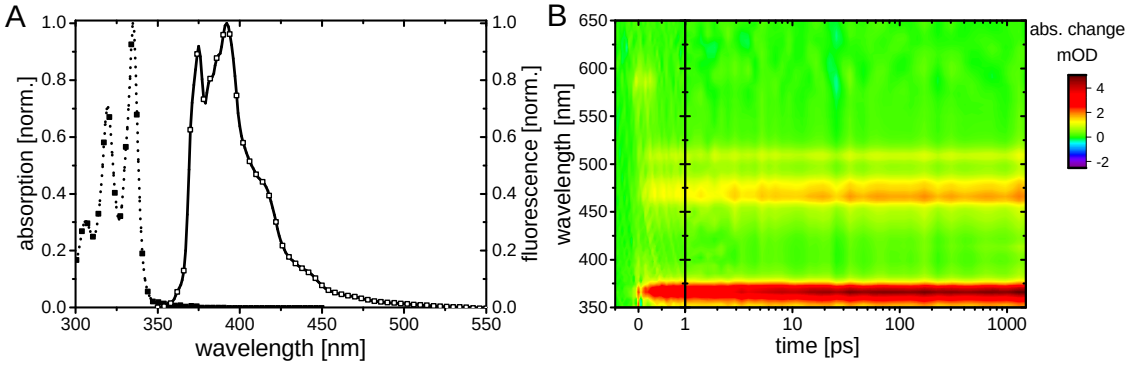

Figure 5.2: Spectra of Py in MeOH. A: Normalized steady-state absorption (dashed line, full symbols) and emission (solid line, open symbols) spectrum of 15 µM Py in MeOH. B: Transient card of 70 µM Py in MeOH excited at 340 nm, (30 nJ).

The reason for the mentioned dependence on the substitution position of Py lies essentially in the properties of Py itself. It is a planar molecule consisting of four fused benzene rings and it is a polycyclic aromatic hydrocarbon with the sum formula $C_{16}H_{10}$.[63]

The $S_0 \rightarrow S_1$ transition dipole moment lies in the plane of the rings and is oriented along the short axis of the molecule.[155] For symmetry reasons, it is

dipole forbidden. In unsubstituted Py, optical excitation is therefore usually performed into the second ES S_2 or into higher ESs because these transitions have a significantly higher extinction than the one to S_1 ($S_0 \rightarrow S_2$: 54000 l/mol/cm at 336 nm; $S_0 \rightarrow S_1$: 160 l/mol/cm at 373 nm).[156] After excitation into the S_2 state, Py in solution undergoes fast IC into the S_1 state. IC is finished after less than 1 ps.[157,158] Steady-state absorption and emission spectra of Py in MeOH are shown in figure 5.2 A.

Figure 5.2 B shows a transient card of Py in MeOH. After the fast initial dynamics several long-lived ESA bands are visible at 366, 466, 510, 590, and 650 nm, which can be assigned to transitions from S_1 to S_{22}, S_{12}, S_{11}, S_{10}, and S_9, respectively.[157] The band at 466 nm has two shoulders at 478 and 446 nm, which are assumed to be vibrational substates of the $S_1 \rightarrow S_{12}$ transition. The transition at 446 nm could also originate from the $S_1 \rightarrow S_{14}$ and $S_1 \rightarrow S_{15}$ transitions.

Due to the small $S_0 \rightarrow S_1$ transition probability, Py has an extraordinarily long fluorescence lifetime τ_f in oxygen-free solvents[35] and at the same time a relatively high quantum yield ϕ_f that depends strongly on the solvent (0.75 ± 0.14 in thoroughly degassed MeOH[35]). Py shows a pronounced vibrational fine structure in both, absorption and emission. The relative intensities of the vibrational bands of absorption and emission are closely related to the solvent polarity ε_r. Comparing the relative emission intensities of the bands I (transition between vibronic states (0-0) at 375 nm) and III ((0-2) transition, 384 nm) is successfully used as a main standard for determining the solvent polarity ε_r.[36,159,160]

The combination of its special photophysical properties makes Py the first fluorophore, in which excimer formation and emission was found.[37,38] This mechanism must neither be confused with fluorescence quenching caused by aggregation of chromophores in their GS, which would affect the absorption spectrum, nor with aggregation of an excited with an unexcited molecule simply leading to a loss of brightness due to quenching.[63] Instead, additionally to the Py-monomer emission between 370 nm and 430 nm (see figure 5.2), a bathochromically shifted and unstructured emission band occurs at ~490 nm for Py concentrations $\gtrsim 1$ mM in thoroughly degassed solutions.

In the following sections, the photophysical behavior of the three PyAs will be presented. There are remarkable differences between the three isomers and also between them and their parent Py.

5.2 Steady-state spectra

5.2.1 Pyrenylethynyl adenosines in MeOH

The absorption spectrum of 2PyA (figure 5.3) resembles that of Py in so far, as it has a pronounced absorption maximum at 336 nm, where the $S_0 \rightarrow S_2$ transition of Py occurs. Additionally, it has smaller absorption at longer wavelengths until 410 nm. This low-energy absorption shoulder has a significantly larger extinction coefficient (~ 1900 and 1400 l/mol/cm at 373 and 385 nm, respectively) than the $S_0 \rightarrow S_1$ transition in Py.

4PyA features a very broad and uniform absorption between 300 and 380 nm. Beyond 405 nm, no significant extinction can be observed, anymore. The lowest-energy absorption of 4PyA coincides with the $S_0 \rightarrow S_1$ transition in Py.

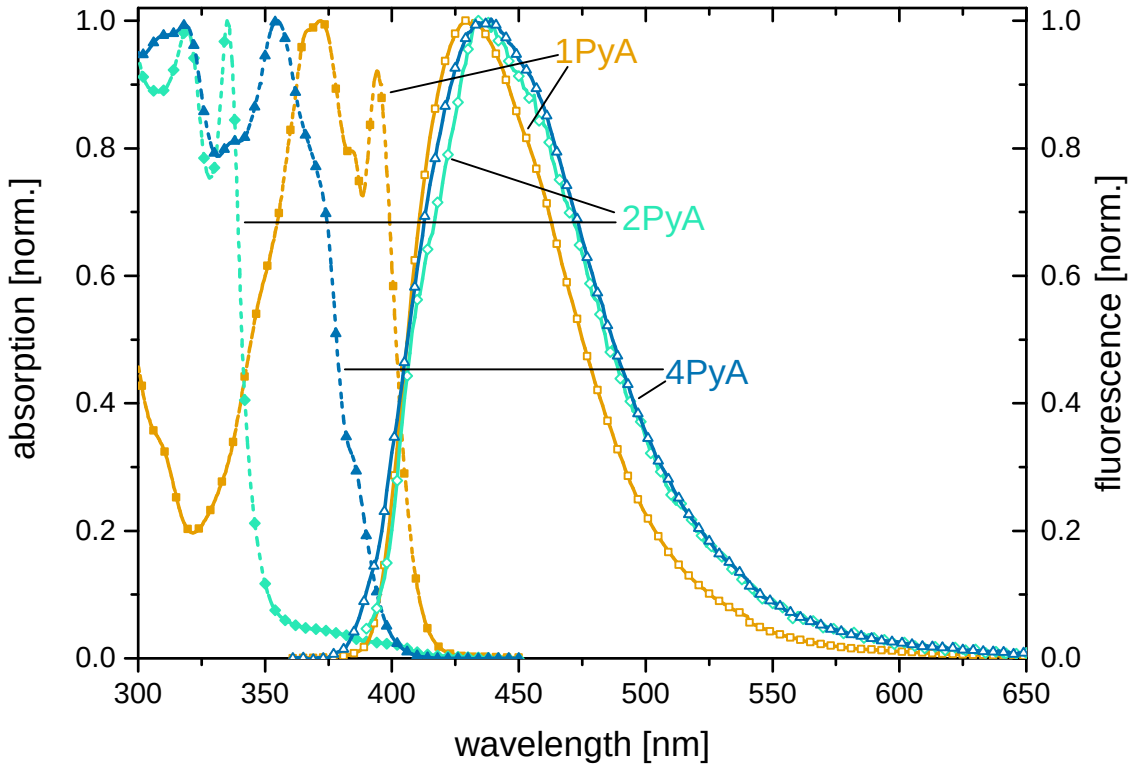

Figure 5.3: Steady-state spectra of the PyAs in MeOH. Normalized steady-state absorption (dashed line, full symbols) and emission (solid line, open symbols) spectra of (10 – 15) µM 1PyA (orange squares), 2PyA (green diamonds), and 4PyA (blue triangles) in MeOH. 1PyA was excited at 385 nm, 2PyA and 4PyA at 335 nm. The importance of the excitation wavelength for 2PyA will become apparent in section 5.2.2.

The absorption spectrum of 1PyA is significantly shifted to longer wavelengths in comparison to Py and both of its isomers with the lowest-energy maximum

showing up at 394 nm and significant absorption occurring until 420 nm. The shifted absorption indicates a considerable amount of electronic interaction between Py, the ethynyl bridge, and the A already in the GS.[xiii] Therefore, it is less straightforward to assign the absorption in 1PyA to transitions known from Py than it appears to be for 2PyA and 4PyA.

The emission spectra of the isomers are energetically close to each other with an onset around 400 nm. This is a considerable bathochromic shift compared to unsubstituted Py (~ 376 nm). The emission of 1PyA has the largest high-energy contribution and the one of 2PyA the smallest. Table 5.1 summarizes the most important spectral characteristics of the three isomers. 2PyA is special in some respects: because the excitation at 385 nm does not allow to measure the whole fluorescence spectrum, $< \nu_e >$ and σ^e cannot be calculated to the same degree of accuracy as for 1PyA and 4PyA.

	absorption		emission			
sample	ν^a_{max}* $10^3\,cm^{-1}$	ϵ at ν^a_{max} 10^3 l/mol/cm	ν^e_{max}* $10^3\,cm^{-1}$	$\langle\nu_e\rangle$ $10^3\,cm^{-1}$	σ^e $10^3\,cm^{-1}$	ϕ_f
1PyA	26.88	40 ± 4	22.99	22.02	1.76	0.79†
2PyA	29.85	44 ± 3	22.73‡	21.6‡	1.9‡	0.58 ± 0.08‡
4PyA	28.17	23.6 ± 1.2	22.62	21.63	1.96	0.62 ± 0.04

Table 5.1: Spectral properties of the PyAs in MeOH. The wavenumber of the absorption maximum in the accessible spectral range ν^a_{max}, the extinction coefficient ϵ at ν^a_{max}, the wavenumber of the emission maximum with the highest energy ν^e_{max}, the mean emission wavenumber $\langle\nu_e\rangle$, the width of the fluorescence spectrum calculated as $\sigma^e = \sqrt{\langle\nu^2\rangle - \langle\nu\rangle^2}$, and the fluorescence quantum yield ϕ_f in air-saturated solution at room temperature. Columns marked with * have an error of $0.10 \times 10^3\,cm^{-1}$. †: determined by Peter Trojanowski.[136] ‡: excited at 385 nm.

5.2.2 Spectral dependence of the emission of 2PyA and 4PyA

The emission of 2PyA depends the excitation wavelength. The excitation spectrum measured at an emission wavelength of 411 nm resembles the absorption spectrum, whereas monitoring the emission at 500 nm deviates significantly between 340 and 400 nm (see figure 5.4 A). The absorption spectrum cannot be compared directly to the excitation spectra because in the former case one considers relative photon numbers on a logarithmic scale and in the latter case, one

[xiii] In the context of this chapter, A usually refers to the adenine moiety because it is the aromatic subunit of the PyAs responsible for the electronic interaction. The role of the 2'-OH group of the ribose is not negligible, though.

considers total photon numbers. Still, the emission profile at 411 nm is clearly closer to the absorption spectrum in terms of the relative absorption and emission in the spectral regime of wavelengths < 340 nm compared to > 340 nm. Obviously, the low-energy part of 2PyAs emission spectrum is excited more efficiently in the weak absorption shoulder around 360 nm than upon excitation in the stronger absorption bands with wavelengths shorter than 340 nm.

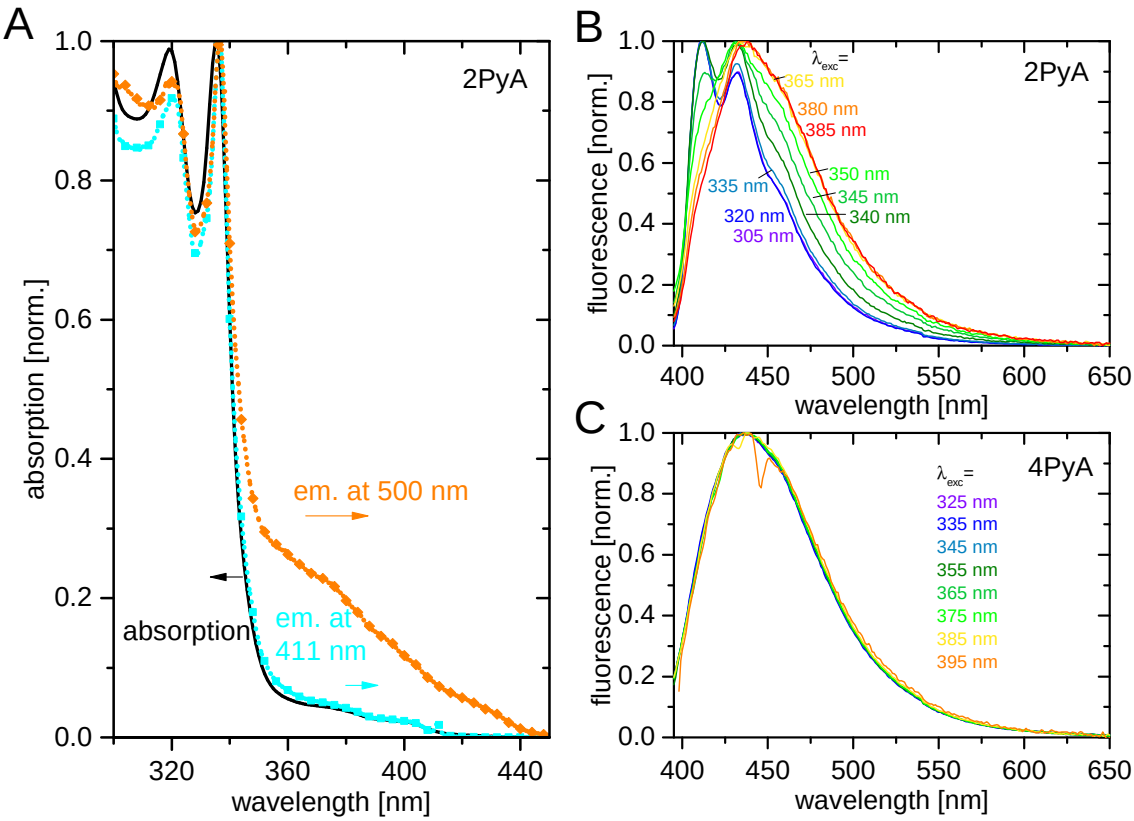

Figure 5.4: Fluorescence spectra of 2PyA and 4PyA in MeOH for various excitation and emission wavelengths. A: Excitation spectra of 2PyA in MeOH detected at 411 and 500 nm presented in cyan and orange, respectively. The black line represents 2PyAs absorption for comparison. B: Emission spectra of 2PyA in MeOH recorded for various excitation wavelengths between 305 and 385 nm. Excitation at 305 and 320 nm are almost indistinguishable. C: Emission spectra of 4PyA in MeOH with excitation wavelengths between 325 and 395 nm.

The difference in the excitation efficiency is also reflected in the emission spectra recorded for different excitation wavelengths (figure 5.4 B). Between 305 and 320 nm, the emission does not change, at all. From excitation wavelengths of around 335 nm on, the emission profile begins to shift to longer wavelengths. The shift is accompanied by a stepwise loss of the vibrational structure: relative intensity is transferred from the maximum at 411 nm to the maximum at 432 nm until the emission band at 411 nm disappears completely for excitation at 365 nm.

Additionally, from about 350 nm on, the maximum at 432 nm begins to shift to 437 nm. It is not completely clear, whether the maximum at 432 nm disappears as does the one at 411 nm and is replaced by an essentially unrelated maximum of the unstructured low-energy emission, or remains and merely shifts by some nanometers. From an excitation wavelength of 380 nm on, the spectra do not change, anymore.

From the absorption spectrum, the fluorescence spectra and ϕ_f for excitation at 336 nm, which is 0.19 ± 0.01, ϕ_f for excitation at 310 nm and 385 nm is estimated to be 0.18 ± 0.02 and 0.52 ± 0.08, respectively. Especially for excitation at 385 nm, a measurement of ϕ_f by the indirect method would have been very error-prone because of the low extinction. To circumvent this, very high concentrations of 2PyA would have had to be used with the risk of aggregation.

Despite the large uncertainty, ϕ_f for excitation at 385 nm is clearly larger than the one at 336 nm, which deviates also strongly from the ones of 1PyA and 4PyA. The difference between 310 and 336 nm is not significant despite the differences in the spectral shapes. Besides ϕ_f, also other spectral properties deviate significantly: the highest-energy emission maximum is shifted hypsochromically by 1540 cm^{-1} and ν^{e}_{max} by 8780 cm^{-1}. At the same time, the emission spectra are 180 cm^{-1} narrower, when the excitation is performed at 310 nm.

In contrast to this, 4PyA does not exhibit any shifts as figure 5.4 C demonstrates. The deformations of the spectra with excitation at 385 and 395 nm, which are visible at 433 and 446 nm, respectively, originate from Raman-scattered excitation light and are subtraction artifacts that were introduced as part of the spectral correction procedures. The minimal shift of the two mentioned spectra is also likely to be artificial. This is assumed, because the normalization may underestimate the true amplitude of the emission spectrum as consequence of the subtraction of both, the scattered excitation light and the Raman contribution in close vicinity of the fluorescence maximum. No significant dependence of 4PyAs excitation spectra on the detection wavelength could be observed, as well.

5.2.3 Pyrenylethynyl adenosines in THF and MeCN

From the literature about pyrenyl and pyrenylethynyl derivatives, it is known that both, locally-excited (LE) and charge-transfer (CT) states can be involved in their photopysics.[161–164] The likelihood to form CT states is relatively high for

Py-labeled nucleotides, where even the formation of contact radical-ion pairs has been observed with pyrimidines (with Py as electron donor) and G (Py as electron acceptor).[165–169] The CT behavior is less pronounced when Py is linked to A and typically no definite direction of the CT can be determined, which is why the formation of radical ion pairs is considered unlikely.[170–172]

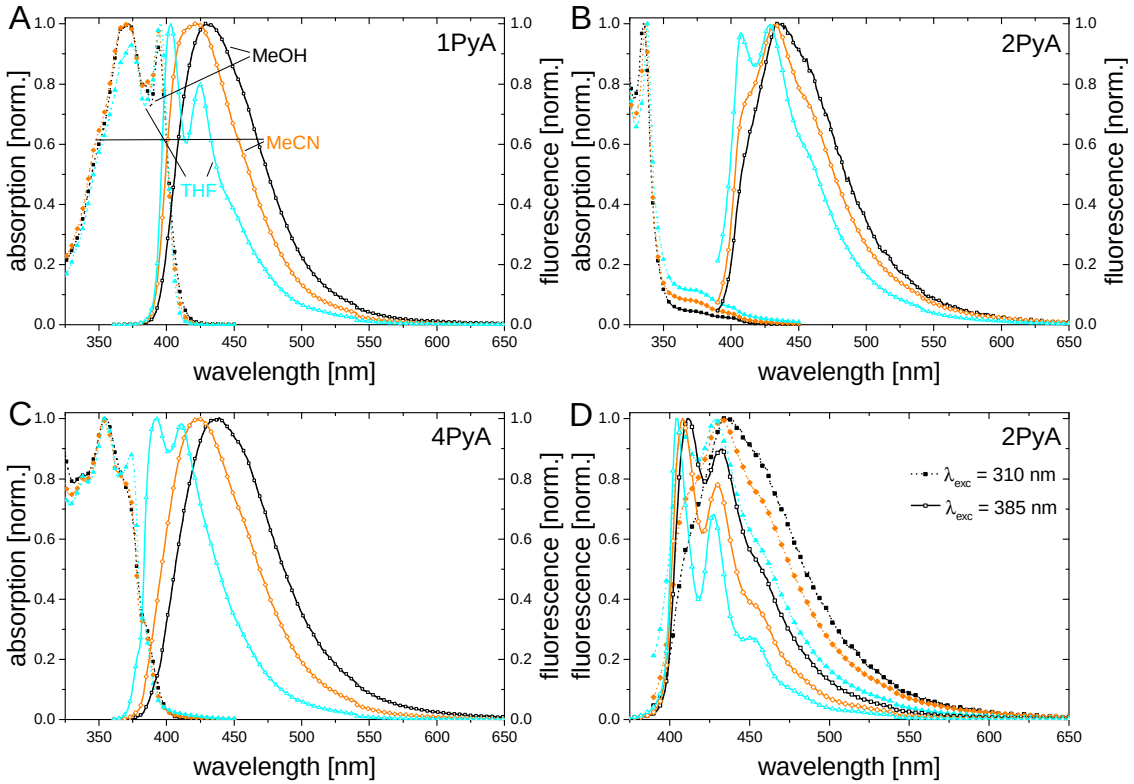

Figure 5.5: Solvent dependent steady-state spectra of the PyA isomers. Normalized steady-state absorption (dashed line, full symbols) and emission (solid line, open symbols) spectra of 1PyA (part A, excited at 335 nm), 2PyA (part B, 385 nm), and 4PyA (part C, 335 nm) in MeOH (black), MeCN (orange), and THF (cyan). D: Emission spectra of 2PyA excited at 385 (dashed line, solid symbols) and at 310 nm (solid line, open symbols). Color coding of solvents is as in the parts A through C.

A CT state is related to a change in the dipole moments, which grows with the amount of charge being transferred. Therefore, a CT state is expected to react sensitively to solvent polarity in the sense that it is stabilized with increasing polarity.[163,164,173] Additionally, this process can be accompanied by solvent-assisted protonation. Stabilization includes here usually bathochromic shifts of at least the emission spectrum and favored population due to lowered S_1 energy. An LE state, which is expected to closely resemble the fluorescent state of unsubstituted Py, on the other hand should be relatively insensitive to the solvent polarity in terms of its overall spectral position.

In order to check for the possible involvement of CT states and intermolecular H-bonding or proton-transfer processes, the three isomers were investigated in THF and MeCN. THF is aprotic and has a low dielectric constant ε_r of 7.6 and MeCN is also aprotic with $\varepsilon_r = 37.5$.[35] Thus, the results in THF and MeCN allow to estimate the influence of the solvent polarity. Comparing the spectra in MeCN with those in MeOH ($\varepsilon_r = 32.6$) is complementing the information derived from THF and MeCN, because it elucidates the potential impact of H-bonds with solvent molecules. The steady-state spectra of the isomers are shown in figure 5.5 and characteristic quantities describing their response to the different solvents are summarized in Table 5.2. For the excitation of 2PyA at 385 nm, $<\nu_e>$ and σ^e have larger uncertainties for the same reasons as stated in section 5.2.1.

sample	solvent	ν^a_{max}* $10^3\,cm^{-1}$	ν^e_{max}* $10^3\,cm^{-1}$	$\langle\nu_e\rangle$ $10^3\,cm^{-1}$	σ^e $10^3\,cm^{-1}$
1PyA	THF	25.32	24.81	22.98	1.71
	MeOH	26.88	22.99	22.02	1.76
	MeCN	26.95	23.47	22.57	1.69
2PyA	THF	29.59	24.51	$22.4^{\dagger}$	$1.9^{\dagger}$
	MeOH	29.85	22.73	$21.6^{\dagger}$	$1.9^{\dagger}$
	MeCN	29.76	22.99	$21.8^{\dagger}$	$2.0^{\dagger}$
4PyA	THF	28.25	25.38	23.60	1.78
	MeOH	28.17	22.62	21.63	1.96
	MeCN	28.33	23.36	22.42	1.87

Table 5.2: Spectral steady-state properties of the PyA isomers in THF, MeCN, and MeOH. The absorption maximum in the measurable spectral range ν^a_{max}, the energetically highest emission maximum ν^e_{max} the mean emission wavenumber $\langle\nu_e\rangle$ >, and the width of the fluorescence spectrum calculated as $\sigma^e = \sqrt{\langle\nu^2\rangle - \langle\nu\rangle^2}$ are given. Columns marked with * have an error of $0.10 \times 10^3\,cm^{-1}$. †: excited at 385 nm, uncertainty > 5 %.

Figure 5.5 A shows the response of 1PyA to various solvents. The absorption spectra are very similar in both, structure and position of the maxima, only their intensity ratios differ significantly. Yet, the ratios cannot be directly attributed to the solvent polarity, because the smallest relative absorption at 394 nm is observed for MeOH and the largest one for THF. MeCN, which has the largest ε_r, lies in the middle. Interestingly, this behavior correlates well with the spectral shift of the emission maxima. In THF, absorption and emission overlap strongly, the emission is structured and looks almost like a perfect mirror image of the absorption, when plotted over the wavenumber. This makes it likely that the electronic densities and accordingly the nuclear configurations of the S_0 the S_1 are very similar to each other. In MeCN and MeOH, the structure is lost and the emission shifts

bathochromically with MeCN being again intermediate between THF and MeOH. The spectral overlap between absorption and emission decreases in MeCN and MeOH.

The absorption spectra of 2PyA (Figure 5.5 B) are in general very similar to each other and have sharp absorption maxima between 335 and 338 nm that show no clear tendency to shift with polarity. The relative amplitude of the low-energy absorption shoulder is also not correlated with ε_r. The emission spectrum in THF has a pronounced band at 407 nm that decreases stepwise from MeCN to MeOH, where it is hardly recognizable, anymore. The disappearance of this band is directly related to the relative amplitude of the low-energy absorption.

4PyA (Figure 5.5 C) is special in the sense that it has the lowest degree of emission structure in all solvents. The absorption spectra in MeCN and MeOH are almost identical, but the emission maximum shifts by 14 nm to longer wavelengths in the presence of H-bonds. In THF, both absorption and emission gain some structure. In the absorption spectrum, an additional band appears at 374 nm at the low-energy band edge, which resembles the increase in absorption observed for 1PyA in THF. The emission is hypsochromically shifted by 31 nm relative to the one in MeCN and shows well separated, but broad bands with maxima at 392 and 411 nm.

As can be seen in figure 5.5 D, the emission spectra of 2PyA keep their strong dependence on the emission wavelength in THF and MeCN. Upon excitation at 310 nm, the emission is significantly shifted to shorter wavelengths compared to excitation at 385 nm and it shows pronounced fine structure in all solvents. The apparent response to polarity is small with bathochromic shifts by 4 nm from THF to MeCN and another 3 nm from MeCN to MeOH. Qualitatively, the ordering of the spectral shifts does not change for the two excitation wavelengths and the spectra tend to lose structural resolution, from THF to MeCN and again to MeOH. Still, the spectral differences are clear and significant.

In THF, the lowest-energy absorption bands of all PyAs gain relative amplitude. The behavior of the absorption of the three isomers is also reflected in the fluorescence. However, the size of the spectral shifts and partial or total loss of the fine structure demonstrates that the S_1 is likely to be more sensitive to the solvent. Additionally, the emission of 2PyA depends strongly on the excitation wavelength: excitation into higher ESs causes the emission to shift hypsochromically and adds pronounced fine structure to the fluorescence spectra. The presence of

the structure is not affected by the solvent parameters, yet the sharpness of the bands and their relative intensities are.

The Stokes-shift is not calculated for practical reasons: it is defined as the energetic difference between the (0-0) transitions from the ground state to the lowest EES of a given spin-multiplicity in absorption and emission.[61] Because the spectral shapes change between the different solvents losing or gaining fine-structure and because it is for some spectra hardly possible to determine the (0-0) transitions due to the strong broadening of the electronic bands (particularly for 2PyA), the resulting uncertainties are too large to give meaningful results.

5.3 Transient absorption spectroscopy

5.3.1 1PyA in MeOH

Figure 5.6 shows the transient absorption spectrum of 1PyA in MeOH (part A) and the lifetime-density map (LDM, figure part B) that is used to analyze the dynamics. The data and the analysis is published in [136] and the experiment was performed by Peter Trojanowski. The analysis is based on lifetime-density analysis (LDA) implemented with OPTIMUS as described in [133] (see Appendix B for more details).

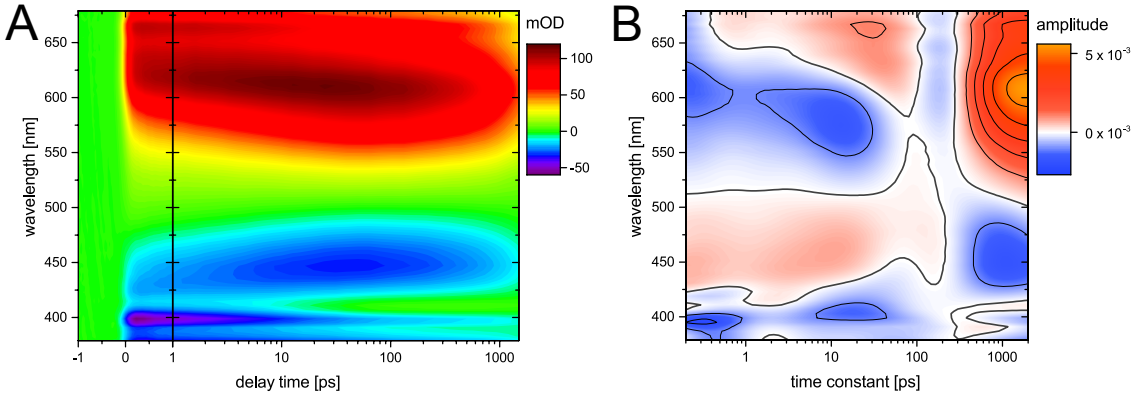

Figure 5.6: TAS data of 1PyA excited at 388 nm. A: Transient card of 150 µM 1PyA in MeOH. B: LDM of the data presented in (A). The black lines correspond to amplitude steps of 1×10^{-3}. The experiment was performed by Peter Trojanowski. The figure is adapted from reference[136], published by the PCCP-owner societies.

At wavelengths longer than 530 nm, the transient card is dominated by two ESA bands, whereas at shorter wavelengths a substantial contribution from GSB

and SE is visible. The LDA yields four characteristic time ranges. A time range is for the sake of simplicity treated as a decay component from GLA and called τ_i. The time ranges are τ_1 with (0.2 – 0.3) ps, τ_2 with (2 – 10) ps, τ_3 with (10 – 30) ps, and τ_4 as broad distribution around a mean value of 2 ns, which is attributed to the fluorescent decay. τ_4 is derived from TCSPC measurements with a better accuracy (see section 5.4.1). The time ranges 2 and 3 overlap strongly in the case of 1PyA in MeOH and it is difficult to separate them from each other. Their existence is nevertheless certain from a series of TAS measurements on 1PyA in different solvents.[136]

The analysis also establishes the existence of two distinct substates on the S_1-PES of 1PyA: one of the substates can be related to structured and and the other one to unstructured emission. The unstructured emission is found to be stabilized by intermolecular H-bonds that compete with the intramolecular H-bond from the 2'-OH of the ribose to N3 of A. Despite the existence of two states with distinct spectra only a single decay component could be measured with streak camera[136] and TCSPC experiments on a closely related compound[162] in all investigated solvents.

5.3.2 2PyA in MeOH

As known from the the steady-state data presented in section 5.2.2, 2PyAs emission depends strongly on the excitation wavelength. Therefore, the ultrafast photophysics of 2PyA is investigated at two different excitation wavelengths. Excitation into the low-energy shoulder and thus the S_1 state is performed at 388 nm. At 310 nm 2PyA is excited into a higher ES (S_2 or S_3). The two wavelengths are chosen because there, the steady-state fluorescence spectra do not change their shape, anymore. Accordingly, mixed excitation of the two distinct pathways is avoided.

Excitation of 2PyA at 388 nm

Excitation into the S_1 state was performed using the SHG of the pulsed laser system as excitation. The OD of 2PyA at 388 nm was 0.05 with a pulse energy of 26 nJ. The results are shown in figure 5.7 A. At wavelengths shorter than 400 nm, the amplitudes are around zero or negative. This spectral range is related to the GSB and SE. Between 400 and 550 nm, the signals are positive, with relatively small

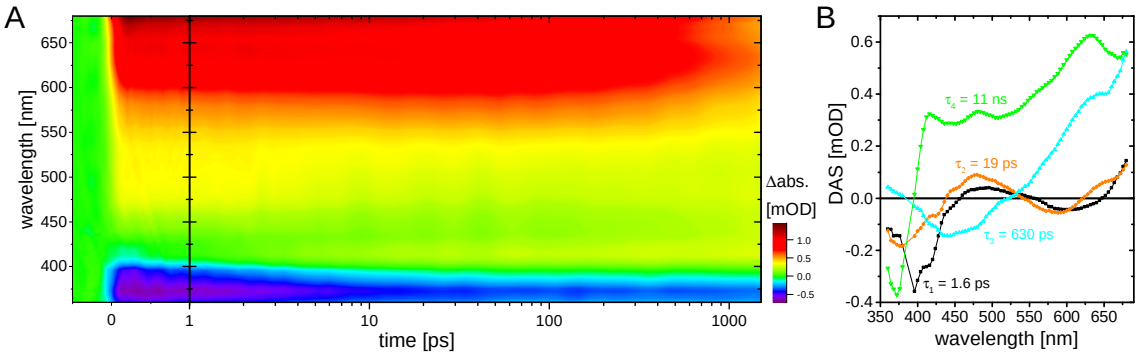

Figure 5.7: TAS data of 2PyA excited at 388 nm. A: Transient card of 300 µM 2PyA in MeOH. B: DAS of the data presented in (A). Fitted time constants are indicated at the corresponding spectra.

amplitudes and at wavelengths longer than 550 nm, the spectrum is dominated by a large and broad positive absorption band.

The time-resolved photophysics can be fitted with four time constants (figure 5.7 B). The fastest time constant τ_1 (1.6 ps) has a strong negative contribution at wavelengths shorter than 450 nm, which describes a signal increase. With τ_2 (19 ps), the GSB recovers to a level that remains constant until the end of the measured time window. The DAS of τ_1 and τ_2 are similar to each other for wavelengths longer than 425 nm. Around 480 to 500 nm, the initial ESA decreases slightly and at the same time, the ESA around 600 nm increases. This is related to the appearance of a weak positive band at 410 nm and looks like a hypsochromic shift of the negative signal below 400 nm.

τ_1 is related to IVR with a hypsochromic shift of the GSB (390 nm) and a bathochromic shift of the SE around 425 nm, which is overlaid with ESA. τ_2 is interpreted as solvent reorganization in the vicinity of the fluorophore. Partial compensation of ESA and SE is likely. Moreover, the interpretation explains the delayed appearance of the weak positive band at 415 nm. Accordingly, the change in sign of the τ_2-DAS at 625 nm represents a hypsochromic shift of the ESA band at long wavelengths.

τ_3 with 630 ps has a negative amplitude around 450 nm, which corresponds to a signal increase correlated with a signal decrease at longer wavelengths. This again relates to the population of additional conformational substates.

GLA yields a value for τ_4 of 11 ns. This is essentially infinite on the accessible time-window of the measurement and the number cannot be accurate. The accurate S_1 lifetime is retrieved from TSCPC measurements with excitation at 388 nm

in section 5.4.2. Its DAS reflects the transient spectrum at the longest delay time (1.5 ns) with the remaining GSB at 370 nm and broad, overlapping ESA bands at longer wavelengths. The steep gradient between 380 and 410 nm and the shape of the ESA band at 410 nm strongly indicate that ESA is also present at shorter wavelengths, but that it is overcompensated by GSB and SE.

Excitation at 310 nm

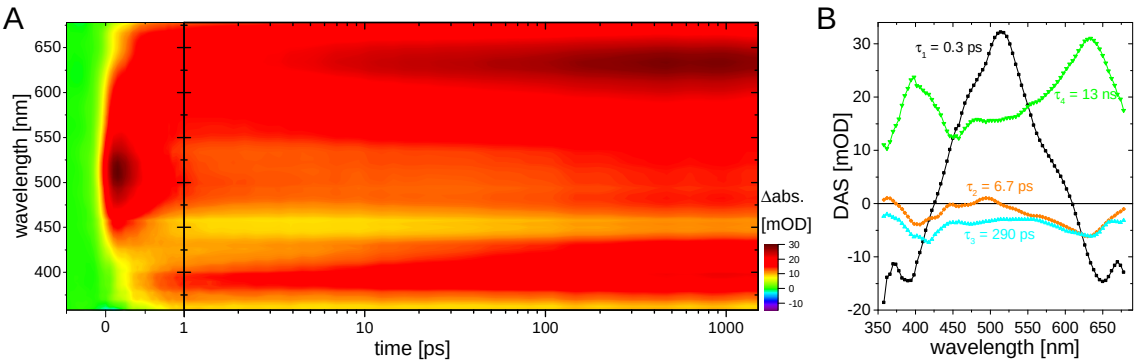

Figure 5.8: TAS data of 2PyA excited at 310 nm. A: Transient card of 100 µM 2PyA in MeOH. B: Corresponding DAS with the fitted lifetimes as indicated.

The transient card of 2PyA in MeOH excited at 310 nm is dominated by ESA throughout the whole spectrum, as all signal amplitudes after zero delay are positive. Still the signal is not completely uniform: the transient card shows a local maximum at 520 nm directly after time zero and minima at wavelengths shorter than 430 and longer than 620 nm. At 630 and at 370 nm after some hundred ps are further maxima and there is a particularly low amplitude at 450 nm in almost the whole measurable time range. Another low amplitude band exists at 410 nm that disappears on a time scale of 10 ps.

The DAS of τ_1 (0.3 ps) has a very pronounced and broad maximum at 515 nm, which is flanked by two negative contributions at wavelengths shorter than 425 and longer than 600 nm. The maximum describes the fast decrease of the ESA in the transient card directly after excitation. The low-energy minimum describes the main contribution of the ESA-build-up around 630 nm. The minimum at the high-energy side of the spectrum corresponds to the appearance of the ESA at 380 nm. Considering that excitation at 310 nm means excitation into a higher ES, τ_1 is attributed to IC into S_1. The time scale of this process is in line with the one observed for unsubstituted Py.[157,158]

τ_2 is 6.7 ps and its DAS resembles the τ_2-DAS from the excitation at 388 nm, although the high-energy minimum is less pronounced and although it is considerably faster. It is correlated with the disappearance of the local minimum at 410 nm in the ESA. The DAS of τ_3 (290 ps) has some similarities to the one of τ_2, it only shows a signal increase between 450 and 500 nm, which is completely absent in the τ_2-DAS. It is likely, that the two DAS describe closely related, but not identical processes. In close analogy to the situation encountered for excitation at 388 nm, the two processes are attributed to solvent and geometrical relaxation, respectively.

τ_4 from GLA (13 ns) is again virtually infinite on the time-window of the measurement. Yet, the trend to yield a longer overall S_1 lifetime after excitation to higher electronic states is consistent to the results obtained from TCSPC (see section 5.4.2). At wavelengths longer than 425 nm, the DAS is very similar to the one of τ_4 from the 388-nm-excitation, but it deviates considerably in the near-UV range, where the negative signal amplitude is completely replaced by a strong ESA band.

Comparison of the excitation-energy dependent dynamics of 2PyA

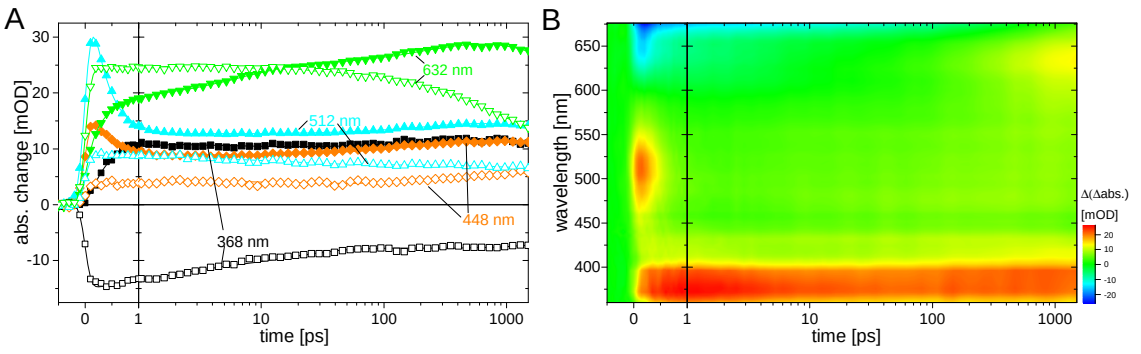

Figure 5.9: Comparison of the TAS data of 2PyA for excitation at 388 and 310 nm. A: Selected transients of 100 µM 2PyA in MeOH excited at 310 nm (solid symbols) and of 300 µM 2PyA in MeOH excited at 388 nm (open symbols). Solid lines are fits from the GLA. The signal amplitude of the 388-nm-transients $S_{388\,\mathrm{nm}}$ was multiplied by a scaling factor s =24. s is the product of the excitation energy times the extinction at 310 nm over the corresponding product at 388 nm to match the effective excitation cross sections. B: Difference of the scaled transient cards: $S_{310\,\mathrm{nm}} - s \times S_{388\,\mathrm{nm}}$.

The transients in figure 5.9 A illustrate the most significant differences between the data sets presented in the two previous sections. Whereas the transient at 368 nm is completely negative after zero delay for the SHG excitation, it is positive for excitation at 310 nm. At the same time, the emergence of the positive signal

is delayed as compared to the negative one. The transients at 448 and 512 nm demonstrate that the delay is not a consequence of a lower time resolution of the excitation at 310 nm. It is interesting to note that the transient pairs mentioned so far develop relatively similar at long delay times showing little changes. Still, shortly after excitation the behavior is very different with a weak and a very strong instantaneous maximum at 448 and 512 nm for 310 nm excitation that rapidly decreases. The corresponding 388-nm-transients show no such features. The amplitudes of the transients at 448 and 512 nm are higher for excitation at 310 nm in the whole measurement window.

The latter is remarkable because the situation changes when one considers the transients recorded at 632 nm. Excitation at 388 nm generates an instantaneous high absorption change that decays monotonously. Excitation at 310 nm shows again a delayed rise directly after excitation that continues slower until ~ 300 ps. The scaled signal amplitudes cross each other at approximately 15 ps. It seems valid to assume that the broad ESAs in the range around 630 nm, that are present for both excitation wavelengths, originate from transitions between identical or at least very similar states. This assumption implies that the population and depletion of the lower lying electronic state occurs with very different dynamics.

Figure 5.9 B is the scaled difference of the transient spectra presented in the two previous sections. The color code emphasizes major differences between the two data sets rather than details that are better discussed in terms of single transients. One dominant feature is the positive signal at wavelengths shorter than 400 nm that persists throughout the whole measurement, but decreases slightly. It reflects the fact that in this spectral range, the transient spectrum is negative for excitation at 388 nm and positive at 310 nm. Accordingly, high-energy excitation opens up a population pathway of an electronic state that is less accessible upon low-energy excitation.

The positive and negative signals at 510 and 630 nm at very early delay times show the close correlation between the depopulation of the higher ESs and the population of the ESA band at 630 nm for excitation at 310 nm. The latter is instantaneously populated with excitation at 388 nm. The weak positive amplitude at 630 nm at very long delay times indicates that besides the population also the depopulation of this state is affected by the excitation energy.

5.3.3 4PyA in MeOH

The transient card of 4PyA and the result of the GLA are shown in figure 5.10. Similar to the spectrum of 2PyA after excitation at 310 nm, ESA dominates large parts of the TA signal. At wavelengths shorter than 400 nm (390 nm at larger time delays), the measured amplitudes are approximately zero or negative. This indicates the presence of a GSB or SE that is more pronounced than for 2PyA but less than for 1PyA. The observation is in line with both, the fact that the steady-state absorption extends to longer wavelengths with high oscillator strengths and that the fluorescence quantum yields grow starting with 2PyA, followed by 4PyA and then 1PyA. In the case of 4PyA, SE is expected to significantly contribute to the transient spectra up to approximately 550 nm, as the steady-state emission at 480 and 530 nm still has 50 and 10 % of its maximal amplitude, respectively.

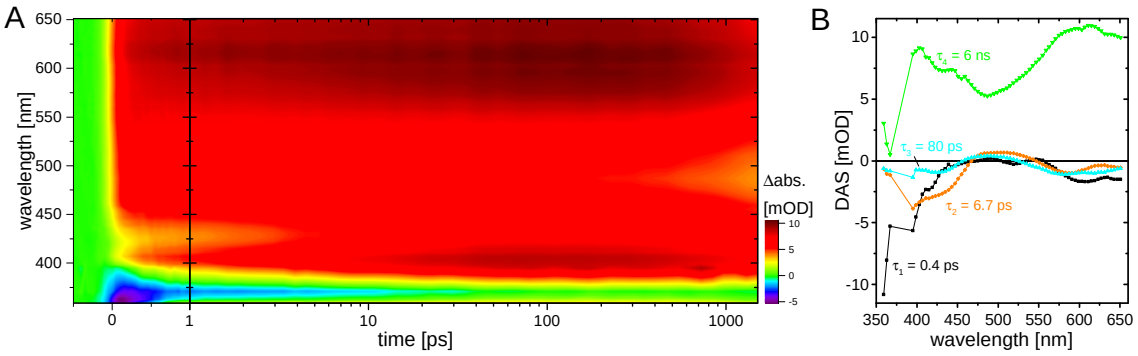

Figure 5.10: TAS data of 4PyA excited at 388 nm. A: Transient card of 300 µM 4PyA in MeOH. B: Corresponding DAS from GLA.

At wavelengths longer than 550 nm, there is broad ESA, which is present immediately after excitation and gains additional strength for another ~ 100 ps. The DAS of τ_1, τ_2, and τ_3 (0.4, 6.7, and 80 ps) reflect this with negative contributions in this spectral range. It indicates the build-up of an ES population occurring on a series of timescales from hundreds of fs to 100 ps.

The main contribution of τ_1 to the transient signals is at wavelengths shorter than 420 nm. In this spectral region, GSB and SE are expected to overlap with each other directly after excitation. There, the DAS describes a rapid signal increase, which means a partial recovery of the GSB and very likely an initial bathochromic shift of the SE due to IVR. τ_2 has its major contribution at considerably longer wavelengths than τ_1 and extends to 470 nm. In the transient card, it is related to the minimum in the ESA around 425 nm that slightly shifts to longer wavelengths.

Additionally, the DAS of τ_2 has a positive contribution between 470 and 550 nm. It therefore likely indicates a dynamic Stokes shift caused by solvent relaxation.

The DAS of τ_3 has relatively little contributions in the high-energy range of the transient spectra. Still, it is slightly negative in this range. It is zero in the center of the spectrum and again negative at the low-energy side. Its time constant is 80 ps and is attributed in analogy to the situation in 2PyA to geometrical reorganizations of the molecule. This reorganization is fast compared to 2PyA, but slow compared to 1PyA. So, 4PyA takes an intermediate position between its two analogues.

τ_4 from GLA (6 ns) is again considerably longer than the measurable time scales of the used TA setup. Therefore the exact value is not very reliable. Yet, it is shorter than the long-lived contributions found for 2PyA. This trend agrees qualitatively well with the fluorescence lifetime presented in section 5.4.3.

To briefly summarize the findings, the ultrafast photodynamics of the three isomers are similar to each other with respect to a hierarchical series of relaxation processes: IVR is followed by solvent and geometry relaxations and finally by an overall ES population decay. The fitted time constants are listed in table 5.3.

It should be noted, that the values found from the fits have relatively large uncertainties, that are difficult to be estimated. The main reasons for this are (i) the spectral shifts in the transient cards. GLA is not optimal for the description of such a non-exponential effect[133], which is most pronounced in 1PyA. Therefore, it was analyzed by LDA.[136] (ii) The distinct processes appear to be strongly nested and overlap temporally and spectrally. (iii) Due to the strong overlap, amplitude-lifetime compensation may play an important role in the fits.[174] (iv) All ESs live longer than the measurement time-window of the TA setup. Therefore, the retrieval of τ_4 is highly insecure in each case. This again can make the influence of point (iii) even worse. Therefore, the uncertainties of τ_i are estimated to be at least 10 %.

sample	1PyA	2PyA		4PyA
λ_{exc} / nm	388	388	310	388
τ_1 / ps	0.2 – 0.3	1.6	0.3	0.4
τ_2 / ps	2 – 10	19	6.7	6.7
τ_3 / ps	10 – 30	630	290	80
τ_4 / ns	2	11	13	6

Table 5.3: Decay constants of the PyA isomers in MeOH. For 1PyA, the τ_i were found with LDA. For 2PyA and 4PyA, the decay components stem from GLA.

However, the general ordering of the dynamical processes is strongly believed to be correct because the differences between the isomers and between the different excitation schemes for 2PyA are large. For excitation into S_1 (388 nm), a clear-cut ordering of the photoreaction dynamics is found with 1PyA being the fastest and 4PyA being again significantly faster than 2PyA. The geometry of 2PyA relaxes two times faster when excited at 310 nm as compared to 388 nm, but its relaxation is still slower than the one of 4PyA.

5.4 Time-resolved fluorescence emission

5.4.1 1PyA

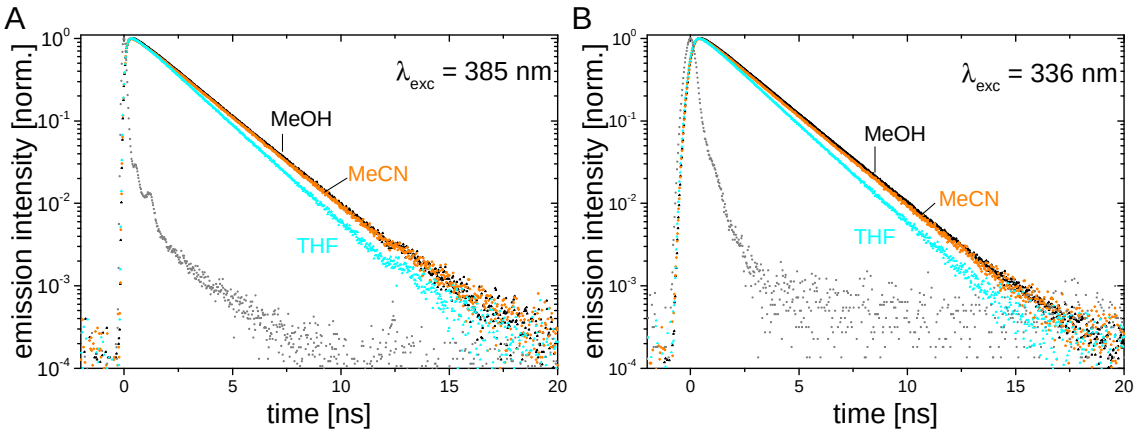

Figure 5.11: Time-resolved fluorescence decays of 5 μM 1PyA in MeOH, MeCN, and THF represented in black, orange, and cyan, respectively. A: Excitation was performed at 385 nm with the pulsed Ti:Sa-laser (Tsunami; em. filters GG395 and GG400). The kink at 12.4 ns stems from leakage of a side pulse from the pulse picker. Its amplitude in the gray depicted IRF is < 0.1 % of the main pulse. The satellites in the main excitation pulse are results of the non-flat spectral phase from the pulse picker. B: Excitation was performed at 336 nm with the pulsed LED PLS340 (em. filters GG385 and GG395, FWHM of the IRF: 500 ps).

Figures 5.11 A and B show the time-dependent fluorescence decays of 1PyA in MeOH, MeCN and THF. The experiments compare excitation at 385 nm derived from the Tsunami to excitation with the pulsed LED PLS340 at 336 nm. Both sets of decays agree well with each other. The lifetime of 1PyA in MeOH τ_{MeOH} is the largest one with (1.93 ± 0.05) ns. The decay in MeCN is only slightly faster with τ_{MeCN} = (1.92 ± 0.04) ns, whereas the decay in THF is the fastest one: τ_{THF} = (1.72 ± 0.03) ns.

The lifetimes in MeOH and MeCN are identical within their respective error margins, although the data points measured in MeOH are on average clearly above the ones in MeCN. The fits of the traces performed for excitation with the Tsunami reveal, why the lifetimes in MeOH and MeCN are identical while the traces appear to differ systematically: the traces yield poor fits with only one time constant τ_{main} (χ^2 between 3 and 12), whereas with a second time constant τ_{on}, the fits are considerably better ($\chi^2 < 1.4$). The amplitude of τ_{on} is however negative, indicating the presence of photophysical processes that affect the decay behavior very early after excitation.

More specifically, negative amplitudes indicate a population process or a dynamic Stokes shift. The τ_{on} values are (140 ± 15) ps in MeOH, (85 ± 8) ps in MeCN, and in THF (110 ± 30) ps with a contribution to the total emission of 2.6, 1.4, and 2.2 %, respectively. τ_{on} for MeCN is approximately half the size of the one for MeOH, which is why MeOH has its maximum at a later time channel after excitation causing the apparently higher amplitude at subsequent timing bins.

A different possible explanation for the delayed onset of the decay is a color-dependent time-shift (a chirp). Yet, it is unlikely that such a process can be observed on the time-scales accessible in the experiment. A chirp usually occurs in less than 1 ps, which is too fast for the TCSPC counting card. Secondly, a chirp should be visible in the other samples, as well.

The shortness of τ_{on} makes it hard to find it in the excitation traces with the pulsed LED because there, the IRF is too wide. For the pulsed LEDs a single-exponential fit is only minimally worse than a bi-exponential decay. The retrieved lifetimes describing the overall decay however agree within the error margins with τ_{main} derived from the Tsunami-based excitation.

The lifetime found by Förster et al. for a close analogue of 1PyA with a different TCSPC setup with an electronic bin width of 1 ns was 2.1 ns[162] and the one found with streak-camera measurements is 2.4 ns[136]. In the first experiment, the low electronic sampling density may explain the small deviation between the lifetimes. Besides that, the compounds are very similar, but not identical. In the streak-camera experiments, the DMSO concentration in the solvent was different (1 % as opposed to 0.05 %, here), which may have affected the outcome.

It is interesting to note, that the τ_{on} in THF is close to the one in MeOH although it is aprotic as is MeCN. So, a straightforward interpretation of the dependence of τ_{on} on ε_r and intermolecular H-bonds is not possible. τ_{main}, which describes

the actual decay behavior of 1PyA, suggests that S_1 lives longer in solvents with higher polarities, but is hardly affected by intermolecular H-bonds. These trends agree with the ones observed previously in a series of different solvents.[136]

5.4.2 2PyA

Figures 5.12 A and B display the fluorescence decays of 2PyA in MeOH, MeCN, and THF after excitation at 385 and 336 nm, respectively. All decay traces are not mono-exponential. This is more obvious for excitation at 385 nm, but it is also true for excitation at 336 nm.

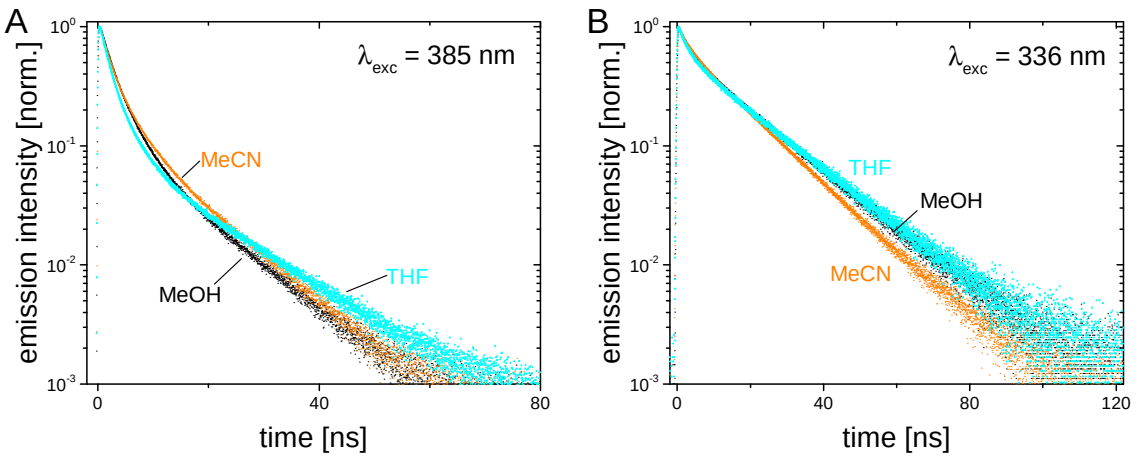

Figure 5.12: Time-resolved fluorescence decays of 2PyA in MeOH (black squares) and MeCN (orange diamonds) and THF (cyan triangles). A: 5 µM 2PyA excited at 385 nm with the Tsunami (GG400 filter). B: 15 µM 2PyA excited at 336 nm and detected with the combination of a WG355 and a GG385 filter in MeOH and 3 µM 2PyA in MeCN and THF.

Fitting the traces in the figure 5.12 A with two lifetimes yields χ^2-values > 3 and the residuals show systematic deviations in the whole time range with significant emission. With three lifetimes, χ^2 reduces to < 1.3, the residuals are equally distributed, and none of the three components contributes less than 20 % of the total emission.[154] The traces in B can be fitted with two components ($\chi^2 \approx 1.3$ – 1.5), but the lifetimes are then inconsistent to the lifetimes found for excitation at 385 nm. Therefore, both sets of decays are evaluated with a tri-exponential model. The χ^2-values for excitation at 336 nm are then reduced to < 1.2. The results are presented in table 5.4.

The lifetimes found for excitation at 385 and 336 nm are similar to each other, but not identical. There are several potential reasons for this: (i) particularly for excitation at 336 nm, the contributions of the first two decay channels are small,

excitation nm	solvent	τ_1 ns	n_1 %	τ_2 ns	n_2 %	τ_3 ns	n_3 %
385	THF	1.3	30	3.8	36	15.6	34
	MeOH	1.5	24	4.0	46	13.1	30
	MeCN	1.3	20	3.8	39	11.8	40
336	THF	0.9	5	4.7	12	18.1	83
	MeOH	0.8	4	4.4	13	17.4	83
	MeCN	0.9	4	4.7	12	15.0	84

Table 5.4: Fit parameters of the time-resolved fluorescence decays of 2PyA. Shown are the lifetimes τ_i with the relative contributions n_i found for the different decay channels in different solvents for excitation at 385 and 336 nm.

which increases the uncertainty of their fits, because of the low total number of counted photons and its impact on Gaussian noise statistics[174] (ii) Lifetimes and amplitudes of fits to exponential decays are correlated to each other[175–177] with the consequence that a shorter lifetime is compensated by an increased amplitude and vice versa. The effect is worse for decay channels with a small contribution to the total number of detected photons. (iii) The IRFs for excitation at 385 and 336 nm have widths of 200 and 500 ps, respectively. Consequently, especially the retrieval of the fastest lifetime is expected to be more difficult for excitation at 336 nm. (iv) The distribution of the populations is obviously very different. Accordingly, the dynamics of the population transfer between the emitting species must be different. Therefore the two longer-lived species may appear to decay slower.[178] This could indicate that a slow exchange between the different species is possible for excitation at 385 nm and less likely for excitation at 336 nm. (v) In principle, a multi-exponential model might be inappropriate to describe the decay behavior because it potentially is truly non-exponential.[174] Unfortunately, it is extremely difficult to differentiate between non- and multi-exponential decays and thus a tri-phasic model is adopted, here. (vi) The S_1 lifetime of 2PyA depends on the cut-on wavelength (see the following paragraphs). The difference of the detection range for the two excitation wavelengths (400 nm as opposed to 385 nm) is also likely to contribute to the observed deviations.

The overall S_1 lifetime of 2PyA after excitation at 336 nm decreases with an increasing cut-on wavelength (figure 5.13 A). Accordingly, the long-lived decay component contributes strongest to the high-energy part of the fluorescence spectrum. In this part of the spectrum, the structured emission dominates, that is only visible upon excitation in higher ESs. Therefore, the long-lived component is assigned to the structured emission with the larger $S_1 \rightarrow S_0$ energy gap.

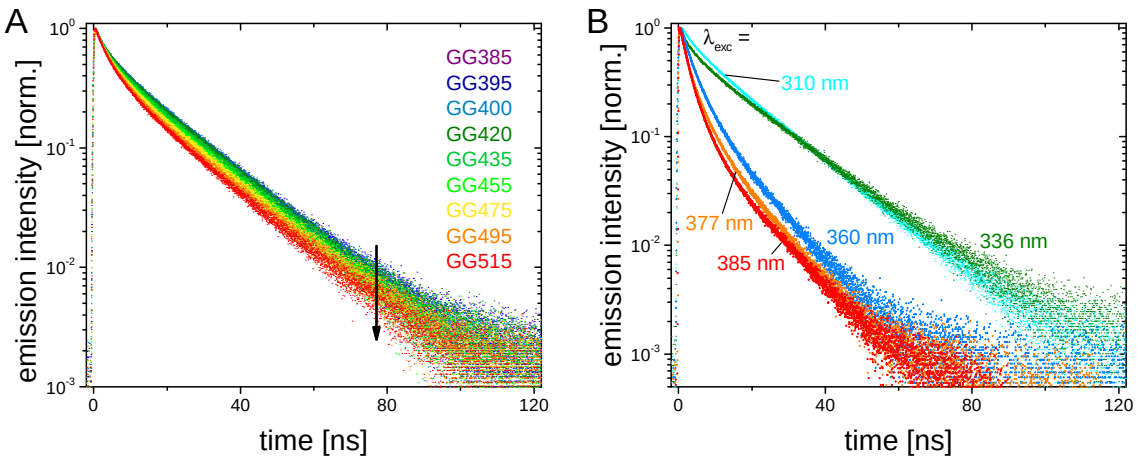

Figure 5.13: Color dependence of the time-resolved fluorescence decays of 15 µM 2PyA in MeOH. A: The used emission filters are a combination of WG355 with the filters indicated in the figure legend. Excitation was performed at 336 nm. B: Different excitation wavelengths as indicated in the figure. 385 and 377 nm originate from the Tsunami, the rest of the excitation wavelengths is from pulsed LEDs (PLS 310, 340-10, and 360).

This assignment is supported by the increase of the S_1 lifetime with decreasing excitation wavelength (figure 5.13 B). The excitation at 360 nm originates from the pulsed LED PLS 360 (FWHM ~ 800 ps). Therefore, the increase cannot be an excitation artifact.

It is interesting to note, that the relative contribution of the long-lived species decreases again slightly for excitation at 310 nm. Therefore, the long-lived state is assumed to be most efficiently populated from one particular ES. Based on quantum-chemical calculations, this particular state is proposed to be the S_2 (see section 5.5).

5.4.3 4PyA

The fluorescence of 4PyA with excitation at 380 nm is shown in figure 5.14 A. It was found to be (3.90 ± 0.08) ns in MeOH. In MeCN and THF, the lifetimes are (3.84 ± 0.10) and (4.45 ± 0.10) ns, respectively. The difference between MeOH and MeCN is extremely small and practically negligible, which indicates that H-bonds are not important. Assuming small differences of the non-radiative de-excitation rates in the various solvents, the ~ 20 % slower decay in THF indicates a decreased oscillator strength in the solvent with the smallest ε_r. This is typical for a strongly allowed transition between S_0 and S_1, where the ES dipole is larger than the one of the GS.[63]

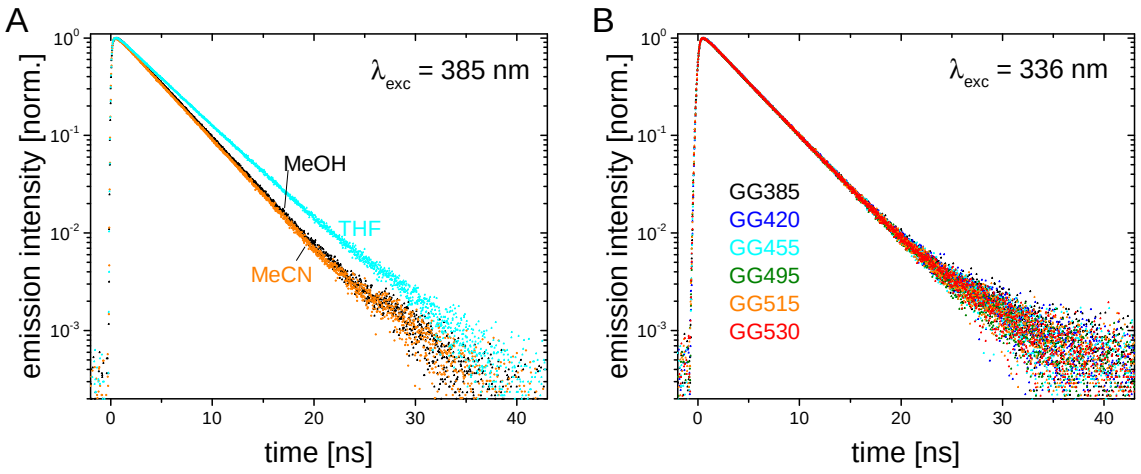

Figure 5.14: Time-resolved fluorescence decays of 4PyA. A: 5 µM 4PyA excited at 380 nm in MeOH (black squares), MeCN (orange diamonds), and THF (cyan triangles) with GG305 as emission filter. B: 10 µM 4PyA in MeOH excited at 336 nm and detected with a WG355 filter combined with the different filters indicated in the legend.

Figure 5.14 B contains decay traces of 4PyA in MeOH measured with different cut-on wavelengths of the emission filters. Within the experimental uncertainty, the decay times are perfectly identical for all used excitation sources and filter combinations. This observation is clearly different from the situation encountered in 2PyA. Yet, this difference agrees well with the observations from the steady-state spectra, where 4PyA showed no significant dependency on both, the excitation and the emission wavelength.

In difference to 1PyA, an additional time constant does not improve the fits significantly, and therefore no apparent build-up time is observed.

5.5 Quantum-chemical calculations

The emission behavior of the PyAs turn them into interesting molecules for theoretical investigations, as 2PyA breaks the Kasha-Vavilov rule[61] and 1PyA and 4PyA do not. The chosen theoretical approach is bipartite. In order to asses the GS properties of all PyAs in a comparative fashion, DFT calculations were performed with Gaussian.[179] There, the rotation angle of Py relative to A around the axis of the ethynyl bridge was altered. Secondly, Turbomole[180,181] combined with TmoleX[182] was used to calculate the electronic properties and optical transitions of 2PyA. Initially, a GS-geometry optimization in vacuum with the second-order approximate coupled-cluster method CC2[183–188] using the def2-TZVP basis set[189,190]

was performed. Based on these results, the singlet[191] and triplet[185,192,193] states and transition energies for the optimized and for a constrained GS geometry were calculated.

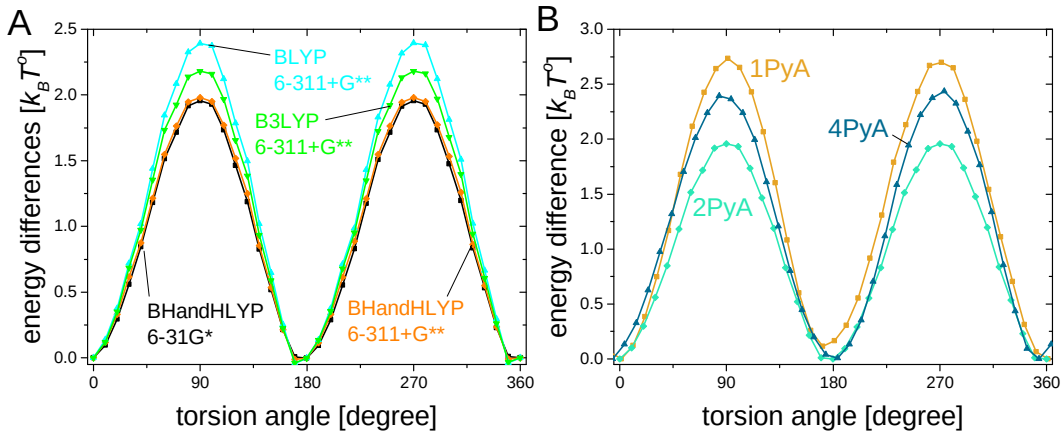

Figure 5.15: Rotameric GS energy barriers of the three PyAs. A: Barriers of 2PyA using different combinations of basis sets and functionals as indicated in the figure. B: Barriers calculated for the three isomers with BHandHLYP/6-31G*. $T^0 = 298$ K.

The calculation of the GS energies for constrained geometries is motivated by the assumption, that Py and A can rotate to different extent around the ethynyl bridge in the three isomers. The height of the rotational barrier around the ethynyl bridge is estimated by a series of GS geometry optimizations with fixed torsion angles between the two planar molecule parts. DFT calculations were performed with Gaussian using different basis sets (6-31G* and 6-311+G**) and functionals (BLYP, B3LYP, and BHandHLYP) for 2PyA, which are shown in figure 5.15 A. The barrier height for the formation of rotamers depends relatively strongly on the used functional, whereas the influence of the basis set is found to be negligible. Local minima are found in each case for torsion angles of 0, 180, and 360 °, respectively. They represent coplanar orientation of Py and A. The minima have identical energy because 2PyA is perfectly symmetric around the ethynyl axis and therefore 0 and 180 ° are indistinguishable.

The combination BHandHLYP/6-31G* was used to investigate the differences between the three isomers because the barrier was found to be flatest for this functional and the smaller basis set allows for faster calculation than its larger counterpart. The results of the comparison are depicted in figure 5.15 B. The ordering of the rotameric barrier height is clearly such that the barrier is highest for 1PyA and smallest for 2PyA.

For 1PyA, the degeneracy for 0 and 180 ° is clearly lifted because the config-

uration of 1PyA is the most asymmetric one with respect to rotation around the ethynyl bridge. For 4PyA, the degeneracy is not lifted notably, but due to the slight asymmetry related to rotation around the ethynyl bridge, a small difference in energy is expected.

The CC2 method under Turbomole also gives coplanar Py and A moieties in the GS. For the optimized GS geometry ('coplanar') and for a geometry with Py and the A rotated by 90 ° ('twisted'), the lowest ten vertical singlet excitations were calculated. The molecular orbitals (MOs) from HOMO-4 to LUMO+3[xiv] are presented in figure 5.16.

For the flat geometry, HOMO with LUMO+1 and HOMO-1 with LUMO are pairwise similar to and distinct from each other. HOMO and LUMO+1 are strictly localized at the Py and strongly resemble the HOMO and the LUMO of unsubstituted Py.[136] For 1PyA, no Py-localized MOs could be observed.[136] HOMO-1 and LUMO of 2PyA are delocalized over the long axis of the molecule defined by the direction of the ethynyl bridge. The main electronic density is located at the bridge itself and at A, although significant density remains at Py, as well.

For the twisted molecule, the Py-localized densities are contained in the HOMO and the LUMO, whereas no delocalized excitation over the whole molecule is visible. Accordingly, the coplanar LUMO+1 becomes the twisted LUMO. The twisted HOMO-1 and LUMO+1 are restricted to the Py and the ethynyl. The LUMO+3 contributes to S_3 and S_4 in case of the twisted 2PyA and it is localized along the short axis of Py.

The first four optical transitions cover the experimentally relevant range and are summarized in table 5.5. In the coplanar case, the transitions are solely composed of the superpositions of transitions between the HOMO-1 to the LUMO+1. In twisted geometry, the LUMO+3 also contributes to transitions to S_3 and S_4. Double excitations contribute less than 10 % to any transition.

Only $S_0 \rightarrow S_2$ is solely localized on Py in both, its start and end state and for both geometries. It is also at virtually the same energy in both geometries. Taking this together with the similarity of these two states with the HOMO and LUMO of unperturbed Py justifies to call this transition LE state and it is extremely Py-like. It is associated with the structured, hypsochromically shifted, and long-lived emission upon excitation at 336 nm. The experimentally available absorption maximum at 336 nm is used to scale the calculated (in vacuo) spectrum to the

[xiv] HOMO: highest occupied molecular orbital; LUMO: lowest unoccupied molecular orbital

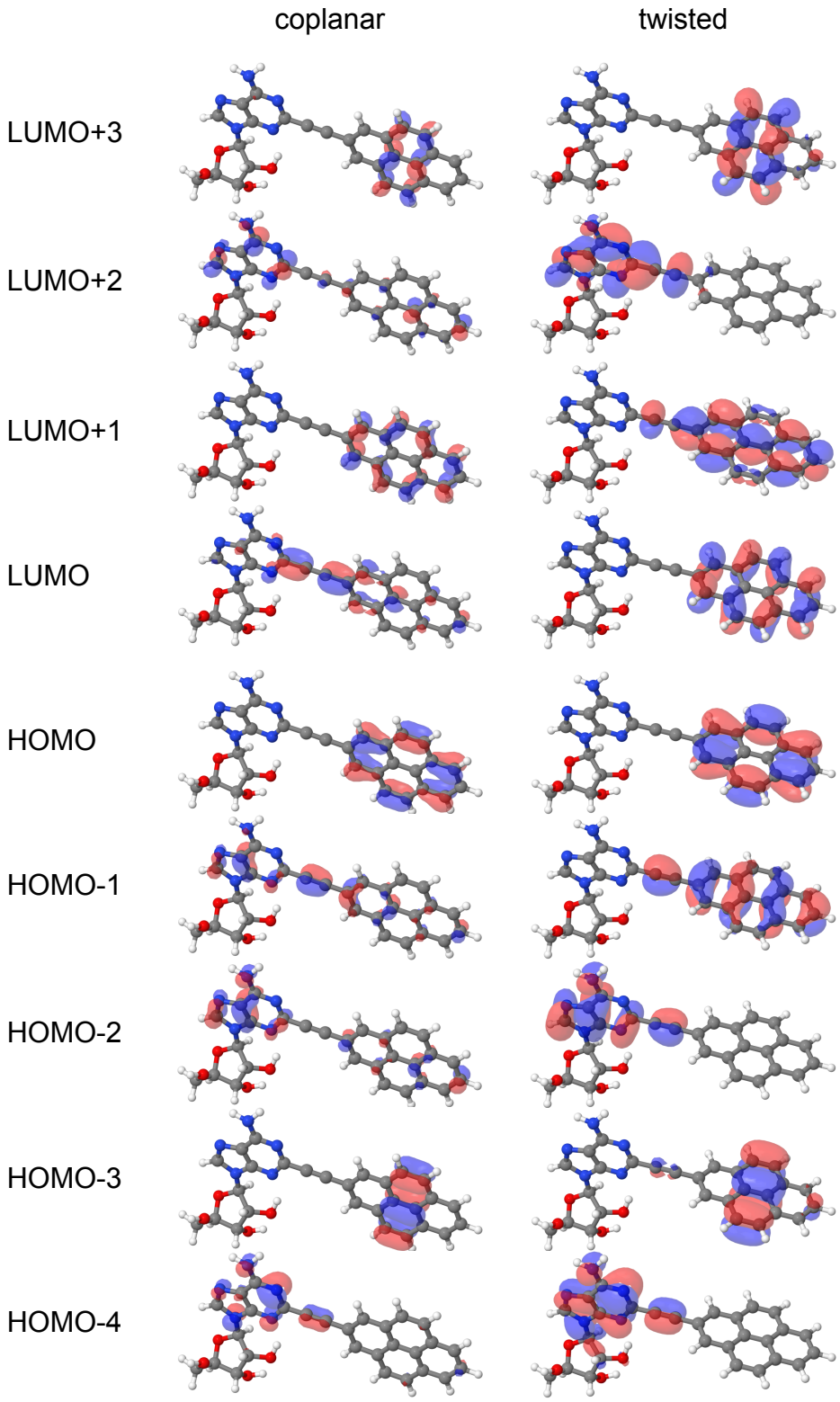

Figure 5.16: Singlet MOs of coplanar (left) and twisted (right) 2PyA around the HOMO. Twisted means that Py and A are rotated by 90 ° relative to each other. The MOs are visualized with Jmol[194] and represent 97 % of the total density.

transition: $S_0 \rightarrow S_n$	MOs (contribution/%)	E/cm^{-1} (nm)	E*/nm	oscillator strength
coplanar				
$n = 1$	HOMO to LUMO (56) HOMO-1 to LUMO+1 (26)	27 638 (362)	391	0.0043
2	HOMO to LUMO+1 (83)	31 838 (314)	336	0.1152
3	HOMO-1 to LUMO (75)	33 542 (298)	318	1.8552
4	HOMO-1 to LUMO (46) HOMO to LUMO (33)	35 262 (284)	301	0.1988
twisted				
1	HOMO to LUMO+1 (57) HOMO-1 to LUMO (40)	28 324 (353)	381	0.0021
2	HOMO to LUMO (88)	31 882 (313)	335	0.3675
3	HOMO to LUMO+3 (68) HOMO-1 to LUMO (12)	36 212 (276)	293	0.0601
4	HOMO-1 to LUMO (42) HOMO to LUMO+1 (28) HOMO to LUMO+3 (20)	36 739 (272)	288	0.2343

Table 5.5: Four lowest lying vertical transitions of 2PyA. Shown are the coplanar and the twisted geometries. MO contributions < 10 % are omitted for clarity. 'E' is the transition energy (values in brackets are in nm). 'E*' is the wavelength resulting from a linear shift of the energies by 2076 cm^{-1} towards smaller energies. Oscillator strengths represent the mixed gauge.

experimental spectra in solvent by shifting the energies adequately (see caption of table 5.5).

The resulting wavelength for the $S_0 \rightarrow S_1$ transition agrees reasonably well with the experimental one for both geometries. The oscillator strength of the transition to S_1 is considerably smaller than the one to S_2, which is also reasonable in terms of the experimental data.

The calculations appear to overestimate the oscillator strength of the $S_0 \rightarrow S_3$ transition in coplanar geometry. The twisted $S_0 \rightarrow S_3$ transition is at a significantly higher energy than in coplanar geometry. Because the coplanar $S_0 \rightarrow S_3$ transition depends on the overlap of the aromatic moieties of Py, A, and the ethynyl, it is likely to react very sensitive to the torsion angle. Therefore, its oscillator strength might rapidly decrease for geometries other than the coplanar one and be therefore less dominant in a rather heterogeneous mixture of GS rotamers. The overestimation of the oscillator strength might also be a consequence of the lack of solvent interactions in the calculations.

The eight lowest-lying triplet state energies relative to the vibrational GS of S_0 for coplanar and twisted 2PyA are presented in table 5.6. The triplet state energies

	coplanar		twisted	
n of T_n	E/cm^{-1} (nm)	E*/nm	E/cm^{-1} (nm)	E*/nm
1	21 042 (475)	527	21 078 (474)	526
2	26 575 (376)	408	28 423 (352)	380
3	27 483 (364)	394	29 145 (343)	370
4	31 323 (319)	342	30 753 (325)	349
5	31 509 (317)	340	31 515 (317)	340
6	31 742 (315)	337	32 366 (308)	330
7	34 439 (290)	309	34 486 (290)	309
8	36 354 (275)	292	36 619 (273)	289

Table 5.6: Triplet energies of 2PyA. The lowest-lying triplet states 2PyA to the S_0 for coplanar and twisted orientation of Py and A. 'E' denotes the energy calculated by Turbomole, 'E*' is the energy shifted by 2076 cm^{-1} to match the experimental (singlet) spectra.

of T_1 and T_5 to T_8 are largely independent of the orientation of Py. T_2, T_3, and—to some extent—T_4 depend on the orientation of Py and A. In coplanar geometry, the contributions are mostly delocalized over the whole molecule, whereas such MOs are absent in the twisted one. The rather similar transitions are usually, at least partially, localized at Py.

The states T_2 through T_7 are energetically suitable receiver states for a potential ISC from S_1 and S_2, respectively. T_1 shows that a potential phosporescence emission is expected at wavelengths longer than 527 nm and stems from a Py-dominated transition. At this wavelength, the steady-state emission spectra have only about 15 and 5 % of their maximum intensity for excitations into the S_1 and the S_2, respectively.

5.6 Discussion

In the previous sections, the photophysical behavior of 1PyA, 2PyA, and 4PyA was presented. The used experimental techniques cover steady-state absorption and emission spectroscopy along with ps-time-resolved fluorescence-emission and ultrafast time-resolved TAS in several solvents. The experimental characterization was complemented by theoretical calculations of the rotameric barrier heights in the GS. 2PyAs general photophysical behavior and in particular its fluorescence was found to be extraordinarily complex as it is multi-phasic and depends both on the spectral excitation and emission wavelength. Therefore, its electronic excitation pattern was investigated by means of quantum-chemical calculations, too.

Because 1PyA and 4PyA decay essentially mono-exponential, the decisive state for their fluorescence properties is solely the S_1 state. Accordingly, first the behavior of the three investigated isomers upon $S_0 \rightarrow S_1$ excitation will be discussed (section 5.6.1). This part of the discussion will cover 1PyA and 4PyA completely. Then, the particular behavior of 2PyA after excitation to higher ESs will be discussed separately in section 5.6.2.

5.6.1 S_1 excitation of the pyrenylethynyl adenosines

The three structural PyA isomers are found to display a bathochromically shifted absorption with respect to Py. The $S_0 \rightarrow S_1$ transition is located around 380 nm and significantly broadened. The $S_0 \rightarrow S_1$ transition of Py occurs at a comparable energy, but has a far smaller oscillator strength. The absorption of the three isomers exhibits increasing oscillator strengths from 2PyA over 4PyA to 1PyA.

Ultrafast TAS measurements with excitation at 388 nm yields transient spectra, which are dominated by broad and unstructured ESA bands at wavelengths longer than 550 nm for all isomers.[136,154] This is in clear contrast to Py, where virtually no TA signal is visible in this spectral range. The ESA tends to dominate the spectra towards shorter wavelengths in 2PyA and even more in 4PyA. Therefore, it is likely that broad ESA is present in all isomers and compensated to different extent by overlapping GSB and SE contributions. The most important difference between the isomers is therefore the time scale of the photodynamics, which becomes faster from 2PyA over 4PyA to 1PyA. The same is true for the overall S_1 decay rates as determined from the fluorescence lifetimes.

The steady-state fluorescence spectra of the isomers after excitation into the S_1 are similar to each other, but remarkably distinct from pure Py, which emits at higher energies. This indicates the involvement of CT states for the substituted Pys. This view is also supported by the response of the labels to the solvent polarity.[63] In THF, all labels gain vibrational fine structure with an energy spacing of approximately 1200 cm^{-1}. The spectral shift of 4PyA from THF to MeCN is the largest one. However, the differences are not very pronounced between the isomers.

The conformational barriers for the formation of rotamers with respect to the relative orientation of the planes of Py and A in the GS of the isomers are compared on the basis of DFT calculations. The barrier is found to be smallest in 2PyA followed by 4PyA and then 1PyA.

From that brief overview over the relevant results presented in the sections 5.2 to 5.5, the ordering of the isomers as going from 2PyA to 1PyA with 4PyA being intermediate between the two others appears to emerge as the natural one. The ordering is easily motivated by considering steric effects for the different attachment sites of the isomers as illustrated in figure 5.17.

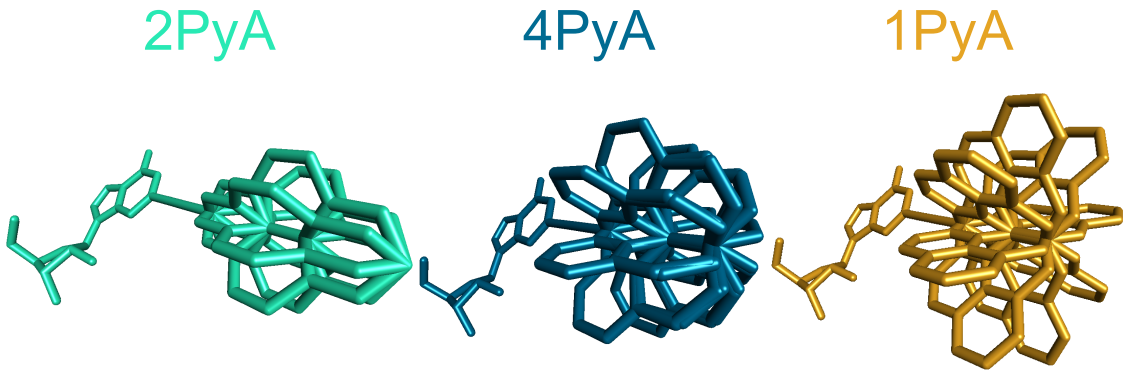

Figure 5.17: Overlaid rotamer structures for the three isomers with tilt angles between 0 and 360 ° in steps of 45 °.

Potential rotamers of 1PyA are clearly more space consuming than those of 4PyA. 2PyA is the isomer where rotation of Py around the ethynyl fills the smallest volume. Additionally, 2PyA is the only isomer, where the rotamers are pairwise identical for a rotation of 180 °.

It appears to be more difficult to assess the role of intermolecular H-bonds. In all cases, MeOH induces the strongest bathochromic shift in the fluorescence spectra and it also causes the strongest loss of vibrational fine structure, although the ε_r of MeCN is larger. For 1PyA, the C2'-OH group is known to act as intramolecular H-bond donor with N3 of A as acceptor.[136] This bond was shown to affect the emission properties, because the loss in fine structure is mainly related to the presence of intermolecular H-bonds provided by the solvent and to a smaller extent to ε_r. The substitution of the intramolecular H-bond by intermolecular ones stabilizes an unstructured and bathochromically shifted substate on the S_1 potential energy surface (PES).

The structure optimizations of 2PyA and 4PyA also show an intramolecular H-bond. Therefore, the peculiarities observed with MeOH are interpreted as being analogous to the well-studied role they play for 1PyA.

The most striking difference between the isomers are the mono-phasic decays of 1PyA and 4PyA as opposed to the tri-phasic one of 2PyA. Dual (bi-exponential)

fluorescence from two distinct emitting states is usually related to the formation of solvent-stabilized CT states, which coexist with an LE state resembling the emission of the unsubstituted parental fluorophore. CT and LE states are usually related to different ES geometries.[178,195]

In 2PyA, the emission is tri-exponential indicating three emitting states. Examples of tri-exponential decays are very rare, but for 1-arylpyrenyls the possible existence of two distinct CT states and the LE state are established.[163,164] Moreover, governed by the polarity-dependent stabilization of the two CT states, all three states can be present simultaneously. The two CT states are called mesomeric and twisted intramolecular CT (MICT and TICT) and correspond to coplanar and perpendicular orientations of Py with respect to the attached aryl group, respectively.

The coplanar MICT state leaves the conjugation of the whole molecule intact and therefore CT can be relatively easily reversed causing higher fluorescence yields than expected for the TICT state, where the conjugation is broken. The CT character of the TICT state is also usually more pronounced than the one of the MICT state. Therefore, the TICT state is expected to be more efficiently stabilized with increasing ε_r of the solvent than the MICT state. The LE state is expected to be largely insensitive to ε_r.

Two questions emerge here: i) why are all three states observable only in 2PyA and ii) why are they observable in all solvents? The answers to these questions are likely to be related to the particular properties of 2PyA compared to 1PyA and 4PyA. One peculiarity is the symmetry of the Py rotation due to substitution at the 2-position as introduced above. A second one is the low electron density of Py at the 2-position both, in S_0 and S_1.[153] This is expected to render the electronic coupling of Py and A relatively small, although the steady-state spectra show that it is not negligible.

The heights of the energy barriers for the formation of rotamers increase from 2PyA to 4PyA and again to 1PyA. Caution is necessary for the interpretation of the significance of this result. DFT calcutions for 1,4-bis(phenylethynyl)benzene were shown to overestimate such rotameric barriers.[196] Accordingly, one would probably overstrain the results, if one relies solely on the calculated values. This is the more true, as the calculations were performed in vacuum.

The ordering of the barrier heights, however, is expected to be correct, because it can easily be understood in terms of steric considerations. Beyond that, the

ordering is assumed to be correct also for the geometries of higher ESs because the fundamental steric arguments hold there, as well. For the ES(s) additional aspects, such as non-coplanar CT configurations may be important, too. Therefore, the GS barrier heights are expected to be smaller in the molecule than the DFT calculations suggest, but the ordering is correct. Additionally, the ES barriers are expected to be even flatter than the GS barriers because of additional substates related to CT processes. The latter is believed to be especially true for 2PyA.

A flat S_1-PES with several local minima has the following implications: Firstly, small barriers exert only small conformational driving forces. Secondly, photoexcitation creates an excited vibrational S_1 state, given the exciting photon has sufficient excess energy. The excess energy may then help the molecule to overcome the small S_1 barriers. Assuming the molecular populations in the GS to be dominated—although not purely consisting of—minimal energy PyAs (that says coplanar geometry), excess energy is likely to be translated into rotational motion around the ethynyl axis and will drive the molecules necessarily into more twisted conformations. Hereby, the barriers may be overcome and a new local minimum can be reached or the molecule will slowly relax back via IVR.

When the barriers are high, the probability for the molecule to reach a different minimum is decreased and at the same time the driving force back to the coplanar state is large because the gradients are steeper. The latter leads to accelerated ES dynamics, which is indeed observed for the three isomers in the ordering that is deduced from the DFT calculations and steric considerations. Therefore, the TAS data and the different rates of the photoreactions upon excitation at 388 nm strongly support this interpretation.

In 1PyA and 4PyA, the electronic coupling between Py and A is stronger than in 2PyA due to the low electron density at the 2-position of Py. Substitution of Py at the 1-position should have a strong potential to mix the dipole moments μ_{01} and μ_{02} for transitions from S_0 to S_1 and S_2 because it is rotated 65 ° with respect to μ_{01} and 25 ° to μ_{02}. For comparison, the 4-position is rotated 15,° with respect to μ_{01} and the 2-position is located on μ_{02}.

The decay behavior of 1PyA and 4PyA is essentially mono-phasic and the shorter lifetime of 1PyA compared to 4PyA can be attributed to the larger extinction coefficient and thus radiative decay rate. This in turn reflects the more efficient mixing of the transitions related to μ_{01} and μ_{02} of unperturbed Py. Therefore, the nature of the states dominating the transitions in the two mainly mono-exponential isomers is essentially identical. For 1PyA, only a weak CT character

of this state is established as consequence of its large ϕ_f in combination with the short lifetime.[136] The two features rule out the dominance of both, a TICT state with strong CT character that would result in small ϕ_f values[161,165] and of an LE state, which is expected to be long-lived. Consequently, 1PyA and 4PyA are dominated by a weak CT state, which is likely to be planar and follows a MICT-like interaction and stabilization pattern.

In 2PyA, all three possible states are observed. A mechanism explaining this will be developed in the following section, which focuses solely on 2PyA and will include the observations made for excitation into higher ESs.

5.6.2 Higher excited states of 2PyA

The steady-state fluorescence of 2PyA was found to heavily depend on the excitation wavelength. With a decreasing excitation wavelength, the fluorescence gains fine structure and shifts hypsochromically. From 320 nm on, no further shift is observed. This shift is dominated by the increase of a vibrational band at 411 nm. The decrease of emission at wavelengths longer than 470 nm reveals an additional small shoulder at approximately 460 nm. The characteristic appearance of structure was observed in all investigated solvents.

The transient card after excitation at 310 nm differs significantly from the one obtained for excitation at 388 nm. The transient card for UV excitation lacks the negative contribution at wavelengths shorter than 400 nm, because it is overcompensated by ESA. The intense ESA band at 650 nm is not instantaneously present, instead it is populated from a different electronic state (ESA at 515 nm). Solvent and geometry related processes are roughly two times faster for excitation at 310 nm and virtually everywhere in the transient card ESA gains intensity and width within the following few hundred ps. In accordance with the lower quantum yield, no negative contribution to the DAS associated with the global S_1 decay (τ_4) is observed.

Time-resolved fluorescence emission experiments reveal a pronounced dependence of the decay traces both, on the excitation and the emission cut-on wavelength. The long-lived species is associated with the high-energy part of the emission spectrum and is addressed most efficiently by excitation at 336 nm. That says, the overall fluorescence lifetime decreases again slightly for excitation at 310 nm compared to 336 nm. At the same time, the relative contribution of short-lived species decreases, as well.

2PyA clearly neither obeys Kasha's rule,[59] nor the Kasha-Vavilov rule.[61] Of course, there are several examples of other fluorophores, which break Kasha's rule. They include various variants of the red-edge effect, fluorescence directly from the second or even higher ESs, and luminescence from metastable states.

The red-edge effect, describes alternative fluorescence responses to selective excitation into the lowest vibronic levels of chromophores in frozen solution. All examples share specific interactions of the fluorophore with the environment (mostly solvent molecules) as explanatory key motif. In the classical version of the red-edge effect, low-energy excitation leads to emission from a conformational sub-ensemble of molecules with increased lifetimes (see [197,198] and literature within), which is in contrast to the effects observed for 2PyA. Other examples of the red-edge effect feature shorter fluorescence lifetimes for low-energy excitation.[199] The shortening of the fluorescence lifetime is there explained in terms of the coupling of nuclear out-of plane vibrations to the lowest (in-plane) electronic states of a heterogeneous sample in rigid solution resulting in out-of-plane transition moments. In line with these observations, time-resolved experiments in cooled solutions demonstrated hypsochromically shifting fluorescence for low-energy excitation[200], which is in strong contrast to the normal dynamic Stokes-shift observable at room temperature.

Most importantly, the dependence of a fluorescence emission from the excitation wavelength was found to be indicative of an inhomogeneous ES rather than of an inhomogeneous GS. The latter would manifest itself only in the dependence of the fluorescence decay from the detection wavelength.[174]

One peculiarity of 2PyA is the observation, that the structured high-energy emission upon excitation into S_2 is correlated with a long-lived emission. Several examples for $S_2 \rightarrow S_0$ fluorescence are known. Azulene shows only fluorescence from S_2 because the $S_1 \rightarrow S_0$ transition is forbidden and, more important, the energy gap ΔE_{01} between S_0 and S_1 is approximately as large as the one between S_1 and S_2 (ΔE_{12} =14 000 cm^{-1}).[201] The large ΔE_{12} prevents IC to occur between the two ESs and therefore radiative deactivation from S_2 to the GS contributes significantly.[202] Substitutions to azulene that decrease ΔE_{12} also decrease the quantum yield for the S_2 fluorescence.[201] The low IC rate from S_2 to S_1 as consequence of a large ΔE_{12} is known as energy-gap law and theory predicts a super-exponential dependence of the IC rate on ΔE_{12}.[203]

Beyond that, $S_2 \rightarrow S_0$ fluorescence could be observed in numerous other aromatic molecules, including Py. In those molecules, high-energy excitation leads

to broadening of the emission spectrum towards higher energies, and the additional emission has the vibrational pattern of the absorption spectrum. This is a strong indication for emission from thermally unrelaxed vibrational states.[204] In trans-azobenzene, the $S_2 \rightarrow S_0$ fluorescence lifetime was found to be extremely small with only 5 ps. The short lifetime explains why the fluorescence occurs from states that are not thermally equilibrated.[205] More precisely, excitation to the $^1(\pi, \pi^*)$-overtone band yields $S_2 \rightarrow S_0$ fluorescence, which is distinct from the $S_1 \rightarrow S_0$ fluorescence (excitation at a $^1(n, \pi^*)$-transition) and results in an excitation dependence of the emission. However, the IC rate from S_2 to S_1 is fast, which explains the small $S_2 \rightarrow S_0$ lifetime. That says, unusual $S_2 \rightarrow S_0$ fluorescence comes mostly from very short-lived states, which is again not the case for the structured emission of 2PyA.

The origin of the usually weak $S_2 \rightarrow S_0$ fluorescence of Py is not due to a large ΔE_{12}, but rather due to a small one (4 000 cm^{-1}) with strong vibration-mediated mixing of the two electronic levels.[205] This ΔE_{12} suits well to the calculated one for 2PyA of 4 200 cm^{-1} for the optimized GS structure. In gas phase, the tight coupling of the two lowest ESs leads to reversible IC processes. The $S_2 \rightarrow S_1$-IC-rate was found to be 2×10^{12} Hz (corresponds to 5 ps) and the reverse rate is 10^7 Hz. Consequently there are hot non-equilibrated $S_1^* \rightarrow S_0$ emission bands. In solution, the repopulation of S_2 and thus S_1^* is however strongly reduced.[206] Moreover, Py was demonstrated to show distinct fluorescence from even higher excited states than the S_2, including $S_4 \rightarrow S_0$ emission.[204] In solution, all of those higher ES fluorescence contributions are expected to be short-lived and small in magnitude. So, none of those examples can directly explain the behavior of 2PyA.

The coupling of the two relevant electronic states depends on the positions and the momenta of the nuclei involved in the relevant vibronic modes. More specifically, an antisymmetric vibration can lead to the efficient coupling of a symmetry-forbidden $S_1^* \rightarrow S_0$ transition with symmetric modes in the S_2. The condition that $S_1^* \rightarrow S_0$ is symmetry-forbidden is necessary for the nuclei to perform significant motions within the S_1 lifetime. Therefore, the Born-Oppenheimer (BO) and the adiabatic approximations fail and the antisymmetric S_1 mode can couple to symmetrical S_2 modes (see [207] and literature therein).

An alternative explanation is the postulation of a metastable state to be responsible for the long-lived high-energy emission of 2PyA. Typical candidates for metastable states are triplets. Py has an extraordinarily high triplet-formation yield (0.27) in thoroughly degassed EtOH, but the phosphorescence yield is very

low (2×10^{-5}).[62] Additionally, there are more examples of molecules with forbidden $S_1^* \rightarrow S_0$ transitions that show enhanced triplet formation from the S_1.[208] However, two questions remain in such an explanatory scheme: (i) why should the triplet yield of 2PyA depend on the excitation wavelengths, given that the triplet formation yield of Py is high mainly because of the long S_1 lifetime? (ii) Can a triplet explain the hypsochromicity of the long-lived emission?

Question (i) is essentially a reversal of the explanatory line of arguments aimed at by invoking triplets. The triplet was supposed to explain the long-lived state as a metastable one. In Py, one rather needs a long-lived state to explain the formation of triplets. Question (ii) has to be denied. In Py, the T_1 lies approximately $10\,000\,\mathrm{cm}^{-1}$ below the S_1.[62] In 2PyA, the calculated energy difference is $6\,600\,\mathrm{cm}^{-1}$. Therefore the phosphorescence is expected to be substantially bathochromically shifted with respect to the fluorescence. Although under convenient circumstances thermal back transfer from T_1 to S_1 is possible in benzene[60], this is extremely unlikely in Py and 2PyA due to the large energy gaps. Additionally for 2PyA, the experimental conditions are very different from the ones used in reference [60].

Therefore, a metastable state that can explain the observations must reside on the S_1-PES. An example is found in naphthalene[209], where the optical transitions from the S_1 are largely forbidden. Such a situation is of course also encountered in unsubstituted Py. Unfortunately, the situation appears to be different for 2PyA, where short-lived substates on the S_1-PES exist with potentially lower enthalpies than the long-lived substate. Nevertheless, no efficient decay of the long-lived substate via the short-lived ones is observed.

In total, 2PyA appears to possess an heterogeneous S_1-PES that supports three independent emitting substates in different solvents at room temperature, which can be addressed with different efficiencies in an excitation–wavelength-dependent manner. The rest of this section is devoted to developing a model capable of qualitatively explaining the nature of the three substates and their relationship to each other. To achieve this, the electronic configurations calculated for the $S_0 \rightarrow S_1$ and $S_0 \rightarrow S_2$ transitions in coplanar and twisted geometries are considered once more.

The spacing of the energy levels in figure 5.18 is not perfectly true to scale. However, the only deviation is that the energy spacing between LUMO and LUMO+1 of the coplanar geometry is expanded by a factor of five for the sake of clarity. The calculated spacing between the two MOs is $11\,\mathrm{cm}^{-1}$ ($\approx 5\,\%$ of $k_\mathrm{B} \times T^o$).

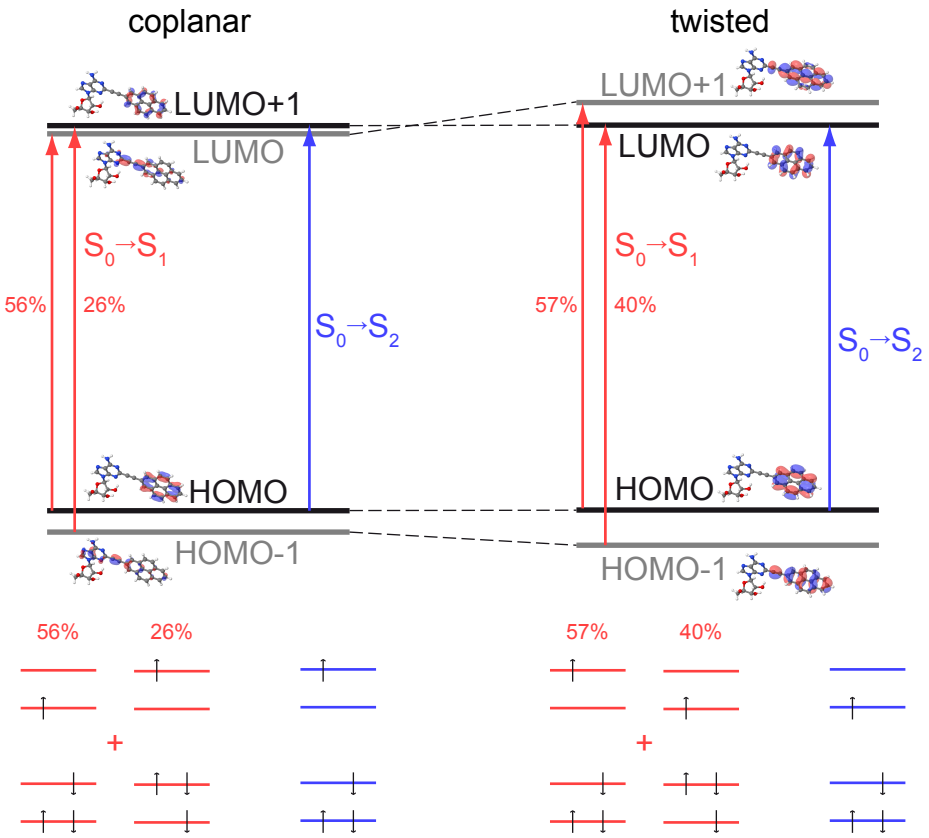

Figure 5.18: Geometry dependent energy-level diagrams of 2PyA. Top: Optical transitions for coplanar (left) and twisted (right) orientation of Py and A. Bottom: Electronic configurations associated with the S_1 and S_2 states directly after excitation.

The two electron-hole pair configurations related to the $S_0 \rightarrow S_1$ transition connect always two MOs of which one is localized solely at Py and the other one is—to a certain degree—delocalized over larger parts of the molecule. In the twisted geometry, MOs have no contributions on Py and A at the same time due to the broken conjugation. That says, a TICT state cannot be excited directly. A MICT state however is directly accessible starting in the coplanar geometry.

When Py rotates out of the plane of A, the coplanar LUMO+1, which is localized purely at Py, becomes lower in energy than the coplanar LUMO. This is likely due to the loss of conjugation between the two aromatic moieties in the molecule. Suppose now there occurs an optical excitation into S_1 in coplanar geometry and yields the minor populated electronic configuration. Let's assume further that excess energy is transferred into rotation of the Py moiety. At some point of the rotation, the previously doubly disadvantageous electronic configuration with the hole in HOMO-1 and the electron in LUMO+1 will flip to a configuration, where the electron resides in the LUMO instead of LUMO+1.

This may provide the mechanism necessary to stabilize the TICT state. If this is true, Py will be the electron acceptor for the TICT state. Additionally, this scheme does not invoke direct FC-excitation of the TICT state. Rather, it is purely a result of (potentially light-induced) molecular motion and the particular electronic properties of 2PyA. If the excess energy is not sufficient for the required molecular rotation or too large and carries Py again out of the presumably rather shallow TICT-minimum, 2PyA will return to a coplanar configuration and form the MICT state. In the coplanar geometry, the electron may be transferred into both directions, which sounds reasonable for an ICT state that is stabilized by mesomeric interactions.

The line of argumentation for excitation to the S_2 is very similar. Starting in coplanar geometry, Py may rotate—driven by excess energy—far enough for LUMO and LUMO+1 to switch their ordering. Interestingly, the electronic configuration is then the most favorable one for any ES with the excited electron in the LUMO and the corresponding hole in the HOMO. In view of this consideration and the large probability for Py derivatives to show significant mixing of their first ESs due to the small energy gap ΔE_{12}[163,164,204,207], it appears reasonable to assume that for some configuration, S_1 and S_2 have an intersection. In this picture, the LE state is mainly populated from the S_2, which provides the necessary driving force to access the LE configuration. For low-energy excitation, the population of the LE might be off-resonant S_2 excitation, or it is the result of vibronic coupling between S_1 and S_2. This also explains, why excitation into S_3 ($\lambda < 320\,\mathrm{nm}$) again changes the shape of the emission spectrum and of the fluorescence decay trace.

Although, ES geometries of conjugated molecules have often larger interatomic distances[210], the ethynyl bridge is rather expected to shorten, when its bonding π-orbitals are effected by photoexcitation[211]. For the CT states, electrostatic attraction between Py and A and in case of the MICT state also the enhanced conjugation of the ethynyl bridge are likely to shorten the distance between Py and A. The LE state on the other hand, is expected to be relatively unaffected by the described mechanisms and the calculations demonstrate the S_2-electron configuration to be insensitive to the relative configuration of Py and A (namely the rotation angle between the two). Therefore the ethynyl bridge length d may be identical or even larger than in the GS (see figure 5.19) in the LE-ES geometry. Provided the proposed larger distance d in the LE-ES is correct, the electronic coupling should decrease even more because the overlap of the electronic orbitals depends exponentially on d.[50]

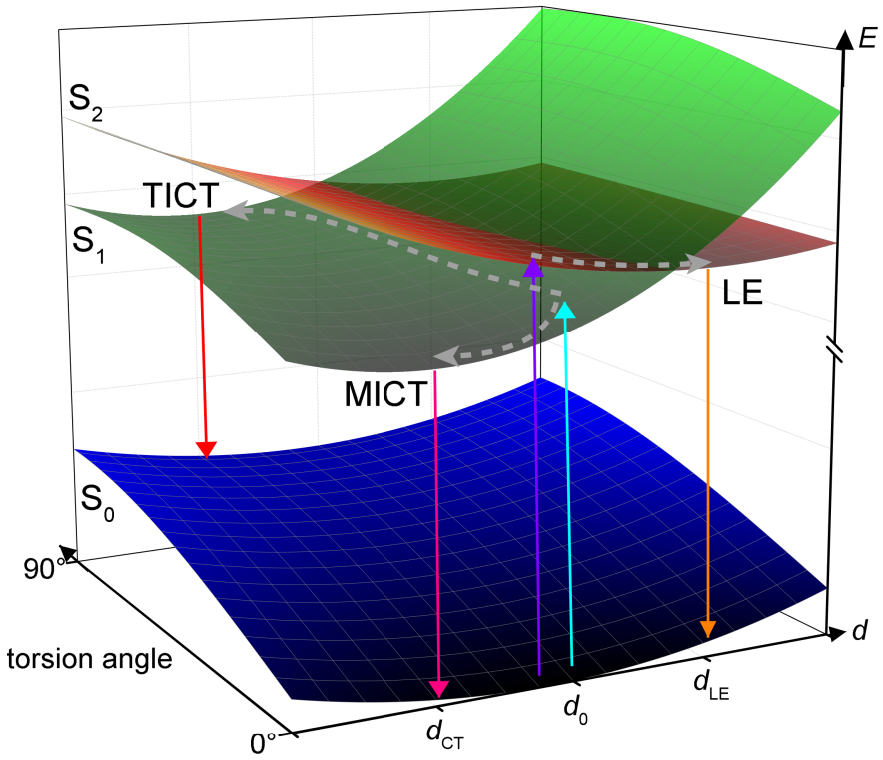

Figure 5.19: After photoexcitation into S_1 (cyan arrow), 2PyA is more likely to populate the MICT and TICT states, than after excitation into S_2 (violet), where population of the LE state dominates. The orange, the magenta, and the red arrow represent radiative transitions from the LE, the MICT, and the TICT state. Dashed arrows indicate the assumed movement on the ES-PESs. d_{CT}, d_0, and d_{LE} denote the minimal energy distance d between Py and A for the CT states, the GS, and the LE state, respectively.

Taking all pieces of information together results in the sketch of the S_1 and S_2-PES as it is depicted in figure 5.19. Please note that the dependence of the S_1 and S_2-PES on d as reaction coordinate is not quantitative and to some degree even speculative. Because the enthalpy of the 2PyA-LE is likely to be insensitive to the rotational configuration of Py and A, it is expected to be entropically favored compared to both the MICT and TICT states, which are restricted to relatively small angular regimes.

To sum this chapter up, based on an extensive investigation of the photophysical properties of the three structural isomers of 2-(pyrenylethynyl) adenosine in several solvents, a unified model of the emission properties was developed. The employed experimental techniques encompass steady-state and time-resolved absorption and emission spectroscopy and they are complemented by a series of quantum-chemical calculations.

The emission of 1PyA and 4PyA can be understood as originating from a

coplanar state with weak CT character. In 2PyA, three emitting species are present, which are identified as MICT, TICT, and LE states, respectively. The MICT state features coplanar Py and A moieties and is amenable to direct optical excitation. In the TICT state, Py and A are rotated by 90 ° relative to each other around the ethynyl bridge as reaction to excess energy from the photoexcitation. The LE and TICT states are observable only in 2PyA because (i) the degree of conjugation in the coplanar geometry is larger in 1PyA and 4PyA and purely local Py states do not exist there[xv] and (ii) the rotational barriers are higher for 4PyA and 1PyA than for 2PyA.

[xv] For 1PyA this is calculated and published in reference [136], for 4PyA, it is deduced as generalization from the observations, the calculations for 1PyA, and the similar electronic properties of positions 1 and 4 of Py in contrast to position 2.

Chapter 6

Results III — The tetracycline-binding aptamer

The TC aptamer is a short, in-vitro selected RNA oligonucleotide that has been optimized and analyzed using point mutations.[18] In contrast to most other artificial aptamers, the TC aptamer can regulate gene expression in vivo. It is known to rely strongly on divalent cations (namely Mg^{2+}) for ligand binding.[21] Due to its relatively small size, its strong reaction to Mg^{2+}, and its versatile applicability in biological research assays, the TC aptamer is a well-suited model system to study the relations of structural kinetics and thermodynamics to function in RNA-based regulation. More specifically, the work presented in this chapter aims at disentangling the effects of Mg^{2+} and TC on the conformational state of the TC aptamer.

In section 6.1, TC and its aptamer are described along with the previously published knowledge about their interaction. Section 6.2 shows Mg^{2+}-titration experiments that were spectroscopically monitored and allow to gain qualitative insights into the system. To acquire quantitative data, heat-monitored titration and temperature-induced de- and renaturation profiles, in the following referred to as melting curves, were recorded and evaluated with a Van't-Hoff-analysis. The results of these experiments and of the analysis are presented in the sections 6.3 and 6.4, respectively. In section 6.5 the findings are discussed and a model is developed that explains the interdependence between TC, its aptamer and Mg^{2+}.

Parts of this chapter have been published in reference [17].

6.1 Introduction of the tetracycline-binding aptamer

The chemical formula of TC and the conformation of TC bound by its aptamer are presented in 6.1 A and B, respectively. TC consists of four six-membered rings, where ring IV with the dimethylamino group is tilted and points out of the plane shared by the rings I – III. Figure 6.1 C shows the consensus secondary structure of the TC aptamer. The core of the aptamer consists of three stems (P1, P2, and P3), two loops (L2 and L3) and two joining regions (J1/2 and J2/3). The version of the TC aptamer used within this work is a 57mer and the numbering is in accordance with the one used in reference [16].

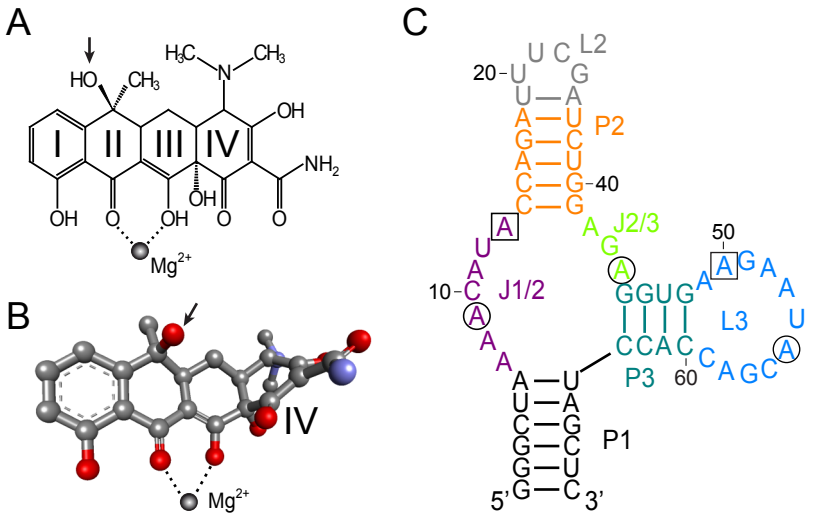

Figure 6.1: Chemical structure of TC and secondary structure of its aptamer. A: Chemical formula of TC. B: 3D representation of TCs conformation within the binding pocket. B is based on the crystal structure 3EGZ.[212] The Cl atom at position 7 is not displayed. The black arrow marks the hydroxy group at the $R_{6\beta}$ position. C: Primary and secondary structure of the minimal version of the TC aptamer used. The secondary structure is based on.[23]

The TC aptamer was initially introduced by Berens et al.[21] as the minimer version of the aptamer cb28. cb28 was found in vitro by SELEX (2.2.3).[213,214] Without Mg^{2+}, TC could neither bind to cb28, nor the minimer.

In 2003, the TC aptamer was successfully employed for translational control of conditional gene expression in *Saccharomyces cerevisiae*.[18,215] Later, control of splicing[216] and direct control of endogenous and at the same time essential genes[19] in *S. cerevisiae* could be demonstrated. An additional control scheme employed in yeast utilized the aptamer as part of a TC-responsive, self-cleaving ribozyme.[217] Recently, the TC aptamer could also be applied in the archaeal

species *Methanosarcina acetivorans*[218] and the TC-responsive ribozyme was used to control gene expression in mammalian cells[20].

Throughout these research projects, systematic alterations of the primary structure and hence stability of the aptamer were routinely applied to adapt it to the various applications and the cellular environments. This kind of re-engineering is in general necessary for the application of aptamers as RSs and is usually considerably easier than re-engineering the AD of a naturally occurring RS to function in a non-native environment.[15]

Consequently, there is not a single primary sequence of the TC aptamer, but several variations that share a common core part. This common core part makes up the structure in figure 6.1 C.

To date, only five in-vitro aptamers are known that can serve as sensing units for synthetic or engineered RSs. The aptamers bind a Hoechst dye[219], malachite green[220], TC, theophylline[221–223], and neomycin[224,225], respectively. On the one hand, some of the regulation-competent aptamers proved to be very versatile tools for the control of gene expression in vivo in various cellular contexts. Especially the theophylline and the TC-binding aptamers were found to have a large variety of applications.[16] On the other hand, the number of aptamers with regulatory capability is surprisingly small given the fact that—in principle—at least one aptamer may exist for each and every ligand one can imagine. Oftentimes, several aptamers can be found for a given ligand.[226]

Tight binding of an aptamer to its cognate ligand alone is not sufficient to generate a good RS. In case of the neomycin-binding aptamer, for example, the aptamer that showed the best regulation properties bound by far worse than the best aptamer found in the same SELEX. The best aptamer had in deed no regulatory activity, at all.[224] Such kind of considerations lead very early to the question, what an in-vitro aptamer needs to act as a functional RS.

The TC aptamer was soon recognized as excellent model system to address this question and its structural and thermodynamical properties were extensively studied. Starting from the initially proposed secondary structure[21], a refinement of the secondary structure was achieved by chemical and enzymatic probing[23]. This work also aimed at determining the structural influence of TC, which lead to the conclusions that most stems are formed already in the absence of both, Mg^{2+} and TC, and that TC stabilizes the tertiary structure of the aptamer. The tertiary structure can be induced by Mg^{2+} and it is stabilized by TC via intramolecular

linkage. The aptamer was found to be significantly preformed already in the absence of TC. A systematic analysis of the binding properties of the TC aptamer with respect to TC and several of its analogs revealed the pivotal importance of the $R_{6\beta}$-OH for recognition and binding[22] (black arrows in figure 6.1). In a buffer with 10 mM Mg^{2+}, a dissociation constant (K_d) of the aptamer-ligand complex of 770 pM was determined.

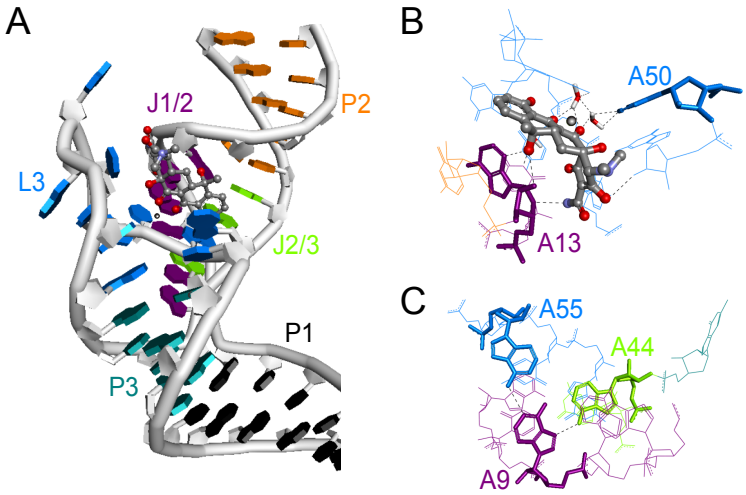

Figure 6.2: Tertiary structure of the tetracycline-binding aptamer. A: Crystal structure of the circularly permutated ligand-aptamer complex of the TC aptamer. Mg^{2+} chelated by TC is depicted as gray ball. B: Close-up of the binding pocket. The chelated ion is represented as in part A. Highly coordinated water molecules interacting with the chelated Mg^{2+} are shown in stick representation. C: Close-up of the A-triplex forming the core part of the tertiary structure of the TC aptamer. The figure is based on the pdb-file 3EGZ.[212]

The crystal structure of the TC aptamer[212] is best suited to discuss the structural findings. The binding pocket is formed by the joining region J1/2 and loop L3. Figure 6.2 A displays the crystal structure of the complex. These findings are in good agreement with the results of structural probing published previously.[21–23] The nucleotides A13[xvi] and A50 are particularly important for TC binding, although the binding pocket consists of several neighboring bases, which is presented in figure 6.2 B. This is also reflected by the fact that 425 Å^2 out of 621 Å^2 of the solvent-accessible surface area (SASA) of TC are buried in the ligand-aptamer complex. More specifically, A13 forms an H-bond to the $R_{6\beta}$-OH of TC, whereas A50 is involved in interactions with the chelated Mg^{2+} and surrounding water molecules. Besides the binding pocket, the TC aptamer has a second cluster of distant nucleotides that form tertiary interactions of major importance: the adenosines A9,

[xvi] In this chapter, the abbreviation 'A' refers exclusively to adenosine.

A44, and A55 in the joining regions J1/2 and J2/3 and loop L3. They form an A-triplex as highlighted in figure 6.2 C. This triplex is the necessary structural basis to form the binding pocket.

Wunnicke et al.[24] performed steady-state EPR and DEER measurements on spin-labeled versions of the TC aptamer emphasizing the effect of TC on the conformational state of the aptamer. Through modeling, two competing conformations were found in the absence of TC, where one strongly resembled the conformation of the complexed aptamer. The second conformation showed a more open junction J1/2 and was not observed in the presence of TC. The distance measurements were performed with 5 mM $MgCl_2$ and $\geq 15\,\%$ glycerol at 50 K. Both conformations are quite similar to each other, with large fractions of the tertiary interactions being formed already without TC.

Förster et al.[25] focused on the dynamics of ligand binding. The experiments utilized fast mixing via stopped-flow and monitored the fluorescence of TC, that strongly increases upon ligand binding and therefore directly and sensitively reports on the complex formation of ligand and aptamer. For the wildtype (WT) aptamer, an unusual bi-exponential binding behavior in 10 mM Mg^{2+} was found. The first binding step is reversible with an on-rate of $35\,s^{-1}$ and an off-rate of $13.1\,(\mu M\,s)^{-1}$. For the typical experimental conditions ([aptamer] = $(1 - 10)\,\mu M$ and [TC] $\geq 15\,\mu M$), this results in a very fast initial component close to the time resolution of the experiment (1.6 ms). The second binding step was found to be irreversible with an on-rate of $155\,s^{-1}$. The results were interpreted in such a way that a fast initial docking step, whose on-rate is essentially diffusion limited, is followed by a relatively slow local rearrangement of the binding pocket (second binding step), unless the initial encounter complex dissociates too fast. Dissociation is represented by the off-rate of step one. The irreversibility of the second step indicates that the complex is extraordinarily stable after it is completely formed and does essentially not dissociate on the time scale of the experimental window (minutes).

The experiments with the WT presented in reference [25] were complemented by experiments with single-point mutants and with DOX replacing TC. The mutants were A9G, A13U, and A50U, where the A at position 9 is replaced by G, and the As at 13 and 50 by U, respectively. Replacement of A9 destroys the A-triplex at the core of the aptamer impeding the preformation of the tertiary structure, while the binding pocket itself remains intact. The point mutations at residues 13 and 50 disturb the binding pocket directly without affecting the preformation.

In A50U, mainly the first binding step was slowed down, whereas in A13U both steps were decelerated. The amplitudes of the fluorescence change of the first binding step remained largely unaffected by mutations in the binding pocket. This indicates that both parts of the binding pocket are important for the initial binding.

In contrast, A50U is of minor importance in the second binding step, probably because the interaction with TC is less direct. Combining the A50U mutant with DOX mimics a double mutant, where both, A13 and A50 are replaced simultaneously because DOX lacks the $R_{6\beta}$-OH interacting with A13. There, no fluorescence change could be observed indicating that binding or rather recognition is not possible when both sides of the binding pocket are not functional.

The situation is very different for A9G, where binding is slowed down dramatically, mainly because the off-rate of the first step rises three orders of magnitude. This observation was interpreted in such a way that either the correct binding pocket is masked or that there is a large set of conformations available, that can bind the ligand but are unable to form the correct binding pocket before the encounter complex dissociates again. The amplitude of the first step is only 7 % of the total fluorescence change as opposed to approximately 50 % for the WT and the other single-point mutants. The second step is still irreversible. That says, that A9G can form the correct binding pocket, but the likelihood is much smaller compared to the wildtype.

The A9G mutant demonstrates the importance of the preformation for the binding efficiency. But it also shows, that binding is possible without preformation, which is not true in the absence of Mg^{2+}. Accordingly, Mg^{2+} and the parts of the aptamer that determine the tertiary structure and their combination are decisive for binding, but their respective contributions and roles are somewhat different.

Beforehand, there has been no systematic investigation of the role of Mg^{2+} and this chapter aims at clarifying its role in the folding and binding process of the TC aptamer. The approach to achieve this aim is designed around monitoring structural responses of the aptamer to varying bulk concentrations of Mg^{2+} both, in the presence and the absence of ligand. Additionally, urea is employed to introduce a folding barrier into the system. This strategy allowed to deduce qualitative insights. It is complemented by thermal melting experiments, that allow for quantitative statements.

6.2 Spectroscopically monitored aptamer folding

Most of the spectroscopy-based methods used in previous studies to investigate the TC aptamer relied on the fluorescence properties of the ligand.[22,25] It is routinely used to measure the K_d values of the ligand-aptamer complex for the diverse aptamer mutants and labeled variants and also in combination with different analogues of TC (see for example[22]).

This strategy has the disadvantage, that it does not allow to observe the global folding state of the bare aptamer. To directly monitor the aptamer itself, it is necessary to employ absorption spectroscopy. As described in section 2.2.4, the extinction coefficient of RNA oligomers is sensitive to its conformation as consequence of excitonic couplings between the nucleotides. This coupling also dominates the CD signal of RNA.

Fluorescence, absorption and CD were employed to follow the folding transitions of the TC aptamer as response to Mg^{2+} titrations. The analysis of the data collected this way is complicated by the facts that TC itself has both, an absorption signal and a CD response that is sensitive to Mg^{2+} because TC has a slightly altered conformation, when it is part of a chelate complex.[227–229] The experiments were designed in such a way that these issues could be circumvented: the OD of the aptamer at 260 nm was adjusted to be around 0.5 and the TC absorption was approximately two orders of magnitude smaller leading to background signals in the range of the experimental uncertainty and clearly smaller than the measured signal changes. Consequently, correcting the aptamer spectra by subtraction of the TC-related background did not affect the titration results significantly and was omitted, therefore.

Figure 6.3 A displays the fluorescence response of TC in different solvation contexts. Without Mg^{2+}, TC shows a basal fluorescence. This residual fluorescence is hardly affected by the aptamer. In absence of the TC aptamer, the addition of Mg^{2+} induces a rise in fluorescence as reaction to the formation of the chelate complex. With aptamer, the fluorescence increases by another factor of 13 in 10.6 mM Mg^{2+} resulting in an easily accessible observable reporting on the ligand–aptamer-complex formation. Additionally, the fluorescence spectrum with aptamer and Mg^{2+} shows a unique fine structure with bands at 424, 449, and 507 nm. This is a consequence of the structural rigidity that TC gains, when it is bound to its aptamer. This gain in rigidity is also the explanation for the increase of ϕ_f and the lifetime of TC.[25]

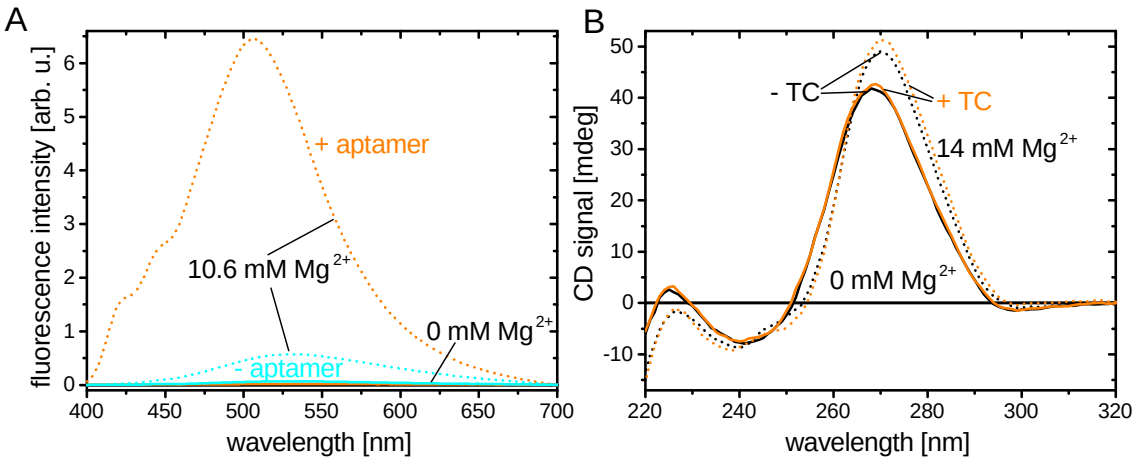

Figure 6.3: Fluorescence and CD spectra of the TC aptamer. A: Fluorescence spectra of TC with (orange) and without (cyan) aptamer in the absence of any (solid lines) and in the presence of 10.6 mM Mg^{2+} (dashed lines) in PBS buffer (pH 7.4). B: CD spectra of 10 µM TC aptamer with 0 (black) and with 10 µM (orange) TC. Solid and dashed lines are recorded with 0 and 14 mM Mg^{2+}, respectively.

Figure 6.3 B shows typical CD spectra of the TC aptamer without Mg^{2+} and with 14 mM Mg^{2+}. The general features of the spectra are fairly similar with maxima around 228 nm and 268 nm and minima at 240 nm and 300 nm. This is in good agreement with the CD spectrum of RNA. That says it represents mainly an A-form helix.[230,231] Observable differences are related to the amplitudes, that are higher at most spectral positions in presence of Mg^{2+} and small spectral shifts of the bands (~ 4 nm). In parallel to the amplitude changes in the CD signal, the absorption of the aptamer at 260 nm decreases with increasing Mg^{2+} concentration and is interpreted as compaction of the oligonucleotide in accordance with literature.[232–234]

The presence of TC has relatively little effect on the CD spectra, especially their shape. This is true as well in absence of any Mg^{2+} as in presence of large quantities of it. The main difference is that the final spectrum with TC has a larger amplitude than the one without ligand. Considering the facts that TC is expected not to interact with its aptamer without Mg^{2+} and not to change the overall conformation of the fully preformed aptamer, this observation is not surprising. It also demonstrates that the spectral signature of the ligand itself is negligible.

In section 6.2.1, the emphasis will be on investigating the effect of TC on the transition between the tertiary-structureless start and the completely structured end point of folding and binding.

6.2.1 Mg^{2+} titrations

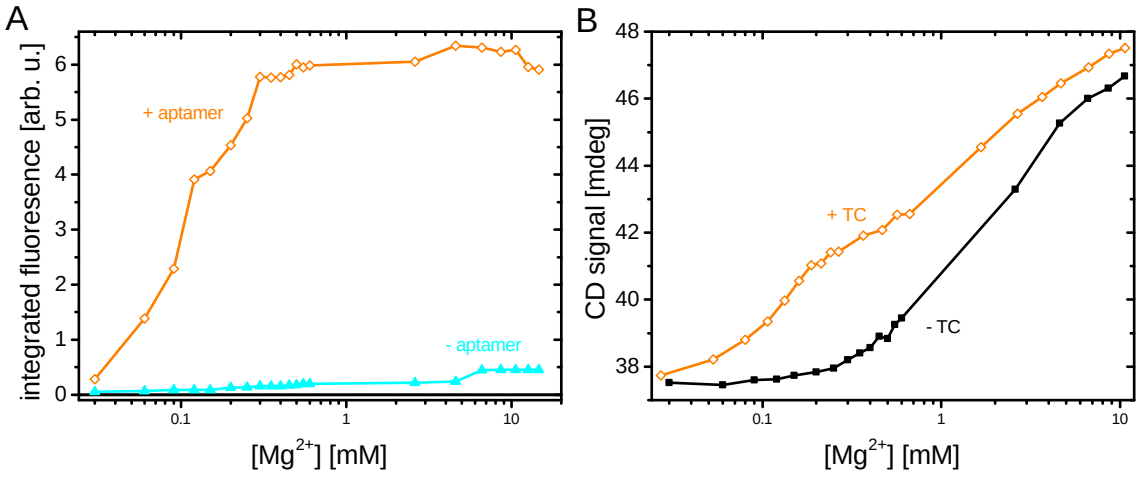

Figure 6.4: Fluorescence- and CD-monitored Mg^{2+} titrations in PBS buffer (pH 7.4). A: Fluorescence increase of 10 µM TC upon titration of Mg^{2+}. The orange curve with the open symbols is recorded in presence of 10 µM aptamer, the cyan curve is recorded without aptamer. The fluorescence signal is integrated within 20 nm around the emission maximum at 510 nm. B: CD amplitudes of the TC aptamer (10 µM) with 10 µM (orange) and without (black) ligand upon titration of Mg^{2+}. The black curve has been shifted by −2 mdeg correcting a small offset of the inital signal level to make the direct comparison of the titration curves easier.

Figure 6.4 A shows two Mg^{2+} titrations of aqueous TC solution in the presence and in the the absence of the TC aptamer. In the absence of Mg^{2+}, the total fluorescence emission is very small and rises monotonically with increasing Mg^{2+} concentration in both cases. The fluorescence increase is significantly stronger in presence of the aptamer and—more important—the increase reaches its half value at Mg^{2+} concentrations as low as $\geq$ 0.1 mM, whereas a significant fluorescence increase in the absence of aptamer occurs only at ~ 4 mM. This fluorescence jump of bare TC is due to the chelation of Mg^{2+} to TC which has a K_d around 2 mM at neutral pH.[227,235] At $[Mg^{2+}]$ = 4 mM, the concentration of chelated TC is therefore approximately 7 µM with 3 µM bare TC remaining. This implies that the quick rise in fluorescence in presence of the TC aptamer is not related to the normal chelation state of TC but must be a consequence of the interaction with the aptamer.

In figure 6.4 B, CD titrations of the TC aptamer in the presence and absence of TC are shown. Both curves rise steadily. The one with TC rises faster and to slightly higher values. From ~ 3 mM Mg^{2+} on, the two curves rise with roughly the same rates indicating an unspecific compaction of the aptamer as consequence of increased electrostatic shielding of the backbone.[76]

The sub-millimolar concentration range is more interesting because the two

curves are clearly distinct, there. The curve with TC shows its steepest increase around 0.15 mM Mg^{2+}, whereas the curve without TC does not increase significantly at less than 0.3 mM. This observation implies that TC plays an active role in compacting the aptamer at lower Mg^{2+} concentrations.

Comparing the titration curves with aptamer and ligand, which were monitored by fluorescence and CD, respectively, reveals interesting similarities but also differences. The fluorescence response occurs already at slightly lower Mg^{2+} concentrations. This is probably due to the different processes about which the two observables report: the CD signal reports exclusively on the conformational state of the aptamer, whereas the fluorescence reports on the conformational state and thus the confinement of TC itself. The fluorescence increases already strongly upon association with the aptamer[25], which implies that the aptamer must not necessarily be able to form the stable final complex with TC to cause a fluorescence increase.

Contrarily, a significant shift of the aptamers conformational equilibrium, that is necessary to strongly affect the CD signal, would be expected to require the formation of the stable complex for a significant fraction of the aptamers. The steeply increasing fluorescence signal flattens from 0.3 mM Mg^{2+} on and shows only small changes at higher Mg^{2+} concentrations. Interestingly, this is the Mg^{2+} concentration at which the bare aptamer begins to react significantly. The response of the aptamer in presence of TC begins to flatten at 0.2 mM Mg^{2+}.

In order to explore the generality of the previously presented findings, titrations in SCC buffer at pH 6.8 were performed. Figure 6.5 A displays a CD-monitored titration. In accordance with the titrations at the higher pH value, TC aids in inducing the folding transition, which appears to be shifted to even slightly smaller Mg^{2+} concentrations. Here, it is important to keep in mind that the aptamer concentration in this experiment is only 50 % of the concentration at pH 7.4. Therefore, a lower magnesium demand is expected. In absence of TC, the signal increase starts delayed and proceeds slower. From ~ 1 mM Mg^{2+} on, both traces develop very similar.

The Mg^{2+} dependent absorption change of 1.5 µM TC aptamer (figure 6.5 B) is less accessible from a purely visual inspection. This is in part due to the facts, that the traces do not superimpose at high Mg^{2+} concentrations and that the absorption continues to decrease for higher Mg^{2+} concentrations. The latter effect is to some extend an artifact of the presentation with a logarithmic [Mg^{2+}] scale. With a linear abscissa, the loss in absorptivity clearly levels out at about 1 mM Mg^{2+}.

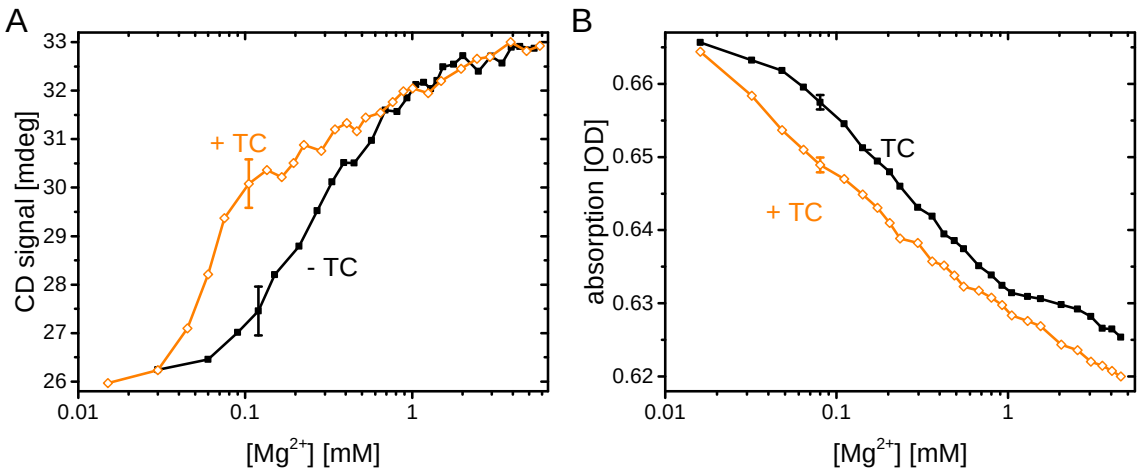

Figure 6.5: CD- and UV–absorption-monitored Mg^{2+} titrations in SCC buffer. A: CD-monitored Mg^{2+} titrations of 4.5 µM TC aptamer with (orange, empty diamonds) and without (black, solid squares) 7.5 µM TC. The titrations were performed with 1.5 µM aptamer in the presence (orange, empty diamonds) and in the absence (black, solid squares) of 7.5 µM TC. The signal without TC was shifted by −0.81 mdeg. B: Absorption around 260 nm of the TC aptamer depending on the Mg^{2+} concentration. The signal without TC was shifted by −0.024 OD. All titrations were performed in SCC buffer (pH 6.8, $[Na^+]$ = 100 mM). Error bars represent the uncertainties of the mean values of the titrations.

The two traces have been shifted along the ordinate axis such that the absorptions without any Mg^{2+} are equal. It is visible that from the first titration step on, the curve with TC lies below the curve without TC and decreases faster until $[Mg^{2+}] \geq 0.1$ mM. From about 1 mM Mg^{2+} on, the two signals decrease with comparable rates.

Further CD-monitored titrations at pH 6.8 were performed with aptamer concentrations of 1.5 and 7.5 µM ([TC] was 0 and 7.5 µM in each case). The fast signal changes at low and the slow ones at high Mg^{2+} concentrations divide each titration curve into two regimes: folding into the native structure (low $[Mg^{2+}]$) and rather unspecific electrostatic compaction of the aptamer. These two regimes were fitted with two straight lines and the intersection was used as estimation of the characteristic bulk Mg^{2+} concentration necessary to induce the folding.

Table 6.1 summarizes the results of these experiments. The trend found for the required ratios of Mg^{2+} to induce the folded structure on the aptamer is stable at approximately 4. It also shows that monitoring the aptamer absorption at 260 nm leads to the same conclusions regarding the folding processes just as the more specific CD-monitored data.

The characteristic Mg^{2+} concentrations do not scale linearly with the aptamer concentration. In part, this can be explained by the fact that rather the activity

technique	[aptamer] [μM]	$[Mg^{2+}]$ [mM] [TC] = 0 μM	$[Mg^{2+}]$ [mM] [TC] = 7.5 μM	ratio*
absorption	1.5	0.40 ± 0.10	0.11 ± 0.04	4 ± 2
CD	1.5	0.57 ± 0.07	0.13 ± 0.04	4 ± 2
CD	4.5	0.40 ± 0.08	0.08 ± 0.05	5 ± 4
CD	7.5	0.47 ± 0.07	0.13 ± 0.04	4 ± 2
average†				4.3 ± 0.5

Table 6.1: Apparent bulk Mg^{2+} concentrations needed to drive the folding and binding transition of various concentrations of the TC aptamer in the presence and the absence of the ligand at pH 6.8. *: The ratio of bulk Mg^{2+} needed without TC over the bulk Mg^{2+} with TC. †: The average and the standard deviation of the best values obtained from the four experiments shown above.

of Mg^{2+} than a direct concentration dependence is observed. Yet, the inspection of the different experimental outcomes also demonstrates a severe experimental scatter, which is reflected in the large uncertainties of the found bulk Mg^{2+} concentrations. Combining the large uncertainties with the relatively small best values obtained for the titrations with TC leads to large uncertainties in the found ratios. This demonstrates both, the principle applicability of absorptive spectroscopic techniques to monitor structural changes in the TC aptamer as well as the limits of the titration approach in terms of signal-to-noise.

Therefore, qualitative statements based on the Mg^{2+} titrations are limited to the observation that TC lowers the aptamers demand for Mg^{2+} to (20 – 25) % compared to the value without TC at pH 6.8. The qualitative observation that TC lowers the amount of Mg^{2+} necessary to induce folding and—where applicable—binding significantly is very robust and reproducible under the investigated buffer conditions.

6.3 Heat-monitored aptamer folding

ITC has become a wide spread and potent tool for investigations of the formation of complexes in solution.[236,237] Among other applications, it is routinely used in studies on protein-protein interactions[238], on drug discovery[239], and on ligand binding[240]. It has also been used to investigate protein-metal interactions[241,242] and RNA biochemistry[243]. The interaction of RNA with metal ions, however, has been assessed relatively rarely.[244]

Titrations of metal ions have several intrinsic difficulties including the necessity to titrate with highly concentrated salt solutions to reach saturation in the

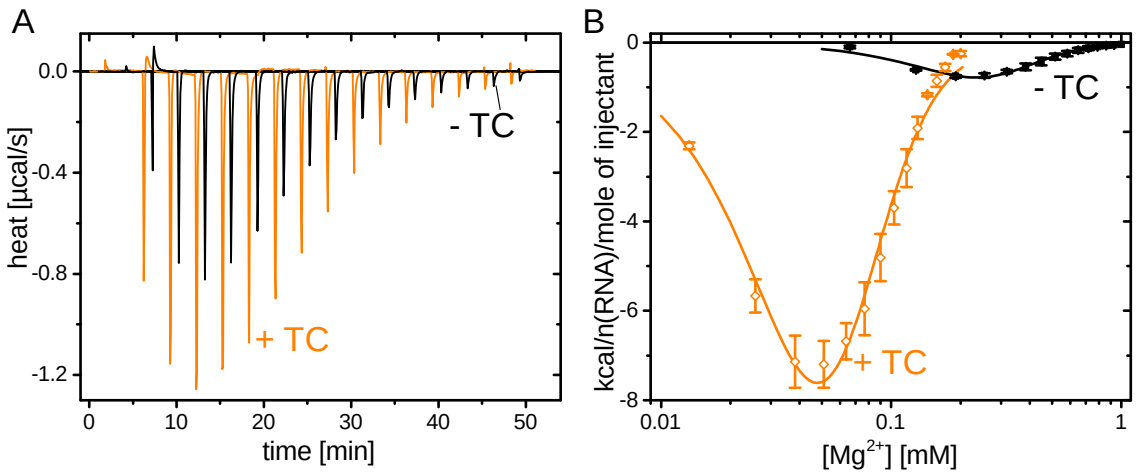

Figure 6.6: Heat-monitored Mg^{2+} titrations of the TC aptamer. A: Titrations of 15 µM TC aptamer in the presence (orange) and the absence (black, shifted by 1 minute) of 46 µM TC. B: Differential heat output calculated from the titrations with TC (open diamonds) and without (black squares). Uncertainties are derived from the deviations of two independent experiments with identical conditions. Solid lines represent fits. The experiments were performed by Marc Vogel (WG Suess, TU Darmstadt).

measurement cell.[245] This leads to large background signals originating from dilution effects, which have to be corrected carefully. In the case of the TC aptamer, the situation is additionally complicated by the direct interaction that is possible between TC and Mg^{2+} in absence of the aptamer. Figure 6.6 A presents the uncorrected raw data of the Mg^{2+} titrations of the TC aptamer. The graph shows the heat dissipation per titration step. The steps are separated by intervals of three minutes.

The final Mg^{2+} concentration of the titration with TC is 200 µM as opposed to 1 mM without TC. That also says that the concentration change per step is five times higher for the curve in the absence of TC. The heat bursts observed for the background measurements were subtracted from the shown data. Compared to the signals in the presence of the aptamer, the background signals were smaller by at least a factor of ten in both cases.

Figure 6.6 B displays the differential heat released per titration step scaled to the amount of substance of the aptamer (3 nmol) after subtraction of the background. The measured signal represents a differential heat change. The total amount of heat released at a given titration step is the integral over all previous titration steps. This is also the reason why the measured raw values of heat dissipation differ only by about 50 % (figure 6.6 A), whereas the scaled values differ by almost one order of magnitude. The error bars for measured points are calculated as the

deviation of two independent runs of each experiment. The solid lines represent fits based on the Hill model.[246] Already the raw data show unambiguously that the Hill coefficients must be significantly larger than unity because otherwise a minimum of the derivative at Mg^{2+} concentrations larger than zero would be impossible.[247]

In order to account for the fact that the Hill equation describes integral binding responses, its first derivative with respect to the Mg^{2+} concentration (here termed x) as independent variable was calculated and used for the fit:

$$\frac{\mathrm{d}H(x)}{\mathrm{d}x} = \frac{H_0 * n * k^n * x^{n-1}}{(k^n + x^n)^2} \tag{6.1}$$

H_0 is the total amount of heat released, when folding and binding saturation is reached, n is the Hill coefficient, k is the characteristic Mg^{2+} concentration of the binding process.

	H_0 [kcal/mol]	k [μM]	n
+ TC	−46 ± 4	68 ± 2	2.4 ± 0.2
- TC	−25 ± 2	340 ± 20	2.54 ± 0.14

Table 6.2: Hill parameters from the ITC-measured Mg^{2+} titrations.

Although the amplitudes of the differential heat bursts are very different, the total amounts of heat H_0 set free upon titration are relatively close to each other for both experiments (see table 6.2). The reason for this is the differing titration step sizes. In the presence of TC, the measured enthalpy reaches roughly twice the value found in its absence. This shows that the full tertiary fold of the aptamer with Mg^{2+} is energetically strongly favored in presence of TC. The surplus of heat is not due to the interaction of TC with Mg^{2+} alone because this contribution is significantly smaller in absence of the aptamer and already subtracted, anyway.

The characteristic Mg^{2+} concentrations required to drive the folding or binding reaction are lowered by a factor of 5.0 ± 0.4 in the presence of TC. This agrees reasonably well with the ratios determined in the spectroscopic titration experiments and strongly support the validity of these experiments. Interestingly, the found Hill coefficients are very similar. Attempts to fit the experimental data to integer values of n = 2 and 3 failed to result in good fits.

Here, it is not valid to interpret the found Hill coefficients as number of Mg^{2+} bound per aptamer molecule. Firstly, it is not possible to fit the data well with a

non-fractional Hill coefficient. Next, the Hill coefficient could only be interpreted in such a straightforward manner, if the binding process was strictly cooperative.[248] That says that the binding of the first Mg^{2+} causes rearrangements of the aptamer that trigger the immediate binding of one or more further Mg^{2+} ions at well-defined sites with clear stoichiometry.

For Mg^{2+}, basically three main interaction modes with the negatively charged backbone of RNA are known: (i) unspecific binding of highly diffuse ions mostly related to simple secondary structures with a multi-layer of remaining water molecules between themselves and the RNA, (ii) semi-localized ions located at negative electrostatic hotspots generated by tertiary interactions. There the ions are still surrounded by at least one monolayer of water molecules, and (iii) strongly localized and coordinated, specifically bound ions within highly charged negative pockets that are at least partially dismantled from water.[234]

Ions from category number (i) bind anticooperatively ($n < 1$) to RNA due to their mutual electrostatic repulsion.[249,250] This kind of interaction occurs primarily in the concentration regimes, where only secondary contacts are formed or a fully folded RNA is merely compacted by the addition of futher Mg^{2+}. But it cannot explain the observed cooperativity. The situation is very different for ions from category (ii). Cooperative binding of Mg^{2+} ions is observed frequently, when it is accompanied by the emergence of additional tertiary interactions.[232,251,252] Ions of category (iii) are unlikely to be involved, because the only Mg^{2+} forming direct contact to a molecule other than water is the chelated Mg^{2+} bound to TC, but it is not directly contacting the aptamer.[212]

Therefore, the Hill coefficient can only be used as an estimate for the minimal number of Mg^{2+} bound per aptamer: in this case, that is three.

6.4 Spectroscopically monitored melting profiles

In this section, the Mg^{2+} dependence of the TC aptamer in its free and complexed form will be assessed by thermal denaturation and renaturation profiles (section 6.4.1). In section 6.4.2, the thermodynamic analysis of the melting profiles will be presented and in section 6.4.3, urea will be used as denaturant at saturating Mg^{2+} concentrations to investigate the influence of a folding barrier on the stability of the aptamer tertiary structure and the complex formation.

6.4.1 Mg^{2+} dependent melting profiles

The Mg^{2+} titrations presented in the previous sections demonstrate that absorption measurements at 260 nm are suited to follow conformational rearrangements of the TC aptamer and that the presence of TC affects the interaction of the TC aptamer with Mg^{2+}. In order to quantify the effects of both, Mg^{2+} and TC, and their mutual interdependence on the stability of the aptamer, a series of UV-monitored melting profiles were recorded. The term 'melting profile' refers here to the average of one thermal denaturation followed by one thermal renaturation profile that were recorded immediately after each other on the identical sample.

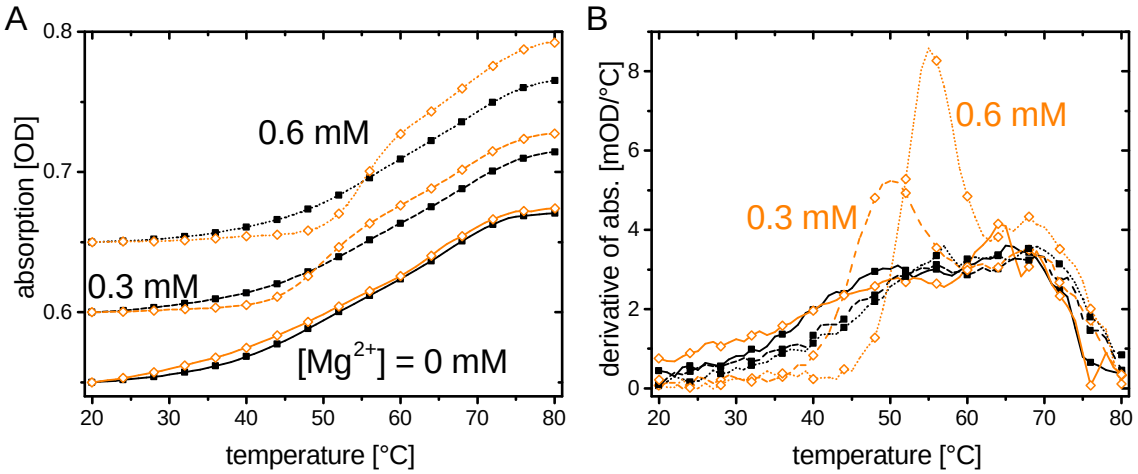

Figure 6.7: Mg^{2+} dependent UV-absorption melting profiles of the TC aptamer in SCC buffer (pH 6.8, $[Na^+]$ = 100 mM). A: 1.5 µM TC aptamer in absence (black, filled squares) and presence of 7.5 µM TC (orange, open diamonds) with three different concentrations of Mg^{2+}. The pairs of melting profiles at 0.0 (solid line), 0.3 (dashed) and 0.6 mM Mg^{2+} (dotted) are shifted to starting ODs of 0.55, 0.60 and 0.65, respectively. B: First derivatives of the melting profiles of part A with identical encoding of the different curves.

In absence of any Mg^{2+}, TC has little influence on the absorption signal except for a slightly shallower course with TC around 40 °C (see figure 6.7 A). From 50 °C on, the profiles run parallel. The large similarity of the two profiles is readily understandable considering the fact that the aptamer cannot interact specifically with TC in absence of Mg^{2+}. With 0.3 mM Mg^{2+} in the buffer, the melting profile with TC remains below the one without TC at low temperatures and rises rapidly at 45 °C. At 50 °C, it crosses the profile recorded in the absence of TC and stays then above it. From about 60 °C on, the profiles are vertically shifted, but run in parallel. At $[Mg^{2+}]$ = 0.6 mM the same systematic pattern shows up as seen for 0.3 mM, but the rapid increase of the graph with TC begins not before 50 °C and the profiles cross at 55 °C.

Melting profiles, which are not shown in this section, are shown in the figures C.1 and C.2 in appendix C. From Mg^{2+} concentrations of at least 0.2 mM on, the profiles with TC show two characteristic main features: (i) a stable low-temperature region without absorption increase followed by (ii) a transition region with a rapidly rising absorption that shifts to higher temperatures with increasing Mg^{2+} concentration. The temperature shift of the transition region can be seen in the first derivatives of the melting profiles as depicted in figure 6.7 B.

The profiles without TC also show the tendency to shift their transition midpoint to higher temperatures with the Mg^{2+} content, but this shift is much weaker than the changes observed with TC. At temperatures beyond the transition point, the melting profiles without TC are similar to those with TC although they may be vertically shifted. The larger signal changes in presence of TC may be indicative of a slightly more compact starting conformation of the TC aptamer.

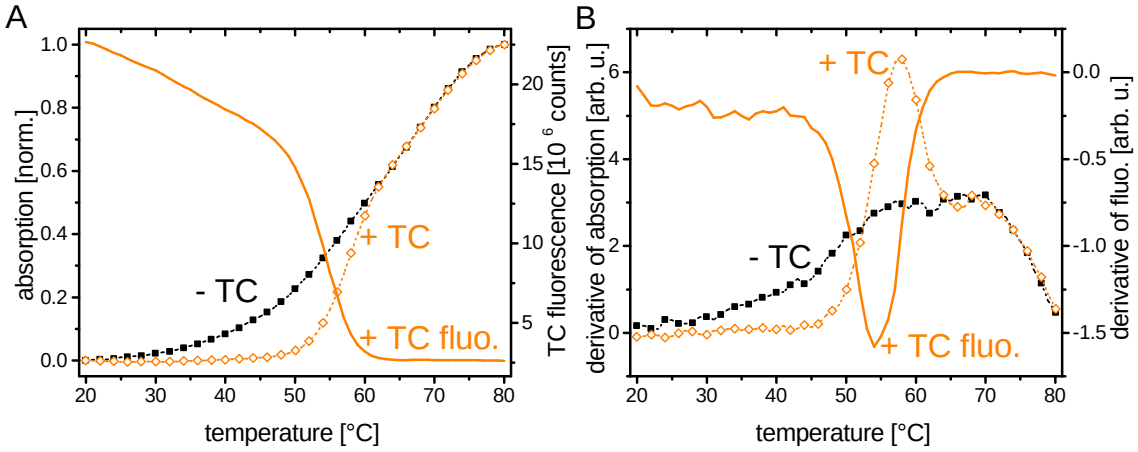

Figure 6.8: Absorption- and fluorescence-monitored melting profiles of the TC aptamer in SCC buffer at 0.8 mM Mg^{2+} (pH 6.8, $[Na^+]$ = 100 mM). A: Fluorescence-monitored melting profile of the TC aptamer (1.5 µM) is shown without symbols. Melting profiles with 7.5 µM TC are represented in orange (absorption with open diamonds) and without TC in black (filled squares). B: First derivatives of the melting profiles.

The insensitivity of the absorption at low temperatures in the presence of TC is believed to be caused by the complexation of TC with its aptamer. This assignment is based on the temperature regime in which it occurs. The complex is expected to be present at low temperatures rather than at high ones. The observed tendency of this regime to extend to higher temperatures with increasing Mg^{2+} concentrations also supports the assignment. In order to verify this, fluorescence-monitored melting profiles with 0.8 mM Mg^{2+} were performed and compared to the corresponding absorption-monitored experiments.

Figure 6.8 A presents the results of these melting experiments. The absorption-monitored profiles show the typical behavior described above. The two profiles are normalized to values between 0 and 1. Therefore, the profile with TC does not cross the one without TC. The fluorescence emission is not normalized and decreases from 20 to 80 °C by one order of magnitude. The fluorescence of TC reports on the complexation state of the ligand with the aptamer. This refers to both, the fully formed complex and labile encounter complexes.[25]

The fluorescence profile exhibits a linear emission decrease from 20 to 45 °C with increasing temperature. This is likely due to increased solvent-induced collision quenching. Then, the profile follows a well-defined two-state transition around 55 °C. At temperatures higher than 65 °C, the emission of TC is in total low and very insensitive to temperature changes. This low emission level and the relative temperature insensitivity is also observed for bare TC in buffer (see figure C.3 in the appendix C). Accordingly, the high-temperature regime is assigned to the emission of unbound TC, whereas the low-temperature regime is associated with emission from complexed TC. At high temperatures, the absorption profiles represent the melting behavior of the bare TC aptamer regardless whether there is TC present or not because the complex is dissociated. Finally, the transition region in the emission profiles reports on the complex dissociation.

The complex dissociation appears to correspond well to the steep transition in the absorption profile with TC. The comparison is even easier based on the derivatives in figure 6.8 B. The minimum in the fluorescence profile is 4 °C lower than the maximum of the corresponding absorption profile, which may be due to several different effects: (i) the extremum in the derivative of a melting profile depends on the shape of the base line[253] and the base lines are obviously different. (ii) The absorption profile is not a simple two state transition, but rather appears to be a coupled transition between at least three states. This can also strongly affect the position of the extremum. (iii) It is possible that the true melting points (which one would see if (i) and (ii) could be excluded or corrected) are slightly different due to the fact that the observed signals are closely related to each other, but not identical: dissociation and unfolding after dissociation do not necessarily have to occur simultaneously.

So far, it is not yet clear, whether the characteristic response of the melting profiles in presence of TC to increasing amounts of Mg^{2+} is unique for the strong and specific interaction of the aptamer and its ligand, or whether it is a consequence of some non-specific interaction and thus not informative with respect to

the conformational state of the aptamer. To exclude such a possibility, several control experiments were performed.

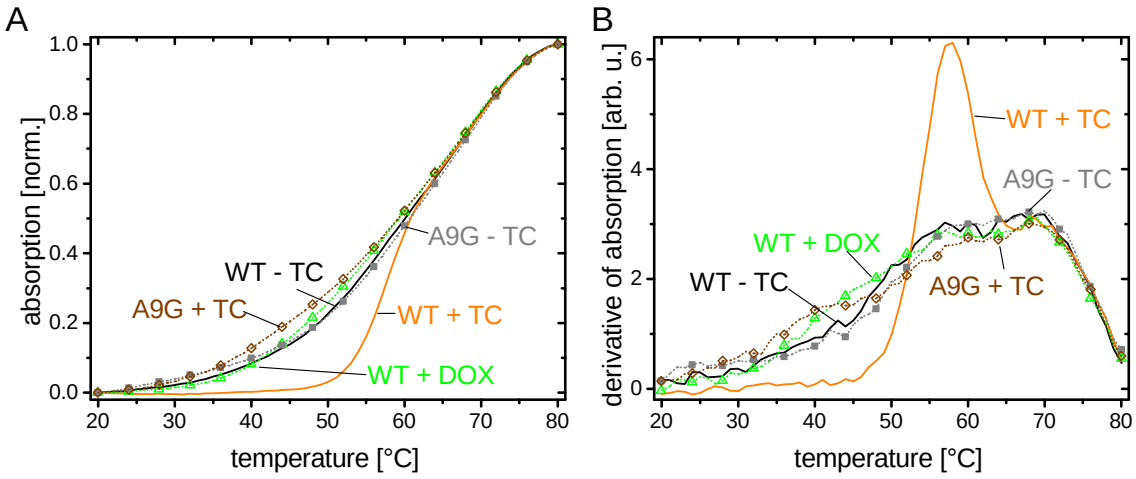

Figure 6.9: Melting profiles with the mutant A9G and DOX in SCC buffer with 0.8 mM Mg^{2+}. A: Normalized, absorption-monitored melting profiles of the TC aptamer (WT) with TC (orange solid line), without TC (black solid line), and with 7.5 µM DOX (green open triangles, dotted line) along with those of 1.5 µM of the A9G mutant in the absence (gray filled squares, dotted line) and the presence (brown open diamonds, dotted line) of TC. B: Derivatives of curves from A.

Figure 6.9 A presents the results of these control experiments. One set of control experiments employs the structural similarity of TC and DOX, where DOX cannot form the stable final complex because it lacks the $R_{6\beta}$-hydroxy group. A second set of experiments employs the A9G mutant, which cannot adopt the stable preformed conformation. Therefore, the complex formation with TC is only transiently. The melting profiles of the WT are shown for comparison.

It is obvious that all control profiles differ significantly from the WT with TC, which demonstrates the special properties of this complex. There are some small differences between the control profiles themselves and also to the WT without TC. The differences are better visible in the derivatives in figure 6.9 B. Those differences appear to be neither systematic, nor do they reproduce the tendency of a stabilized low-temperature regime in presence of ligand (namely A9G with TC and the WT with DOX). Thus the control experiments clearly demonstrate that both, an intact tertiary structure of the aptamer and a ligand capable of specific interaction are necessary to generate the characteristic melting profile of the completely formed complex.

To summarize this section, absorption-monitored melting profiles are found to be a valuable tool to follow unfolding and complex-dissociation processes of the TC aptamer with a high signal-to-noise ratio. This explicitly includes a specific

signature of the complex dissociation despite the fact that the UV absorption of the aptamer is not site specific.

6.4.2 Thermodynamic analysis of the absorption-monitored melting profiles

For a quantitative evaluation of the melting profiles with respect to the stability of the tertiary-structure of the TC aptamer, a Van't-Hoff-evaluation scheme[253] is employed. The general idea is to calculate the fraction of folded or complexed aptamer $f(T)$ depending on the temperature and the Mg^{2+} content. From f, the equilibrium constant of folding K_f can be calculated via

$$K_f = \frac{f}{1-f} \tag{6.2}$$

The relation

$$-RT \cdot \ln\Big(K_f(T)\Big) = \Delta G(T) = \Delta H^o - T \cdot \Delta S^o \tag{6.3}$$

then allows to retrieve the changes of the standard folding enthalpy ΔH^o and entropy ΔS^o as linear fit parameters and to calculate the apparent standard folding energy ΔG^o_a as

$$\Delta G^o = \Delta H^o - T^o \cdot \Delta S^o \tag{6.4}$$

with $T^o = 298\,K$.

The approach is both, powerful and robust. Still, there are several pitfalls that need to be considered, particularly for the melting profiles of the TC aptamer with ligand. (i) The calculation of f from the melting profiles requires base lines to be fitted properly. In the presence of significant amounts of Mg^{2+}, the melting point is shifted to higher temperatures. At the same time, Mg^{2+} catalyzes the self cleavage of RNA, especially at high temperatures.[254,255] Therefore, heating the sample beyond 80 °C caused excessive sample degradation resulting in a loss of the characteristic binding behavior of the TC aptamer at renaturation. This limits the maximum temperature to 80 °C, making it relatively difficult to adjust the upper base line. This can be accounted for by carefully and systematically testing

the influence of base-line variations. The size of the uncertainty related to these effects turned out to be comparable to the overall experimental uncertainty. (ii) The Van't-Hoff-evaluation is strictly applicable only to pure two-state transitions, which is not the case for the measurements with TC. (iii) The evaluation described in the equations 6.2 – 6.4 is derived for the conformational transitions of single molecules and not for bi-molecular reactions as is the case for the ligand-aptamer complex.

The last two points affect only the evaluation of the melting profiles with TC. The deviation caused by point (iii) under the conditions of the performed experiments is estimated to be smaller than 1.5 %, which is within the experimental uncertainty. Additionally, the model of a bi-molecular reaction is also only valid in solutions with sufficient Mg^{2+} content to enable effective binding. So, strictly speaking, one would have to change the evaluation model at an arbitrary Mg^{2+} concentration from which on the reaction is believed to be bi-molecular. To avoid this, the uni-molecular model is applied to all melting profiles. Point (ii) represents the more important difficulty because it can neither be circumvented, nor can its impact be estimated in a straightforward manner. Fortunately, the validity of the melting profiles with a non-two-state behavior can be checked by comparing them to the fluorescence-monitored melting profiles, that resemble a two-state system reasonably well. Nevertheless, it is important to note that the fit parameters found for the experiments with TC are only estimates of the true values and should be understood as apparent energies, enthalpies and entropies.

From the fluorescence profile and the two base lines that are depicted in figure 6.10 A, the fraction of folded aptamers f is calculated. The melting temperature T_m is the temperature, where f equals 0.5. The figure illustrates the impact of base line corrections as opposed to mere normalization. In figure 6.10 B, the f values calculated from the absorption-monitored profiles are presented and compared to the one based on the fluorescence experiment. The profile without TC shows broad melting between 30 and 70 °C. It differs significantly from the f curves calculated from melting profiles in the presence of TC. There, f remains one up to 45 °C and then drops rapidly. The fluorescence-based curve differs in two respects from the absorption-based one: firstly, the transition midpoint (the melting temperature) is shifted to higher temperatures by 4 °C. The offset is already visible in the melting profiles (compare with figure 6.8 B). Secondly, the absorption-based f has a shoulder at 63 °C, whereas the fluorescence-based one shows a clear two-state transition.

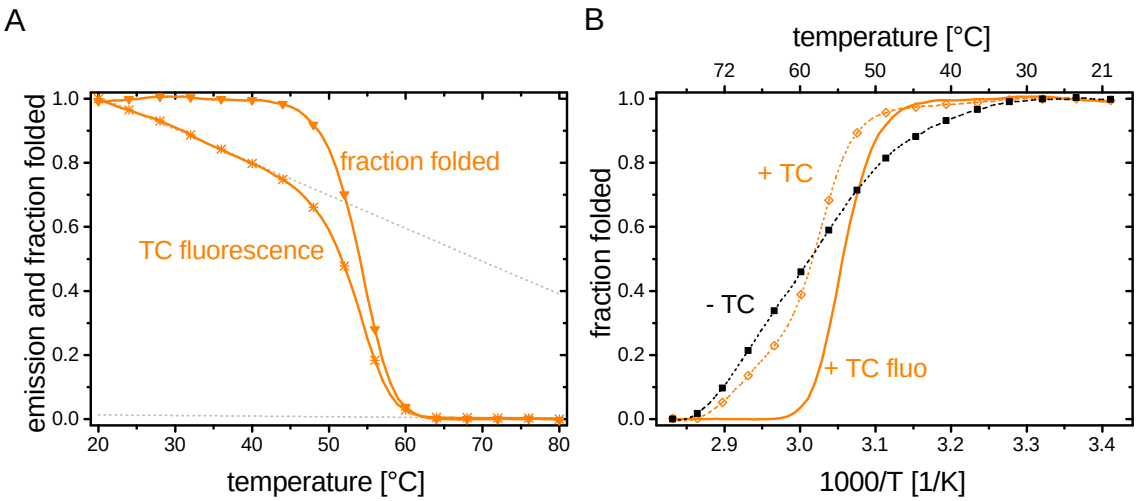

Figure 6.10: Comparative analysis of melting profiles of the TC aptamer with 0.8 mM Mg^{2+}. A: Normalized TC emission (orange, solid line with asterisks) with upper and lower base lines (gray, dashed lines) and f (orange, solid line with triangles). B: f calculated from the absorption profiles (dashed lines with symbols, absence of TC indicated by black, filled squares) and from the fluorescence profile (orange, solid line).

Potential reasons for the temperature offset were already discussed above. At this point, it is important to quantify the impact of the differences on the energetics. Table 6.3 gives the characteristic values retrieved from the f curves presented above according to the equations 6.2 – 6.4.

	ΔH^o [kcal/mol]	ΔS^o [cal/mol/K]	ΔG^o_a [kcal/mol]
− TC, absorption	−29.5 ± 0.3	−89.0 ± 0.8	−3.0 ± 0.4
+ TC, absorption	−73.0 ± 1.0	−220 ± 3	−7.4 ± 1.4
TC fluo.	−92.5 ± 0.3	−283 ± 3	−8.2 ± 1.2

Table 6.3: Thermodynamic parameters from melting profiles in SCC-buffer with 0.8 mM Mg^{2+}.

The differences between the enthalpies and entropies of the two profiles with Mg^{2+} amount up to 20 %. This is remarkable because the calculated apparent standard folding energies ΔG^o_a agree with each other. A likely reason for this is the well-known entropy-enthalpy compensation.[256,257] It describes the commonly encountered phenomenon of the two quantities showing a strong correlation, which means that an increase in one quantity is counteracted by an increase in the other. Because the ΔG^o is calculated as the difference of the enthalpic and the entropic contribution, the compensation leads to robust results for ΔG^o.

Therefore, the discussion of the effects of the Mg^{2+} concentration on the stability of the aptamer will focus on the apparent standard energy ΔG^o_a, which is anyway a better measure for the effective stability of the structure, than the enthalpies and

entropies. Discussions of the latter two will be limited to the following aspects: the ΔH^o values in the absence of TC change little from 0 to 2 mM $MgCl_2$. They rise slowly from approximately 25 to 30 kcal/mol. In the presence of TC, ΔH^o varies from 23 to almost 80 kcal/mol with a very strong increase from about 0.2 mM Mg^{2+} on. ΔS^o mirrors that behavior with roughly 80 cal/mol/K in the absence of TC or at Mg^{2+} concentrations below 0.2 mM and a fast rise with TC at higher Mg^{2+} concentrations to more than 200 cal/mol/K.

The ΔG^o_a values of the control experiments described in the previous section are (2.4±0.5) kcal/mol for the WT with DOX and (2.3±0.5) kcal/mol for the A9G mutant with TC. The evaluation of the mutant without TC gives ΔG^o_a = (3.6±0.5) kcal/mol. These values are in accordance with the folding free energy found for the bare WT (see table 6.3). Noteworthy, all values of ΔG^o_a found in the presence of a ligand when the binding to the aptamer is severely impeded are smaller than those values found in absence of any ligand. Here, it is not important, whether the WT or the mutant is considered and also, whether the binding is impeded due to the added ligand, the Mg^{2+} content, or a mutation of the aptamer itself.

For $[Mg^{2+}] \geq 0.2$ mM, TC tends to stabilize the structure of the aptamer, a trend that becomes significant at 0.3 mM (see figure 6.11). Without any Mg^{2+}, TC has no impact on the stability of the aptamer.

At 0.1 mM Mg^{2+}, the stability appears to be inverted. There, a very complex mixture of conformational states is likely to be present: as there is some Mg^{2+} present, the aptamer can in principle fold to compact tertiary structures, but the concentration is too low for the correctly folded structure to dominate in quantity. This complexity may explain the apparent inversion. The dynamic nature of the conformational equilibrium implies that either the on-rate of the reaction is small or the off-rate is large compared to the situation with higher Mg^{2+} concentrations, or both rates are affected at the same time.

The titrations in section 6.2.1 show that 0.1 mM Mg^{2+} is sufficient to induce a 50 % fluorescence increase. With the results of Förster et al.,[25] the observations can be consolidated in such a way that the aptamer can recognize the ligand (causing the 50 % emission increase), but cannot yet form a long-time stable complex. This implies that an increased off-rate is the more likely explanation. Additionally, it is possible that the TC–Mg^{2+}-chelate complexes, which are expected to be present as minor fraction, interact with the aptamer in a non-specific way through stacking favored by electrostatic attraction. This kind of interaction should rather destabilize the aptamer structure.

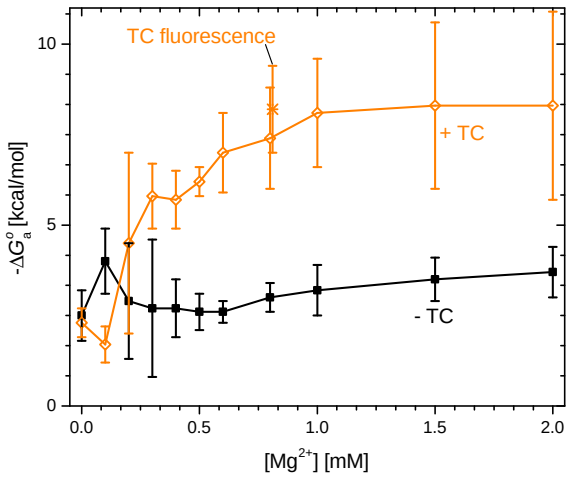

Figure 6.11: ΔG^o_a calculated from the melting profiles. UV-observed melting behavior is represented by filled black squares in the absence and open orange diamonds in the presence of TC. The orange asterisk represents the fluorescence-monitored melting profile at 0.8 mM Mg^{2+} (point is shifted by +10 µM).

Around 0.2 to 0.3 mM Mg^{2+}, the aptamer becomes capable of forming a stable complex with a probability and thermal stability that makes it clearly observable within the experimental uncertainty. The stabilization of the tertiary structure in presence of TC rises gradually up to 1 mM Mg^{2+}, where ΔG^o_a saturates. ΔH^o and ΔS^o rise significantly faster, but the increase of ΔH^o is slightly over-proportional compared to the one of ΔS^o. This is why ΔG^o_a rises slowly. In the absence of TC, ΔG^o_a is by far less sensitive to Mg^{2+}, although it tends to rise, as well.

Accordingly, TC influences the conformational equilibrium of its aptamer most strongly at Mg^{2+} concentrations between 0.2 and 1 mM. In this Mg^{2+} regime, TC causes a shift of the conformational equilibrium of the TC aptamer towards and a significant thermodynamic stabilization of the fully folded conformation by complex formation.

6.4.3 Urea dependent aptamer melting

Additionally to Mg^{2+} dependent melting profiles, urea dependent experiments were performed (figure 6.12). Urea is a well-established denaturant for nucleic acids[232,258] with the potential to assist in thermodynamic analysis[259]. Urea competes with water molecules in the hydration shell of the investigated macromolecule and disturbs its native conformation.[260]

Three pairs of absorption-monitored profiles in the absence and the presence of TC are presented in figure 6.12 A. The urea concentrations vary between 0 and

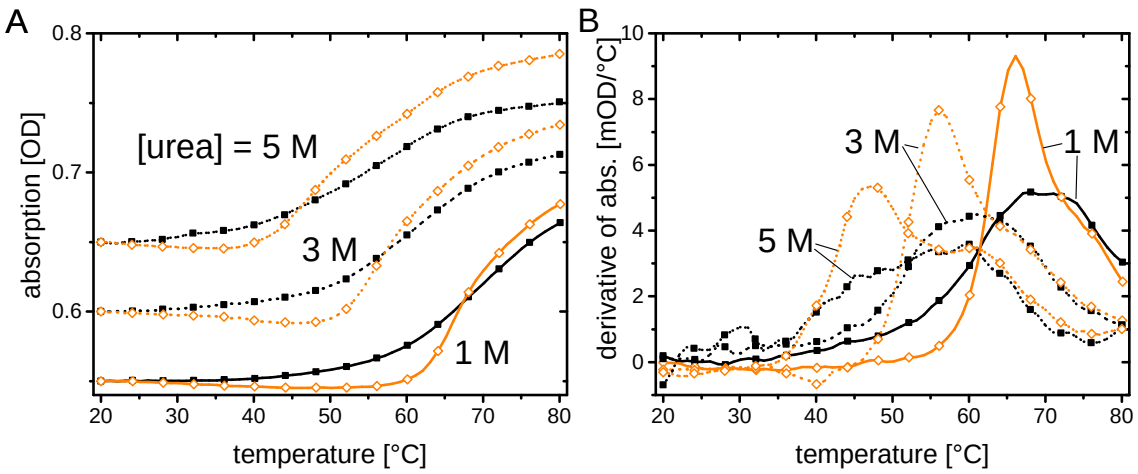

Figure 6.12: Urea dependent UV–absorption-melting profiles of the TC aptamer in SCC buffer. A: 1.5 µM TC aptamer in the presence of 7.5 µM (open orange diamonds) and in the absence of TC (full black squares). The starting values of the melting profiles in presence of 1 M (solid lines), 3 M, (dashed) and 5 M urea (dotted) are shifted to 0.55, 0.60, and 0.65 OD, respectively. All experiments were performed with 5 mM Mg^{2+} and 100 mM Na^{+}. B: First derivatives of the profiles from part A with identical encoding.

5 mM. Figure 6.12 B shows the first derivatives of the melting profiles. The profiles share the overall characteristics of the Mg^{2+} dependent profiles. The changes of the amplitudes are larger for the profiles with TC and are significantly steeper around T_{m}, while there is an insensitive low-temperature range. T_m decreases with increasing urea content.

Interestingly, the melting profiles with TC tend to decrease at low temperatures with higher urea concentrations. This may be explained by the following mechanism: When RNA unfolds, its SASA increases and urea can interact more easily with the aptamer. In the competition between water and urea, urea molecules will associate and dissociate from the RNA with a certain likelihood. This process is governed by a dynamic equilibrium. Both, the on-rate of the RNA-urea interaction and its off-rate are expected to increase with temperature. Previously, urea was demonstrated to destabilize mainly the tertiary structure of nucleic acids.[261] If the tertiary structure of the aptamer is prevented from unfolding by TC, it will not increase its surface area and thus the on-rate will change little (except for an increased probability to form short-lived encounter complexes). Consequently, in a temperature regime, in which the complex is intact, the urea-off-rate would increase faster than the on-rate. This shifts the equilibrium to the bound form.

However, the exact nature of the interaction of oligonucleotides with urea is still a subject of ongoing debate.[261–263] Therefore, the abovementioned explanation

is necessarily speculative. In support of the proposed mechanism, there are single-molecule studies, where the folding and unfolding rates of RNA pseudoknots were found to depend in a distinct manner on the urea concentration.[258]

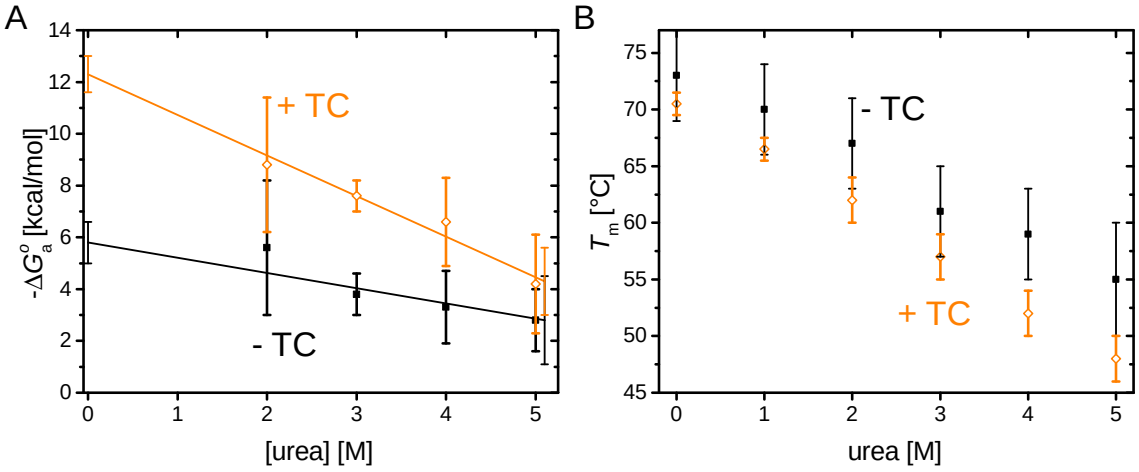

Figure 6.13: Evaluation of urea dependent melting profiles of the TC aptamer. A: ΔG^o_a values in the presence (open, orange diamonds) of 7.5 µM and in the absence of any TC (full, black squares). Straight lines represent fits, error bars without symbols at the ends of the lines are derived from the uncertainties of the fits. B: T_m values estimated from the maxima of the first derivatives of the melting profiles.

The results of a Van't-Hoff analysis of the urea dependent melting profiles are presented in figure 6.13 A and B. The analysis as it is described in section 6.4.2 was not possible for the profiles with less than 2 mM urea because the T_m values are too high to determine reasonable upper base lines. Still, four urea concentrations could be evaluated with and without TC. They were fitted to the linear model

$$\Delta G^o_a\big([\text{urea}]\big) = \Delta G^o_0 - m \cdot [\text{urea}], \tag{6.5}$$

where m is the so-called m value and ΔG^o_0 is the apparent folding-free energy retrieved from extrapolating to zero denaturant. The m value in the presence of TC is (1.6 ± 0.4) kcal/mol/M and differs significantly from the one found in the absence of TC, which is (0.6 ± 0.5) kcal/mol/M.[xvii]

The m value of an unfolding transition is closely correlated with the change of the solvent-accessible surface area ΔSASA between the folded and the unfolded state, especially for proteins.[266] The correlation is not as good established for RNA, mainly because it is difficult to determine ΔSASA correctly.[259,262] This might be

[xvii] m values around 0.5 to 2 kcal/mol/M are common (see for example references [233,264,265]).

simplified by using thermal denaturation to estimate the *m* value because denaturation should lead to almost complete unfolding, whereas a Mg^{2+} titration in presence of some 100 mM monovalent cations usually starts from an already collapsed intermediate structure, rather than from an unfolded one.[77] Additionally, the *m* value of RNA is strongly salt dependent.[262] The *m* value can change for example from 0.4 to 1.7 kcal/mol/M depending on whether the ions in solution are mono- or divalent.[267]

The *m* value of the TC aptamer with TC is relatively large given the fact, that it is only a 57mer. Large *m* values are usually expected for large biomolecules due to the proportionality to the surface area. The differences observed for the TC aptamer could be interpreted in such a way that ΔSASA is more than two times larger in presence of TC. From the crystal structure 3EGZ[212], the SASA of the complex is estimated to be $(8\,900 \pm 500)$ Å^2.[xviii] The relatively large uncertainty is due to the fact that the sequence of the crystallized construct deviates from the used construct.

Estimating the unfolded structure with the identical method leads to 13 200 Å^2 with the unfolded aptamer taken to be a ss A-form helix and to 27 900 Å^2 by adding up the SASA values of all 57 isolated nucleotides of the aptamer. The first area will underestimate the true SASA because at high temperatures, the nucleobases will unstack. The latter value overestimates the unfolded SASA. From the crystal structure[212], it is also known that 425 Å^2 of the ligand are covered by RNA. Therefore, the ΔSASA with TC is between 4 300 and 19 000 Å^2. Taking into account a slightly more open conformation of the aptamer in the absence of ligand as indicated by EPR-measurements[24], this will not account for more than 20 % change in the SASA of the fully preformed aptamer in the absence of TC compared to its presence. Thus, the ΔSASA expected should be between 40 (50, if one includes the 500 Å^2 error margin) and < 10 %. Thus, the observed differences of the *m* values of > 60 % cannot be explained in terms of the ΔSASA, alone.

Consequently, the closer bound and denser Mg^{2+} atmosphere around the complexed aptamer is proposed to be responsible for the remaining 20 to 50 % difference in the observed *m* values.

[xviii] The estimate was derived with Discovery Studio 3.5. A critical radius around a residue of 1.4 Å and 240 grid points per residue were used.

6.5 Discussion

A series of spectroscopy and heat-monitored titrations and thermal denaturation experiments was performed. The aim was to unravel the influence of Mg^{2+} on the conformational state of the TC aptamer and the role of its ligand TC. This was complemented by experiments using urea to impair folding and binding. In the current section, the results will be related to each other and a model will be developed that summarizes and explains the findings in view of its physiological relevance.

Fluorescence-, absorption-, and CD-monitored Mg^{2+} titrations, find TC to significantly affect the response of the TC aptamer to Mg^{2+}. As consequence, the apparent bulk Mg^{2+} concentrations necessary to induce the folding transition of the aptamer to its fully-folded state is approximately four times lower in presence of TC. At slightly higher aptamer concentrations, this ratio is found to be five when using ITC. The values agree well with each other considering the relatively large uncertainty of the spectroscopically monitored titrations, the fact that the observables are of a different nature, and the differing aptamer concentrations. The last point is relevant because the titrations actually monitor the activity of Mg^{2+}, which is expected to depend on the RNA concentration. The found ratios reflect TC-induced activity differences of Mg^{2+}. ITC demonstrates that the binding enthalpy of the aptamer to Mg^2 is roughly doubled when TC is present.

Spectroscopically monitored melting curves of the TC aptamer allow to identify a characteristic signature indicative of and unique for the temperature-induced dissociation of the ligand-aptamer complex. Analysis of the melting profiles leads to a quantitative estimate of the thermodynamic stability of the complexed and bare TC aptamer in the presence of a variety of Mg^{2+} concentrations. Three concentration regimes for Mg^{2+} can be distinguished with qualitatively different impacts of TC on the conformational state of its aptamer. TC affects the stability of the tertiary structure of the aptamer most strongly between 0.2 and 1 mM Mg^{2+} with virtually no interaction present at lower concentrations and comparatively little additional stabilization at higher concentrations.

The use of urea as denaturant in presence of sufficient amounts of Mg^{2+} to preform the aptamer in absence of TC leads to two sets of urea dependent ΔG^o_a values and allows to calculate m values in the presence and absence of TC. In the presence of TC, it is found to be significantly larger than in its absence. The observed differences are too large to be understandable solely by the ΔSASA. The

remaining differences are interpreted as consequence of distinct salt contents in the solvation shell of the TC aptamer in the presence and the absence of TC.

The melting profiles indicate a stabilization of the complex as compared to the bare aptamer by the steepness of the melting transition.[268] The steepness implies a cooperative melting behavior in presence of TC and is directly related to the entropy of the transition. The melting in absence of TC also becomes slightly more cooperative, but the effect is by far less pronounced. The appearance of the steep melting transition in its dependence of the Mg^{2+} concentration coincides well with the transition point of the aptamer-complex dissociation found in the titration experiments, where it is between 0.1 and 0.2 mM. The 68 µM found in the ITC are a half-value, and must be doubled when one considers saturation of the binding transition. Accordingly, the characteristic complex-melting transition can only be observed clearly, when the binding transition is completely saturated.

The increased cooperativity is interpreted in such a way that the complex requires both, the tertiary and the secondary structure to be intact, which is why the structures cannot melt before the complex dissociates. In the bare aptamer, the tertiary and the secondary structure are expected to melt independently. This also implies that distant parts of the secondary structure can melt at different temperatures. Therefore, the melting profiles extend over a broad temperature range.

The increased ΔS^o in presence of TC is interesting in several respects: (i) the stable complex is according to Förster et al. very long-lived.[25] Therefore, thermal fluctuations of large portions of the aptamer must be strongly suppressed in presence of TC. (ii) It is very likely that this includes fluctuations of at least some of the salt ions involved in tertiary structure formation and also for water molecules, particularly those involved in ligand binding. (iii) The interaction with TC as additional factor is expected to increase the entropy. (iv) The increased entropy explains why the melting temperatures are hardly affected by the presence of TC—actually, they are lower in presence of ligand—and why the complex is at the same time thermodynamically more stable at temperatures below the melting point with ligand than without.

The fluorescence-monitored titrations indicate an interaction between aptamer and ligand at slightly lower Mg^{2+} concentrations. There, the interaction is believed to originate from transiently formed encounter complexes that lack the remarkable long-term stability of the fully formed complex.

One possibility to check the accuracy of the ΔG^o_a values in the presence of TC derived from the melting curves, is to compare them to values derived from measuring the K_d of the ligand-aptamer complex at different Mg^{2+} concentrations. They can be measured with fluorescence-monitored aptamer titrations.[22] For 0.3 and 0.8 mM Mg^{2+}, K_d values of (29 ± 4) and (2.0 ± 0.2) nM were found, respectively.[17] For comparison, at 10 mM, a value of (0.77 ± 0.11) nM was previously found.[22] The K_d of the TC aptamer is found to increase almost by a factor of forty between 0.3 and 10 mM. From the K_d values, the difference of the binding-free energies $\Delta\Delta G^o$ from 0.3 to 0.8 mM can be calculated according to $\Delta\Delta G^o = \Delta G^o_{0.3} - \Delta G^o_{0.8} = -RT^o \cdot \ln(K_{d,\,0.8}/K_{d,\,0.3})$ ($T^o = 298$ K).[234] The calculation yields $\Delta\Delta G^o = (1.58 \pm 0.11)$ kcal/mol, which agrees well with the value calculated from the melting profiles: (1.6 ± 1.7) kcal/mol.

The found ΔG^o_a values lead to the conclusion that TC causes the TC aptamer to adopt the fully formed tertiary structure with a likelihood that is between two and three orders of magnitude higher than in the absence of TC. The exact difference of the probabilities is dependent on the bulk Mg^{2+} concentration as the K_d varies significantly in the sub-mM Mg^{2+}-concentration range.

Between 0.2 and 1 mM Mg^{2+}, the aptamer reacts strongly to the presence of its ligand. Remarkably, the concentration of unbound Mg^{2+} is established to coincide with this range in many eukaryotes (see [269–272] and literature therein). Additionally, RNA folding has been observed to react to other non-specific cosolutes and crowders most strongly in the physiological regime.[273] Divalent cations are generally accepted to play an indispensable role in RNA compaction and folding. This is particularly true for Mg^{2+} because it is the physiologically relevant divalent cation and it is the one with the highest charge density due to its small radius.[250,274] The main reason for the impact of Mg^{2+} is the strongly favorable electrostatic attraction to the negatively charged backbone of RNA.[81] Due to its high positive charge density, Mg^{2+} is ideal for screening the negative charges of the backbone, allowing the RNA to access unique tertiary folds. As consequence, the local Mg^{2+} density in solution is higher in proximity of RNA molecules than in bulk solution causing a Mg^{2+}-concentration gradient.[76]

In the context of the TC aptamer, this says that TC enforces the recruitment of Mg^{2+} from the bulk at much lower overall concentrations than it would be possible without TC. The recruitment occurs in spite of a significantly larger concentration gradient towards the bulk. Consequently, TC forces its aptamer into the native structure in the presence of a minimal amount of Mg^{2+} creating negatively charged

hotspots in the tertiary structure of the aptamer. These hotspots in turn attract more Mg^{2+} to stabilize the folded structure.[76]

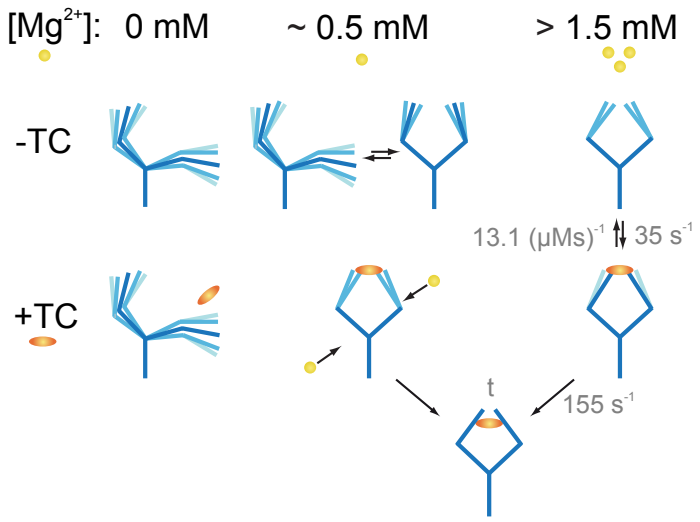

Figure 6.14: Model of the interaction pattern of TC, the TC aptamer, and magnesium including previously established and newly found information. The reaction rates are taken from.[25]

Figure 6.14 represents the interaction modes of the TC aptamer with its ligand in different Mg^{2+} regimes. As first relevant finding, it is important to note that it is not sufficient to consider only how Mg^{2+} affects the interaction between ligand and aptamer. It is equally important to consider how the ligand affects the interaction between Mg^{2+} and the aptamer, and how the presence of the aptamer affects the interaction of TC with Mg^{2+}, too.

In total, three main interaction regimes can be identified depending on the Mg^{2+} content: (i) without Mg^{2+}, TC and its aptamer do not interact. This is known since the aptamer was presented for the first time.[21] (ii) In the range of physiological Mg^{2+} concentrations between 0.2 and 1 mM, the aptamer can bind TC. The binding process shifts the conformational equilibrium of the aptamer towards the fully folded, compact tertiary structure. This structure then recruits more Mg^{2+} than it could in the absence of TC. The recruitment generates the stable, long-lived complex. It is important to note, that in this regime the aptamer was found not to be fully preformed. At the same time, the chelate complex of TC with Mg^{2+} is stabilized within the binding pocket decreasing the K_d of the chelate complex as compared to bulk solution conditions. Based on the crystal structure 3EGZ[212], negatively charged hotspots are likely to emerge in the vicinity of the irregular triple helix, which is composed of the junctions J1/2 and J2/3 and loop L3. (iii) At unphysiologically high Mg^{2+} concentrations (> 1 mM), the aptamer

is largely preformed in a near-to-binding conformation already in the absence of TC. This is supported by results from size-exclusion chromatography.[22] Here, TC stabilizes the complex through intramolecular linkage[212] but it induces only minor shifts of the conformational equilibrium[24]. In this regime, the aptamer can bind TC very fast and in a two-step mechanism due to the preformation.[25]

Consequently, there is no need for significantly higher Mg^{2+} concentrations for the TC aptamer to firmly bind its ligand than the ones available in most living cells.

Soon after the general capability of RNA to modulate gene expression was recognized in *C. elegans*[275], the concept of ncRNA strands to recognize and bind small metabolite molecules and control the expression of numerous essential genes in several species in response to the binding process was established[276]. Since then, huge progress was made in discovery and understanding of RS function.[87,277] In addition to naturally occurring RSs, there are in-vitro selected aptamers available that can act as RSs in vivo. Although these engineered RSs could be employed in numerous cellular and regulatory contexts (see for example [223,278]), the number of aptamers that are in principle capable to act as sensing platform for an engineered RS is surprisingly small, as is detailed in section 6.1. The question, what turns a good aptamer into a suitable building block of an engineered RS is thus both, highly relevant and non-trivial.

It is established for many RSs that the AD is required to adopt a binding-competent conformation, the so-called apo-form, before it can function appropriately.[279] The particular importance of divalent cations and, in living organisms namely of Mg^{2+}, is known for natural[280–284] as well as for engineered RSs[79,285]. Several studies on the Mg^{2+} sensitivity of naturally occurring RSs found concentrations around 0.5 mM as necessary prerequisite for ligand binding and significant conformational changes of the ADs were observed, as well.[279–283,286] In some cases, unique tertiary contacts are induced solely by the ligand, in some they are not. Therefore, it is not mandatory for the AD to posses a unique tertiary structure in the complexed state to generate a functional RS.

Nevertheless, the possible responses of naturally occurring ADs to Mg^{2+} show a large variability between RSs of different classes and also within a certain class.[88,91] This variability is likely to be necessary because different RSs act in different organisms, which says under different physiological conditions, and they act at different stages of gene regulation.[287] For cotranscriptional RSs for

example, ligand binding and recognition processes must occur on timescales that are comparable and compatible with expression processes and the delicate adjustment of expression processes and folding is governed by folding kinetics and energetics, including kinetic traps.[288–290] Because engineered RSs are oftentimes smaller than naturally occurring ones, they are well-suited model systems to investigate such effects.

The reactions of in-vitro aptamers usable for engineered RSs to Mg^{2+} are quite heterogeneous despite their limited number. The theophylline-binding aptamer is, along with the TC aptamer, the artificial aptamer that is to date used in most cellular environments and different control schemes.[221–223,291] Very much alike the TC aptamer, it needs Mg^{2+} for high affinity binding. The required concentration is 1 mM and thus comparatively high.[79,292] Yet, this does not contradict the findings on the TC aptamer because the association strength between TC and aptamer is found to be not yet saturated at sub-mM Mg^{2+} concentrations, either.[17] For the theophylline aptamer, it is also known that binding can be assisted by Mn^{2+} and Co^{2+} more effectively than by Mg^{2+}. Several other divalent and trivalent cations are inadequate for that purpose.[79]

The neomycin-binding aptamer has been used several times in an RS, as well.[224,225,293] EPR-based distance measurements on doubly spin labeled versions of the neomycin aptamer using the PELDOR-technique showed no significant global rearrangement of the aptamer upon ligand binding.[294] The K_d of the neomycin aptamer increases with increasing Mg^{2+} concentration (Dr. Julia Weigand, personal communications). The increase is due to the high positive charge of neomycin: excess Mg^{2+} clouds around the aptamer decrease the likelihood for the formation of encounter complexes and should also destabilize the complex due to electrostatic repulsion. Therefore, this observation does not directly allow to draw conclusions about a potentially positive structural influence of Mg^{2+} on the binding affinity of the neomycin aptamer because such a hypothetical effect is potentially overcompensated by electrostatics.

The malachite-green aptamer can bind malachite green and its close analogue tetramethylrosamine with almost identical affinities. Yet, the response of the affinities to increasing Mg^{2+} concentrations is exactly contrary to each other. Mg^{2+} impedes the aptamer binding malachite green and helps binding tetramethylrosamine.[295] The reason for the distinct response to the two ligands lies in the fact, that malachite green consists of two aromatic subunits that can rotate freely. The ligand can sample a large variety of different conformations, but only a small

subset of the conformations is suitable for binding.[295] Tetramethylrosamine lacks this conformational freedom.

Mg^{2+} leads to a compaction of the malachite-green aptamer, which causes the accessibility and flexibility of the binding pocket to decrease. Binding and recognition of malachite green is thus impeded by Mg^{2+} because the aptamer loses some of its conformational freedom needed in this special case to adapt the binding pocket to the high conformational freedom of the ligand. Therefore, the premises are very different for malachite green compared to the ones of TC, as the conformational space of TC is much smaller. It is more reasonable to compare TC to tetramethylrosamine, where the affinity also improves with increasing Mg^{2+} content.

For the pioneering engineered RS of Werstuck et al.[219], no information on the Mg^{2+} dependence is published. This lack of information is probably a consequence of the fact that the aptamer never found a broader range of applications.

Most of the abovementioned engineered RSs, appear to require Mg^{2+} and benefit from it in terms of ligand binding as much as many natural ones do. Whenever Mg^{2+} is found to impede binding, this is not due to the structural changes induced in the aptamer, but due to special properties of the ligands that are not applicable to TC.

In cellular environments, ligand binding has to occur under several disturbing influences such as crowding effects, binding competition with the machinery for translation initiation, and different temperature and salt conditions in different species or cell cultures.[288,296] In order to adapt a given aptamer to new cellular environments or regulation schemes, the sequence of the engineered RS is routinely altered by mutagenesis to adapt the energetics and stability.[18,215,221,222,224]

The crucial roles of energetics, binding competence, and switching capability as prerequisite for a strong signal transduction from the AD to the EP and the impact of the Mg^{2+} concentration on them bring up the question, whether the TC aptamer could actually function in a high Mg^{2+} environment. There seems to be no need for extremely tight ligand binding, for which the low K_d at 10 mM Mg^{2+} allows. Rather, a significant impact of the ligand on the conformational state at moderate, more physiological concentrations seems to be important. Tight binding in high Mg^{2+} concentrations was necessary in the SELEX process (10 mM Mg^{2+} in the SELEX buffer[21]). Contrarily to this, the ability to function in vivo appears to rely on the lower K_d combined with pronounced switching behavior.

Interestingly, in the case of the neomycin-binding aptamer, it was not the aptamer variant with the best binding properties that turned out to be a good RS building block. Instead, the neomycin aptamer was found by a dedicated in-vivo screening as a weak binder from the final SELEX pool.[224]

To conclude, spectroscopically and heat-monitored Mg^{2+} titration and spectroscopically monitored melting experiments were used to investigate the Mg^{2+} dependence of the TC aptamer. The obtained results allow for the thermodynamical analysis of the aptamer stability depending on the bulk Mg^{2+} concentration in the presence and absence of TC. Based on the findings, a model of the interaction pattern of the three partners TC, aptamer, and Mg^{2+} was developed. The findings were discussed in view of their biological relevance. Most important, physiological Mg^{2+} concentrations of (0.2 – 1 mM) are sufficient to support binding of TC and the impact of TC on the conformational state of its aptamer is maximal in this concentration range.

Chapter 7

Summary

7.1 English version

In the previous three chapters, the experimental implementation of a time-resolved fluorometer (chapter 4), the photophysical characterization of the 2-(pyrenylethynyl) adenosines (PyAs), a family of fluorescent RNA-nucleoside analogs (chapter 5), and the interaction pattern of the TC aptamer with TC and Mg^{2+} (chapter 6) are presented.

The time-resolved fluorometer is realized on the basis of the TCSPC technique. It is equipped with two different excitation sources—pulsed LEDs and a frequency-doubled titan-doped sapphire laser—covering an excitation-wavelength range from 550 to 310 nm with IRFs between 200 and 800 ps and an optimal achievable time-resolution between 50 and 80 ps. The timing accuracy is shown to be reliable within an uncertainty of less than 0.02 %.

The functionality and performance of the fluorometer is demonstrated by a comprehensive comparative study of the fluorescence properties of the three PyAs.

The fluorescence decays of the three PyAs, which represent the full set of possible structural isomers for the PyA-family, are complemented with steady-state absorption and fluorescence, as well as time-resolved ultrafast transient absorption spectroscopy in various solvents and supported by quantum-chemical calculations. The fluorescence of 2-(2-pyrenylethynyl) adenosine (2PyA) is found to be very sensitive to the excitation wavelength, whereas 2-(1-pyrenylethynyl) adenosine (1PyA) and 2-(4-pyrenylethynyl) adenosine (4PyA) obey Kasha's rule.

In addition to its excitation dependence, the fluorescence of 2PyA decays tri-exponentially and the relative contributions of the different decay components depend on the detected spectral range. Again, no such dependence is present for 1PyA and 4PyA, which decay essentially mono-exponential.

The fundamentally important observation of three simultaneously emitting subspecies of 2PyA can be explained in terms of the existence of locally-excited, mesomeric, and twisted intramolecular charge-transfer states. In order to explain the similarities and differences of the photophysical behavior of the three isomers, a unified model is developed. The minimal energy ground state configuration of all three 2-(pyrenylethynyl) adenosines has coplanar adenine and pyrene moieties. The energetic barriers for the formation of rotamers of the pyrene around the ethynyl axis is found to be smallest for 2PyA and largest for 1PyA. The excited state barriers are believed to be even smaller, especially for 2PyA. Additionally, for 2PyA purely pyrene-located optical transitions exist.

1PyA and 4PyA are concluded to emit from planar (mesomeric) intramolecular charge-transfer states, whereas 2PyA can emit from a planar and from a twisted intramolecular charge-transfer state, where pyrene and adenine are rotated by 90 ° relative to each other. The twisted state cannot be excited directly from the planar ground state geometry, instead, is populated via conformational change in the excited state. The locally-excited state of 2PyA is very pyrene-like and can be addressed most efficiently by excitation into the S_2. Excitation of the locally-excited state with 385 nm ($S_0 \rightarrow S_1$) is therefore believed to be non-resonant.

In chapter 6, the complex formation of the TC aptamer with TC and the structural stability of the TC aptamer depending on the presence of its ligand with varying contents of Mg^{2+} and urea are investigated. Absorption, circular–dichroism, and fluorescence-monitored titrations and melting profiles are combined with calorimetric experiments leading to a detailed picture of the interaction pattern of the TC aptamer with TC and Mg^{2+}.

Without Mg^{2+}, the TC aptamer cannot interact with TC, at all. The reason for this is that Mg^{2+} provides the necessary electrostatic stabilization of the negatively charged RNA backbone. This allows the TC aptamer to form compact tertiary structures. At saturating Mg^{2+} concentrations (> 1 mM), the aptamer is strongly preformed in a near-to-binding conformation, which leads to the fast, approximately diffusion-limited, formation of the extremely stable aptamer-ligand complex. There, TC has little influence on the conformation of its aptamer.

At physiological Mg^{2+} concentrations between 0.2 and 0.8 mM Mg^{2+}, the aptamer can sample compact conformations with tertiary structures. The near-to-binding conformation is, however, not yet dominating. Rather, it is one out of many. Therefore, intermediate Mg^{2+} concentrations open up parts of the comformational space to the TC aptamer, that are inaccessible without Mg^{2+}. In this regime, TC stabilizes selectively the binding conformation by forming a stable complex with the TC aptamer providing thermodynamic stability to the native tertiary structure and a significant change of the aptamer conformation as robust signal for riboswitch function. Within this process, the TC aptamer recruits additional Mg^{2+} ions from the bulk against a steeper cation concentration gradient than it could in the absence of TC.

7.2 Deutsche Version

Das zentrale Dogma der Molekularbiologie wurde 1958 von Francis Crick formuliert. Es beschreibt die möglichen Richtungen des Informationsflusses im Rahmen der Genexpression: Information fließt stets von DNA und RNA in Richtung der Proteine, niemals aber von den Proteinen zurück zu den Nukleinsäuren. Trotz der prinzipiellen Spielräume, die das Dogma den möglichen Funktionen der Nukleinsäuren einräumt, dominierte über lange Zeiträume ein sehr eingeengtes Verständnis des Dogmas das Bild ihrer Rollen. Im Standardbild der Molekularbiologie vom Prozess der Genexpression dient DNA als Vorlage und hochgradig geschützter Langzeitspeicher für Informationen, während RNA nur als kurzzeitiger Bote (mRNA) und Mittler (tRNA) in Erscheinung tritt. Die (Protein-)Biosynthese wird dabei im Wesentlichen von anderen Proteinen durchgeführt und die dazu notwendigen Prozesse sowie ihre Steuerung werden von (anderen) Proteinen überaus engmaschig überwacht oder katalysiert.

In Eukaryoten ist die mRNA nach der Transkription im Allgemeinen noch nicht in ihrer endgültigen Form, weswegen sie prä-mRNA genannt wird. Die prä-mRNA muss vielmehr erst noch verarbeitet werden, ehe sie zu vollwertiger mRNA wird. Einer der Verarbeitungsschritte – das sogenannte Spleißen – verändert die Basenabfolge der ursprünglichen prä-mRNA insofern, als dass Bereiche, welche keine proteinkodierenden Informationen beinhalten (Introns), entfernt und nur die (erwünschten) kodierenden Bereiche (Exonen) behalten und in einer sinnvollen Reihenfolge wieder zusammengesetzt werden. Im Unterschied zu

Exons, welche als kodierend (c von *coding*) bezeichnet werden, werden Introns nichtkodierend (nc von *non-coding*) genannt. Jeder einzelne Teilschritt der Genexpression unterliegt potentieller Einflussnahme durch Bestandteile der intrazellulären Umgebung. Deswegen können aus ein und demselben DNA-Abschnitt unterschiedliche Proteine synthetisiert werden.

In der bisherigen Schilderung ist die Rolle der RNA vollständig passiv, zumal sämtliche Verarbeitungs- und Steuerungsprozesse ausschließlich von Proteinen durchgeführt werden.

Im zurückliegenden Vierteljahrhundert wurden dementgegen einige Klassen nichtkodierender RNA (ncRNA) entdeckt, welche die Abläufe im Rahmen der Genexpression aktiv beeinflussen und regulieren. Diese Klassen beinhalten microRNAs und ‚kleine interferierende' RNAs (siRNA von *small interfering*), welche die beschleunigte Zersetzung der bindungsfähigen (m)RNA durch teilweise oder vollständige Basenpaarung verursachen. ‚Kleine nucleolare' RNAs (snoRNA von *small nucleolar*) und die eng verwandten ‚kleinen RNAs aus dem Cajal-Körper' (scaRNA von *small Cajal-body*) können sowohl steuernd als auch katalytisch agieren. Längere ncRNAs (> 200 Nukleotide) wie macroRNAs oder mRNAs können als Antagonisten zu demjenigen Protein auftreten, welches sie kodieren. Die noch wesentlich größeren kreisförmigen RNAs regulieren die Konzentration von miRNAs, indem sie als miRNA-Schwämme fungieren. Jenseits der seit Längerem vertrauten katalytisch aktiven RNAs, welche Schlüsselpositionen in Ribonucleoproteinen wie dem Ribosom als ribosomale (r)RNA einnehmen, sind RNAs zudem wichtige Teilnehmer an Prozessen wie der DNA-Methylierung, der Chromatinmodifikation, der genomische Prägung, der Telomeraseverarbeitung und der RNA-Editierung.

Die genannten ncRNAs und die alternativen Expressionsabläufe, mit denen sie verknüpft sind, herrschen in Eukaryoten vor. Ihre Häufigkeit und relative Wichtigkeit nimmt mit der Komplexität der betrachteten Organismen zu. Im Unterschied hierzu treten Riboschalter gleichermaßen in allen Reichen des Lebens auf. Dies ist ein starkes Indiz dafür, dass ihr evolutionärer Ursprung wesentlich früher liegt, als derjenige der meisten anderen RNA-basierten Genregulationsmechanismen. Riboschalter sind nichtkodierende Abschnitte von mRNAs und als Teil des untranslatierten Bereiches am 5'-Ende der mRNA werden sie vor den kodierenden Bereichen exprimiert. Sie können durch eine Aptamerdomäne mit hoher Selektivität einen oder mehrere Metaboliten erkennen und binden: ihre Liganden. Die Bindung eines Liganden kann Einfluss auf die Sekundär- und

Tertiärstruktur von Bereichen der mRNA nehmen, die von der Bindungstasche räumlich entfernt sind. Diese entfernten Bereiche werden, wenn sie Einfluss auf die Genexpression nehmen können, als Expressionplattform bezeichnet. Dementsprechend kann die Ligandenkonzentration den weiteren Ablauf der Genexpression beeinflussen.

Außer natürlichen Riboschaltern gibt es auch vom Menschen entworfene. Sie basieren auf ligandenerkennenden Aptameren, welche durch in vitro durchgeführte Experimente auf künstlichem Wege gefunden wurden. Künstlich entworfene Riboschalter sind als wertvolle Werkzeuge für biologische Untersuchungen etabliert. Die Anzahl an geeigneten Aptameren, welche auch in lebenden Zellen als signalgebende Aptamerdomänen eines entworfenen Riboschalters dienen können, ist indessen erstaunlich gering.

Das tetracyclinbindende (TC-) Aptamer ist eines der vielseitigsten künstlichen Riboschalteraptamere mit Anwendungen, die von Hefe bis hin zu menschlichen Zellen reichen. Aufgrund seiner relativ geringen Größe sowie seiner hohen Selektivität und Bindungsaffinität hat es erhebliche Aufmerksamkeit als Modellsystem erhalten. Es wurde insbesondere in Hinblick auf den Zusammenhang zwischen starker Ligandenbindung und Mg^{2+}-induzierter struktureller Präformation untersucht.

Eine Besonderheit von RNA im biologischen Kontext, aber auch jenseits davon, ist ihre große konformationelle Komplexität und auch Flexibilität sowie der Umstand, dass die Flexibilität bedeutsam für die biologische Funktionalität einer RNA sein kann. Die schnellsten strukturellen Änderung sind das Auf- und Zuklappen einzelner Basenpaare, welche schneller als eine Nanosekunde ablaufen. Fluoreszenz stellt die optimale Observable für derartig schnelle Prozesse dar, weil sie überaus empfindlich und zeitnah auf Änderungen in der lokalen Umgebung des Fluorophors reagiert und im Prinzip mit einem herausragenden Signal-zu-Rauschverhältnis abgefragt werden kann. Die fluoreszierenden Sonden können Farbstoffe sein, die sich selbstständig und stochastisch in die RNA einfügen oder aber an bestimmten Stellen in der RNA eingebracht werden. Ihre Anwendungsgebiete umfassen Experimente im stationären Gleichgewicht, schnelle Mischprozesse zur Aufklärung von Bindungskinetiken und Messungen von Fluoreszenzlebensdauern, welche durch die Konformationen der RNA beeinflusst werden.

Im Rahmen der vorliegenden Arbeit wurde Pyren als Fluoreszenzsonde verwendet, weil es eine Reihe vorteilhafter Eigenschaften aufweist: es besitzt

eine große Fluoreszenzquantenausbeute und -lebensdauer in sauerstofffreien Lösungsmitteln, es reagiert empfindlich auf die Lösungsmittelpolarität und es kann fluoreszierende Excimere bilden. Ein Excimer bezeichnet ein angeregtes Heterodimer (Kunstwort als Kontraktion von *excited dimer*). Entsprechend häufig wurde es in unterschiedlichen biophyskalischen Untersuchungen verwendet, wie zum Beispiel der Messung von Umlagerungszeiten über Lipidmembranen hinweg oder zur Messung ihrer Dicke.

Zur Untersuchung von Nukleinsäuren eignen sich Pyrene in ganz besonderem Maße, weil sie als molekulare Signalmarkierungen verwendbar sind, die zwischen DNA- und RNA-Strängen gleicher Primärsequenz unterscheiden können. Die Eignung von Pyren als Sonde für Nukleinsäuren ist eng verknüpft mit seiner Neigung sich selbst in die Stränge einzubetten sowie mit der Beobachtung, dass es seine Fähigkeit zur Bildung fluoreszierender Excimere auch dann behält, wenn es in Nukleinsäuresträngen eingefügt ist.

Diese Dissertation beschäftigt sich vornehmlich mit RNA und, genauer, dem Zusammenhang zwischen der räumlichen Struktur und der Funktion dieses Makromoleküls.

Die Projekte, welche in den Kapiteln 4 und 5 vorgestellt werden, beschreiben die experimentelle Realisierung eines Aufbaus zum Messen zeitaufgelöster Fluoreszenzzerfälle und seine Verwendung zur Charakterisierung zweier zuvor nicht verfügbarer pyrenbasierter, fluoreszierender Analoga von RNA-Nukleotiden. Diese Charakterisierung stellt dabei einen ersten notwendigen Schritt hin zur Etablierung dieser neuen Sonden zur Untersuchung von RNA-Strukturen dar.

Das zeitaufgelöste Fluorometer basiert auf der Messtechnik des zeitkorrelierten Einzelphotonenzählens. Das Fluorometer verfügt über zwei unabhängige Anregungsquellen – gepulste LEDs und einen frequenzverdoppelten, titandotierten Saphirlaser – welche zusammen einen Wellenlängenbereich von 550 bis 310 nm abdecken. Die Breiten der Instrumentenantwort liegen dabei zwischen 200 und 800 ps mit optimal erreichbaren Zeitauflösungen zwischen 50 und 80 ps. Die Unsicherheit der elektronischen Zeitmessung betragen weniger als 0,02 %.

Die Funktions- und Leistungsfähigkeit des zeitaufgelösten Fluorometers wird durch umfassende Experimente an den drei möglichen 2-Pyrenylethinyl-Adenosinen (PyAs) demonstriert.

Die Fluoreszenzzerfälle der drei PyAs, welche gemeinsam den vollständi-

gen Satz möglicher Konfigurationsisomere für diese Familie von Verbindungen repräsentieren, werden durch Absorptions- und Fluoreszenzexperimente im stationären Gleichgewicht, ultraschnelle zeitaufgelöste Absorptionsspektroskopie und quantenchemische Rechnungen ergänzt. Die Fluoreszenz von 2-(2-Pyrenylethinyl)-Adenosin (2PyA) zeigt eine ausgeprägte Abhängigkeit von der Anregungswellenlänge, wohingegen 2-(1-Pyrenylethinyl)-Adenosin (1PyA) und 2-(4-Pyrenylethinyl)-Adenosin (4PyA) der Kasha-Regel gehorchen. Zusätzlich zu seiner Anregungswellenlängenabhängigkeit zerfällt die Fluoreszenz von 2PyA triexponentiell und die relative Wichtigkeit der verschiedenen Zerfallskanäle hängt von der Detektionswellenlänge ab. Für die im Wesentlichen monoexponentiell zerfallenden Verbindungen 1PyA und 4PyA lässt sich ein solches Verhalten hingegen nicht nachweisen.

Die zeitaufgelösten Absorptionsspektren aller drei Isomere weisen im gesamten messbaren Spektralbereich eine breite und wenig strukturierte Absorption der angeregten Zustände auf. Die Absorption der angeregten Zustände ist in unterschiedlichem Maße durch das Ausbleichen des Grundzustands und durch stimulierte Emission überlagert. 2PyA besitzt zudem eine charakteristische Signatur, welche die schnelle innere Umwandlung hin zum S_1-Zustand nach Anregung in höhere elektronische Zustände anzeigt.

Die fundamental bedeutsame Beobachtung dreier gleichzeitig emittierender Unterzustände von 2PyA wird erklärt durch die Existenz eines lokal angeregten Zustandes, sowie eines mesomeren und eines verdrillten intramolekularen Ladungstransferzustandes. Um die Gemeinsamkeiten und Unterschiede der Photodynamik der drei Isomere zu verstehen, wird für sie eine einheitliche Modellvorstellung entwickelt.

Die Grundzustandskonfigurationen aller Isomere verfügen über koplanar ausgerichtete Pyren- und Adeninuntereinheiten. Die Energiebarriere der Bildung von Rotationsisomeren, definiert durch den Drehwinkel zwischen Pyren und Adenin entlang der Ethinylachse, ist am geringsten für 2PyA und am größten für 1PyA. Die entsprechenden Barrieren im ersten angeregten Zustand sind sehr wahrscheinlich noch flacher, insbesondere diejenige von 2PyA. Zusätzlich gibt es für 2PyA optische Übergänge die ausschließlich am Pyren lokalisiert sind.

Hiervon ausgehend werden 1PyA und 4PyA eine Emission aus planaren (mesomeren) intramolekularen Ladungstransferzuständen zugeordnet, wohingegen 2PyA sowohl aus einem planaren, als auch aus einem verdrillten intramolekularen

Ladungstransferzustand emittiert. Bei Letzterem ist das Pyren um 90 ° gegen das Adenin verdreht. Der verdrillte Zustand kann nicht direkt aus dem Grundzustand angeregt werden, stattdessen wird er durch konformationelle Änderungen im angeregten Zustand bevölkert. Der lokal angeregte Zustand von 2PyA ist sehr pyrenartig und kann am effizientesten über den S_2-Zustand angeregt werden.

Kapitel 6 befasst sich mit der Reaktion des TC-Aptamers auf seinen Liganden bei unterschiedlichen Mg^{2+}-Konzentrationen. Das Hauptaugenmerk dieser Experimente liegt auf den Fragen, welche strukturellen Eigenschaften des TC-Aptamers seine Riboschalterfunktion in vivo mit physiologischen Mg^{2+}-Konzentrationen ermöglichen und wie diese Funktionalität mit der strukturellen Präformation des Aptamers in hochkonzentrierten Mg^{2+}-Lösungen zusammenhängt.

Hierzu wird die Komplexbildung und die konformationelle Stabilität des TC-Aptamers abhängig von seinem Liganden TC in Gegenwart verschiedener Mg^{2+}-und Harnstoffkonzentrationen untersucht. Auf Grundlage von Titrationen und thermischen De- und Renaturierungsexperimenten, welche mittels Absorptions-, Zirkulardichroismus- und Fluoreszenzspektroskopie gemessen wurden, sowie kalorimetrischer Experimente ergibt sich ein detailliertes Bild vom Wechselwirkungsgeflecht zwischen dem TC-Aptamer, TC und Mg^{2+}.

Ohne jegliches Mg^{2+} kann das TC-Aptamer nicht mit TC interagieren. Das Mg^{2+} ermöglicht es dem Aptamer erst, eine kompakte Konformation mit einer Tertiärstruktur anzunehmen. Das Mg^{2+} schirmt hierzu einerseits die negative Ladung des RNA-Rückgrates ab und kontrahiert die RNA andererseits durch seine elektrostatische Anziehung zum Rückgrat. In sättigenden Mg^{2+}-Lösungen (> 1 mM) ist das Aptamer weitgehend vorgeformt in einer Konfiguration, die der gebundenen Konformation im Komplex sehr ähnelt. In diesem Regime bindet das Aptamer seinen Liganden sehr schnell (im Wesentlichen diffusionslimitiert) und bildet einen extrem stabilen, langlebigen Komplex, wobei TC kaum Einfluss auf die Konformation seines Aptamers hat.

Im Bereich physiologischer Mg^{2+}-Konzentrationen zwischen circa 0,2 und 0,8 mM kann das TC-Aptamer kompakte Konformationen mit Tertiärstruktur bevölkern. Die endgültig vorgeformte Konformation, welche der gebundenen ähnelt, ist jedoch noch nicht alleine vorherrschend, sondern nur eine unter vielen. Dementsprechend eröffnen moderate Mg^{2+}-Konzentrationen dem TC-Aptamer Bereiche seines Konformationsraumes, welche ohne Mg^{2+} unzugänglich sind.

In diesem Konzentrationsbereich stabilisiert TC selektiv die bindende Konformation seines Aptamers, indem es einen stabilen Komplex bildet. Im Zuge dieses Prozesses rekrutiert das TC-Aptamer weitere Mg^{2+}-Ionen aus der Lösung gegen einen steileren Konzentrationsgradienten als dies ohne TC möglich wäre. Dadurch stabilisiert TC die native Tertiärstruktur thermodynamisch und induziert zugleich eine signifikante Änderung der vorherrschenden Aptamerkonformation, wodurch eine robuste Signalgebung im funktionellen Kontext eines Riboschalters begünstigt wird.

Bibliography

[1] F. Crick, "Central Dogma of Molecular Biology," *Nature*, vol. 227, pp. 561–563, 1970.

[2] J. Watson, T. Baker, S. Bell, A. Gann, M. Levine, and R. Losick, *Molecular Biology of the Gene: International Ed*.
Prentice Hall, 6th ed., 2007.

[3] R. R. Breaker and G. Joyce, "The Expanding View of RNA and DNA Function," *Chemistry & Biology*, vol. 21, pp. 1059–1065, 2014.

[4] J. S. Mattick and I. V. Makunin, "Non-coding RNA," *Human Molecular Genetics*, vol. 15, pp. R17–R29, 2006.

[5] T. R. Mercer, M. E. Dinger, and J. S. Mattick, "Long non-coding RNAs: insights into functions," *Nature Reviews Genetics*, vol. 10, pp. 155–159, 2009.

[6] T. B. Hansen, T. I. Jensen, B. H. Clausen, J. B. Bramsen, B. Finsen, C. K. Damgaard, and J. Kjems, "Natural RNA circles function as efficient microRNA sponges," *Nature*, vol. 495, pp. 384–388, 2013.

[7] R. F. Gesteland, T. R. Cech, and J. F. Atkins, eds., *The RNA World, Third Edition*.
Cold Spring Harbor, N.Y: Cold Spring Harbor Laboratory Press, 3rd ed., 2005.

[8] H. U. Göringer, *RNA Editing*.
Heidelberg: Springer, 2007.

[9] M. T. McManus and P. A. Sharp, "Gene silencing in mammals by small interfering RNAs," *Nature Reviews Genetics*, vol. 3, pp. 737–747, 2002.

[10] M. J. O'Neill, "The influence of non-coding RNAs on allele-specific gene expression in mammals," *Human Molecular Genetics*, vol. 14, pp. R113–R120, 2005.

[11] P. Landgraf, M. Rusu, R. Sheridan, A. Sewer, N. Iovino, A. Aravin, S. Pfeffer, A. Rice, A. O. Kamphorst, M. Landthaler, C. Lin, N. D. Socci, L. Hermida, V. Fulci, S. Chiaretti, R. Foà, J. Schliwka, U. Fuchs, A. Novosel, R.-U. Müller, B. Schermer, U. Bissels, J. Inman, Q. Phan, M. Chien, D. B. Weir, R. Choksi, G. De Vita, D. Frezzetti, H.-I. Trompeter, V. Hornung, G. Teng, G. Hartmann, M. Palkovits, R. Di Lauro, P. Wernet, G. Macino,

C. E. Rogler, J. W. Nagle, J. Ju, F. N. Papavasiliou, T. Benzing, P. Lichter, W. Tam, M. J. Brownstein, A. Bosio, A. Borkhardt, J. J. Russo, C. Sander, M. Zavolan, and T. Tuschl, "A Mammalian microRNA Expression Atlas Based on Small RNA Library Sequencing," *Cell*, vol. 129, pp. 1401–1414, 2007.

[12] H. Mouilleron, V. Delcourt, and X. Roucou, "Death of a dogma: eukaryotic mRNAs can code for more than one protein," *Nucleic Acids Research*, vol. 44, pp. 14–23, 2016.

[13] M. Mandal and R. R. Breaker, "Gene regulation by riboswitches," *Nature Reviews Molecular Cell Biology*, vol. 5, pp. 451–463, 2004.

[14] R. R. Breaker, "Natural and engineered nucleic acids as tools to explore biology," *Nature*, vol. 432, pp. 838–845, 2004.

[15] J. E. Weigand and B. Suess, "Aptamers and riboswitches: perspectives in biotechnology," *Applied Microbiology and Biotechnology*, vol. 85, pp. 229–236, 2009.

[16] A. Wittmann and B. Suess, "Engineered riboswitches: Expanding researchers' toolbox with synthetic RNA regulators," *FEBS Letters*, vol. 586, pp. 2076–2083, 2012.

[17] A. J. Reuss, M. Vogel, J. E. Weigand, B. Suess, and J. Wachtveitl, "Tetracycline Determines the Conformation of Its Aptamer at Physiological Magnesium Concentrations," *Biophysical Journal*, vol. 107, pp. 2953–2962, 2014.

[18] B. Suess, S. Hanson, C. Berens, B. Fink, R. Schroeder, and W. Hillen, "Conditional gene expression by controlling translation with tetracycline-binding aptamers," *Nucleic Acids Research*, vol. 31, pp. 1853–1858, 2003.

[19] P. Kötter, J. E. Weigand, B. Meyer, K.-D. Entian, and B. Suess, "A fast and efficient translational control system for conditional expression of yeast genes," *Nucleic Acids Research*, vol. 37, pp. e120 (1–7), 2009.

[20] K. Beilstein, A. Wittmann, M. Grez, and B. Suess, "Conditional Control of Mammalian Gene Expression by Tetracycline-Dependent Hammerhead Ribozymes," *ACS Synthetic Biology*, vol. 4, pp. 526–534, 2015.

[21] C. Berens, A. Thain, and R. Schroeder, "A tetracycline-binding RNA aptamer," *Bioorganic & Medicinal Chemistry*, vol. 9, pp. 2549–2556, 2001.

[22] M. Müller, J. E. Weigand, O. Weichenrieder, and B. Suess, "Thermodynamic characterization of an engineered tetracycline-binding riboswitch," *Nucleic Acids Research*, vol. 34, pp. 2607–2617, 2006.

[23] S. Hanson, G. Bauer, B. Fink, and B. Suess, "Molecular analysis of a synthetic tetracycline-binding riboswitch," *RNA*, vol. 11, pp. 503–511, 2005.

[24] D. Wunnicke, D. Strohbach, J. E. Weigand, B. Appel, E. Feresin, B. Suess, S. Müller, and H.-J. Steinhoff, "Ligand-induced conformational capture of a synthetic tetracycline riboswitch revealed by pulse EPR," *RNA*, vol. 17, pp. 182–188, 2011.

[25] U. Förster, J. E. Weigand, P. Trojanowski, B. Suess, and J. Wachtveitl, "Conformational dynamics of the tetracycline-binding aptamer," *Nucleic Acids Research*, vol. 40, pp. 1807–1817, 2012.

[26] N. Leulliot and G. Varani, "Current topics in RNA-protein recognition: control of specificity and biological function through induced fit and conformational capture," *Biochemistry*, vol. 40, pp. 7947–7956, 2001.

[27] T. Hermann, "Rational ligand design for RNA: the role of static structure and conformational flexibility in target recognition," *Biochimie*, vol. 84, pp. 869–875, 2002.

[28] T. Xia, "Taking femtosecond snapshots of RNA conformational dynamics and complexity," *Current Opinion in Chemical Biology*, vol. 12, pp. 604–611, 2008.

[29] L. Zhao and T. Xia, "Probing RNA conformational dynamics and heterogeneity using femtosecond time-resolved fluorescence spectroscopy," *Methods*, vol. 49, pp. 128–135, 2009.

[30] F. Wachowius and C. Höbartner, "Chemical RNA Modifications for Studies of RNA Structure and Dynamics," *ChemBioChem*, vol. 11, pp. 469–480, 2010.

[31] D. P. Millar, R. J. Robbins, and A. H. Zewail, "Torsion and bending of nucleic acids studied by subnanosecond time-resolved fluorescence depolarization of intercalated dyes," *The Journal of Chemical Physics*, vol. 76, pp. 2080–2094, 1982.

[32] R. A. Tinsley and N. G. Walter, "Pyrrolo-C as a fluorescent probe for monitoring RNA secondary structure formation," *RNA*, vol. 12, pp. 522–529, 2006.

[33] H.-W. Lee, K. T. Briggs, and J. P. Marino, "Dissecting structural transitions in the HIV-1 dimerization initiation site RNA using 2-aminopurine fluorescence," *Methods*, vol. 49, pp. 118–127, 2009.

[34] M. Kaul, C. M. Barbieri, and D. S. Pilch, "Fluorescence-Based Approach for Detecting and Characterizing Antibiotic-Induced Conformational Changes in Ribosomal RNA: Comparing Aminoglycoside Binding to Prokaryotic and Eukaryotic Ribosomal RNA Sequences," *Journal of the American Chemical Society*, vol. 126, pp. 3447–3453, 2004.

[35] D. S. Karpovich and G. J. Blanchard, "Relating the polarity-dependent fluorescence response of pyrene to vibronic coupling. Achieving a fundamental understanding of the py polarity scale," *The Journal of Physical Chemistry*, vol. 99, pp. 3951–3958, 1995.

[36] D. C. Dong and M. A. Winnik, "The Py scale of solvent polarities," *Canadian Journal of Chemistry*, vol. 62, pp. 2560–2565, 1984.

[37] T. Förster and K. Kasper, "Ein Konzentrationsumschlag der Fluoreszenz des Pyrens," *Zeitschrift für Elektrochemie, Berichte der Bunsengesellschaft für physikalische Chemie*, vol. 59, pp. 976–980, 1955.

[38] T. Förster, "Excimers," *Angewandte Chemie International Edition in English*, vol. 8, pp. 333–343, 1969.

[39] P. Müller, S. Schiller, T. Wieprecht, M. Dathe, and A. Herrmann, "Continuous measurement of rapid transbilayer movement of a pyrene-labeled phospholipid analogue," *Chemistry and Physics of Lipids*, vol. 106, pp. 89–99, 2000.

[40] S. Mazor, S. Vanounou, and I. Fishov, "Pyrene as a membrane depth gauge: Wavelength selective fluorescence approach to monitor pyrene localizations in the membrane," *Chemistry and Physics of Lipids*, vol. 165, pp. 125–131, 2012.

[41] R. Häner, S. Biner, S. Langenegger, T. Meng, and V. Malinovskii, "A Highly Sensitive, Excimer-Controlled Molecular Beacon," *Angewandte Chemie International Edition*, vol. 49, pp. 1227–1230, 2010.

[42] U. B. Christensen and E. B. Pedersen, "Intercalating nucleic acids containing insertions of 1-O-(1-pyrenylethynyl)glycerol: stabilization of dsDNA and discrimination of DNA over RNA," *Nucleic Acids Research*, vol. 30, pp. 4918–4925, 2002.

[43] M. Nakamura, Y. Fukunaga, K. Sasa, Y. Ohtoshi, K. Kanaori, H. Hayashi, H. Nakano, and K. Yamana, "Pyrene is highly emissive when attached to the RNA duplex but not to the DNA duplex: the structural basis of this difference," *Nucleic Acids Research*, vol. 33, pp. 5887–5895, 2005.

[44] I. V. Astakhova and V. A. Korshun, "2-and 4-phenylethynylpyrenes, novel fluorescent labels for DNA," *Russian Journal of Bioorganic Chemistry*, vol. 34, pp. 510–512, 2008.

[45] U. Förster, K. Lommel, D. Sauter, C. Grünewald, J. W. Engels, and J. Wachtveitl, "2-(1-Ethynylpyrene)-Adenosine as a Folding Probe for RNA—Pyrene in or out," *ChemBioChem*, vol. 11, pp. 664–672, 2010.

[46] U. Förster, C. Grünewald, J. W. Engels, and J. Wachtveitl, "Ultrafast Dynamics of 1-Ethynylpyrene-Modified RNA: A Photophysical Probe of Intercalation," *The Journal of Physical Chemistry B*, vol. 114, pp. 11638–11645, 2010.

[47] P. Conlon, C. J. Yang, Y. Wu, Y. Chen, K. Martinez, Y. Kim, N. Stevens, A. A. Marti, S. Jockusch, N. J. Turro, and W. Tan, "Pyrene Excimer Signaling Molecular Beacons for Probing Nucleic Acids," *Journal of the American Chemical Society*, vol. 130, pp. 336–342, 2008.

[48] C. Grünewald, T. Kwon, N. Piton, U. Förster, J. Wachtveitl, and J. W. Engels, "RNA as scaffold for pyrene excited complexes," *Bioorganic & Medicinal Chemistry*, vol. 16, pp. 19–26, 2008.

[49] H. Haken and H. C. Wolf, *Molekülphysik und Quantenchemie: Einführung in die experimentellen und theoretischen Grundlagen*.
Springer, 4th ed., 2002.

[50] W. Demtröder, *Experimentalphysik 3: Atome, Moleküle und Festkörper*.
Springer, 4th ed., 2010.

[51] F. Schwabl, *Quantenmechanik (QM I): Eine Einführung*.
Springer, 6th ed., 2004.

[52] A. Nitzan, *Chemical Dynamics in Condensed Phases: Relaxation, Transfer, and Reactions in Condensed Molecular Systems*.
Oxford University Press, 1st ed., 2006.

[53] A. Einstein, "Über einen die Erzeugung und Verwandlung des Lichtes betreffenden heuristischen Gesichtspunkt," *Annalen der Physik*, vol. 322, pp. 132–148, 1905.

[54] J. J. Sakurai, *Modern Quantum Mechanics*.
Addison Wesley, revised ed., 1993.

[55] R. P. Feynman, R. B. Leighton, and M. Sands, *The Feynman Lectures on Physics, Vol. III: The New Millennium Edition: Quantum Mechanics*.
Basic Books, first trade paper ed., 2011.

[56] J. C. Maxwell, *A Treatise on Electricity and Magnetism*.
Cambridge: Cambridge University Press, 1873.

[57] H. E. Lessing and A. Von Jena, "Separation of rotational diffusion and level kinetics in transient absorption spectroscopy," *Chemical Physics Letters*, vol. 42, pp. 213–217, 1976.

[58] A. Jaboski, "Efficiency of Anti-Stokes Fluorescence in Dyes," *Nature*, vol. 131, pp. 839–840, 1933.

[59] M. Kasha, "Characterization of electronic transitions in complex molecules," *Discussions of the Faraday Society*, vol. 9, pp. 14–19, 1950.

[60] M. Kasha, "Phosphorescence and the Role of the Triplet State in the Electronic Excitation of Complex Molecules.," *Chemical Reviews*, vol. 41, pp. 401–419, 1947.

[61] S. Braslavsky, E., "Glossary of Terms used in photochemistry 3rd edition (IUPAC recommendations 2006)," *Pure and Applied Chemistry*, vol. 79, pp. 293–465, 2007.

[62] J. Langelaar, R. P. H. Rettschnick, and G. J. Hoijtink, "Studies on Triplet Radiative Lifetimes, Phosphorescence, and Delayed Fluorescence Yields of Aromatic Hydrocarbons in Liquid Solutions," *The Journal of Chemical Physics*, vol. 54, pp. 1–7, 1971.

[63] J. R. Lakowicz, *Principles of Fluorescence Spectroscopy*.
Springer US, 3rd ed., 2006.

[64] D. M. Gray, T. N. Taylor, and D. Lang, "Dehydrated circular DNA: Circular dichroism of molecules in ethanolic solutions," *Biopolymers*, vol. 17, pp. 145–157, 1978.

[65] S. Lemieux and F. Major, "RNA canonical and non-canonical base pairing types: a recognition method and complete repertoire," *Nucleic Acids Research*, vol. 30, pp. 4250–4263, 2002.

[66] J. H. Cate, A. R. Gooding, E. Podell, K. Zhou, B. L. Golden, C. E. Kundrot, T. R. Cech, and J. A. Doudna, "Crystal Structure of a Group I Ribozyme Domain: Principles of RNA Packing," *Science*, vol. 273, pp. 1678–1685, 1996.

[67] P. F. Crain and J. A. McCloskey, "The RNA modification database," *Nucleic Acids Research*, vol. 25, pp. 126–127, 1997.

[68] T. Hermann and D. J. Patel, "RNA bulges as architectural and recognition motifs," *Structure*, vol. 8, pp. R47–R54, 2000.

[69] P. C. J. Haasnoot, J. F. Bol, and R. C. L. Olsthoorn, "A Plant Virus Replication System to Assay the Formation of RNA Pseudotriloop Motifs in RNA–protein Interactions," *Proceedings of the National Academy of Sciences*, vol. 100, pp. 12596–12600, 2003.

[70] C. Cheong, N.-K. Kim, and C. Cheong, "RNA Structure: Tetraloops," in *eLS*, pp. 1–6, John Wiley & Sons, Ltd, 2010.

[71] R. Stefl and F. H. T. Allain, "A Novel RNA Pentaloop Fold Involved in Targeting ADAR2," *RNA*, vol. 11, pp. 592–597, 2005.

[72] S. Huang, Y.-X. Wang, and D. E. Draper, "Structure of a Hexanucleotide RNA Hairpin Loop Conserved in Ribosomal RNAs," *Journal of Molecular Biology*, vol. 258, pp. 308–321, 1996.

[73] C. Tuerk, P. Gauss, C. Thermes, D. R. Groebe, M. Gayle, N. Guild, G. Stormo, Y. d'Aubenton Carafa, O. C. Uhlenbeck, and I. Tinoco, "CUUCGG hairpins: extraordinarily stable RNA secondary structures associated with various biochemical processes," *Proceedings of the National Academy of Sciences*, vol. 85, pp. 1364–1368, 1988.

[74] D. W. Staple and S. E. Butcher, "Pseudoknots: RNA Structures with Diverse Functions," *PLoS Biol*, vol. 3, p. e213, 2005.

[75] K. Réblová, N. Špačková, J. E. Šponer, J. Koča, and J. Šponer, "Molecular dynamics simulations of RNA kissing-loop motifs reveal structural dynamics and formation of cation-binding pockets," *Nucleic Acids Research*, vol. 31, pp. 6942–6952, 2003.

[76] D. E. Draper, "RNA Folding: Thermodynamic and Molecular Descriptions of the Roles of Ions," *Biophysical Journal*, vol. 95, pp. 5489–5495, 2008.

[77] S. A. Woodson, "Compact Intermediates in RNA Folding," *Annual Review of Biophysics*, vol. 39, pp. 61–77, 2010.

[78] G. M. Arachchilage, A. C. Dassanayake, and S. Basu, "A Potassium Ion-Dependent RNA Structural Switch Regulates Human Pre-miRNA 92b Maturation," *Chemistry & Biology*, vol. 22, pp. 262–272, 2015.

[79] G. R. Zimmermann, C. L. Wick, T. P. Shields, R. D. Jenison, and A. Pardi, "Molecular interactions and metal binding in the theophylline-binding core of an RNA aptamer.," *RNA*, vol. 6, pp. 659–667, 2000.

[80] Y. V. Bukhman and D. E. Draper, "Affinities and selectivities of divalent cation binding sites within an RNA tertiary structure," *Journal of Molecular Biology*, vol. 273, pp. 1020–1031, 1997.

[81] E. Koculi, C. Hyeon, D. Thirumalai, and S. A. Woodson, "Charge Density of Divalent Metal Cations Determines RNA Stability," *Journal of the American Chemical Society*, vol. 129, pp. 2676–2682, 2007.

[82] R. Shiman and D. E. Draper, "Stabilization of RNA tertiary structure by monovalent cations," *Journal of Molecular Biology*, vol. 302, pp. 79–91, 2000.

[83] M. J. Fedor, "Comparative Enzymology and Structural Biology of RNA Self-Cleavage," *Annual Review of Biophysics*, vol. 38, pp. 271–299, 2009.

[84] S. C. Dahm and O. C. Uhlenbeck, "Role of divalent metal ions in the hammerhead RNA cleavage reaction," *Biochemistry*, vol. 30, pp. 9464–9469, 1991.

[85] M. Forconi and D. Herschlag, "[5] - Metal Ion-Based RNA Cleavage as a Structural Probe," in *Methods in Enzymology*, vol. 468 of *Biophysical, Chemical, and Functional Probes of RNA Structure, Interactions and Folding: Part A*, pp. 91–106, Academic Press, 2009.

[86] A. Sreedhara and J. A. Cowan, "Structural and catalytic roles for divalent magnesium in nucleic acid biochemistry," *Biometals*, vol. 15, pp. 211–223, 2002.

[87] A. Serganov and E. Nudler, "A Decade of Riboswitches," *Cell*, vol. 152, pp. 17–24, 2013.

[88] A. D. Garst, A. L. Edwards, and R. T. Batey, "Riboswitches: Structures and Mechanisms," *Cold Spring Harbor Perspectives in Biology*, vol. 3, 2011.

[89] A. Peselis and A. Serganov, "Themes and variations in riboswitch structure and function," *Biochimica et Biophysica Acta (BBA) - Gene Regulatory Mechanisms*, vol. 1839, pp. 908–918, 2014.

[90] A. Lussier, L. Bastet, A. Chauvier, and D. A. Lafontaine, "A Kissing-Loop is Important for BtuB Riboswitch Ligand Sensing and Regulatory Control," *Journal of Biological Chemistry*, vol. 290, pp. 26739–26751, 2015.

[91] A. Ramesh and W. C. Winkler, "Magnesium-sensing riboswitches in bacteria," *RNA Biology*, vol. 7, pp. 77–83, 2010.

[92] E. Loh, O. Dussurget, J. Gripenland, K. Vaitkevicius, T. Tiensuu, P. Mandin, F. Repoila, C. Buchrieser, P. Cossart, and J. Johansson, "A trans-Acting Riboswitch Controls Expression of the Virulence Regulator PrfA in Listeria monocytogenes," *Cell*, vol. 139, pp. 770–779, 2009.

[93] M. Famulok and G. Mayer, "Aptamers and SELEX in Chemistry & Biology," *Chemistry & Biology*, vol. 21, pp. 1055–1058, 2014.

[94] X. Fang and W. Tan, "Aptamers Generated from Cell-SELEX for Molecular Medicine: A Chemical Biology Approach," *Accounts of Chemical Research*, vol. 43, pp. 48–57, 2010.

[95] R. R. Breaker and G. F. Joyce, "A DNA enzyme that cleaves RNA," *Chemistry & Biology*, vol. 1, pp. 223–229, 1994.

[96] H. U. Göringer, M. Homann, and M. Lorger, "In vitro selection of high-affinity nucleic acid ligands to parasite target molecules," *International Journal for Parasitology*, vol. 33, pp. 1309–1317, 2003.

[97] R. Stoltenburg, C. Reinemann, and B. Strehlitz, "SELEX—A (r)evolutionary method to generate high-affinity nucleic acid ligands," *Biomolecular Engineering*, vol. 24, pp. 381–403, 2007.

[98] W. C. Johnson and I. Tinoco, "Circular dichroism of polynucleotides: A simple theory," *Biopolymers*, vol. 7, no. 5, pp. 727–749, 1969.

[99] I. Tinoco, "Hypochromism in Polynucleotides," *Journal of the American Chemical Society*, vol. 82, pp. 4785–4790, 1960.

[100] M. Kasha, H. R. Rawls, and E.-B. M. Ashraf, "The exciton model in molecular spectroscopy," *Pure and Applied Chemistry*, vol. 11, pp. 371–392, 1965.

[101] W. Rhodes, "Hypochromism and Other Spectral Properties of Helical Polynucleotides," *Journal of the American Chemical Society*, vol. 83, pp. 3609–3617, 1961.

[102] L. Rosenfeld, "Quantenmechanische Theorie der natürlichen optischen Aktivität von Flüssigkeiten und Gasen," *Zeitschrift für Physik*, vol. 52, pp. 161–174, 1929.

[103] J. G. Kirkwood, "On the Theory of Optical Rotatory Power," *The Journal of Chemical Physics*, vol. 5, pp. 479–491, 1937.

[104] J. Brahms, "Circular Dichroism of Helical Polynucleotide Chains," *Proceedings of the Royal Society of London. Series A, Mathematical and Physical Sciences*, vol. 297, pp. 150–162, 1967.

[105] I. Tinoco and R. W. Woody, "Optical Rotation of Oriented Helices. IV. A Free Electron on a Helix," *The Journal of Chemical Physics*, vol. 40, pp. 160–165, 1964.

[106] J.-C. Diels and W. Rudolph, *Ultrashort Laser Pulse Phenomena*. Academic Press, 2006.

[107] R. W. Boyd, *Nonlinear Optics*.
Amsterdam ; Boston: Academic Press, 3rd ed., 2008.

[108] W. Demtröder, *Laser Spectroscopy, Vol. 1: Basic Principles*.
Springer Berlin Heidelberg, 4th ed., 2008.

[109] T. Fließbach, *Elektrodynamik: Lehrbuch zur Theoretischen Physik II*.
Spektrum Akademischer Verlag, 6th ed., 2012.

[110] R. J. Iorio Jr. and V. de Magalhaes Iorio, *Fourier Analysis and Partial Differential Equations*.
Cambridge University Press, 1st ed., 2001.

[111] A. M. Weiner, *Ultrafast Optics*.
Wiley Series in Pure and Applied Optics, John Wiley & Sons, Ltd, 1st ed., 2009.

[112] D. N. Nikogosyan, *Nonlinear Optical Crystals: A Complete Survey*.
Springer, 1st ed., 2005.

[113] J. A. Giordmaine, "Mixing of Light Beams in Crystals," *Physical Review Letters*, vol. 8, pp. 19–20, 1962.

[114] P. D. Maker, R. W. Terhune, M. Nisenoff, and C. M. Savage, "Effects of Dispersion and Focusing on the Production of Optical Harmonics," *Physical Review Letters*, vol. 8, pp. 21–22, 1962.

[115] W. Zinth and U. Zinth, *Optik: Lichtstrahlen - Wellen - Photonen*.
Oldenbourg Wissenschaftsverlag, improved ed., 2011.

[116] A. Shirakawa and T. Kobayashi, "Noncollinearly phase-matched femtosecond optical parametric amplification with a 2000 cm-1 bandwidth," *Applied Physics Letters*, vol. 72, pp. 147–149, 1998.

[117] E. Riedle, M. Beutter, S. Lochbrunner, J. Piel, S. Schenkl, S. Spörlein, and W. Zinth, "Generation of 10 to 50 fs pulses tunable through all of the visible and the NIR," *Applied Physics B*, vol. 71, pp. 457–465, 2000.

[118] F. Silva, D. R. Austin, A. Thai, M. Baudisch, M. Hemmer, D. Faccio, A. Couairon, and J. Biegert, "Multi-octave supercontinuum generation from mid-infrared filamentation in a bulk crystal," *Nature Communications*, vol. 3: 807, pp. 1–5, 2012.

[119] A. L. Gaeta, "Catastrophic Collapse of Ultrashort Pulses," *Physical Review Letters*, vol. 84, pp. 3582–3585, 2000.

[120] H. Ward and L. Bergé, "Temporal Shaping of Femtosecond Solitary Pulses in Photoionized Media," *Physical Review Letters*, vol. 90, pp. 053901 (1–4), 2003.

[121] J. Liu, H. Schroeder, S. L. Chin, R. Li, and Z. Xu, "Nonlinear propagation of fs laser pulses in liquids and evolution of supercontinuum generation," *Optics Express*, vol. 13, pp. 10248–10259, 2005.

[122] B. Wetzel, A. Stefani, L. Larger, P. A. Lacourt, J. M. Merolla, T. Sylvestre, A. Kudlinski, A. Mussot, G. Genty, F. Dias, and J. M. Dudley, "Real-time full bandwidth measurement of spectral noise in supercontinuum generation," *Scientific Reports*, vol. 2: 882, pp. 1–7, 2012.

[123] S. Coen, A. H. L. Chau, R. Leonhardt, J. D. Harvey, J. C. Knight, W. J. Wadsworth, and P. S. J. Russell, "Supercontinuum generation by stimulated Raman scattering and parametric four-wave mixing in photonic crystal fibers," *Journal of the Optical Society of America B*, vol. 19, pp. 753–764, 2002.

[124] E. P. Ippen, H. A. Haus, and L. Y. Liu, "Additive pulse mode locking," *Journal of the Optical Society of America B*, vol. 6, p. 1736, 1989.

[125] K. R. Tamura, E. P. Ippen, H. A. Haus, L. E. Nelson, and C. R. Doerr, "Stretched-pulse fiber laser,", 1997.
Patent; US Classification 372/6, 372/10, 372/25, 372/94, 372/70, 372/18; International Classification H01S3/098, H01S3/067; Enterprise Classification H01S3/1112, Y10S372/70, H01S3/06725, H01S3/06791, H01S3/06712, H01S2301/08; European Classification H01S3/067R.

[126] P. Maine, D. Strickland, P. Bado, M. Pessot, and G. Mourou, "Generation of ultrahigh peak power pulses by chirped pulse amplification," *IEEE Journal of Quantum Electronics*, vol. 24, pp. 398–403, 1988.

[127] D. Strickland and G. Mourou, "Compression of amplified chirped optical pulses," *Optics Communications*, vol. 56, pp. 219–221, 1985.

[128] M. Pessot, P. Maine, and G. Mourou, "1000 times expansion/compression of optical pulses for chirped pulse amplification," *Optics Communications*, vol. 62, pp. 419–421, 1987.

[129] J. E. Midwinter and J. Warner, "The effects of phase matching method and of uniaxial crystal symmetry on the polar distribution of second-order non-linear optical polarization," *British Journal of Applied Physics*, vol. 16, p. 1135, 1965.

[130] T. Wilhelm, J. Piel, and E. Riedle, "Sub-20-fs pulses tunable across the visible from a blue-pumped single-pass noncollinear parametric converter," *Optics Letters*, vol. 22, pp. 1494–1496, 1997.

[131] S. Lochbrunner, T. Wilhelm, J. Piel, P. Huppmann, S. Spörlein, and E. Riedle, "Tunable Visible and NIR Parametric Amplifiers at 1 kHz and Pulse Lengths Down to 10 fs," in *Ultrafast Phenomena XI* (F. P. Schäfer, J. P. Toennies, and W. Zinth, eds.), vol. 63, pp. 57–59, Springer Berlin Heidelberg, 1998.

[132] J. Warner, "Phase-matching for optical up-conversion with maximum angular aperture — theory and practice," *Opto-electronics*, vol. 1, pp. 25–28, 1969.

[133] C. Slavov, H. Hartmann, and J. Wachtveitl, "Implementation and Evaluation of Data Analysis Strategies for Time-Resolved Optical Spectroscopy," *Analytical Chemistry*, vol. 87, pp. 2328–2336, 2015.

[134] S. A. Kovalenko, A. L. Dobryakov, J. Ruthmann, and N. P. Ernsting, "Femtosecond spectroscopy of condensed phases with chirped supercontinuum probing," *Physical Review A*, vol. 59, pp. 2369–2384, 1999.

[135] A. L. Dobryakov, S. A. Kovalenko, A. Weigel, J. L. Pérez-Lustres, J. Lange, A. Müller, and N. P. Ernsting, "Femtosecond pump/supercontinuum-probe spectroscopy: Optimized setup and signal analysis for single-shot spectral referencing," *Review of Scientific Instruments*, vol. 81, pp. 113106 (1–9), 2010.

[136] P. Trojanowski, J. Plötner, C. Grünewald, F. F. Graupner, C. Slavov, A. J. Reuss, M. Braun, J. W. Engels, and J. Wachtveitl, "Photo-physical properties of 2-(1-ethynylpyrene)-adenosine: influence of hydrogen bonding on excited state properties," *Physical Chemistry Chemical Physics*, vol. 16, pp. 13875–13888, 2014.

[137] V. V. Filichev, I. V. Astakhova, A. D. Malakhov, V. A. Korshun, and E. B. Pedersen, "1-, 2-, and 4-Ethyhnylpyrenes in the Structure of Twisted Intercalating Nucleic Acids: Structure, Thermal Stability, and Fluorescence Relationship.," *Chemistry - A European Journal*, vol. 14, pp. 9968–9980, 2008.

[138] M. J. Robins and B. Uznański, "Nucleic acid related compounds. 33. Conversions of adenosine and guanosine to 2,6-dichloro, 2-amino-6-chloro, and derived purine nucleosides," *Canadian Journal of Chemistry*, vol. 59, pp. 2601–2607, 1981.

[139] V. Nair and S. G. Richardson, "Modification of Nucleic Acid Bases via Radical Intermediates: Synthesis of Dihalogenated Purine Nucleosides," *Synthesis*, vol. 1982, pp. 670–672, 1982.

[140] K. Sonogashira, "Development of Pd–Cu catalyzed cross-coupling of terminal acetylenes with sp2-carbon halides," *Journal of Organometallic Chemistry*, vol. 653, pp. 46–49, 2002.

[141] V. Nair and D. A. Young, "A new synthesis of isoguanosine," *The Journal of Organic Chemistry*, vol. 50, pp. 406–408, 1985.

[142] A. Matsuda, M. Shinozaki, M. Suzuki, K. Watanabe, and T. Miyasaka, "A Convenient Method for the Selective Acylation of Guanine Nucleosides," *Synthesis*, vol. 1986, pp. 385–386, 1986.

[143] P. V. Vyas, A. K. Bhatt, G. Ramachandraiah, and A. V. Bedekar, "Environmentally benign chlorination and bromination of aromatic amines, hydrocarbons and naphthols," *Tetrahedron Letters*, vol. 44, pp. 4085–4088, 2003.

[144] H. Vollmann, H. Becker, M. Corell, and H. Streeck, "Beiträge zur Kenntnis des Pyrens und seiner Derivate," *Justus Liebigs Annalen der Chemie*, vol. 531, pp. 1–159, 1937.

[145] A. Musa, B. Sridharan, H. Lee, and D. L. Mattern, "7-Amino-2-pyrenecarboxylic Acid," *The Journal of Organic Chemistry*, vol. 61, pp. 5481–5484, 1996.

[146] D. M. Connor, S. D. Allen, D. M. Collard, C. L. Liotta, and D. A. Schiraldi, "Efficient Synthesis of 4,5,9,10-Tetrahydropyrene: A Useful Synthetic Intermediate for the Synthesis of 2,7-Disubstituted Pyrenes," *The Journal of Organic Chemistry*, vol. 64, pp. 6888–6890, 1999.

[147] M. Bydder, A. Rahal, G. D. Fullerton, and G. M. Bydder, "The magic angle effect: A source of artifact, determinant of image contrast, and technique for imaging," *Journal of Magnetic Resonance Imaging*, vol. 25, pp. 290–300, 2007.

[148] K. Suzuki, A. Kobayashi, S. Kaneko, K. Takehira, T. Yoshihara, H. Ishida, Y. Shiina, S. Oishi, and S. Tobita, "Reevaluation of absolute luminescence quantum yields of standard solutions using a spectrometer with an integrating sphere and a back-thinned CCD detector," *Physical Chemistry Chemical Physics*, vol. 11, pp. 9850–9860, 2009.

[149] L. M. Bollinger and G. E. Thomas, "Measurement of the Time Dependence of Scintillation Intensity by a Delayed-Coincidence Method," *Review of Scientific Instruments*, vol. 32, pp. 1044–1050, 1961.

[150] D. V. O'Connor, *Time-Correlated Single Photon Counting*.
Academic Press, 1984.

[151] P. Kapusta, M. Wahl, and R. Erdmann, eds., *Advanced Photon Counting: Applications, Methods, Instrumentation*.
Springer Series on Fluorescence, Springer, 2015.

[152] W. Becker, *The bh TCSPC Handbook*.
Berlin: http://www.becker-hickl.de/, 6th ed., 2015.

[153] A. G. Crawford, A. D. Dwyer, Z. Liu, A. Steffen, A. Beeby, L.-O. Palsson, D. J. Tozer, and T. B. Marder, "Experimental and Theoretical Studies of the Photophysical Properties of 2- and 2,7-Functionalized Pyrene Derivatives," *Journal of the American Chemical Society*, vol. 133, pp. 13349–13362, 2011.

[154] A. J. Reuss, C. Grünewald, M. Braun, J. W. Engels, and J. Wachtveitl, "The Three Possible 2-(Pyrenylethynyl) Adenosines: Rotameric Energy Barriers Govern the Photodynamics of These Structural Isomers," *ChemPhysChem*, pp. 1–8, 2016.

[155] A. Bree and V. V. B. Vilkos, "Assignment of the Two Lowest Singlet States of Pyrene," *The Journal of Chemical Physics*, vol. 40, pp. 3125–3126, 1964.

[156] I. B. Berlman, *Handbook of Fluorescence Spectra of Aromatic Molecules*. Academic Pr, 2nd ed., 1971.

[157] P. Foggi, L. Pettini, I. Santa, R. Righini, and S. Califano, "Transient absorption and vibrational relaxation dynamics of the lowest excited singlet state of pyrene in solution," *The Journal of Physical Chemistry*, vol. 99, pp. 7439–7445, 1995.

[158] F. V. R. Neuwahl and P. Foggi, "Direct Observation of S2–S1 Internal Conversion in Pyrene by Femtosecond Transient Absorption," *Laser Chemistry*, vol. 19, pp. 375–379, 1999.

[159] A. Nakajima, "Effects of isomeric solvents on vibronic band intensities in fluorescence spectrum of pyrene," *Journal of Molecular Spectroscopy*, vol. 61, pp. 467–469, 1976.

[160] K. Kalyanasundaram and J. K. Thomas, "Environmental effects on vibronic band intensities in pyrene monomer fluorescence and their application in studies of micellar systems," *Journal of the American Chemical Society*, vol. 99, pp. 2039–2044, 1977.

[161] J. Sung, P. Kim, Y. O. Lee, J. S. Kim, and D. Kim, "Characterization of Ultrafast Intramolecular Charge Transfer Dynamics in Pyrenyl Derivatives: Systematic Change of the Number of Peripheral N,N-Dimethyaniline Substituents," *The Journal of Physical Chemistry Letters*, vol. 2, pp. 818–823, 2011.

[162] U. Förster, N. Gildenhoff, C. Grünewald, J. W. Engels, and J. Wachtveitl, "Photophysics of 1-ethynylpyrene-modified RNA base adenine," *Journal of Luminescence*, vol. 129, pp. 1454–1458, 2009.

[163] W. Weigel, W. Rettig, M. Dekhtyar, C. Modrakowski, M. Beinhoff, and A. D. Schlüter, "Dual Fluorescence of Phenyl and Biphenyl Substituted Pyrene Derivatives," *The Journal of Physical Chemistry A*, vol. 107, pp. 5941–5947, 2003.

[164] M. Dekhtyar, W. Rettig, and W. Weigel, "Mesomeric and twisted intramolecular-charge-transfer states as a key to polarity-dependent fluorescence of donor–acceptor-substituted aryl pyrenes," *Chemical Physics*, vol. 344, pp. 237–250, 2008.

[165] T. L. Netzel, K. Nafisi, J. Headrick, and B. E. Eaton, "Direct Observation of Photoinduced Electron Transfer in Pyrene-Labeled dU Nucleosides and Evidence for Protonated 2'-Deoxyuridine Anion, dU(H), as a Primary Electron Transfer Product," *The Journal of Physical Chemistry*, vol. 99, pp. 17948–17955, 1995.

[166] M. Raytchev, E. Mayer, N. Amann, H.-A. Wagenknecht, and T. Fiebig, "Ultrafast Proton-Coupled Electron-Transfer Dynamics in Pyrene-Modified Pyrimidine Nucleosides: Model Studies towards an Understanding of Reductive Electron Transport in DNA," *ChemPhysChem*, vol. 5, pp. 706–712, 2004.

[167] A. Trifonov, I. Buchvarov, H.-A. Wagenknecht, and T. Fiebig, "Real-time observation of hydrogen bond-assisted electron transfer to a DNA base," *Chemical Physics Letters*, vol. 409, pp. 277–280, 2005.

[168] A. Trifonov, M. Raytchev, I. Buchvarov, M. Rist, J. Barbaric, H.-A. Wagenknecht, and T. Fiebig, "Ultrafast Energy Transfer and Structural Dynamics in DNA," *The Journal of Physical Chemistry B*, vol. 109, pp. 19490–19495, 2005.

[169] P. Kaden, E. Mayer-Enthart, A. Trifonov, T. Fiebig, and H.-A. Wagenknecht, "Real-Time Spectroscopic and Chemical Probing of Reductive Electron Transfer in DNA," *Angewandte Chemie International Edition*, vol. 44, pp. 1636–1639, 2005.

[170] M. Manoharan, K. L. Tivel, M. Zhao, K. Nafisi, and T. L. Netzel, "Base-Sequence Dependence of Emission Lifetimes for DNA Oligomers and Duplexes Covalently Labeled with Pyrene: Relative Electron-Transfer Quenching Efficiencies of A, G, C, and T Nucleosides toward Pyrene," *The Journal of Physical Chemistry*, vol. 99, pp. 17461–17472, 1995.

[171] E. Mayer, L. Valis, R. Huber, N. Amann, and H.-A. Wagenknecht, "Preparation of pyrene-modified purine and pyrimidine nucleosides via Suzuki-Miyaura cross-couplings and characterization of their fluorescent properties," *Synthesis*, vol. 15, pp. 2335–2340, 2003.

[172] R. Huber, T. Fiebig, and H.-A. Wagenknecht, "Pyrene as a fluorescent probe for DNA base radicals," *Chemical Communications*, pp. 1878–1879, 2003.

[173] K. A. Zachariasse, "Comment on "Pseudo-Jahn–Teller and TICT-models: a photophysical comparison of meta-and para-DMABN derivatives" [Chem. Phys. Lett. 305 (1999) 8]: The PICT model for dual fluorescence of aminobenzonitriles," *Chemical Physics Letters*, vol. 320, pp. 8–13, 2000.

[174] A. S. Ladokhin, "Red-Edge Excitation Study of Nonexponential Fluorescence Decay of Indole in Solution and in a Protein," *Journal of Fluorescence*, vol. 9, pp. 1–9, 1999.

[175] I. Isenberg and R. D. Dyson, "The Analysis of Fluorescence Decay by a Method of Moments," *Biophysical Journal*, vol. 9, pp. 1337–1350, 1969.

[176] A. Gafni, R. L. Modlin, and L. Brand, "Analysis of fluorescence decay curves by means of the Laplace transformation.," *Biophysical Journal*, vol. 15, pp. 263–280, 1975.

[177] E. Fišerová and M. Kubala, "Mean fluorescence lifetime and its error," *Journal of Luminescence*, vol. 132, pp. 2059–2064, 2012.

[178] A. Demeter, T. Bérces, and K. A. Zachariasse, "Dual Fluorescence and Intramolecular Charge Transfer with N-Phenylphenanthridinones," *The Journal of Physical Chemistry A*, vol. 105, pp. 4611–4621, 2001.

[179] M. J. Frisch, G. W. Trucks, H. B. Schlegel, G. E. Scuseria, M. A. Robb, J. R. Cheeseman, G. Scakmani, V. Barone, B. Mennucci, G. A. Petersson,

H. Nakatsuji, M. Caricato, X. Li, H. P. Hratchian, A. F. Izmaylov, J. Bloino, G. Zheng, J. l. Sonnenberg, M. Hada, M. Ehara, K. Toyota, R. Fukuda, J. Hasegawa, M. Ishida, T. Nakajima, Y. Honda, O. Kitao, H. Nakai, T. Vreven, J. A. Montgomery, J. E. Peralta, Jr., F. Ogliaro, M. Bearpark, J. J. Heyd, E. Brothers, K. N. Kudin, V. N. Staroverov, R. Kobayashi, J. Normand, K. Raghavachari, A. Rendell, J. C. Burant, S. S. Iyengar, J. Tomasi, M. Cossi, N. Rega, J. M. Millam, M. Klene, J. E. Knox, J. B. Cross, V. Bakken, C. Adamo, J. Jaramillo, R. Gomperts, R. E. Stratmann, O. Yazyev, A. J. Austin, R. Cammi, C. Pomelli, J. W. Ochterski, R. L. Martin, K. Morokuma, V. G. Zakrzewski, G. A. Voth, P. Salvador, J. J. Dannenberg, S. Dapprich, A. D. Daniels, . Farkas, J. B. Foresman, J. V. Ortiz, J. Cioslowski, and D. J. Fox, "Gaussian 09, Revision D.01," *Gaussian, Inc., Wallingford CT*, 2009.

[180] University of Karlsruhe and Forschungszentrum Karlsruhe GmbH (1989–2007) and TURBOMOLE GmbH (since 2007), "Turbomole V6.4," *http//:www.turbomole.com*, 2012.

[181] R. Ahlrichs, M. Bär, M. Häser, H. Horn, and C. Kölmel, "Electronic structure calculations on workstation computers: The program system turbomole," *Chemical Physics Letters*, vol. 162, pp. 165–169, 1989.

[182] C. Steffen, K. Thomas, U. Huniar, A. Hellweg, O. Rubner, and A. Schroer, "TmoleX—A graphical user interface for TURBOMOLE," *Journal of Computational Chemistry*, vol. 31, pp. 2967–2970, 2010.

[183] F. Haase and R. Ahlrichs, "Semidirect MP2 gradient evaluation on workstation computers: The MPGRAD program," *Journal of Computational Chemistry*, vol. 14, pp. 907–912, 1993.

[184] O. Christiansen, H. Koch, and P. Jørgensen, "The second-order approximate coupled cluster singles and doubles model CC2," *Chemical Physics Letters*, vol. 243, pp. 409–418, 1995.

[185] C. Hättig and F. Weigend, "CC2 excitation energy calculations on large molecules using the resolution of the identity approximation," *The Journal of Chemical Physics*, vol. 113, pp. 5154–5161, 2000.

[186] C. Hättig, "Geometry optimizations with the coupled-cluster model CC2 using the resolution-of-the-identity approximation," *The Journal of Chemical Physics*, vol. 118, pp. 7751–7761, 2003.

[187] C. Hättig, A. Hellweg, and A. Köhn, "Distributed memory parallel implementation of energies and gradients for second-order Møller–Plesset perturbation theory with the resolution-of-the-identity approximation," *Physical Chemistry Chemical Physics*, vol. 8, pp. 1159–1169, 2006.

[188] R. Ahlrichs, "Efficient evaluation of three-center two-electron integrals over Gaussian functions," *Physical Chemistry Chemical Physics*, vol. 6, pp. 5119–5121, 2004.

[189] F. Weigend and R. Ahlrichs, "Balanced basis sets of split valence, triple zeta valence and quadruple zeta valence quality for H to Rn: Design and assessment of accuracy," *Physical Chemistry Chemical Physics*, vol. 7, pp. 3297–3305, 2005.

[190] F. Weigend, M. Häser, H. Patzelt, and R. Ahlrichs, "RI-MP2: optimized auxiliary basis sets and demonstration of efficiency," *Chemical Physics Letters*, vol. 294, pp. 143–152, 1998.

[191] C. Hättig and A. Köhn, "Transition moments and excited-state first-order properties in the coupled-cluster model CC2 using the resolution-of-the-identity approximation," *The Journal of Chemical Physics*, vol. 117, pp. 6939–6951, 2002.

[192] C. Hättig and K. Hald, "Implementation of RI-CC2 triplet excitation energies with an application to trans-azobenzene," *Physical Chemistry Chemical Physics*, vol. 4, pp. 2111–2118, 2002.

[193] C. Hättig, A. Köhn, and K. Hald, "First-order properties for triplet excited states in the approximated coupled cluster model CC2 using an explicitly spin coupled basis," *The Journal of Chemical Physics*, vol. 116, pp. 5401–5410, 2002.

[194] "Jmol: an open-source Java viewer for chemical structures in 3d. http://www.jmol.org/," 2013.

[195] Z. R. Grabowski, K. Rotkiewicz, and A. Siemiarczuk, "Dual fluorescence of donor-acceptor molecules and the Twisted Intramolecular Charge Transfer (TICT) states," *Journal of Luminescence*, vol. 18–19, Part 1, pp. 420–424, 1979.

[196] S. J. Greaves, E. L. Flynn, E. L. Futcher, E. Wrede, D. P. Lydon, P. J. Low, S. R. Rutter, and A. Beeby, "Cavity Ring-Down Spectroscopy of the Torsional Motions of 1,4-Bis(phenylethynyl)benzene," *The Journal of Physical Chemistry A*, vol. 110, pp. 2114–2121, 2006.

[197] W. C. Galley and R. M. Purkey, "Role of Heterogeneity of the Solvation Site in Electronic Spectra in Solution," *Proceedings of the National Academy of Sciences*, vol. 67, pp. 1116–1121, 1970.

[198] K. Itoh and T. Azumi, "Shift of emission band upon excitation at the long wavelength absorption edge. 1. A preliminary survey for quinine and related compounds," *Chemical Physics Letters*, vol. 22, pp. 395–399, 1973.

[199] B. Valeur and G. Weber, "A new red-dege effect in aromatic molecules: Anomaly of apparent rotation revealed by fluorescence polarization," *The Journal of Chemical Physics*, vol. 69, pp. 2393–2400, 1978.

[200] A. N. Rubinov, V. I. Tomin, and B. A. Bushuk, "Kinetic spectroscopy of orientational states of solvated dye molecules in polar solutions," *Journal of Luminescence*, vol. 26, pp. 377–391, 1982.

[201] S. Murata, C. Iwanaga, T. Toda, and H. Kokubun, "Fluorescence yields of azulene derivatives," *Chemical Physics Letters*, vol. 13, pp. 101–104, 1972.

[202] T. Förster, "Molecular Electronic Spectroscopy," *Annual Review of Physical Chemistry*, vol. 8, pp. 331–352, 1957.

[203] R. Englman and J. Jortner, "The energy gap law for radiationless transitions in large molecules," *Molecular Physics*, vol. 18, pp. 145–164, 1970.

[204] H.-B. Lin and M. R. Topp, "Low quantum-yield molecular fluorescence. Aromatic hydrocarbons in solution at 300 K," *Chemical Physics Letters*, vol. 48, pp. 251–255, 1977.

[205] C. G. Morgante and W. S. Struve, "S2 → S0 fluorescence in trans-azobenzene," *Chemical Physics Letters*, vol. 68, pp. 267–271, 1979.

[206] P. A. Geldof, R. P. H. Rettschnick, and G. J. Hoytink, "Fluorescence from the second excited singlets of pyrene and 3,4-benzpyrene," *Chemical Physics Letters*, vol. 4, pp. 59–61, 1969.

[207] P. A. Geldof, R. P. H. Rettschnick, and G. J. Hoytink, "Vibronic coupling and radiative transitions," *Chemical Physics Letters*, vol. 10, pp. 549–558, 1971.

[208] M. Chessin, R. Livingston, and T. G. Truscott, "Direct evidence for the sensitized formation of a metastable state of beta-carotene," *Transactions of the Faraday Society*, vol. 62, pp. 1519–1524, 1966.

[209] M. Kasha and R. V. Nauman, "The Metastability of the Lowest Excited Singlet Level of Naphthalene," *The Journal of Chemical Physics*, vol. 17, pp. 516–520, 1949.

[210] A. Warshel and M. Karplus, "Calculation of ground and excited state potential surfaces of conjugated molecules. I. Formulation and parametrization," *Journal of the American Chemical Society*, vol. 94, pp. 5612–5625, 1972.

[211] C. Adamo and D. Jacquemin, "The calculations of excited-state properties with Time-Dependent Density Functional Theory," *Chemical Society Reviews*, vol. 42, pp. 845–856, 2013.

[212] H. Xiao, T. E. Edwards, and A. R. Ferré-D'Amaré, "Structural Basis for Specific, High-Affinity Tetracycline Binding by an In Vitro Evolved Aptamer and Artificial Riboswitch," *Chemistry & Biology*, vol. 15, pp. 1125–1137, 2008.

[213] F. R. Kramer, D. R. Mills, P. E. Cole, T. Nishihara, and S. Spiegelman, "Evolution in vitro: Sequence and phenotype of a mutant RNA resistant to ethidium bromide," *Journal of Molecular Biology*, vol. 89, pp. 719–736, 1974.

[214] A. D. Ellington and J. W. Szostak, "In vitro selection of RNA molecules that bind specific ligands," *Nature*, vol. 346, pp. 818–822, 1990.

[215] S. Hanson, K. Berthelot, B. Fink, J. E. G. McCarthy, and B. Suess, "Tetracycline-aptamer-mediated translational regulation in yeast," *Molecular Microbiology*, vol. 49, pp. 1627–1637, 2003.

[216] J. E. Weigand and B. Suess, "Tetracycline aptamer-controlled regulation of pre-mRNA splicing in yeast," *Nucleic Acids Research*, vol. 35, pp. 4179–4185, 2007.

[217] A. Wittmann and B. Suess, "Selection of tetracycline inducible self-cleaving ribozymes as synthetic devices for gene regulation in yeast," *Molecular BioSystems*, vol. 7, pp. 2419–2427, 2011.

[218] S. Demolli, M. M. Geist, J. E. Weigand, N. Matschiavelli, B. Suess, and M. Rother, "Development of beta-Lactamase as a Tool for Monitoring Conditional Gene Expression by a Tetracycline-Riboswitch in *Methanosarcina acetivorans*," *Archaea*, vol. 2014, pp. e725610 (1–10), 2014.

[219] G. Werstuck and M. R. Green, "Controlling Gene Expression in Living Cells Through Small Molecule-RNA Interactions," *Science*, vol. 282, pp. 296–298, 1998.

[220] D. Grate and C. Wilson, "Inducible regulation of the S. cerevisiae cell cycle mediated by an RNA aptamer–ligand complex," *Bioorganic & Medicinal Chemistry*, vol. 9, pp. 2565–2570, 2001.

[221] B. Suess, B. Fink, C. Berens, R. Stentz, and W. Hillen, "A theophylline responsive riboswitch based on helix slipping controls gene expression in vivo," *Nucleic Acids Research*, vol. 32, pp. 1610–1614, 2004.

[222] D.-S. Kim, V. Gusti, S. G. Pillai, and R. K. Gaur, "An artificial riboswitch for controlling pre-mRNA splicing," *RNA*, vol. 11, pp. 1667–1677, 2005.

[223] M. Wachsmuth, S. Findeiß, N. Weissheimer, P. F. Stadler, and M. Mörl, "De novo design of a synthetic riboswitch that regulates transcription termination," *Nucleic Acids Research*, vol. 41, pp. 2541–2551, 2013.

[224] J. E. Weigand, M. Sanchez, E.-B. Gunnesch, S. Zeiher, R. Schroeder, and B. Suess, "Screening for engineered neomycin riboswitches that control translation initiation," *RNA*, vol. 14, pp. 89–97, 2007.

[225] J. E. Weigand, S. R. Schmidtke, T. J. Will, E. Duchardt-Ferner, C. Hammann, J. Wöhnert, and B. Suess, "Mechanistic insights into an engineered riboswitch: a switching element which confers riboswitch activity," *Nucleic Acids Research*, vol. 39, pp. 3363–3372, 2011.

[226] L. C. Bock, L. C. Griffin, J. A. Latham, E. H. Vermaas, and J. J. Toole, "Selection of single-stranded DNA molecules that bind and inhibit human thrombin," *Nature*, vol. 355, pp. 564–566, 1992.

[227] S. R. Martin, "Equilibrium and kinetic studies on the interaction of tetracyclines with calcium and magnesium," *Biophysical Chemistry*, vol. 10, pp. 319–326, 1979.

[228] E. C. Newman and C. W. Frank, "Circular dichroism spectra of tetracycline complexes with Mg+2 and Ca+2," *Journal of Pharmaceutical Sciences*, vol. 65, pp. 1728–1732, 1976.

[229] L. Lambs, B. Decock-Le Reverend, H. Kozlowski, and G. Berthon, "Metal ion-tetracycline interactions in biological fluids. 9. Circular dichroism spectra of calcium and magnesium complexes with tetracycline, oxytetracycline, doxycycline, and chlortetracycline and discussion of their binding modes," *Inorganic Chemistry*, vol. 27, pp. 3001–3012, 1988.

[230] V. I. Ivanov, L. E. Minchenkova, A. K. Schyolkina, and A. I. Poletayev, "Different conformations of double-stranded nucleic acid in solution as revealed by circular dichroism," *Biopolymers*, vol. 12, pp. 89–110, 1973.

[231] B. Ranjbar and P. Gill, "Circular Dichroism Techniques: Biomolecular and Nanostructural Analyses- A Review," *Chemical Biology & Drug Design*, vol. 74, pp. 101–120, 2009.

[232] T. Pan and T. R. Sosnick, "Intermediates and kinetic traps in the folding of a large ribozyme revealed by circular dichroism and UV absorbance spectroscopies and catalytic activity," *Nature Structural & Molecular Biology*, vol. 4, pp. 931–938, 1997.

[233] T. R. Sosnick, X. Fang, and V. M. Shelton, "[24] Application of circular dichroism to study RNA folding transitions," in *Methods in Enzymology*, vol. 317 of *RNA - Ligand Interactions, Part A*, pp. 393–409, Elsevier, 2000.

[234] D. E. Draper, D. Grilley, and A. M. Soto, "Ions and RNA Folding," *Annual Review of Biophysics and Biomolecular Structure*, vol. 34, pp. 221–243, 2005.

[235] L. Jin, X. Amaya-Mazo, M. E. Apel, S. S. Sankisa, E. Johnson, M. A. Zbyszynska, and A. Han, "Ca2+ and Mg2+ bind tetracycline with distinct stoichiometries and linked deprotonation," *Biophysical Chemistry*, vol. 128, pp. 185–196, 2007.

[236] M. L. Doyle, "Characterization of binding interactions by isothermal titration calorimetry," *Current Opinion in Biotechnology*, vol. 8, pp. 31–35, 1997.

[237] R. Ghai, R. J. Falconer, and B. M. Collins, "Applications of isothermal titration calorimetry in pure and applied research-survey of the literature from 2010," *Journal of Molecular Recognition*, vol. 25, pp. 32–52, 2012.

[238] M. M. Pierce, C. Raman, and B. T. Nall, "Isothermal Titration Calorimetry of Protein–Protein Interactions," *Methods*, vol. 19, pp. 213–221, 1999.

[239] W. H. Ward and G. A. Holdgate, "Isothermal titration calorimetry in drug discovery," *Progress in Medicinal Chemistry*, vol. 38, pp. 309–376, 2001.

[240] M. W. Freyer and E. A. Lewis, "Isothermal Titration Calorimetry: Experimental Design, Data Analysis, and Probing Macromolecule/Ligand Binding and Kinetic Interactions," in *Methods in Cell Biology*, vol. 84, pp. 79–113, Elsevier, 2008.

[241] D. E. Wilcox, "Isothermal titration calorimetry of metal ions binding to proteins: An overview of recent studies," *Inorganica Chimica Acta*, vol. 361, pp. 857–867, 2008.

[242] F. Zidane, A. Matéos, C. Cakir-Kiefer, L. Miclo, S. Rahuel-Clermont, J.-M. Girardet, and C. Corbier, "Binding of divalent metal ions to 1–25 beta-caseinophosphopeptide: An isothermal titration calorimetry study," *Food Chemistry*, vol. 132, pp. 391–398, 2012.

[243] A. L. Feig, "Applications of isothermal titration calorimetry in RNA biochemistry and biophysics," *Biopolymers*, vol. 87, pp. 293–301, 2007.

[244] C. Hammann, A. Cooper, and D. M. J. Lilley, "Thermodynamics of Ion-Induced RNA Folding in the Hammerhead Ribozyme: An Isothermal Titration Calorimetric Study," *Biochemistry*, vol. 40, pp. 1423–1429, 2001.

[245] N. E. Grossoehme, A. M. Spuches, and D. E. Wilcox, "Application of isothermal titration calorimetry in bioinorganic chemistry," *JBIC Journal of Biological Inorganic Chemistry*, vol. 15, pp. 1183–1191, 2010.

[246] A. V. Hill, "The possible effects of the aggregation of the molecules of haemoglobin on its dissociation curves," *The Journal of Physiology*, vol. 40, pp. iv–vii, 1910.

[247] S. Goutelle, M. Maurin, F. Rougier, X. Barbaut, L. Bourguignon, M. Ducher, and P. Maire, "The Hill equation: a review of its capabilities in pharmacological modelling," *Fundamental & Clinical Pharmacology*, vol. 22, pp. 633–648, 2008.

[248] J. N. Weiss, "The Hill equation revisited: uses and misuses.," *The FASEB Journal*, vol. 11, pp. 835–841, 1997.

[249] V. K. Misra and D. E. Draper, "The linkage between magnesium binding and RNA folding," *Journal of Molecular Biology*, vol. 317, pp. 507–521, 2002.

[250] V. K. Misra, R. Shiman, and D. E. Draper, "A thermodynamic framework for the magnesium-dependent folding of RNA," *Biopolymers*, vol. 69, pp. 118–136, 2003.

[251] X. Fang, T. Pan, and T. R. Sosnick, "A Thermodynamic Framework and Cooperativity in the Tertiary Folding of a Mg^{2+} -Dependent Ribozyme," *Biochemistry*, vol. 38, pp. 16840–16846, 1999.

[252] S. A. Woodson, "Metal ions and RNA folding: a highly charged topic with a dynamic future," *Current Opinion in Chemical Biology*, vol. 9, pp. 104–109, 2005.

[253] J.-L. Mergny and L. Lacroix, "Analysis of Thermal Melting Curves," *Oligonucleotides*, vol. 13, pp. 515–537, 2003.

[254] D. M. Lilley, "Structure, folding and catalysis of the small nucleolytic ribozymes," *Current Opinion in Structural Biology*, vol. 9, pp. 330–338, 1999.

[255] L. Jovine, S. Djordjevic, and D. Rhodes, "The crystal structure of yeast phenylalanine tRNA at 2.0 Å resolution: cleavage by Mg2+ in 15-year old crystals," *Journal of Molecular Biology*, vol. 301, pp. 401–414, 2000.

[256] K. Sharp, "Entropy–enthalpy compensation: Fact or artifact?," *Protein Science*, vol. 10, pp. 661–667, 2001.

[257] A. Cornish-Bowden, "Enthalpy–entropy compensation: a phantom phenomenon," *Journal of Biosciences*, vol. 27, pp. 121–126, 2002.

[258] E. D. Holmstrom and D. J. Nesbitt, "Single-Molecule Fluorescence Resonance Energy Transfer Studies of the Human Telomerase RNA Pseudoknot: Temperature-/Urea-Dependent Folding Kinetics and Thermodynamics," *The Journal of Physical Chemistry B*, vol. 118, pp. 3853–3863, 2014.

[259] V. M. Shelton, T. R. Sosnick, and T. Pan, "Applicability of Urea in the Thermodynamic Analysis of Secondary and Tertiary RNA Folding," *Biochemistry*, vol. 38, pp. 16831–16839, 1999.

[260] B. J. Bennion and V. Daggett, "The molecular basis for the chemical denaturation of proteins by urea," *Proceedings of the National Academy of Sciences*, vol. 100, pp. 5142–5147, 2003.

[261] E. D. Holmstrom, N. F. Dupuis, and D. J. Nesbitt, "Kinetic and Thermodynamic Origins of Osmolyte-Influenced Nucleic Acid Folding," *The Journal of Physical Chemistry B*, vol. 119, pp. 3687–3696, 2015.

[262] D. Lambert and D. E. Draper, "Denaturation of RNA Secondary and Tertiary Structure by Urea: Simple Unfolded State Models and Free Energy Parameters Account for Measured m-Values," *Biochemistry*, vol. 51, pp. 9014–9026, 2012.

[263] J. Yoon, D. Thirumalai, and C. Hyeon, "Urea-Induced Denaturation of $PreQ_1$ -Riboswitch," *Journal of the American Chemical Society*, vol. 135, pp. 12112–12121, 2013.

[264] L. J. Su, M. Brenowitz, and A. M. Pyle, "An Alternative Route for the Folding of Large RNAs: Apparent Two-state Folding by a Group II Intron Ribozyme," *Journal of Molecular Biology*, vol. 334, pp. 639–652, 2003.

[265] R. Russell, R. Das, H. Suh, K. J. Travers, A. Laederach, M. A. Engelhardt, and D. Herschlag, "The Paradoxical Behavior of a Highly Structured Misfolded Intermediate in RNA Folding," *Journal of Molecular Biology*, vol. 363, pp. 531–544, 2006.

[266] E. S. Courtenay, M. W. Capp, R. M. Saecker, and M. T. Record Jr., "Thermodynamic analysis of interactions between denaturants and protein surface exposed on unfolding: Interpretation of urea and guanidinium chloride m-values and their correlation with changes in accessible surface area

(ASA) using preferential interaction coefficients and the local-bulk domain model," *Proteins: Structure, Function, and Bioinformatics*, vol. 41, pp. 72–85, 2000.

[267] V. M. Shelton, T. R. Sosnick, and T. Pan, "Altering the Intermediate in the Equilibrium Folding of Unmodified Yeast tRNAPhe with Monovalent and Divalent Cations," *Biochemistry*, vol. 40, pp. 3629–3638, 2001.

[268] E. Tøstesen, S.-J. Chen, and K. A. Dill, "RNA Folding Transitions and Cooperativity," *The Journal of Physical Chemistry B*, vol. 105, pp. 1618–1630, 2001.

[269] B. Raju, E. Murphy, L. A. Levy, R. D. Hall, and R. E. London, "A fluorescent indicator for measuring cytosolic free magnesium," *American Journal of Physiology - Cell Physiology*, vol. 256, pp. C540–C548, 1989.

[270] N.-E. L. Saris, E. Mervaala, H. Karppanen, J. A. Khawaja, and A. Lewenstam, "Magnesium: An update on physiological, clinical and analytical aspects," *Clinica Chimica Acta*, vol. 294, pp. 1–26, 2000.

[271] T. Günther, "Concentration, compartmentation and metabolic function of intracellular free Mg2+," *Magnesium Research*, vol. 19, pp. 225–236, 2006.

[272] C. A. Strulson, N. H. Yennawar, R. P. Rambo, and P. C. Bevilacqua, "Molecular Crowding Favors Reactivity of a Human Ribozyme Under Physiological Ionic Conditions," *Biochemistry*, vol. 52, pp. 8187–8197, 2013.

[273] C. A. Strulson, J. A. Boyer, E. E. Whitman, and P. C. Bevilacqua, "Molecular crowders and cosolutes promote folding cooperativity of RNA under physiological ionic conditions," *RNA*, vol. 20, pp. 331–347, 2014.

[274] A. Pyle, "Metal ions in the structure and function of RNA," *JBIC Journal of Biological Inorganic Chemistry*, vol. 7, pp. 679–690, 2002.

[275] A. Fire, S. Xu, M. K. Montgomery, S. A. Kostas, S. E. Driver, and C. C. Mello, "Potent and specific genetic interference by double-stranded RNA in Caenorhabditis elegans," *Nature*, vol. 391, pp. 806–811, 1998.

[276] M. Mandal, B. Boese, J. E. Barrick, W. C. Winkler, and R. R. Breaker, "Riboswitches Control Fundamental Biochemical Pathways in Bacillus subtilis and Other Bacteria," *Cell*, vol. 113, pp. 577–586, 2003.

[277] R. R. Breaker, "Prospects for Riboswitch Discovery and Analysis," *Molecular Cell*, vol. 43, pp. 867–879, 2011.

[278] P. Ketzer, J. K. Kaufmann, S. Engelhardt, S. Bossow, C. v. Kalle, J. S. Hartig, G. Ungerechts, and D. M. Nettelbeck, "Artificial riboswitches for gene expression and replication control of DNA and RNA viruses," *Proceedings of the National Academy of Sciences*, pp. E554–E562, 2014.

[279] P. K. Choudhary and R. K. O. Sigel, "Mg2+-induced conformational changes in the btuB riboswitch from E. coli," *RNA*, vol. 20, pp. 36–45, 2014.

[280] T. Yamauchi, D. Miyoshi, T. Kubodera, A. Nishimura, S. Nakai, and N. Sugimoto, "Roles of Mg2+ in TPP-dependent riboswitch," *FEBS Letters*, vol. 579, pp. 2583–2588, 2005.

[281] M. Ali, J. Lipfert, S. Seifert, D. Herschlag, and S. Doniach, "The Ligand-Free State of the TPP Riboswitch: A Partially Folded RNA Structure," *Journal of Molecular Biology*, vol. 396, pp. 153–165, 2010.

[282] Q. Vicens, E. Mondragón, and R. T. Batey, "Molecular sensing by the aptamer domain of the FMN riboswitch: a general model for ligand binding by conformational selection," *Nucleic Acids Research*, vol. 39, pp. 8586–8598, 2011.

[283] S. P. Hennelly, I. V. Novikova, and K. Y. Sanbonmatsu, "The expression platform and the aptamer: cooperativity between Mg2+ and ligand in the SAM-I riboswitch," *Nucleic Acids Research*, vol. 41, pp. 1922–1935, 2013.

[284] J. Buck, J. Noeske, J. Wöhnert, and H. Schwalbe, "Dissecting the influence of Mg2+ on 3d architecture and ligand-binding of the guanine-sensing riboswitch aptamer domain," *Nucleic Acids Research*, vol. 38, pp. 4143–4153, 2010.

[285] J. B. Da Costa, A. I. Andreiev, and T. Dieckmann, "Thermodynamics and Kinetics of Adaptive Binding in the Malachite Green RNA Aptamer," *Biochemistry*, vol. 52, pp. 6575–6583, 2013.

[286] R. K. Montange and R. T. Batey, "Riboswitches: Emerging Themes in RNA Structure and Function," *Annual Review of Biophysics*, vol. 37, pp. 117–133, 2008.

[287] N. J. Baird and A. R. Ferré-D'Amaré, "Idiosyncratically tuned switching behavior of riboswitch aptamer domains revealed by comparative small-angle X-ray scattering analysis," *RNA*, vol. 16, pp. 598–609, 2010.

[288] A. Haller, M. F. Soulière, and R. Micura, "The Dynamic Nature of RNA as Key to Understanding Riboswitch Mechanisms," *Accounts of Chemical Research*, vol. 44, pp. 1339–1348, 2011.

[289] H. M. Al-Hashimi and N. G. Walter, "RNA dynamics: it is about time," *Current Opinion in Structural Biology*, vol. 18, pp. 321–329, 2008.

[290] J. Buck, A. Wacker, E. Warkentin, J. Wöhnert, J. Wirmer-Bartoschek, and H. Schwalbe, "Influence of ground-state structure and Mg2+ binding on folding kinetics of the guanine-sensing riboswitch aptamer domain," *Nucleic Acids Research*, vol. 39, pp. 9768–9778, 2011.

[291] M. M. Rudolph, M.-P. Vockenhuber, and B. Suess, "Synthetic riboswitches for the conditional control of gene expression in Streptomyces coelicolor," *Microbiology*, vol. 159, pp. 1416–1422, 2013.

[292] R. D. Jenison, S. C. Gill, A. Pardi, and B. Polisky, "High-resolution molecular discrimination by RNA," *Science*, vol. 263, pp. 1425–1429, 1994.

[293] J. E. Weigand, S. R. Gottstein-Schmidtke, S. Demolli, F. Groher, E. Duchardt-Ferner, J. Wöhnert, and B. Suess, "Sequence Elements Distal to the Ligand Binding Pocket Modulate the Efficiency of a Synthetic Riboswitch," *ChemBioChem*, vol. 15, pp. 1627–1637, 2014.

[294] I. Krstić, O. Frolow, D. Sezer, B. Endeward, J. E. Weigand, B. Suess, J. W. Engels, and T. F. Prisner, "PELDOR Spectroscopy Reveals Preorganization of the Neomycin-Responsive Riboswitch Tertiary Structure," *Journal of the American Chemical Society*, vol. 132, pp. 1454–1455, 2010.

[295] J. E. Sokoloski, S. E. Dombrowski, and P. C. Bevilacqua, "Thermodynamics of Ligand Binding to a Heterogeneous RNA Population in the Malachite Green Aptamer," *Biochemistry*, vol. 51, pp. 565–572, 2012.

[296] A. Reining, S. Nozinovic, K. Schlepckow, F. Buhr, B. Fürtig, and H. Schwalbe, "Three-state mechanism couples ligand and temperature sensing in riboswitches," *Nature*, vol. 499, pp. 355–359, 2013.

Appendix A

2PyA purified with the standard and the extended procedure

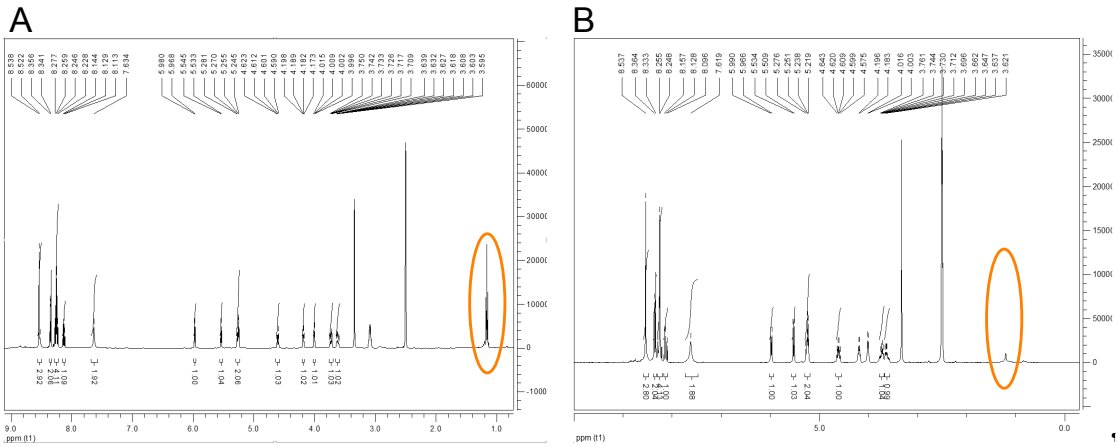

Figure A.1: ^{1}H-NMR spectra of 2PyA. A: Purification according to the standard procedure. B: Purification according to the extended procedure. Orange ellipses mark the triethyl amine caused signature. Solvent peaks: DMSO d6 at 2.50 ppm and H_2O at 3.33 ppm.

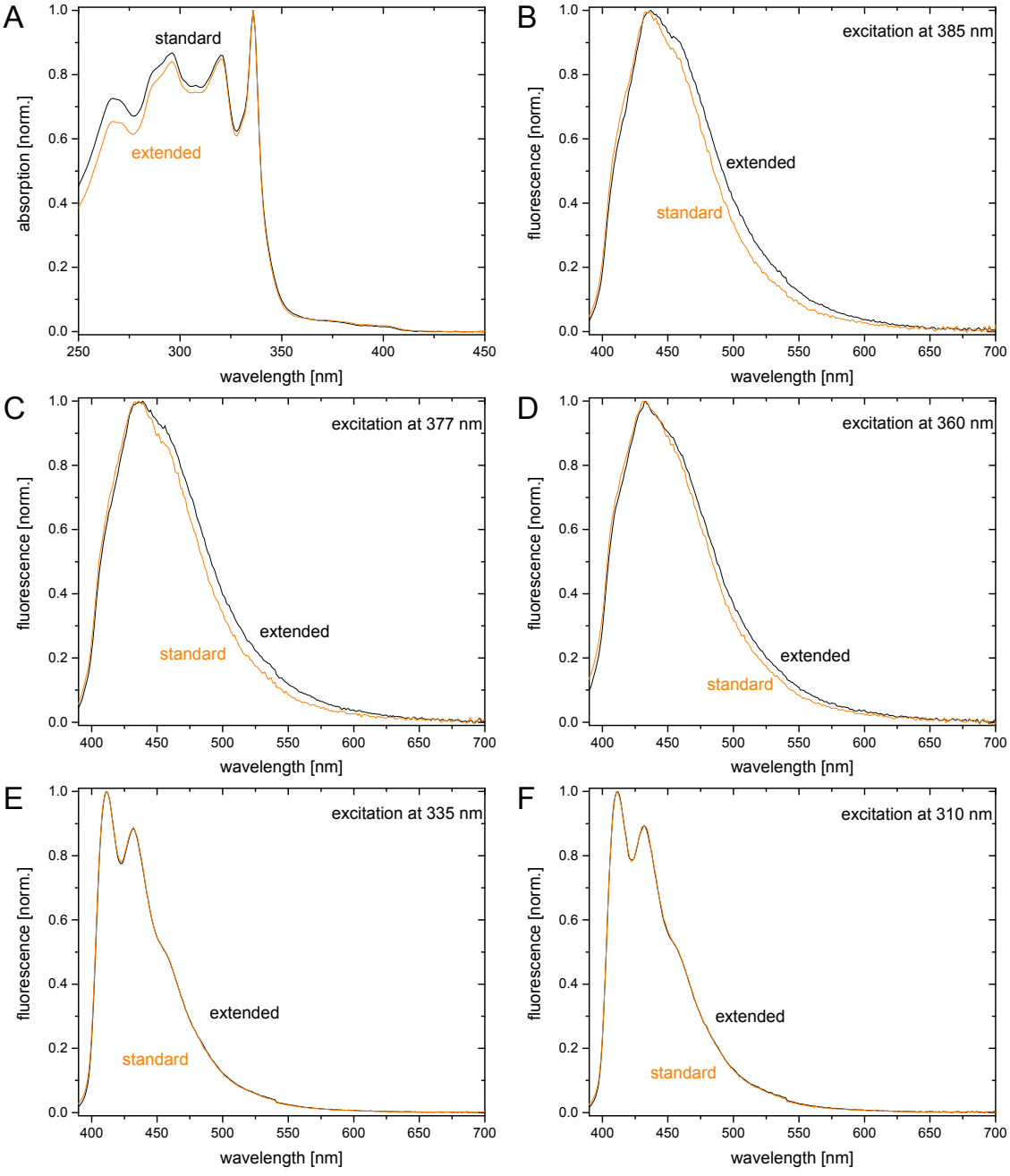

Figure A.2: Steady-state absorption and fluorescence spectra of 5 µM 2PyA in MeOH. Extended (black) purification is compared to standard purification (orange). A: Absorption. B: Emission after excitation at 385 nm. C: Emission after excitation at 377 nm. C: Emission after excitation at 360 nm. D: Emission after excitation at 335 nm. E: Emission after excitation at 310 nm.

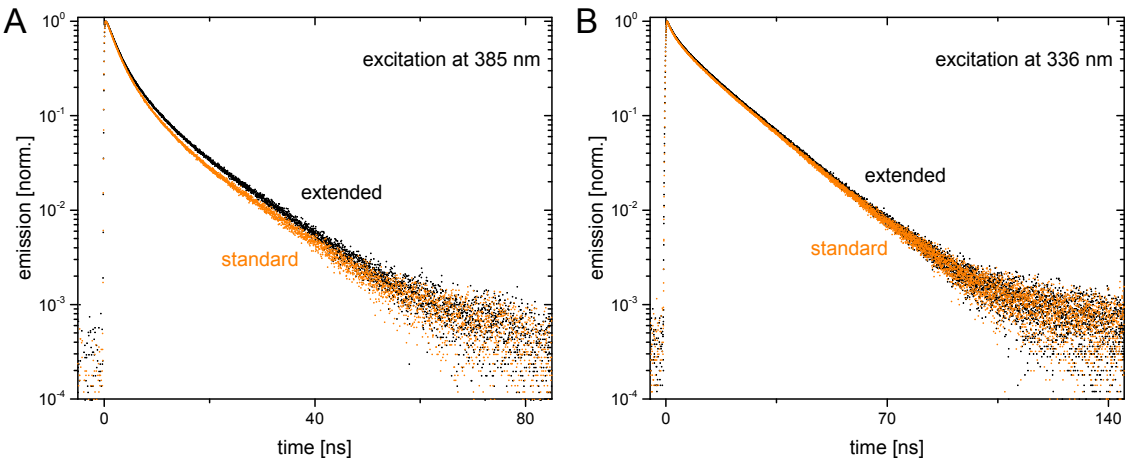

Figure A.3: Time-resolved fluorescence emission of 5 µM2PyA in MeOH. Extended (black) purification is compared to standard purification (orange). A: Excitation at 385 nm (GG400 filter). B: Excitation at 336 nm (GG385 filter).

Appendix B

Lifetime-density analysis

LDA was performed with Optimus and its implementation is described in detail in reference.[133] The TAS signal of 1PyA was evaluated with LDA and the result of the analysis is represented with an LDM (see figure 5.6).

LDM is based on a model closely related to the one of GLA:

$$S(\lambda_{\text{pump}}, \lambda_{\text{probe}}, t) = \int_0^\infty \mathrm{d}\tau \left(\Phi_(\lambda_{\text{pump}}, \lambda_{\text{probe}}, t) \times \exp[-t/\tau] \right) \tag{B.1}$$

The measured TA signal $S(\lambda_{\text{pump}}, \lambda_{\text{probe}}, t)$ is the Laplace transform of the spectral distribution function $\Phi(\lambda_{\text{pump}}, \lambda_{\text{probe}}, \tau)$. Φ is a continuous quantity and is replaced for computational reasons by a discrete (quasi-continuous) distribution, which is represented by a finite sum of amplitude-weighted exponential decay terms with lifetimes τ_i. The number of terms in this sum is typically > 50.

An LDM uses a color code to show the sizes of the pre-exponential factors ($\Phi(\lambda_{\text{probe}}, \tau_i)$) found in the LDA ordered along the spectral and the lifetime dimension in an intuitive way. Red represents positive amplitudes and this corresponds to the decrease of the signal (ESA decay or increase of GSB and SE). Blue represents negative amplitudes, which means th increase of the overall TA signal.

In difference to GLA, the τ_i are fixed and distributed evenly on a logarithmic scale to the base ten. The measured signal is then fitted to the sum according to an rms minimization, whereby only the pre-exponential factors are varied. The result represents a numeric inverse Laplace-transform of S.

Because this inverse Laplace-transform is a mathematically ill-posed problem, it is prone to yield oscillatory and unstable distributions due to overparametrization in the presence of experimental noise. Therefore, Thikonov-regularization is necessary to enforce smoothness and stability on the solution. The quality of the fit is then not only judged by the minimal rms value, but by the sum of the rms value and a regularization penalty weighed with a regularization factor α. The exact value of α is varied for each analysis and the optimal value is validated using the L-curve criterion, the minimal product method, and generalized cross validation.

Appendix C

Additional melting profiles of the TC aptamer

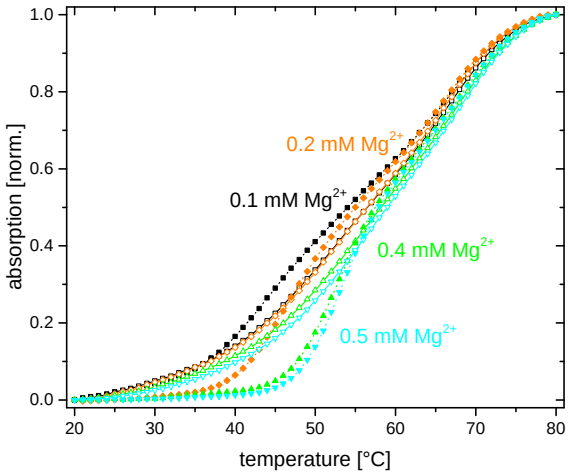

Figure C.1: Additional melting profiles of the TC aptamer in SCC buffer. [Mg^{2+}] is 0.1, 0.2, 0.4, and 0.5 mM in black, orange, green, and cyan, respectively. Open symbols with dashed lines represent the absence of TC and filled symbols with solid lines the presence of 7.5 μM TC. [RNA] = 1.5 μM.

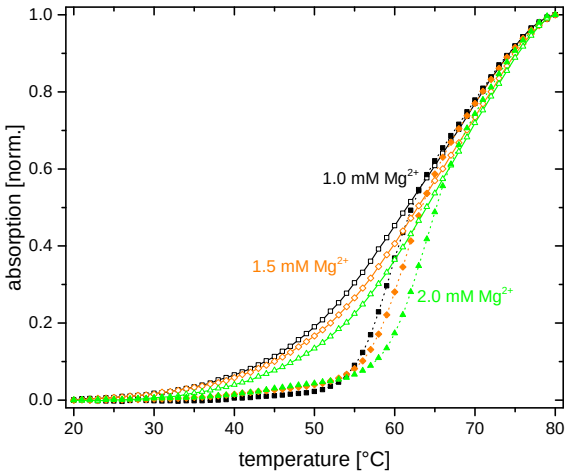

Figure C.2: Additional melting profiles of the TC aptamer in SCC buffer. [Mg^{2+}] is 1.0, 1.5, and 2.0 mM in black, orange, and green respectively. Open symbols with dashed lines represent the absence of TC and filled symbols with solid lines the presence of 7.5 µM TC. [RNA] = 1.5 µM.

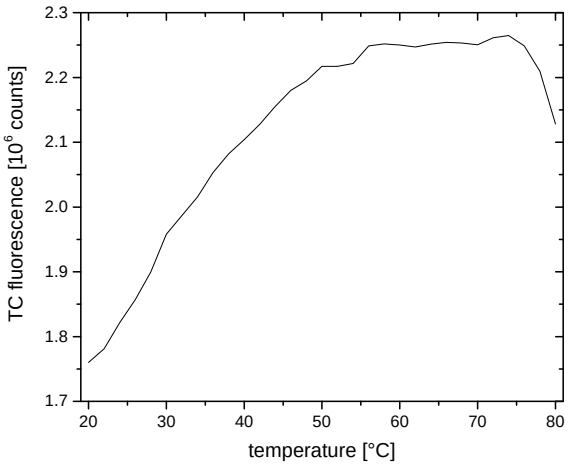

Figure C.3: Temperature dependent emission of bare TC (7.5 µM) in SCC buffer with 0.8 mM Mg^{2+}.